University of Windsor

Scholarship at UWindsor

2008

Metallic bipolar plates for proton exchange membrane (PEM) fuel cells

Yan Wang
University of Windsor

Follow this and additional works at: https://scholar.uwindsor.ca/etd

METALLIC BIPOLAR PLATES FOR PROTON EXCHANGE MEMBRANE (PEM) FUEL CELLS

By

Yan Wang

A Dissertation
Submitted to the Faculty of Graduate Studies
through Engineering Materials
in Partial Fulfillment of the Requirements
for the Degree of Doctor of Philosophy at the
University of Windsor

Windsor, Ontario, Canada

2008

DECLARATION OF CO-AUTHORSHIP/PREVIOUS PUBLICATION

I. Co-Authorship Declaration

I hereby declare that this thesis incorporates material that is result of joint research, as follows: In all cases, the key ideas, primary contributions, experimental designs, data analysis and interpretation, were performed by the author, and the contribution of co-authors was primarily through the provision of supervision, guidance, funding and facilities.

I am aware of the University of Windsor Senate Policy on Authorship and I certify that I have properly acknowledged the contribution of other researchers to my thesis, and have obtained written permission from each of the co-author(s) to include the above material(s) in my thesis.

I certify that, with the above qualification, this thesis, and the research to which it refers, is the product of my own work.

II. Declaration of Previous Publication

This thesis includes [10] original papers that have been previously published/submitted for publication in peer reviewed journals, as follows:

Thesis Chapter	Publication title/full citation	Publication status
Chapter 4	An investigation on metallic bipolar plate corrosion in simulated anode and cathode environments of PEM fuel cells using potential-pH diagrams	Published
Chapter 4	An investigation of commercial Grade 2 titanium as a bipolar plate material for PEM fuel cells	Published
Chapter 4	Life-limiting Aspects of the Corrosion of Metallic Bipolar Plates for PEM Fuel Cells	Published
Chapter 4	An Electrochemical Investigation of Potential Metallic Bipolar Plate Materials for PEM Fuel Cells	Submitted
Chapter 5	Effects of O_2 and H_2 on the corrosion of SS316L metallic bipolar plate materials in simulated anode and cathode environments of PEM fuel cells	Published
Chapter 6	An investigation into TiN-coated 316L stainless steel as a bipolar plate material for PEM Fuel Cells	Published
Chapter 7	An investigation into polypyrrole coated 316L stainless steel as a bipolar plate material for PEM fuel cells	Published
Chapter 7	An investigation into the effects of a nano gold interlayer on polypyrrole coatings on 316L stainless steel for the bipolar plates of PEM fuel cells	Published
Chapter 7	An investigation into the nucleation and growth of an electropolymerized polypyrrole coating on a 316L stainless steel surface	Published
Chapter 7	Optimization of the Polypyrrole-coating Parameters for Proton Exchange Membrane Fuel Cell (PEMFC) Bipolar Plates using the Taguchi Method	Published

I certify that I have obtained a written permission from the copyright owner(s) to include the above published material(s) in my thesis. I certify that the above material describes work completed during my registration as graduate student at the University of Windsor.

I declare that, to the best of my knowledge, my thesis does not infringe upon anyone's copyright nor violate any proprietary rights and that any ideas, techniques, quotations, or any other material from the work of other people included in my thesis, published or otherwise, are fully acknowledged in accordance with the standard referencing practices. Furthermore, to the extent that I have included copyrighted material that surpasses the bounds of fair dealing within the meaning of the Canada Copyright Act, I certify that I have obtained a written permission from the copyright owner(s) to include such material(s) in my thesis.

I declare that this is a true copy of my thesis, including any final revisions, as approved by my thesis committee and the Graduate Studies office, and that this thesis has not been submitted for a higher degree to any other University of Institution.

ABSTRACT

With escalating oil prices and increasing environmental concerns, increasing attention is being paid to the development of proton exchange membrane fuel cells (PEMFCs). A significant part of the PEMFC stack is the bipolar plates (BPs), which account for about 80% of the total weight and 45% of the stack cost. Bipolar plates have traditionally been made of non-porous graphite, which suffers from high cost, heavy weight, low mechanical strength and the need to machine the flow channels. Metallic bipolar plates have many potential advantages, but in the operating environment of the fuel cell they are prone to corrosion or dissolution. To overcome these difficulties, six metals, including SS316L, SS347, SS410, A36 steel, Al6061 and Grade 2 Ti, were investigated as potential bipolar plate materials in the simulated PEMFC working conditions. Based on the corrosion and interfacial contact resistance results and price, SS316L was chosen as the candidate bipolar plate material.

TiN was coated on SS316L using a Plasma Assisted Physical Vapor Deposition (PAPVD) coating technology and the coatings were about 15μm thick. The TiN-coating increased the polarization resistance by a factor of 30 and reduced the corrosion current density by a factor of 40.

Polypyrrole, a conductive polymer, has been coated on SS316L using electrochemical methods. Potentiodynamic tests showed that the corrosion current density is decreased by a factor of 17 and polarization resistance was increased by a factor of 10.5 by coating with polypyrrole. The nucleation and growth of polypyrrole can be divided into three stages. The first stage is the incubation period. The second stage is a combination of instantaneous nucleation with 2-D (IN2D) or 3-D growth (IN3D). The third stage is a combination of instantaneous nucleation or progressive nucleation and 3-D growth (IN3D and PN3D). A Taguchi DOE method was then used to optimize the polypyrrole-coating parameters for SS316L for metallic bipolar plate application. In order to further improve the characteristics of polypyrrole coating, an Au interlayer was coated on SS316L before coating polypyrrole.

ACKNOWLEDGEMENTS

Table of Contents

LIST OF TABLES

LIST OF FIGURES

Chapter 3

Chapter 4

Chapter 5

Chapter 6

Chapter 7

NOMENCLATURE

ABBREVIATIONS

AFC	Alkaline fuel cell
AFM	Atom force microscopy
BMC	Bulk-moulding compound
BP	Bipolar plate
BSD	Back scattered detector
CB	Carbon black
CNT	Carbon nanotube
DC	Direct current
DLC	Diamond like carbon
DMFC	Direct methanol fuel cell
EDX	Energy dispersive x-ray
EIS	Electrochemical impedance spectroscopy
ESEM	Environmental scanning electron microscope
EW	Equivalent weight
FCC	Face centered cubic
FTIR	Fourier transform infrared spectroscopy
GDL	Gas diffusion layer
HVOF	High velocity oxy-fuel
ICP-MS	Inductively coupled plasma mass spectrometry
ICP-OES	Inductively coupled plasma optical emission spectrometry
ICR	Interfacial contact resistance
IN	Instantaneous nucleation
IEMFC	Ion exchange membrane fuel cell
K	Equilibrium constant
MBTS	Dibenzothiazyl disulphide
MCFC	Molten carbonate fuel cell
MEA	Membrane electrode assembly
OCP	Open circuit potential

PAFC	Phosphoric acid fuel cell
PEMFC	Polymer electrolyte membrane fuel cell
PET	Polyethylene terephthalate
PN	Progressive nucleation
PP	Polypropylene
ppm	Parts per million
PPS	Polyphenylene sulfide
PSEPVE	Perfluoro-sulfonylfluoride ethyl-propyl-vinyl ether
PVD	Physical vapor deposition
PVDF	Polyvinylidene fluoride
SCE	Saturated calomel electrode
SEM	Scanning electron microscopy
SOFC	Solid oxide fuel cell
SP(E)FC	Solid polymer (electrolyte) fuel cell
SS	Stainless steel
TFE	Tetrafluorethylene
TiN	Titanium nitride
TMTD	Tetramethylthiuram disulphide
XRD	X-ray diffraction
2-D	2-dimensional
3-D	3-dimensional

SYMBOLS

a	Chemical activity
e	Electrode potential
e^o	Standard electrode potential
F	Faraday constant
i	Current density
i_0	Exchange current density
i_{corr}	Corrosion current density
i_L	Limiting current density

n	Number of electrons transferred in the reaction
R	Universal gas constant
R_a	Roughness
R_p	Polarization resistance
T	Temperature

GREEK SYMBOLS

α	Electron transfer coefficient of the reaction at the electrode
β_a	Tafel slopes of the anodic reaction
β_c	Tafel slopes of the cathodic reaction
η_{act}	Activation overvoltage
η_{conc}	Concentration polarization
η_{ohm}	Ohmic overpotential

CHAPTER 1

INTRODUCTION

Fuel cells are electrochemical devices which are continuously fueled by fuel and oxygen. Each cell consists of an electrolyte (a conducting ionic membrane) with an integrated porous anode and cathode. Hydrogen and/or hydrocarbon fuels react at the anode side, while oxygen (from air) reacts at the cathode side. The output is electrical energy in the form of direct current [1].

Although there are different types of fuel cell, generally a fuel cell assembly is composed of the following components [1]:

- Electrolyte membrane (with high ionic conductivity and retained hermetic seal)
- Anode (fuel side of the electrode with a porous composite structure containing ion-conducting media, high surface areas for reaction, and catalysts lodged at the triple points where the reaction occurs among the gases, ions, and electrons)
- Cathode (air side of the electrode, with the same properties as the anode but in an oxidizing environment), and
- Separator and gas-flow structures (supplying air and fuel flow to the electrodes and also separating each cell hermetically while conducting electrons).

Fuel cells are environmentally friendly devices for energy conversion and power generation, and are one of the most promising candidates as a zero-emission power source. Hence, they are often regarded as one of the advanced energy technologies of the future. In reality, fuel cells are one of the oldest energy conversion devices known to humankind, although their development and deployment for practical applications lags far behind other competitive technologies, mainly heat engines such as the steam turbine and the internal combustion engine [2]. Nowadays, with escalating oil prices and increasing environmental concerns, increasing attention is being paid to the development of fuel cells [3-11]. The solid-state fuel cell has the potential to generate another new age, in the areas of distributed energy, a cleaner environment, and more efficient use of the earth's natural resources. The need for cleaner energy-producing equipment is becoming

a commercial necessity and will continue to grow in importance as the demand for oil outpaces production capacity in the next decade [12]. Advancements in materials science, chemical engineering, as well as in mechanical engineering, will be needed to ensure the chemical and mechanical long-term reliability of fuel cell technologies

1.1 Proton exchange membrane (PEM) fuel cell

Among the various fuel cell systems known today, the polymer electrolyte membrane fuel cell (PEMFC) system has proven to be an attractive and more promising option than alkaline, solid oxide, or molten carbonate fuel cell systems for power generation in portable, stationary, and mobile (automobile) applications [6]. Polymer electrolyte membrane fuel cells are also known as ion exchange membrane fuel cells (IEMFCs), solid polymer (electrolyte) fuel cells (SP(E)FCs), and proton exchange membrane fuel cells (PEMFCs). The use of a solid polymer membrane as an electrolyte separator in fuel cell applications offers several advantages, such as selectivity, system simplicity, and improved reliability compared with systems based on a liquid electrolyte.

1.2 Bipolar plates of PEM fuel cell

A significant part of the PEM fuel cell stack is the bipolar plates (BPs) [13], which account for about 80% of total weight and 45% of stack cost [14]. They are designed to accomplish many functions, such as distribute reactants uniformly over the active areas, remove heat from the active areas, carry current from cell to cell and prevent leakage of reactants and coolant. Furthermore, the plates must be of inexpensive, lightweight materials and must be easily (inexpensively) manufactured. Efforts are underway to develop bipolar plate materials that satisfy these demands. The main materials studied to date include non-porous graphite, sheet metal (coated and uncoated) and graphite polymer composites. Currently, the non-porous graphite is the most commonly used bipolar plate material because of its chemical and thermal stability in the PEM fuel cell environments. However, it is fraught with problems of high cost, low mechanical strength and the need for machining the flow channels [15]. Hence, other suitable materials are being studied in order to replace the non-porous graphite.

1.3 Focus of this study

Metallic materials have good mechanical stability, electrical conductivity and thermal conductivity and can be readily and consistently stamped to desired shape to accommodate the flow channels [16]. Unfortunately, metallic materials are prone to corrosion in the PEM fuel cell conditions. Some researchers [17, 18] have reported that metal ions, such as those produced by corrosion of metallic materials, can migrate to the membrane and that levels as low as 5~10ppm can degrade the membrane performance. Furthermore, any corrosion layer that is formed, will lower the electrical conductivity of the bipolar plates, and increase the potential loss because of a higher electrical resistance. Therefore, in order to be suitable bipolar plate material, metals need to have superior corrosion resistance.

The focus of this dissertation is an investigation of potential metallic bipolar plate materials and their corrosion behaviour of metallic bipolar plates in simulated PEM fuel cell environments. Different coating methods and materials have been investigated to improve the corrosion resistance of the base materials. Six metals, including SS316L, SS347, SS410, A36 steel, Al6061 and Grade 2 Ti, were investigated as potential bipolar plate materials. The corrosion mechanism in the PEM fuel cell environments was investigated using potentiodynamic, potentiostatic and electrochemical impedance methods. SS316L was the main material studied as a candidate bipolar plate material because of its high corrosion resistance and relatively cheap price. Furthermore, in order to improve the corrosion resistance of the base materials, both polypyrrole (a conductive polymer) and TiN were coated on the metals by electrochemical and PVD methods, respectively.

References

1. R.W.Lashway, Fuel cells: the next evolution. MRS Bulletin, 30(2005)581-583.

2.X.Li, Principles of Fuel Cells, Taylor & Francis Group, LLC, 2006, pp1.

3. D.A.Boysen., T.Uda, C.R.I.Chisholm, S.M.Haile, High-performance solid acid fuel cells through humidity stabilization. Science, 303(2004)68-70.

4. Z.Zhan and S.A.Barnett, An octane-fueled solid oxide fuel cell. Science, 308(2005)844-847.

5. P.Costamagna, C.Yang, A.B.Bocarsly, S.Srinivasan, Nafion® 115/zirconium phosphate composite membrane for operation of PEMFCs above 100°C. Electrochimica Acta, 47(2002)1023-1033.

6. R.G.Rajendran, Polymer electrolyte membrane technology for fuel cells. MRS Bulletin, 30(2005)587-590.

7 T.A.Morris, E.A.Barringer, S.C.Kung, and R.W.McKain, An all-ceramic interconnect for use in solid-oxide fuel cell stacks. MRS Bulletin, 30(2005)596-600.

8. M.Farooque, C.Yuh, and H.C.Maru, Carbonate fuel cell technology and materials. MRS Bulletin, 30(2005)602-606.

9. N.P.Brandon, S.Skinner, and B.C.H.Steele, Recent advances in materials for fuel cells. Annu Rev Mater Res., 33(2003)183-213.

10.V.R.Stamenkovic, B.Fowler, B.S.Mun, G.Wang, P.N.Ross, C.A.Lucas and N.M. Markovic, Improved oxygen reduction activity on [Pt.sub.3]Ni(111)via increased surface site availability. Science 315(2007)493-497.

11. V.Mehta, J.S.Cooper, Review and analysis of PEM fuel cell design and manufacturing. J. Power Sources, 114(2003)32-53.

12.T.Appenzeller, National Geographic (June 2004) pp80.

13. R.L.Borup, N.E.Vanderborgh, Design and testing criteria for bipolar plate materials for PEM fuel cell applications. Mat.Res.Soc.Symp.Proc., 393(1995)151-155.

14. H.Tsuchiya, O.Kobayashi, Mass production cost of PEM fuel cell by learning curve. Int.J.Hydrogen Energy, 29 (2004) 985-990.

15. R.C.Makkus, A.H.H.Janssen, F.A.De Bruijin, R.K.A.M.Mallant, Stainless steel for cost-competitive bipolar plates in PEMFCs. Fuel Cell Bull., 3(2000)5-9.

16. A.Hermann, T.Chaudhuri, P.Spagnol, Bipolar plates for PEM fuel cells: A review. Int.Hydrogen Energy, 30(2005)1297-1302.

17 L.Ma, S.Warthesen, D.A.Shores, Evaluation of materials for bipolar plates in PEMFCs. J. New Mater. Electrochem. Syst., 3(2000)221-228.

18. M.P.Brady, K.Weisbrod, I,Paulauskas, R.A.Buchanan, K.L.More, H.Wang, M.Wilson, F.Garzon, L.R.Walker, Preferential thermal nitridation to form pin-hole free Cr-nitrides to protect proton exchange membrane fuel cell metallic bipolar plates. Scripta Mater., 50(2004)1017-1022.

CHAPTER 2

LITERATURE REVIEW

2.1 What is a fuel cell?

A fuel cell is an electrochemical device that converts the chemical energy of a fuel directly into electricity (Figure 2.1) [1]. Fuel cells are different from batteries. Chemicals deposit inside batteries. However, fuel and oxidant deposit outside the fuel cell. Theoretically, if fuel and oxidant are supplied continually, the fuel cell can produce electricity.
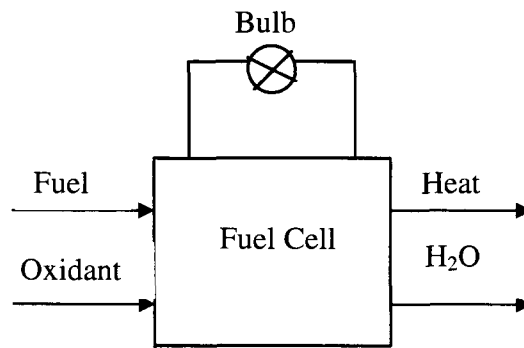
Fig 2.1. Fuel cell working principles [1]

2.1.1 The history of fuel cells

In 1839 William Grove first discovered the fuel cell working principles and he built a fuel cell using electrolytic H_2 and O_2 as shown in Fig 2.2 [2,3].
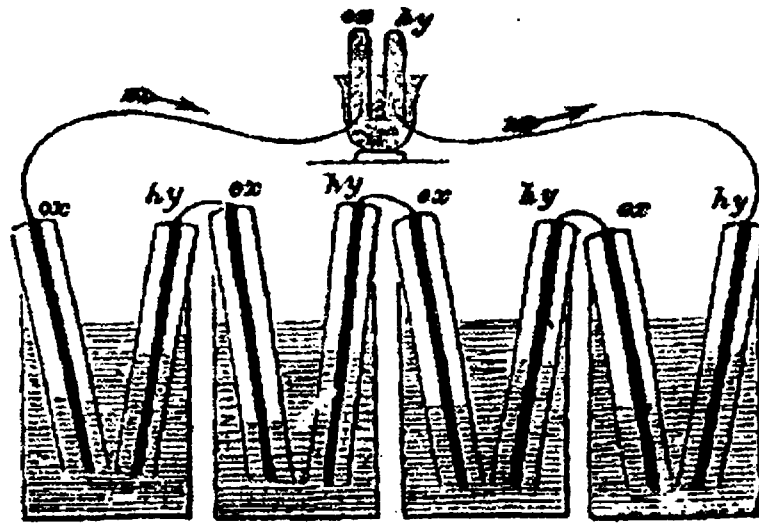
Fig 2.2 William Grove's fuel cells connected to an electrolysis cell for decomposition of water to hydrogen and oxygen [2, 3]

However, the generator was invented at the same time. Therefore, people lost interest in fuel cell research. Another reason why fuel cells were not researched is that electrode dynamics was not fully developed. In the 1960s, American spaceflight technology was developed. In 1966, the Apollo space mission was launched and people showed a great interest in fuel cells. Fig 2.3 [4] is a photograph of the fuel cells in the Apollo space missions.
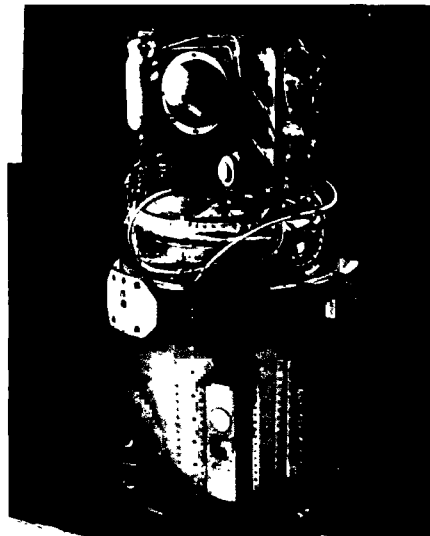
Fig 2.3 Fuel cells for Apollo space missions [4]

7

Following the Apollo program, the extent of fuel cell research gradually decreased because of the end of the moon missions. In the 1970s, with the war in the Middle East, many countries were developing fuel cells in order to solve the energy crisis. Nowadays, there is renewed interest in developing fuel cells because of escalating oil prices and increasing environmental concerns. The world is using more and more oil and oil prices are increasing rapidly. Fig 2.4 [5] shows the increasing petroleum consumption since 1960.
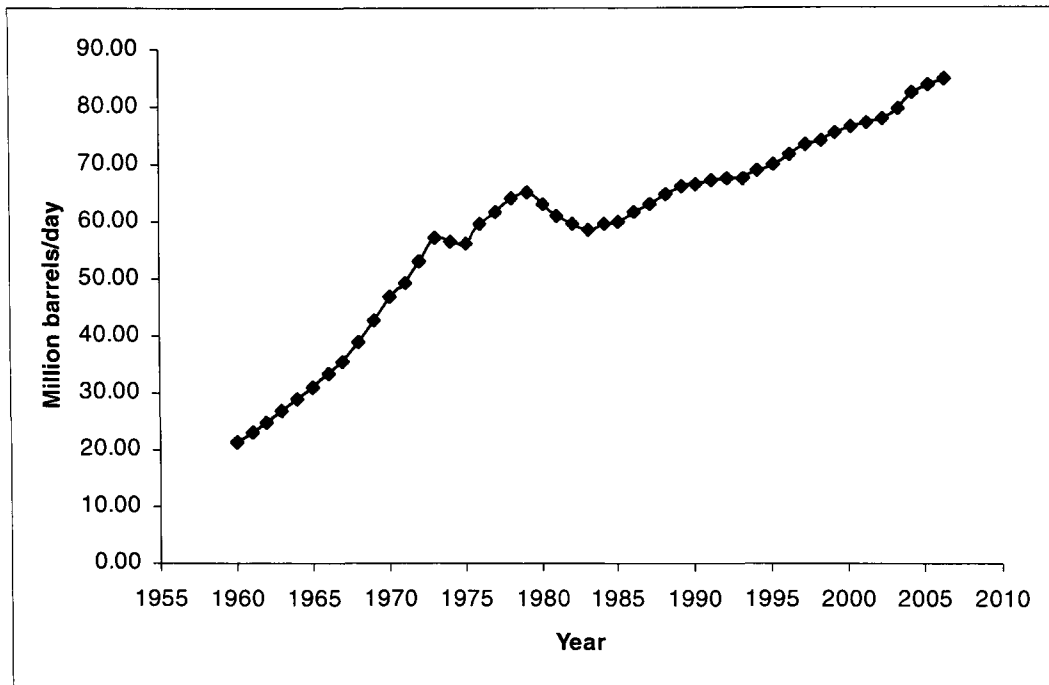
Fig 2.4 Petroleum consumption in the world [5]

Fig 2.5 [6] shows us the oil price in the last 30+ years. Although oil prices often fluctuate, the overall trend is increasing. Oil was US$40/barrel in 2004, but is currently more than US$120/barrel. Furthermore, petroleum reserves are decreasing as more petroleum is consumed. Oil is becoming one of the most important factors to prevent the growth of the economy in many countries.
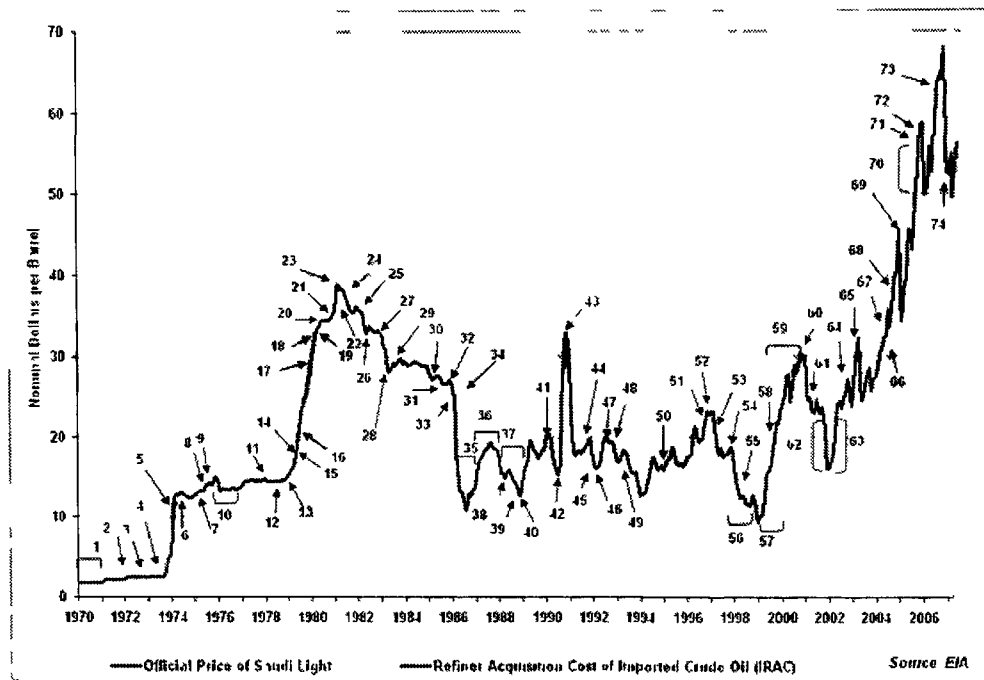
Fig 2 5 The petroleum price [6]

2.1.2 Types of fuel cell

In general, fuel cells can be classified in terms of the electrolyte Table 2 1 [7] is a summary of the types of fuel cell and their working characteristics

9

Table 2.1.Fuel cell types and their operating characteristics [7]

	Type					
	AFC	PEMFC	DMFC	PAFC	MCFC	SOFC
Electrolyte	aqueous potassium hydroxide (30-40%)	sulphonated organic polymer (hydrated during operation)	sulphonated organic polymer (hydrated during operation)	phosphoric acid	molten lithium/sodium/ potassium carbonate	yttria-stabilised zirconia
Operating temperature, °C	60-90	70-100	90	150-220	600-700	650-1000
Charge carrier	OH^-	H^+	H^+	H^+	CO_3^{2-}	O^{2-}
Anode	nickel (Ni) or precious metal	platinum (Pt)	platinum-ruthenium (Pt, Ru)	platinum (Pt)	nickel/chromium oxide	nickel/yttria-stabilised zirconia
Cathode	platinum (Pt) or lithiated NiO	platinum (Pt)	platinum-ruthenium (Pt, Ru)	platinum (Pt)	nickel oxide (NiO)	strontium (Sr) doped lanthanum manganite
Co-generation heat	none	low quality	none	acceptable for many applications	high	high
Electrical efficiency, %	60	40-45	30-35	40-45	50-60	50-60
Fuel sources	H_2 Removal of CO_2 from both gas streams necessary	H_2 Reformate with less than 10 ppm CO	water/methanol solution	H_2 reformate	H_2, CO, natural gas	H_2, CO, natural gas

AFC: Alkaline fuel cell

PEMFC: Proton exchange membrane fuel cell

DMFC: Direct methanol fuel cell

PAFC: Phosphoric acid fuel cell

MCFC: Molten carbonate fuel cell

SOFC: Solid oxide fuel cell

2.1.2.1 Alkaline fuel cell (AFC)

The AFC's (Fig 2.6) operating temperature is between 60-90°C. The electrolyte is aqueous potassium hydroxide. Platinum is presently being used as both the anode and cathode electrocatalyst and some non-precious metals, such as Ni, are also being researched in order to lower the price. The major problem in AFCs is carbonation, which is because the strongly alkaline electrolytes that are used adsorb CO_2, which can reduce the electrolyte conductivity. This means that H_2 containing CO_2 can not be used as a fuel,

10

and air has to "scrubbed" free of CO_2 prior to use as an oxidant in an AFC. Therefore, AFCs have only been used in niche markets, for example in space applications [8].

The electrochemical reactions in an AFC are as follows:

Anode Reaction: $2H_2 + 4OH^- => 4H_2O + 4e^-$ **2.1**

Cathode Reaction: $O_2 + 2H_2O + 4e^- => 4OH^-$ **2.2**

Overall Cell Reaction: $2H_2 + O_2 => 2H_2O$ **2.3**
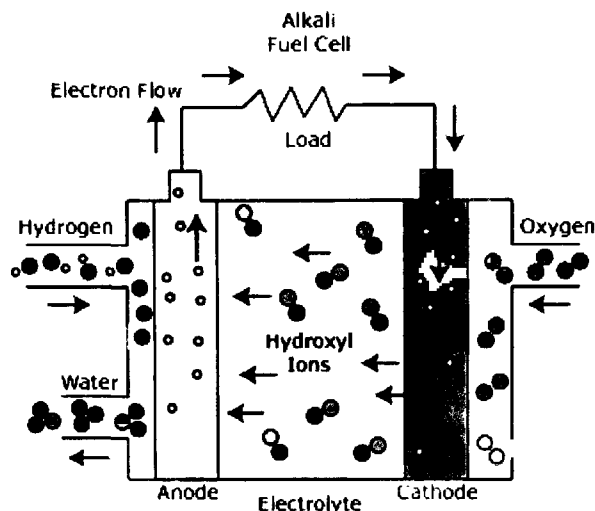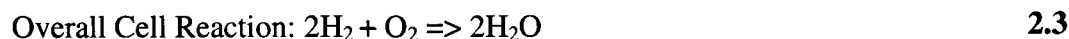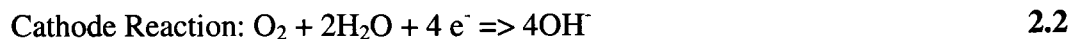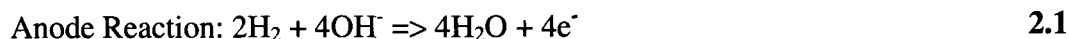
Fig 2.6 A schematic illustration of the alkaline fuel cell [9]

2.1.2.2 Proton exchange membrane fuel cell (PEMFC)

A PEMFC's (Fig 2.7) operating temperature range is between 70-100°C. The electrolyte is a proton exchange polymer membrane. Nowadays, PEMFC are one of the most promising candidates for use in the automotive industry. The Nafion membrane, produced by Du Pont, is being widely used as an electrolyte in PEMFCs because it has a high conductivity and low equivalent weight. Platinum and platinum alloys, supported on carbon black, are being used as both anode and cathode electrocatalysts.

The electrochemical reactions in a PEMFC are as follows:

Anode Reaction: $2H_2 => 4H^+ + 4e^-$ **2.4**

Cathode Reaction: $O_2 + 4H^+ + 4e^- => 2H_2O$ **2.5**

Overall Cell Reaction: $2H_2 + O_2 => 2H_2O$ **2.6**
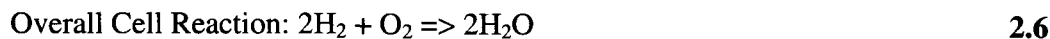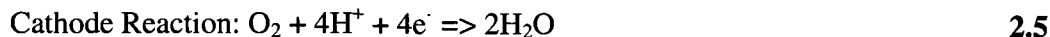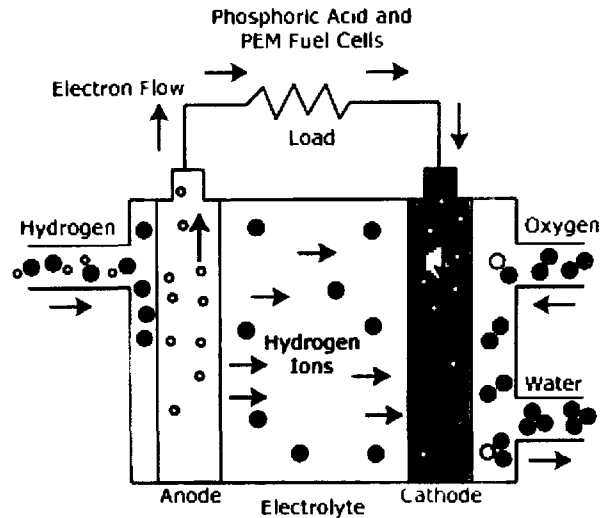
Fig 2.7 A schematic illustration of the proton exchange membrane and phosphoric acid fuel cells [10]

In fact, DMFC is a PEM fuel cell that use methanol as a fuel because its electrolyte is also sulphonated organic polymer. The DMFC operates at about 90°C and methanol is fed directly into the fuel cell. Poor anode electrocatalyst activity and methanol crossover from the anode to the cathode are the major drawbacks facing the development of DMFCs.

The electrochemical reactions in a DMFC are as follows:

Anode Reaction: $CH_3OH + H_2O => CO_2 + 6H^+ + 6e$ **2.7**

Cathode Reaction: $3/2O_2 + 6 H^+ + 6e^- => 3H_2O$ **2.8**

Overall Cell Reaction: $CH_3OH + 3/2O_2 => CO_2 + 2H_2O$ **2.9**
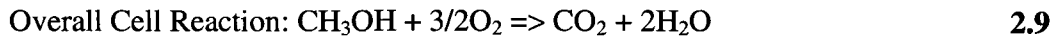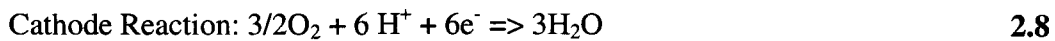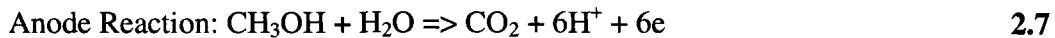
2.1.2.3 Phosphoric acid fuel cell (PAFC)

A PAFC (Fig 2.7) is mainly operated between 150-220°C, which gives this type of fuel cell higher performance than a PEMFC because the reaction rate is increased with the higher temperature. Platinum based electrocatalysts are being used in PAFCs for both the anode and cathode electrodes.

The electrochemical reactions in a PAFC are as follows:

Anode Reaction: $2H_2 => 4H^+ + 4e^-$ **2.10**

Cathode Reaction: $O_2 + 4H^+ + 4e^- => 2H_2O$ **2.11**
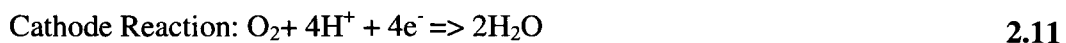
12

2.1.2.4 Molten carbonate fuel cell (MCFC)

The idea of using coal directly to produce electricity from a fuel cell was behind the invention of the MCFC (Fig 2.8) in the 1960s. Natural gas, rather than coal, is being used today to enhance the MCFC efficiency. At high temperatures, between 600-700°C, hydrocarbons can be internally reformed [11]. Li_2CO_3/Na_2CO_3 materials stabilized in an alumina-based matrix are widely used today as the electrolyte. Ni is used as an anode electrocatalyst. Al and Cr are being used added to the Ni anode electrocatalyst to enhance its corrosion resistance. Lithiated NiO materials also have been used as cathode electrocatalysts [11].

The electrochemical reactions in a MCFC are as follows:

Anode Reaction: $CO_3^{2-} + H_2 => H_2O + CO_2 + 2e^-$ **2.13**

Cathode Reaction: $CO_2 + 1/2O_2 + 2e^- => CO_3^{2-}$ **2.14**

Overall Cell Reaction: $H_2(g) + \frac{1}{2}O_2(g) + CO_2 => H_2O(g) + CO_2$ **2.15**
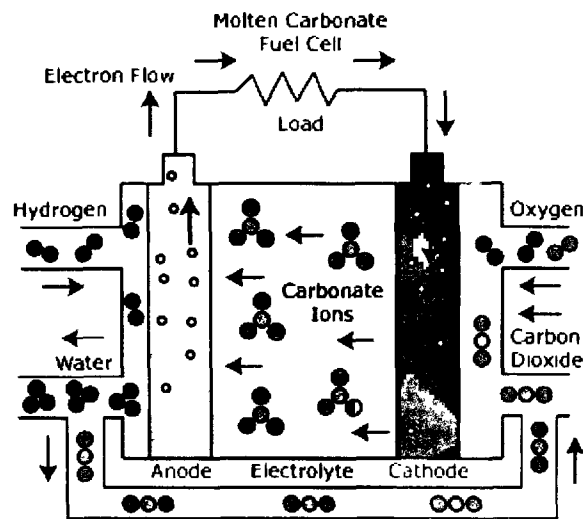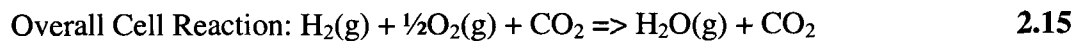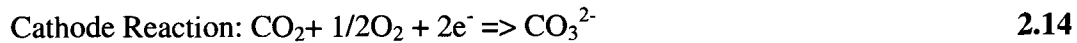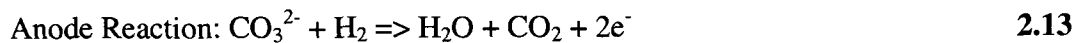
Fig 2.8 A schematic illustration of the molten carbonate fuel cell [12]

2.1.2.5 Solid oxide fuel cell (SOFC)

A SOFC (Fig 2.9) operates between 650-1000°C, which facilitates the ionic conductivity of the ceramic material and the internal reforming of hydrocarbon fuels. It uses a ceramic solid phase electrolyte such as yttria-stabilized zirconia (Y_2O_3-ZrO_2).

Ruthenium, supported on either TiO_2 or $LaCrO_3$, has been found to be the best anode electrocatalyst, while doped lanthanum magnetite ($LaMnO_3$) is being used as a cathode electrocatalyst [11].

The electrochemical reactions in a SOFC are as follows:

Anode Reaction: $2H_2 + 2O^{2-} => 2H_2O + 4e^-$ **2.17**

Cathode Reaction: $O_2 + 4e^- => 2O^{2-}$ **2.18**

Overall Cell Reaction: $2H_2 + O_2 => 2H_2O$ **2.19**
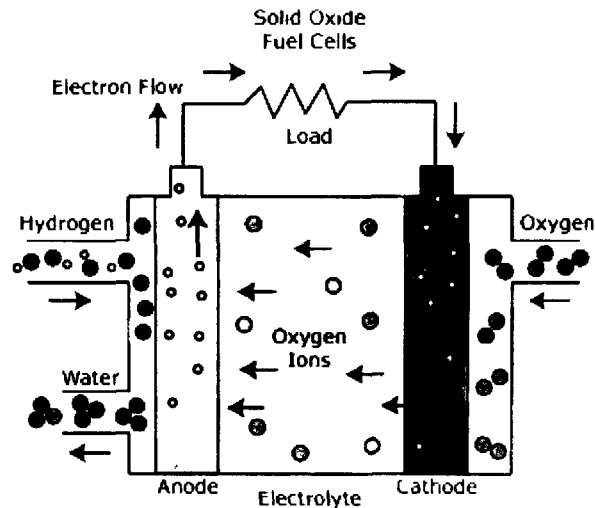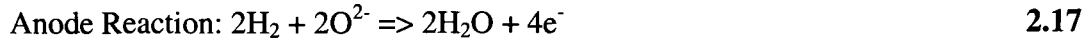
Fig 2.9 A schematic illustration of the solid oxide fuel cell [13]

2.2 Advantages of fuel cells

Fuel cells have many advantages when compared with traditional energy conversion technologies [14]. The advantages include:

• High efficiency: Fuel cell reactions are at anode and cathode, and it does not generate heat energy, so the reaction efficiency is not limited by the carnot cycle.

• Low or zero pollution: When fuel cells operate on hydrogen, they do not generate any pollution and the only exhaust is unused air and water. If other fuels are used in fuel cells, the emissions are much lower than for other energy technologies (Table 2.2) [15,16].

14

Table 2.2 Emissions of Fuel Cell Power Plants versus Traditional Combustion-Based
Power Plants [15,16]

	NO$_x$ Emissions (lbs/MWh)	SO$_2$ Emissions (lbs/MWh)
Average U.S. Fossil Fuel Plant	4.200	9.210
Microturbine	0.490	0.000
Small Gas Turbine	0.467	0.000
Combined-Cycle Gas Turbine	0.230	0.005
Carbonate Fuel Cell	0.016	0.000

• National security: Fuel cells use hydrogen or other materials as fuel. Although hydrogen is not easy to acquire, there are still some methods to produce it, for example, electrolysis of water, reforming hydrocarbon fuels and biomass hydrogen. This will reduce dependence on foreign oil, which has an important impact on national security.

• Quiet: Fuel cells are extremely quiet in operation due to their nature of operation. Therefore, fuel cells can be used in residential and military areas where the noise is not allowed [17].

• Size and weight: Fuel cells can be made in different sizes and weights, ranging from microwatts to megawatts, which can be very useful in all kinds of applications.

2.3 Why are PEM fuel cells important?

PEM fuel cells have significant advantages compared with other type's fuel cells. Because PEMFC has a solid electrolyte, it provides excellent resistance to gas crossover. PEMFCs are operated in low temperature; therefore they allow for rapid start-up. Test results have shown that PEMFCs are capable of high power densities of over 2kW/l and 2W/cm^2 [18]. These characteristics allow PEMFC to be used in transportation, mobile/small devices and telecommunications [19]. Figures 2.10 and 2.11 [20] show two examples of where PEM fuel cells are used.
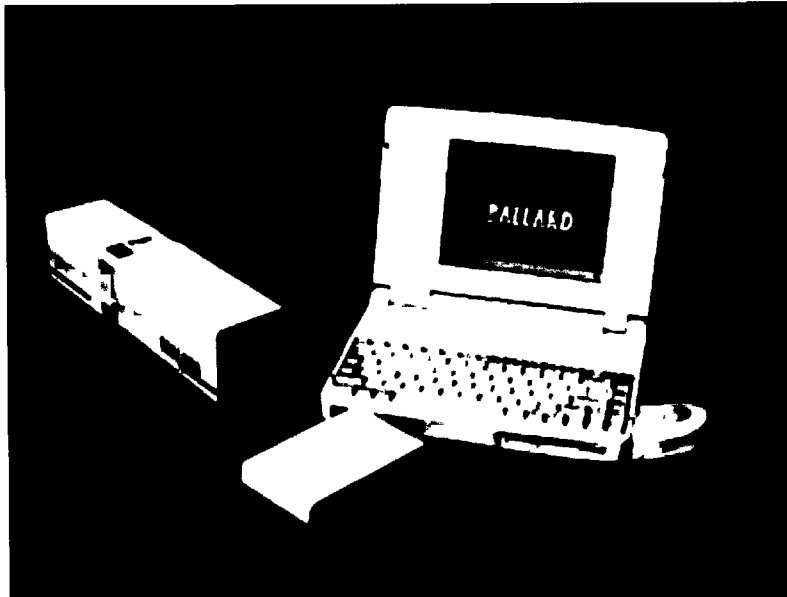
Fig 2.10 Ballard laptop power [20]
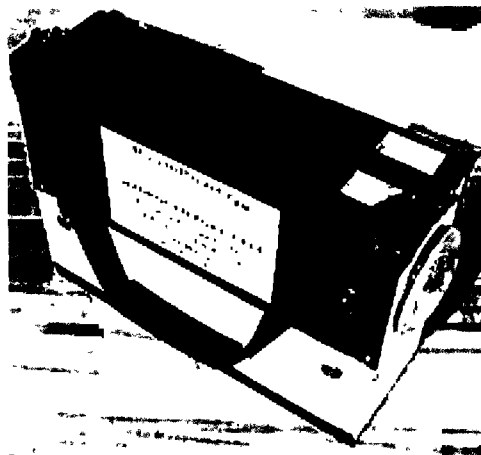
Fig 2.11 Portable fuel cell power unit [20]

Nowadays, almost all large automotive companies are pursuing research work on PEMFC cars in order to take a lead position in future automotive markets. Figs 2.12 to 2.15 [21] show examples of vehicles powered by PEMFCs.

Fig 2.12 Ford Focus FCV [21]

Fig 2.13 GM: Sequel [21]

Fig 2.14 Honda: FCX-V4 [21]

Fig 2.15 Toyota: FCHV-4 [21]

2.3.1 Working principles of a PEM fuel cell

PEMFCs consist of a polymeric membrane as an electrolyte. Hydrogen or hydrocarbon fuels react at the anode side, while oxygen reacts at the cathode side. The output is electrical energy in the form of direct current. When hydrogen is used as the fuel, the final exhaust product is simply water. Fig 2.16 [22] illustrates how a PEMFC works.

First, hydrogen or a hydrocarbon is oxidized at the anode, and then hydrogen ions migrate to the cathode through the membrane. Oxygen from the cathode reacts with hydrogen ions and electrons to produce water. The theoretical potential for a PEMFC is 1.229V However, because of activation polarization, ohmic polarization and concentration polarization (Fig 2.17), the working potential for PEMFC is about 0.7V From Fig 2.17, we can see that activation polarization is the dominant type of polarization when the current density is low. With increasing current density, ohmic polarization (η_{ohm}) becomes the main polarization mechanism. When the current density is very high, the dominant polarization mechanism is concentration polarization.
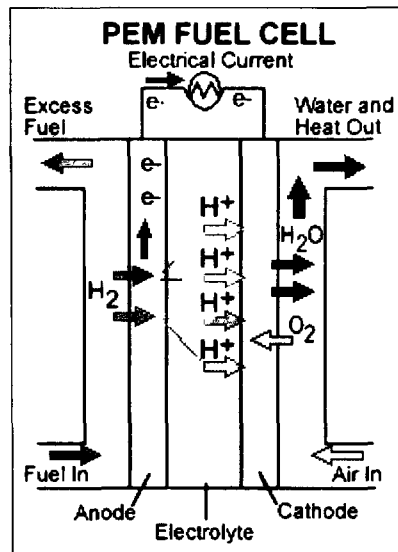
Fig 2.16 PEM fuel cell working principles [22]
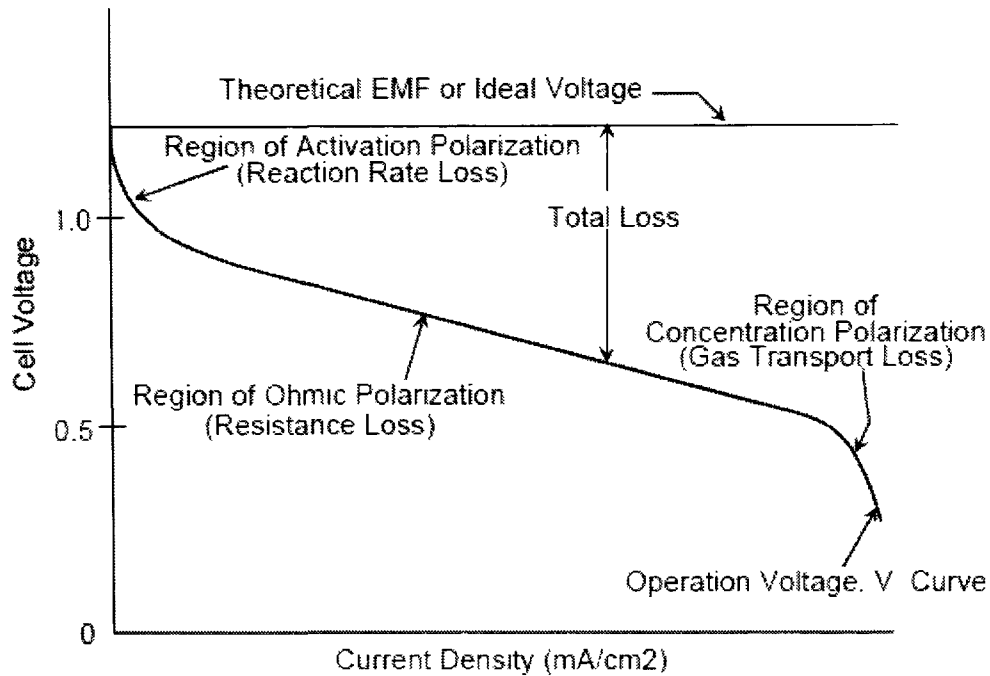
Fig 2.17 Ideal and actual fuel cell voltage/current characteristics [11]

2.3.1.1 Activation polarization

Some electrode reactions are inherently slow and it is the slowness that gives rise to activation polarization. As with all chemical reactions, slow kinetics are associated with an activation energy. The same is true for electrode reactions. The extra voltage, which is called the activation overvoltage (η_{act}), is required for the electrochemical reactions [11, 23, 24]. This activation overvoltage is given by equation 2.20:

$$\eta_{act} = \frac{RT}{anF} \ln \frac{i}{i_o} \qquad \qquad \textbf{2.20}$$

where α is the electron transfer coefficient of the reaction at the electrode being addressed, i_o is the exchange current density, n is the number of electrons transferred in the reaction, and F is the Faraday constant.

2.3.1.2 Ohmic polarization

Ohmic polarization is attributed to the resistance both to the electron transfer through the cell materials including the electrode, and to the ion transfer through the electrolyte. The ohmic overpotential can be calculated as follows [11, 24]:

20

$$\eta_{ohm} = iR_{ohm}$$ **2.21**

where i is the current density and R is the total cell resistance (electronic, ionic, and contact resistance).

2.3.1.3 Concentration polarization

A concentration gradient formed due to the depletion of the fuel at the electrode causes this type of polarization. The concentration polarization can be determined using equation 2.22 [11, 24]:

$$\eta_{conc} = \frac{RT}{anF}\ln(1 - \frac{i}{i_L})$$ **2.22**

where α is the electron transfer coefficient of the reaction at the electrode, i_L is the limiting current density, n is the number of electrons transferred in the reaction, and F is the Faraday constant.

2.3.1.4 Reactant crossover and internal current losses

Fuel crossover is one of the major drawbacks of the most polymer exchange membrane fuel cell (PEMFC) systems. Fuel migration through the electrolyte to the cathode can cause a decrease in the cathode performance, and thus, a loss in overall fuel cell efficiency [24, 25].

2.4 The components of PEM fuel cell

Fig 2.18 [26] shows us the typical structure of PEM fuel cells. In the heart, there is proton exchange membrane. The catalyst layers are between the gas diffusion layers and the proton exchange membrane. The gas diffusion layers are outside the catalyst layers. Bipolar plates are at the outer side. The hydrogen and air (or oxygen) enters from the bipolar plates. One side of the bipolar plates contacts with the anode, and the other side contacts with the cathode. That is the reason why they are called bipolar plates. In PEM fuel cells, many cells need to be connected together in order to get the required potential and current.
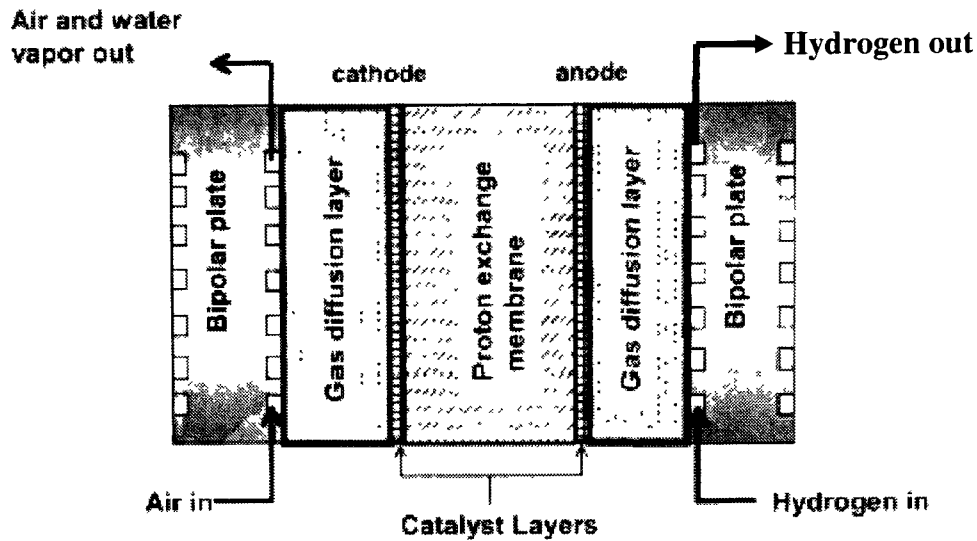
Fig 2.18 The structure of bipolar plates and the MEA [26]

2.4.1 Membrane

The membrane is one of the most important characteristics of PEM fuel cells when compared to other types of fuel cells. The membrane is a solid polymer that can reduce the difficulties of sealing and circulating liquid [27]. A PEM fuel cell membrane must exhibit high proton conductivity and zero electronic conductivity, high mechanical strength, high cation transport number, must be chemically and mechanically stable in PEM fuel cell environments and must be an adequate barrier to mixing of fuel and oxidant, have an acceptable water transport number, and ideally be easy and inexpensive to manufacture [28, 29]. An early breakthrough in PEM fuel cell technology occurred in 1955 when General Electric announced their successful demonstration of fuel cell operation with the first concept membrane, poly(styrene sulfonic acid). However, this type of membrane had a limited life (less than 200h) and failed prematurely by peroxide attack at the benzylic hydrogen [30]. The real success of PEM fuel cell was in 1960s when DuPont introduced a perfluorinated ionomer membrane named Nafion™, which is copolymer of tetrafluorethylene (TFE) and perfluoro-sulfonylfluoride ethyl-propyl-vinyl ether (PSEPVE). Fig 2.19 illustrates the structure of Nafion™ [31, 32].

$$-(CF_2 - CF_2)_2 - (CF_2 - CF)_\backslash -$$
$$O - [CF_2 - CF - O]_m - CF_2 - CF_2 - SO_2F$$
$$CF_3$$
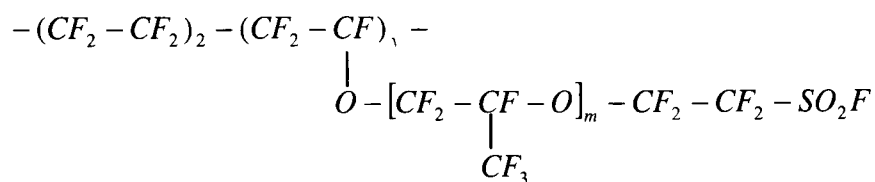
fluoroethylene (TFE)   perfluorovinyl ether (PSEPVE)

Fig 2.19 The structure of Nafion [31, 32]

TFE gives the Nafion membrane chemical and thermal stability and SO_3H makes the membrane proton conductive. In general, the Nafion membrane is marked with a letter N and 3 or 4 digits. The first two digits represent the equivalent weight divided by 100; the last one or two is the membrane thickness in mills. For instance, Nafion™ 117 has equivalent weight of 1100 and it is 7 mills thick. The equivalent weight (EW) of a polymer membrane can be expressed by equation 2.23:

EW=100n+446   **2.23**

where n is the number of TFE groups on average per PSEPVE monomer [28]. The proton conductivity of the membrane is strongly dependent on the water content in the membrane and equivalent weight affects the water uptake. Therefore, equivalent weight affects the proton conductivity. In general, EW values ranging from 800 to 1500 are preferred for practical PEM fuel cells because they afford the best proton conductivity [30]. However, PFSA membranes still have some problems, e.g. the swelling of the membrane when exposed to water can lead to poor handling and mechanical properties.

Therefore many researchers are trying to develop other types of membrane. Currently, there are two main directions of research for the proton exchange membrane. The first direction is to modify the existing PFSA membrane to improve their properties. The second one is to develop partially fluorinated and non-fluorinated membrane. Ballard Power Systems have developed a partially fluorinated membrane named BAM3G based on sulphonated copolymer incorporating α, β, β-trifluorostyrene and a series of substituted- α, β, β-trifluorostyrene comonomers and have acquired more than 100000h accumulated operation [33-36].

2.4.2 Electrode

A fuel cell electrode is the catalyst layer between the membranes and the gas diffusion layer (GDL) and electrochemical reactions take place on the catalyst.

For the anode, the catalyst is Pt or a Pt alloy because they exhibit a high activity for H_2 electro-oxidation. Because H_2 often contains CO, and CO can be absorbed on the surface of platinum, the electrode can lose activity. There are three main strategies to overcome the CO poisoning problem in PEM fuel cells. The first is to bleed very low levels of oxidant, such as oxygen, into the fuel stream post reforming. This oxidizes the CO to CO_2, at the expense of some fuel loss and increased system cost. The second approach is to operate the PEM fuel cell at higher temperatures, which helps suppress the adverse impact of CO. However, this requires the development of new high-temperature membrane, in itself a significant materials challenge. The third is to develop new CO-tolerant electrocatalysts [37]. Most work in this area has concentrated on Pt-M (where M is usually a transition metal) bimetallic catalysts [38-43]. Some success has been reported using high-energy milling of Pt, Pt-Ru, Pt-Mo, and Pt-Re catalysts [44-46]. Igarashi et al. [38] have reported new CO-tolerant catalysts by alloying Pt with a second non-precious metal, so as to reduce cost, and Pt-Fe, Pt-Ni, Pt-Co, and Pt-Mo alloys were reported to exhibit excellent CO tolerance in H_2 oxidation, similar to that of the Pt-Ru alloy. Haug et al. [40] placed a layer of carbon-supported Ru between the Pt catalyst and the anode flow field to promote the conversion of adsorbed CO to CO_2. Escudero et al. [41] have prepared electrocatalysts based on Pt, Pt-Ru and Pt-Pd by microemulsion methods, which allows the production of a very narrow distribution of metal particles, with an average size smaller than that of conventional electrocatalysts prepared by impregnation.

Pt is at least 10^6 times less active for oxygen reduction than for H_2 oxidation [47], so the cathode needs more Pt. In order to reduce the cost of catalyst, many groups are conducting research on lowering the platinum loading on the electrodes [48-54]. Also, the platinum particle size has been optimized, with general agreement that a ~3.5nm particle size on suitable carbon support is close to optimal: the activity per unit mass of platinum is near optimal under these conditions. In parallel, there have been numerous efforts to substitute other materials for platinum. Most of these attempts focused either on gold or

on platinum alloys (usually with transition metals). So far, these efforts have not demonstrated a decisive cost advantage over pure platinum catalysts [18].

2.4.3 Gas diffusion layer

The layer between the bipolar plates and catalyst is the gas diffusion layer (GDL), which is an essential component that can affect the characteristics of PEMFCs [55]. The GDL is made from carbon cloth or carbon paper and it has following functions in a PEMFC [56]:

• provides the pathway for reactant gases from bipolar plates.

• provides the pathway from the catalyst layer to the bipolar plates for the product water.

• provides the pathway from the catalyst layer to the bipolar plates for electrons to complete the electrical circuit.

• removes heat generated by electrochemical reactions in PEMFC.

• affords mechanical support to the MEA.

Both carbon paper and carbon cloth are widely used as the gas diffusion layer in PEMFCs. Figs 2.20 and 2.21 [57] show the detailed structure of these two types of gas diffusion layer. It has been experimentally observed that the performance of PEMFCs employing carbon cloth GDLs is different from that with carbon paper GDLs under low- or high-humidity operations [58-60]. Ralph et al. [58] demonstrated that carbon cloth exhibited much better performance than carbon paper at high current density operations ($>0.5A/cm^2$) with internal humidification. Williams et al. [59] characterized the properties of both commercial and in-house GDL substrates, including limiting current, electronic resistance, fraction of hydrophobic pores, gas permeability, pore size distribution, and morphology. Their experimental results indicated that carbon cloth and carbon paper show different performance at the atmospheric pressure operation. Similar results were also presented by Frey and Linardi [60]. Yun et al. [57] concluded that the highly tortuous structure of the carbon paper leads to severe mass transport limitations under high-humidity operations. In addition, its smooth surface makes water-droplet detachment difficult, resulting in severe water coverage on the surface and increased mass transport loss. Thus, the carbon cloth is a better choice as the GDL substrate for high humidity operations. However, under the dry condition, the carbon paper is found to

be superior due to its highly torturous pore structure, which retains product water in the MEA and improves the membrane hydration hence its proton conductivity. In addition, the two GDL materials display similar performance at low current densities controlled by the electrochemical kinetics.
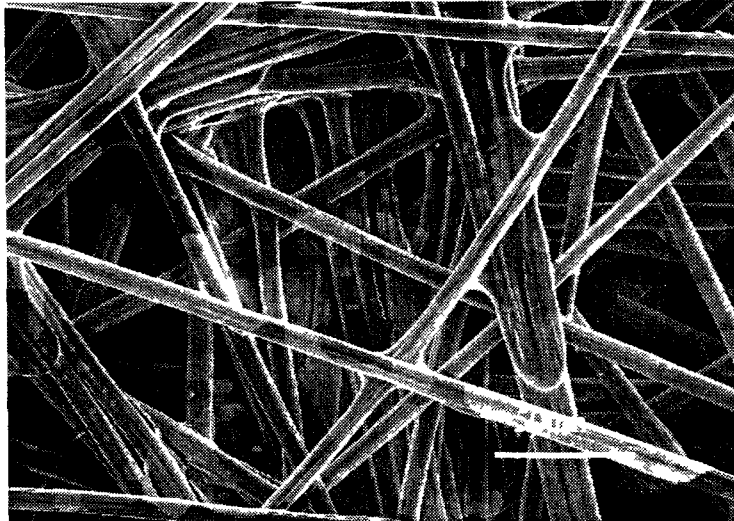
Fig 2.20 SEM micrograph of the structure of Toray carbon paper
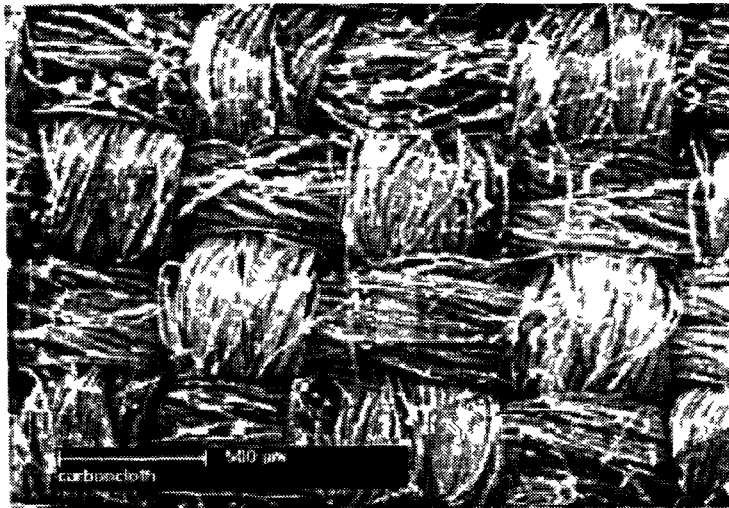
Fig 2.21 SEM micrograph of the structure of carbon cloth [57]

2.4.4 Bipolar plates and their design

Bipolar plates are one of the most important components in PEM fuel cells. They are designed to accomplish many functions, including: distribute the fuel and oxidant in the

stack; facilitate water management within the cell; separate the individual cells in the stack and carry current away from the cell; and facilitate heat management [61]. Furthermore, the plates must be made of inexpensive, lightweight materials and must be easily and inexpensively manufactured. Efforts are underway to develop bipolar plates that satisfy these demands.

The present cost of fuel cell is about $200kW^{-1} which is the major barrier for commercialization in automotive applications [62]. Figs 2.22 and 2.23 [63] show us the weight and cost structure of PEMFCs. It can be seen that bipolar plates account for about 80% of the total weight and 45% of stack cost. In order to compete with an internal combustion engine, the cost of the total fuel cell stack should be reduced to $50 kW^{-1} and the cost of bipolar plates should be reduced to $10 kW^{-1} However, currently in the PEMFC stack, the cost of bipolar plates is about $90 kW^{-1} This is the primary incentive for research on less expensive materials and processes for the manufacture of bipolar plates for PEMFCs.
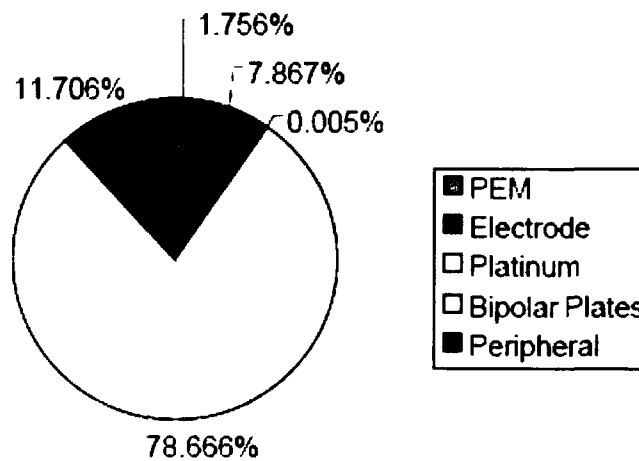
Fig 2.22 Weight structure of fuel cell stack [63]

27
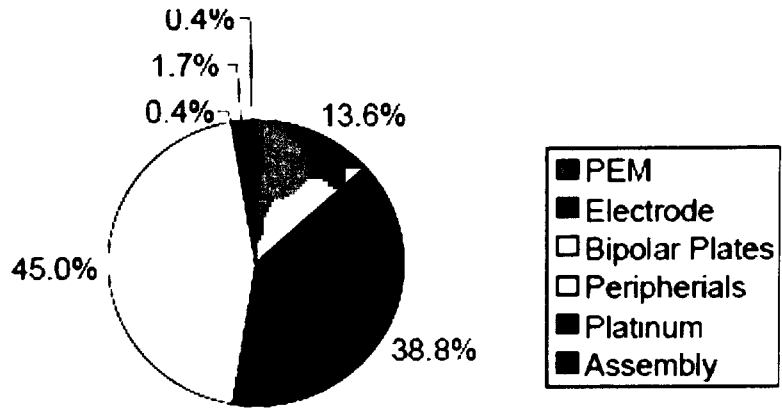
Fig 2.23 Cost structure of fuel cell stack [63]

Bipolar plates are designed in many configurations of flow fields in order to fulfill their functions. Currently, the "popular" designs of bipolar plates include the pin-type flow field, the series-parallel flow field, the serpentine flow field, the integrated flow field, the interdigitated flow field, and the flow-field designs made from metal sheets.

• **Pin-type flow field**

Fig 2.24 [64, 65] shows the pin-type flow field for bipolar plate design. In the pin-type flow field, different shaped pins are used to form channels and the fuel and oxidant flow across the plates through the grooves formed by the pins. The advantage of this design is the low reactant pressure drop. However, the problem with this kind of design is that gases always flow through the least resistance areas, which leads to the formation of stagnant areas, uneven distribution of gases, inadequate product water removal and poor fuel cell performance [66].

28
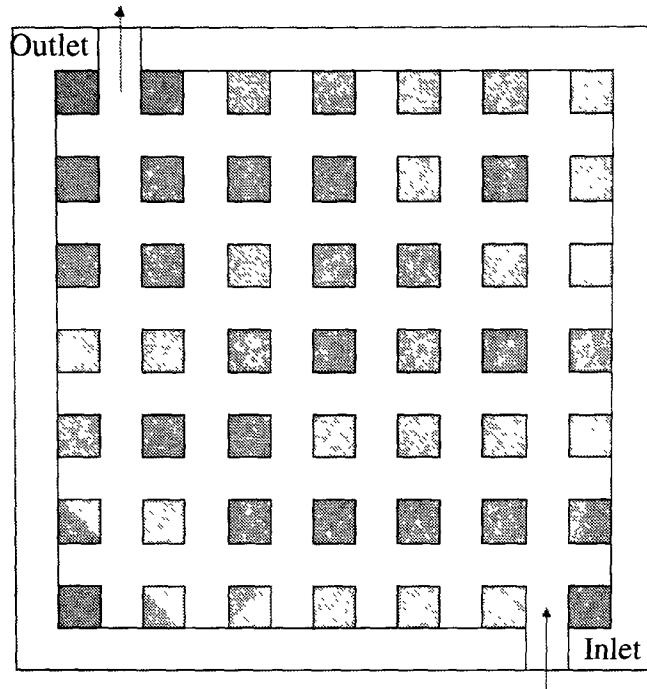
Fig 2.24 Pin-type flow field design of bipolar plate [64]

• **Straight flow field**

Figure 2.24[67] illustrates the straight flow design of bipolar plate. In this design, the gas flow-field plate includes a number of separated parallel flow channels connected to the gas inlet and exhaust headers, which are parallel to the edges of the plate. The problem with this type of design has been a low and unstable cell voltage after a period of operation because of cathode gas flow distribution and cell water management. Another problem is that the straight and parallel channels in the bipolar plates tend to be relatively short and have no directional changes. Therefore, the reactant gas has a very small pressure drop, which results in non-uniform flow distribution of reactant gas in the fuel cell stack [66].
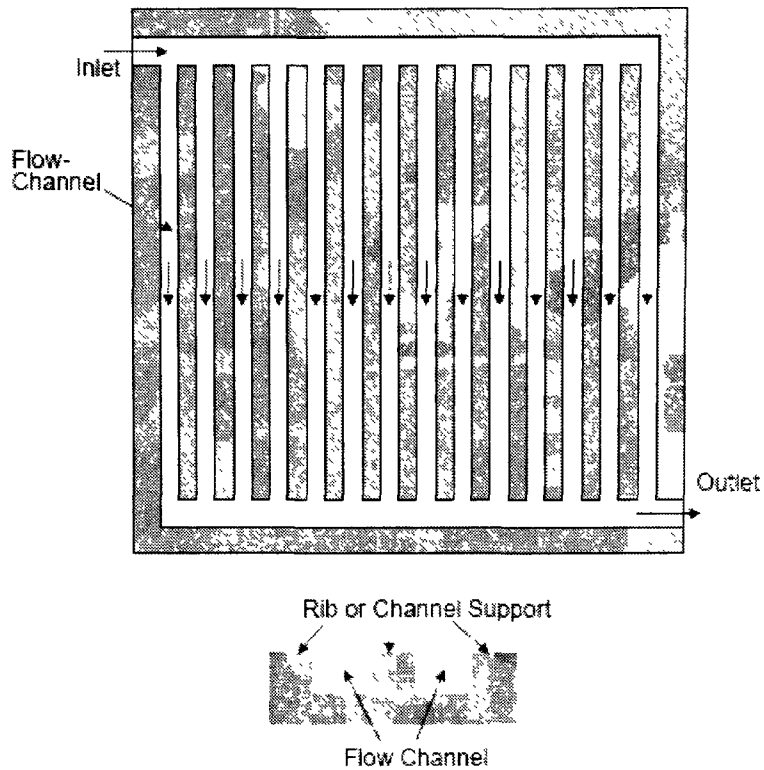
Fig 2.25 Straight flow field design of bipolar plate [67]

• **Serpentine flow field**

Fig 2.26 [68] illustrates one type of serpentine flow field design for bipolar plates. A serpentine flow field can solve flooding problems that result from inadequate water removal from the cell. Such a single serpentine flow field forces the reactant flow to traverse the entire active area of the corresponding electrode thereby eliminating areas of stagnant flow. However, this channel layout results in a relatively long reactant flow path, hence a substantial pressure drop and significant concentration gradients from the flow inlet to outlet [66].

30
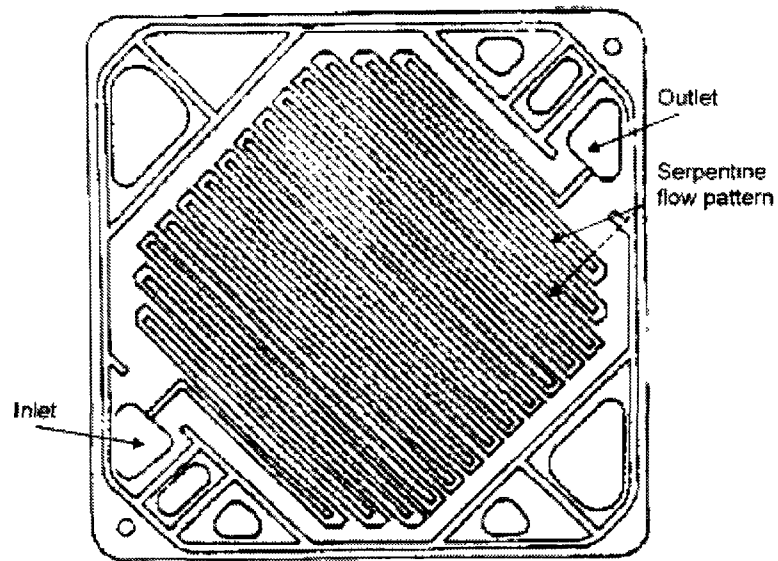
Fig 2.26 Serpentine flow field design for bipolar plates [68]

• Integrated Flow Field

Fig 2.27 [69] shows one design of integrated flow fields. In the integrated design, both the reactant gas flow field and the cooling flow field are on the same plate surface. In this design, a fluid flow field plate is divided into multiple fluid flow sub-plates. Each sub-plate is electrically insulated from all other sub-plates of the same plate assembly, and has its own reactant flow field adjacent to the electrochemically active area of the nearby MEA. A cooling flow field may be positioned in-between and around each of the gas flow sub-plates. However, this kind of design can not maintain a uniform temperature distribution in the fuel cell stack [66, 69].

31

Reactant Flow Field
Adjacent To Active Cell

Coolant
Flow Field
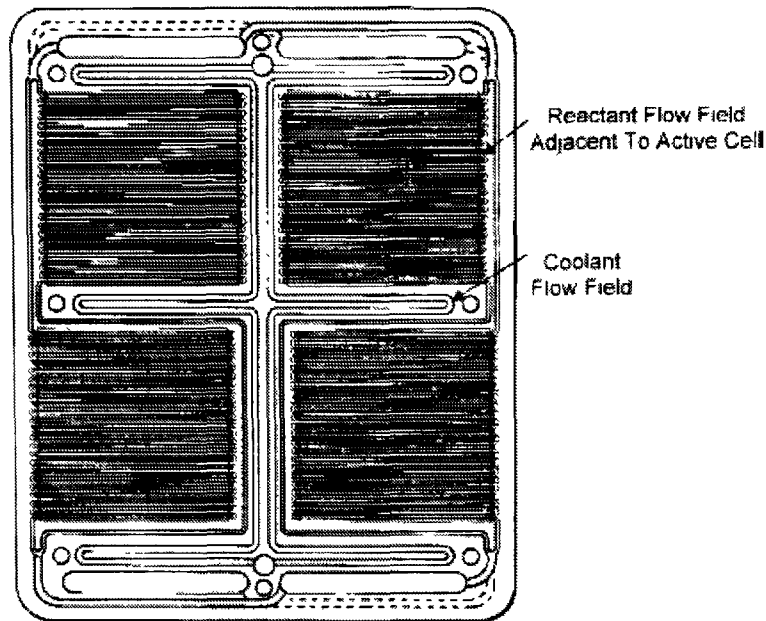
Fig 2.27 Intergrated flow field design of bipolar plate [69]

• **Interdigitated flow field**

Fig 2.28 [70] shows one type of interdigitated flow fields. In an interdigitated flow field design, the dominant reactant flow is in the direction parallel to the electrode surface, and the reactant flow to the catalyst layer, required for electrochemical reaction and electric power generation, is predominantly by molecular diffusion through the electrode backing layer. Not only is molecular diffusion a slow process, which easily leads to the occurrence of large concentration gradients across the backing layer and a mass transfer limitation phenomenon for the cell operation, but it is also difficult to remove the water which exists in the porous region of the backing layer. This difficulty is compounded by the fact that the typical flow in the flow channels is laminar due to the small gas velocity and the small flow channel dimensions [66].

32
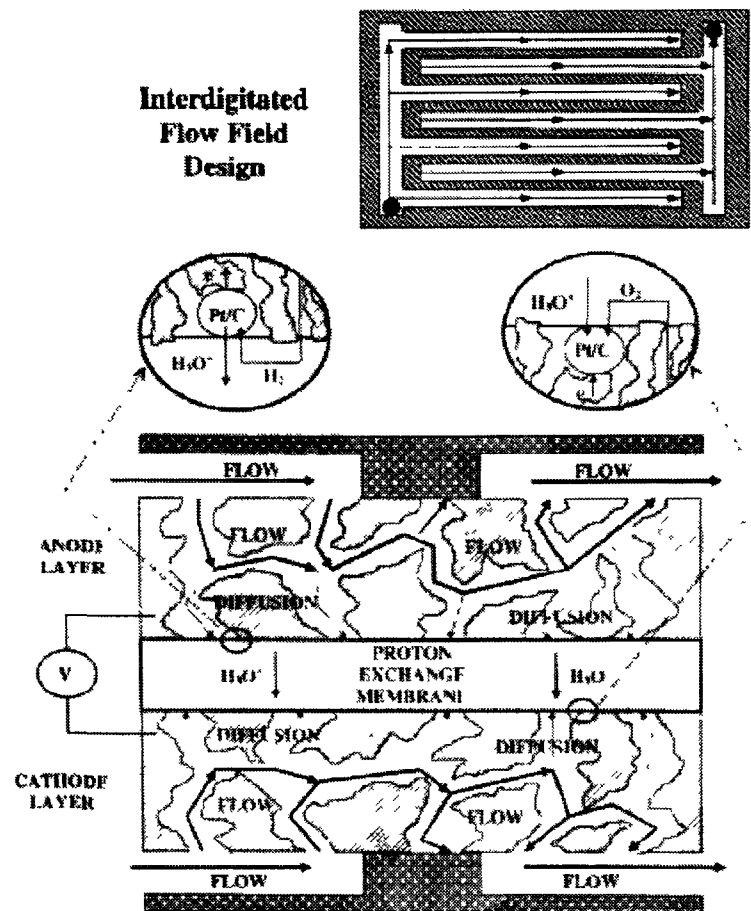
Fig 2.28 Interdigitated flow fielding design of bipolar plates [70]

• **Flow-field designs made from metal sheets**

Fig 2.29 [71] shows one kind of flow fields made from metal sheets. Flow through porous carbon has been proposed for improved water management; a better method may be the use of flow through porous metallic meshes (with high resistance to corrosion) to improve gas distribution on the cell plane. The plates comprise corrosion-resistant thin metal sheets and reactant gas flow fields on the two outside surfaces of the sheets. Such a bipolar plate design eliminates the need for a separate cooling plate, decreases material usage for stack construction and reduces the weight and volume of the stack [66].
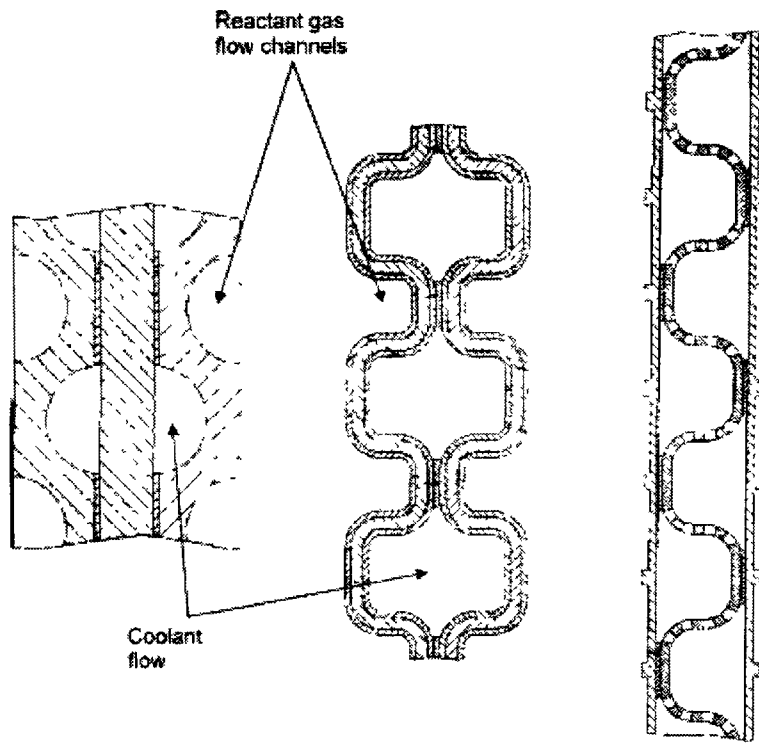
Fig 2.29 Configurations for flow fields made by metal sheets [71]

2.5 Materials of bipolar plates

Bipolar plates are required to perform many functions as has been discussed in Section 2.4.4. In order to satisfactorily perform these functions, certain physical and chemical properties are required of the bipolar plate material. Table 2.3 provides a summary of these functions together with the required physical and chemical properties specific to that function.

Table 2.3 Functions and physical and chemical properties of bipolar plates [61]

Function	Physical and chemical properties
Distribution and management of fuel and oxidants and residual gases and liquids	H_2 permeability (dry, non-porous plates), bubble pressure (wet, porous plates), corrosion resistance
Conduct electrical current	Electrical conductivity
Facilitate heat management	Thermal conductivity
Separate the individual cells in the stack	Compressive strength

Other physical properties of bipolar plate materials that are of importance are coefficient of thermal expansion, density and hydrophobicity. Therefore, for a material to qualify for use as a bipolar plate, the criteria listed in Table 2.4 have been suggested [72, 73, 74]:

Table 2.4 The criteria for the bipolar plates [72, 73, 74]

Electrical conductivity	Plate resistance$<0.01\Omega/cm^2$
Thermal conductivity	As high as possible
Hydrogen/gas permeability	$<10^{-4}cm^3/s\cdot cm^2$
Corrosion resistance	$1\mu A/cm^2$
Compressive strength	$1.55kg/cm^2$
Density	As low as possible
Cost	As low as possible

The main materials studied to date have included: non-porous graphite; polymer composites; and uncoated and coated metallic sheets.

2.5.1 Graphite bipolar plates

One of the first materials to be used for bipolar plates in PEMFCs was non-porous graphite (Fig 2.30) because of its chemical and thermal stability. The advantages of graphite are: excellent resistance to corrosion; low bulk resistivity; low specific density; and low electrical contact resistance with the electrode backing materials. They are

35

manufactured by mixing carbon powder, or graphite powder, with a resin. Adding a resin such as an epoxy resin can reduce gas permeability. Furthermore, machining flow channels using a computerized numerical control machine on non-porous graphite bipolar plates also takes much time and money. Because of their brittleness, machining non-porous bipolar plates is very difficult. Also, the bipolar plates need to have a thickness of several millimeters, which makes the fuel cell stack very heavy and voluminous [62, 75]. Even if the non-porous graphite bipolar plates are relatively thick, they still easily crack. Therefore, other materials, such as metals and composites, are being researched in order to substitute for non-porous graphite.
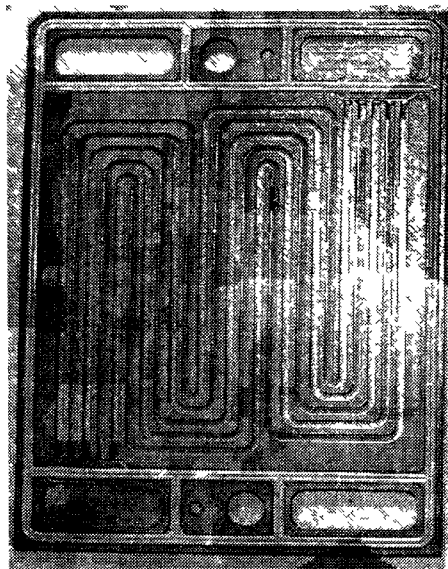
Fig 2.30 Non-porous graphite bipolar plate

2.5.2 Composite bipolar plates

Composite bipolar plates are a very promising alternative to graphite, and have the advantages of low cost, ease in machining, good corrosion resistance and low weight.

Los Alamos National Laboratory has developed a metal-based composite bipolar plate [72. 76]. In this design, porous graphite, polycarbonate plastic and stainless steel are combined in order to retain the benefits of each of the different materials. Since producing porous graphite plates is not as time consuming or expensive as producing non-porous graphite plates, it can be used since the impermeability requirement is

36

provided by the stainless steel and polycarbonate parts. Stainless steel also provides rigidity to the structure while the graphite provides the corrosion resistance. The polycarbonate provides chemical resistance and can be molded to any shape to provide for gaskets and manifolding. The layered plate appears to be a very good alternative from stability and cost standpoints.

Scholta et al [77, 78] reported that SGL Technik GmbH had developed a novel type of low-cost composite bipolar plates. In their study, the performance during a 120h test showed that within that operation time, no performance losses caused by leaching of the composite bipolar plate could be observed. Although the composite bipolar plate was a very promising candidate for PEMFC, extended life tests should be performed and further reduction of material resistance will be increased. They then successfully designed a 10kW PEMFC with the composite bipolar plates.

Acosta et al [79] have reported on the preparation and structural and electrical characterization of composites consisting of ethylene-propylene-norbornen, polypropylene and carbon black (CB) blends. An EPDM terpolymer containing 46.5% ethylene, 50% propylene, and 3.5% norbornene was Dutral Ter 054E from Enichem. Isotactic PP was ISPLEN PP-050 supplied from Repsol Químicas and carbon black was Black Pearls 2000 supplied by Cabot. Blends were prepared in a Rheomix 600-Haake with Banbury type rotors at 175°C blending temperature. They were carried out with the simultaneous incorporation of the EPDM and PP; carbon black was incorporated after the PP was melted; and the blending time was roughly 12 min. The crosslinked samples were prepared following the same procedure, but incorporating several curing agents: ZnO (5%), stearic acid (1%), tetramethylthiuram disulphide (TMTD) (1%), 2, 2'-Dibenzothiazyl disulphide (MBTS) (0.5%) and sulfur (2%). The blending time was 20 min. Structural analysis provided evidence of the reinforcing effect of carbon black on the properties and conducting properties. The mechanical properties and the relative ease of processing, make them suitable as bipolar plates for PEMFCs. In a later paper, Acosta et al [80] studied carbon black (CB) and polyvinylidene fluoride (PVDF) composites. The results showed that CB incorporation into PVDF yielded polymer composite materials with electrical conductivity of about 2.4S/cm, which may be thermally processed and given any convenient shape in the field of polymer technologies, and they

found CB concentration slightly affected the microstructural parameters of the composites.

NedStack [81] has developed a conductive composite material and a production process for fuel cell plates. The material had a high electric and thermal conductivity, and could be processed into bipolar plates by a proprietary molding process. Process cycle time has been reduced to less than 10s, making the material and process suitable for economical mass production. Other development work to increase material efficiency resulted in thin bipolar plates with integrated cooling channels, and integrated seals, and in two-component bipolar plates. Total thickness of the bipolar plates was now less than 3 mm, and would be reduced to 2 mm in the near future. With these thin integrated plates it was possible to increase power density up to 2 kW/l and 2 kW/kg, while at the same time reducing cost by integrating other functions and less material use.

Cho et al [82] developed two kinds of carbon composite plate using the same compound powder, which was composed of ~90% graphite powder, ~10% unsaturated polymer and small amount of organic solvents and additives. Composite A was manufactured into a plate by hot-pressing the compound powder and then gas channels were machined in its surface to make a bipolar plate; composite B was fabricated directly into a bipolar plate by molding the compound powder by applying compression pressure at an adequate high temperature. The results showed both of the carbon composites satisfied the development targets of PEMFC bipolar plates with regard to electrical and physical properties. In initial and long-term operation, performance of the composite bipolar plates was comparable to that of graphite bipolar plates. In spite of similar bulk and contact resistance of the carbon composites, composite B bipolar plates showed slightly better performance than composite A bipolar plates, particularly at high current densities, due to the higher surface energy resulting in better water removal. All those results showed that carbon composites A and B were very promising candidates for PEMFC bipolar plates.

Mighri et al [26] developed highly conductive, lightweight, and low-cost bipolar plates for PEM fuel cells. Injection and compression molding of carbon-filled polypropylene, PP, and polyphenylene sulfide, PPS, were used to fabricate the bipolar plates. Loadings up to 60wt% in the form of graphite, conductive carbon black, and

38

carbon fibers were investigated. Two bipolar plate designs were successfully fabricated by molding the gas flow channels over aluminum plates to form a metallic/polymer composite plate or simply by direct injection molding of the conductive polymer composite. The requirement for bipolar plate application is that the overall plate resistance should be below 0.1 Ohm·cm. For the first design, overall plate volume resistivities of 0.2 and 0.1 Ohm·cm were respectively attained using PP and PPS blends as the conductive over molded layer. A lower volume resistivity of around 0.06 Ohm·cm was attained for the second design with injection molded plates made of the PPS-based blend.

Heinzel et al [83] developed injection moulded low cost bipolar plates. They identified a number of carbon-polymer composites with densities of 1.6g/cm3, specific bulk conductivities between 5 and 150 S/cm and material prices between 2 and 10 €/kg. Standard composite mixtures consisted of a thermoplast and a carbon compound mixture with additional additives to increase the conductivity of the compound material. The composites generally showed high corrosion resistance in the PEMFC environment. Composite material samples proved to be stable in immersion tests in sulphuric acid and deionized water under a pure oxygen atmosphere for several thousand hours. Furthermore, they successfully demonstrated the production of bipolar plates by injection moulding with cycle times of 30-60s. With the help of tailored moulds, injection moulding of bipolar plates becomes price competitive even in the range of several thousand plates. PEMFC stacks with injection moulded bipolar plates of 2.5-4mm thickness and an electrical power of up to 200 W have been constructed and successfully operated.

Kuan et al [84] developed a composite bipolar plate that has been prepared by a bulk-moulding compound (BMC) process. The electrical resistance of the composite material decreased from 20Ω to 5.8mΩ as the graphite content was increased from 60 to 80 wt%. Meanwhile, the electrical resistance of composite increased from 6.5 to 25.2mΩ as the graphite size was decreased from 1000 to 177μm. The oxygen permeability of the composite bipolar plate was 5.82×10^{-8}(cm^3/cm^{2}s) when the graphite content was 75 wt% and increased from 6.76×10^{-8} to 3.28×10^{-5} (cm^3/cm^{2}s) as the graphite size was longer or smaller than 75 wt%. The flexibility of the plate decreased with increasing graphite

39

content. The flexural strength of the plate decreased with decrease in graphite size from 31.25MPa (1000-177μm) to 15.96MPa (53μm). The flexural modulus decreased with decrease of graphite size from 6923MPa (1000-177μm) to 4585MPa (53 μm). The corrosion currents for plates containing different graphite contents and graphite sizes were all less than $10^{-7}Acm^{-2}$ The composite bipolar plates with different graphite contents and graphite sizes met UL-94V-0 tests (Flame resistance test developed by Underwriters' Laboratory Standard) whose specification is achieved if each after-flame time does not exceed 10s, and the sum of the after-flame time for the five samples does not exceed 50s. The surgical cotton below the specimen should not be ignited with flaming drippings. Testing showed that composite bipolar plates with optimum composition were very similar to the graphite bipolar plate.

Oh et al [85] prepared a polymer composite material by coating noble metal on its surfaces. The power density was 0.37 W/cm^2 for polymer composite bipolar plate at 50°C under atmospheric pressure in external humidified hydrogen and air conditions. It was shown that no visible decrease of efficiency occurred in Pd-Ni coated polymer composite bipolar plate for 300h during the unit cell long-run test at 50°C under atmospheric pressure in external humidified hydrogen and air condition.

Wu et al [86] developed a novel concept of a triple-continuous structure to provide carbon-filled polymer blends with high electrical conductivity and tensile strength simultaneously. The microstructure consists of a binary polymer blend, both phases of which are continuous in 3D space. The conductive carbon is preferentially located in one phase and its concentration is high enough to form a continuous structure so that a continuous electrical conductive path is present in the polymer. Low-cost fabrication of such a triple-continuous structure through injection molding has been demonstrated using the carbon nanotube (CNT) filled polyethylene terephthalate (PET)/polyvinylidene fluoride (PVDF) blend. The CNT-filled PET/PVDF blend exhibited 2500% improvement in electrical conductivity, 36% increase in tensile strength and 320% improvement in elongation over the CNT-filled PET at the same carbon loading. The proposed concept had the potential to produce low-cost conductive polymers with superior conductivity and strength for bipolar plate applications of PEMFCs.

Polymer-graphite composite bipolar plates are now available in the market and are sold by such companies as Dupont, H2Economy, ICM Plastics, and NedStack [61]. The main problem of polymer bipolar plates is the low bulk electrical conductivity. The target electrical conductivity should higher than 100S/cm, however, the obtained electrical conductivity is around 20~30S/cm. Table 2.5 summarizes the types of composite bipolar plates and their properties.

Table 2.5 The properties of composite bipolar plates

Composite bipolar plates	Properties
Metal based composite bipolar plates which are made of porous graphite, polycarbonate plastic, and stainless steel [72, 76].	Retains the benefits of each of the constituent materials.
Low cost composite bipolar plates [77, 78].	No performance losses caused by leaching of the composite bipolar plates in a 120h fuel cell test.
Composite of ethylene-propylene-norbornen, polypropylene and carbon black (CB) blends [79].	The composite has good mechanical properties and a relative ease of processing.
Composite consists of carbon black (CB) and polyvinylidene fluoride (PVDF) [80].	The electrical conductivity of the polymer composite materials is about 2.4S/cm, and they may be thermally processed and given any convenient shape in the field of polymer technologies,
Composite material has high electrical and thermal conductivity, and could be processed into bipolar plates by a proprietary molding process [81].	With these thin integrated plates it was possible to increase power density up to 2 kW/l and 2 kW/kg, while at the same time reducing cost by integrating other functions and less material use.
Two types of Carbon composite plate using the same compound powder, which was composed of ~90% graphite powder, ~10% unsaturated polymer and small amount of organic solvents and additives [26].	The two carbon composites were very promising candidates for PEMFC bipolar plates.
Highly conductive, lightweight, and low-cost bipolar plates for PEM fuel cells [82].	Overall plate volume resistivities of 0.2 and 0.1 Ohm·cm were respectively attained using PP and PPS blends as the conductive over molded layer. A lower volume resistivity of around 0.06 Ohm·cm was attained for the second design with injection molded plates made of the PPS-based blend.
Injection moulded low cost bipolar plates [83].	The composites generally showed high corrosion resistance in the PEMFC environment.
A composite bipolar plate prepared using a bulk-moulding compound (BMC) process [84].	The composite bipolar plates with optimum composition were very similar to the graphite bipolar plate.
A polymer composite material prepared by coating a noble metal on its surfaces [85].	No visible decrease of efficiency occurred in Pd-Ni coated polymer composite bipolar plate for 300h during the unit cell long-run test at 50°C under atmospheric pressure in external humidified hydrogen and air condition.
A novel concept of a triple-continuous structure to make composite [86].	The composite has high electrical conductivity and tensile strength.

2.5.3 Metallic bipolar plates

Metals have good mechanical stability, electrical conductivity and thermal conductivity and can be recyclable. Furthermore, they can be easily stamped to the desired shape to accommodate the flow channels. However, metals are easily corroded in the PEMFC environments, and the metal ions can affect the conductivity of membrane. Furthermore, the corrosion or oxidation layer will increase the contact resistance between the bipolar plates and the gas diffusion layer. Thus far, several metals including stainless steel, aluminum, titanium, and nickel have been investigated as the base materials for bipolar plates.

2.5.3.1 Uncoated metals

Stainless steel is the only uncoated metal that has been widely researched as a bipolar plate material. In order to offer some fundamental information for the use of stainless steels as bipolar plate materials for PEMFC, Li et al [87] examined the electrochemical corrosion characteristics of type 316 stainless steel in a simulated anode environment. They concluded that 316 stainless steel could not passivate spontaneously in the simulated environment. The absorbed (and/or adsorbed) hydrogen atoms from anodic corrosion reactions on the steel surface may deteriorate the passivity and the current increases with immersion time. EIS spectra also revealed that a porous corrosion product layer formed on the steel surface during the active dissolution in the test solutions.

Wang et al [88,89,90] have investigated several metals, principally stainless steels. They concluded 349^{TM} stainless steel exhibited superior anti-corrosion behavior in a simulated PEMFC environment and would be an excellent candidate material for bipolar plates. They also researched stainless steels AISI 434, AISI436, AISI441, AISI444, and AISI446. The results suggested that AISI446 had barely acceptable characteristics for use as PEMFC bipolar plates. They also researched the duplex 2205 stainless steel whose nickel content was between 349^{TM} and AISI446. Both electrochemical polarization and interfacial contact resistance measurements indicated that duplex 2205 stainless steel was a possible bipolar plate candidate.

Davis et al [91] evaluated different bipolar plate materials and presented long term fuel cell data for 316 and 310 stainless steels. The properties of the passive film on the

surface of 316 and 310 stainless steels were markedly different. Type 310 stainless steel tended to produce higher fuel cell performance and no degradation was observed after 1400h testing. Analysis of the passive film indicated that this increased performance was related to the decreased thickness of the oxide film.

Hermann et al [61] reported that aluminum, stainless steel, titanium and nickel exposed to an operating environment similar to that of a fuel cell are prone to corrosion or dissolution. Moreover, a corrosion layer on the metal surface increases electrical resistance and decreases output of the cell. While this surface oxide layer can protect the metal from corrosion, it can lower the electrical conductivity.

Lafront et al [92] studied the corrosion behavior of SS316L and bulk amorphous $Zr_{75}Ti_{25}$ (AB) using electrochemical noise in simulated PEMFC working conditions. They concluded that AB alloy has a higher corrosion resistance in the anode environment. However, in the cathode environment, SS316L has a higher corrosion resistance.

Nikam et al [93, 94] studied a copper-beryllium alloy in the simulated fuel cell environment. The corrosion rate for the alloy was 0.05 and 0.28μm year^{-1} at 25 and 70°C, respectively. Due to their good corrosion resistance and high conductivity the alloy could be considered as a candidate material for bipolar plate. Then the alloy was tested in an actual fuel cell. Standard parallel flow field design with 16cm^2 surface area was machined. The single cell showed good performance without degradation of MEA and bipolar plates for 100h at a constant load of 1A.

2.5.3.2 Coated metals

Two types of coatings, carbon-based and metal-based, have been investigated for the metallic bipolar plates. Carbon-based coatings include graphite, conductive polymer, diamond-like carbon, and organic self-assembled monopolymers. Noble metals, metal nitrides and metal carbides are some of the metal-based coatings. The coating methods mainly included physical vapor deposition methods such as electron beam evaporation, sputtering and glow discharge decomposition, chemical vapor deposition and liquid phase chemical techniques such as electro-plating and electroless-plating, chemical anodization/oxidation over-coating, and painting.

Borup and Vanderborgh[95] suggest that coatings for bipolar plates should be conductive and adhere to the base material properly to protect the substrate from the operating environment. Stainless steel is the most widely researched base metal because of its inherent corrosion resistance. Researchers have examined 316, 310, 904, 349, 317, 444, 436, 434, 441, 446, and 2205 stainless steels. Of these stainless steels, 316 is the most widely researched.

In order to avoid the formation of the oxide layer and nickel dissolution, Wind et al [96] studied 316L stainless steel with a gold coating. The current –voltage curve measured in single cells with gold coated bipolar plates (SS 316L) clearly demonstrated that there was no difference between these plates and graphite plates. After measuring the I-V curves, the fuel cell was operated under the standard conditions for 1000h. There was almost no deterioration of the cell voltage. They concluded the oxide layer was so thin that it had no effect on cell resistance and also the amount of contaminants in the MEA was so low that it did not affect the cell performance. The chemical analysis of the MEA after the cell test showed that the amount of nickel was reduced considerably, whereas the iron content in the MEA was enhanced. The reduction of the amount of nickel showed that the gold coating was a good diffusion barrier for nickel under the operation conditions of PEMFCs. As almost no additional resistance was measured, oxygen also did not diffuse under the gold coating. However, the high cost of gold prevented its use in commercial PEMFCs. Wind et al adopted the low cost coating materials and low cost coating process and chose the most promising coating materials. Research showed that these layers were stable for at least 1000h. Both oxide formation and poisoning of the MEA were reduced. However, the researchers did not provide the details of coating materials and procedures.

Li et al [97] investigated the corrosion behavior of TiN coated type 316 stainless steel in simulated PEMFC environments, i.e. 0.01 M HCl+0.01 Na_2SO_4 solutions bubbled with pure oxygen and hydrogen gases, respectively, by using electrochemical measurement techniques. The 316SS substrate passivated spontaneously in the simulated cathode environment, while it was in an active state at the corrosion potential in the simulated anode environment. TiN coatings provided much better corrosion resistance and passivity under both simulated anode and cathode conditions. No significant degradation took

place in the TiN coatings under the typical load conditions of a fuel cell for 4h. There was a small loss of coating thickness during the immersion tests of TiN coatings in the oxygen environment for 1000h, and in the hydrogen environment for 240h, but the exposed substrate areas were passivated in both environments. Thus a TiN coating could provide 316SS with both a high corrosion resistance and high electrical conductivity.

Cho el al [98] compared TiN-coated 316 stainless steel with graphite and bare 316 stainless steel as a bipolar plate material for PEMFCs. Electrical contact resistance and water contact angle of TiN-coated 316 SS were comparable to those for graphite. Surface energy of bipolar plates is an important factor affecting cell performance particularly at high current density since water produced by the cathode reaction should be properly removed. Bipolar plates with low surface energy readily flood the cathode side of a cell. The lower the contact angle is, the lower is the surface energy of the material. In a single cell test, the initial performance and lifetime of the TiN-coated 316 bipolar plates was significantly improved over those for bare 316SS bipolar plates, even though they were still lower than for the graphite bipolar plates. Dissolution of metallic elements such as Fe, Ni, Cr and Ti from TiN-coated 316SS bipolar plates into the MEA could increase the ohmic resistance and the charge transfer resistance of a single cell by contaminating the membrane and active catalytic sites. A 12-cell short stack was manufactured using the TiN-coated 316 stainless steel as bipolar plate material and it exhibited a maximum power of 1.18kW and operated for 1028h at a current of 48A. The degradation rate of the stack was 11%/1000h, and the lowest and the highest degradation rate of each unit cell were measured to be 1.2%/1000h and 31%/1000h, respectively.

Lee et al [99] treated 316L stainless steel with an electrochemical surface treatment before use as bipolar plates. Metallurgical analysis showed that the Cr content on the surface of the treated stainless steel bipolar plate had been greatly increased through a selective dissolution process. At the same time, the Fe content was greatly decreased. The metallurgical structure of the surface had become defect-free, solid, and integral. The Cr oxide, Cr_2O_3, formed a protective passive film, which increased the corrosion-resistance of the stainless steel bipolar plates. Corrosion tests showed that the corrosion current was reduced to one fourth of the original value. When immersed in 0.5M H_2SO_4 at 70°C, the corrosion current remained stable indicating it may survive long term fuel cell operation.

Because of the clean and integral surface, the surface electrical conductivity increased despite the increase in Cr content. The surface characteristics became hydrophobic which could improve the flow of H_2, air and water. Because of the smooth surface, the micro-potential difference between the MEA and the metallic bipolar plates was reduced which may further reduce localized corrosion of the metallic bipolar plates.

Cunningham et al [100] coated a high carbon content polymer on 316 stainless steel. One of these polymers (M2-48 which is shown in Fig 3.10.), with a low specific resistance at a low pyrolysis temperature and pyrolysis time, could be easily sprayed on stainless steel 316L. The layer of M2-48 on SS316L was used as a first layer of a three-layer coating, which was able, after its pyrolysis at 750°C, to protect the stainless steel against corrosion in fuel cell tests. The second and third layers of the 70-100μm thick protective coating were made of a commercial graphite spray and a top layer of M2-48, respectively. There remain some challenges before this coating procedure could be used commercially. The long term (>1000h) stability of the coatings has still to be assessed. It is also of interest to use high carbon content polymers with a lower cost than M2-48 that was synthesized from purified m-diethynylbenzene.
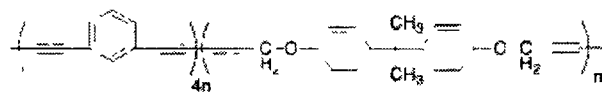
Fig 2.31 Formula of M2-48 [100]

Wang et al [101,102] have studied thermally nitrided stainless steels for polymer electrolyte membrane fuel cell bipolar plates. Thermal nitridation of a Ni-50Cr alloy at 1100°C for 2h in pure nitrogen resulted in the formation of a continuous, protective CrN/Cr2N surface layer with a low interfacial contact resistance. Application of similar nitridation parameters to an austenitic stainless steel, 349TM, however, resulted in a discontinuous mixture of discrete CrN, Cr_2N and $(Cr, Fe)_2N_{1-x}(x=0-0.5)$ phase surface particles overlying an exposed γ austenite-based matrix, rather than a continuous nitride surface layer. The interfacial contact resistance of the 349TM was reduced significantly by the nitridation treatment. However, in the simulated PEMFC environments, very high corrosion currents were observed under both anodic and cathodic conditions. This poor

47

behavior was linked to the lack of continuity of the Cr-rich nitride surface formed on 349TM. They then examined the nitridation behavior of a high Cr, superferritic stainless steel, 446. This alloy was more amenable to Cr-nitride layer formation, although a continuous layer was not achieved under the nitridation conditions employed. However, a new nitride-based surface modification phenomenon, which showed good promise for PEMFC bipolar plate applications, was observed. Nitridation for 2h at 1100°C resulted in little nitrogen uptake and a tinted surface. Analysis by SEM, XPS, and AES suggested a complex heterogeneous modification of the native passive oxide film by nitrogen rather than the desired microns-thick exclusive Cr-rich nitride layer. This modification resulted in both good corrosion resistance under simulated cathodic and anodic conditions and low ICR, well over an order of magnitude lower than the untreated alloy. Further, little increase in ICR was observed under passivating polarization conditions.

Aluminium is a lightweight metal compared to stainless steel. However, the high corrosion resistance and electrical conductivity requirements for fuel cell components preclude most uncoated aluminium alloys from being used [103]. Hentall et al [104] coated gold on the aluminum for use as bipolar plates. These plates were used in a fuel cell and during the initial warm-up procedure the data indicated performance very similar to graphite. However, very quickly the performance degraded. Surface analysis revealed that some of the gold layer had lifted from the plate and become embedded in the membrane.

El-Khatib et al [105] investigated the corrosion stability of high velocity oxy-fuel (HVOF) sprayed SS316L coatings on an aluminium substrate as lightweight bipolar plate materials. The HVOF thermal spraying technique provided hard SS316L coatings with high electrical conductivity. The corrosion rates of the coated plates were about one order of magnitude lower than that of uncoated aluminium, and the rate decreased with increase in coating thickness. The corrosion behaviour was related both to the thickness of the coating and to the composition of the substrate. Bulk and coated SS316L plates, as cathode materials, provided corrosion current levels that were higher than was acceptable for the adequate performance of fuel cell stack, and their failure would eventually contaminate the polymer membrane and catalyst layers. This meant that HVOF sprayed

SS316L coatings could not be used directly in PEM fuel cells, even with the further increase in the number of coating passes or coat thickness.

Lee et al [106] investigated diamond like carbon (DLC) coated 5052 aluminum on the corrosion resistance for the metallic bipolar plates in PEMFCs. The Al-coated plates had better contact resistance and single cell performance than that of the graphite material at the low voltage and shorter cell life.

Titanium is a good candidate material for bipolar plates since it is lightweight compared to stainless steel, and it is easily machined, and has good electrical conductivity. However, pure titanium forms a passive oxide layer in air, which is electrically insulating. Hodgson et al [103] used metal based bipolar plates in polymer electrolyte membrane fuel cells with an active coating on titanium to reduce voltage losses due to the formation of passive layers. Lifetimes in excess of 8000h have been achieved and power densities in excess of $1.8kW \, dm^{-3}$ and $1kWkg^{-1}$ were predicted.

Brady et al [107] used preferential thermal nitridation to form a pin-hole defect free CrN/Cr_2N surface on a model Ni-Cr alloy. Excellent corrosion resistance and a negligible increase in contact resistance were observed over a 4100h exposure in 80°C sulfuric acid and when used as a metallic bipolar plate in a 1000h proton exchange membrane fuel cell test.

Prospective metallic materials and their coatings for bipolar plates of PEMFCs are summarized in Fig 3.11 and the performance characteristics are given in Table 2.6.

The present cost of fuel cells (about $200 kW^{-1}) is a major barrier for commercialization and use in automotive applications [53]. The cost is much higher than the goal ($50 kW^{-1}). In the cost of PEM fuel cells, bipolar plates account for about 45% ($90 kW^{-1}) of total cost. Since the materials and manufacturing processes for non-porous graphite are very expensive, it is not feasible to use non-porous graphite in commercial automotive applications. Metals and composite materials are two potential directions for bipolar plate materials and both are being widely researched.

Bipolar plates

Non-porous graphite plates   Metallic bipolar plates   Composite bipolar plates

coated   Non-coated   Carbon-based   Metal-based

Base material:
Aluminum
Titanium
Nickel
Stainless steel

Coating method:
PVD
CVD
CVI
Electro and electroless deposition
Painting
Chemical anodization/oxidation coating

Coating materials:
Conductive polymers
Diamond-like carbon
Monopolymer
Noble metals
Nitride
Carbide
Oxide

Resin:
Thermoplastics
Poly(vinylidene fluoride)
Polypropylene
Polyethylene
Thermoset
Vinyl ester
Phenolic resin
Furan resin
Epoxy resin

Graphite
Polycarbonate

Filler:
Carbon/graphite particles
Carbon black
Graphite powder
Coke-graphite powder

Fiber:
Carbon/graphite fibers
Cellulose fibers
Carbon fibers
Cotton flock

Fig 2.32 Materials used for bipolar plates in PEMFCs

Table 2.6 The properties of metallic bipolar plates and their coatings.

Base metal	Coating material	Coating method	Performance characteristics
SS316L [96]	Gold, low cost materials.	N/A	These layers were stable for at least 1000h.
SS316 [97]	TiN	Hollow cathode discharge ion plating	There was a small loss of coating thickness during the immersion tests of TiN coatings in the oxygen environment for 1000h, and in the hydrogen environment for 240h
SS316 [98]	TiN	Hollow cathode discharge ion plating	Electrical contact resistance and water contact angle of TiN-coated 316 SS were comparable to those for graphite.
SS316L [99]	N/A	Electrochemical surface treatment	Corrosion tests showed that the corrosion current was reduced to one fourth of the original value.
SS316 [100]	Polymer	Spray	Low specific resistance
Ni-Cr alloy and 349TM [101, 102]	N/A	Thermally nitrided	Good corrosion resistance and little increase of interfacial contact resistance.
Al [104]	Gold	N/A	The performance is very similar to graphite at first. However, very quickly the performance degraded.
Al [105]	SS316L	HVOF thermal spray	The corrosion rates of the coated plates were about one order of magnitude lower than that of uncoated aluminium,
Al [106]	Diamond like carbon	PVD	The Al-coated plates had better contact resistance and single cell performance than that of the graphite material at the low voltage and shorter cell life.
Ni-Cr alloy [107]	Thermal nitridation	N/A	Excellent corrosion resistance and a negligible increase in contact resistance were observed over a 4100h exposure in 80°C sulfuric acid

References

1. F.Barbir, PEM Fuel Cells, Elsevier Academic Press, 2005, PP1.

2. W.R.Grove, On voltaic series and the combination of gases by platinum. London and Edinburgh Philosophical Magazine and Journal of Science, 3,14(1839),127-130.

3. P.G.Grimes, Historical pathways for fuel cells. Aerospace and Electronic Systems Magazine, IEEE, 15(2000)7-10.

4. http://www.nasm.edu/galleries/attm/atmimages/99-15155-6.f.jpg, Last retrieved on October 21, 2006.

5. http://www-cta.ornl.gov/data/tedb27/Spreadsheets/Table1_04.xls, Last retrieved on August 25, 2008.

6. http://www.eia.doe.gov/cabs/chron.html, Last retrieved on August 25, 2008.

7. M.A.Laughton, Fuel cells. Power Engineering Journal, 16(2002)37-47.

8. G.Hoogers, Fuel Cell Technology Handbook, CRC Press, 2003, PP1-3.

9. http://www.fctec.com/fctec_types_afc.asp, Last retrieved on July 30, 2008.

10. http://www.fctec.com/fctec_types_pem.asp, Last retrieved on July 30, 2008.

11. J.H.Hirschenhofer, D.B.Stauffer, R.R.Engleman, and M.G.Klett, Fuel Cell Handbook, U.S.Dept of Energy, Parsons Corporation, 4th Ed. (1998). Last retrieved 2002 from http://www.seca.doe.gov/pubs/4-fuelcell.pdf

12. http://www.fctec.com/fctec_types_mcfc.asp, Last retrieved on July 30, 2008.

13. http://www.fctec.com/fctec_types_sofc.asp, Last retrieved on July 30, 2008.

14. F.Barbir, PEM Fuel Cells, Elsevier Academic Press, 2005, PP12-13.

15. Fuelcell Energy Inc, Form 10-K, 2005, PP11.

16. M.Farooque, C.Yuh, and H.C.Maru, Carbonate fuel cell technology and materials. MRS Bulletin, 30(2005)602-606.

17.http://www.esru.strath.ac.uk/EandE/Web_sotes/00-01/fuel_cells/Fuel%20cell%20 advantages.htm, Last retrieved on October 21, 2006.

18. EG&G Technical Services, Inc. Fuel Cell Handbook (seventh edition), 2004.

19. R.W.Lashway, Fuel cells: the next evolution, MRS Bulletin. MRS Bulletin, 30(2005)581-583.

20. http://americanhistory.si.edu/fuelcells/pem/pem4.htm, Last retrieved on July 30, 2008.

21. http://www.fuelcells.org/basics/gallery.html, Last retrieved on July 30, 2008.

22. http://images.google.com/images?hl=en&lr=&rls=RNWE%2CRNWE%3A2005-19%2CRNWE%3Aen&q=PEM+FUEL+CELL+PICTURE. Last retrieved on July 21, 2008.

23. H.B.Oldham, J.C.Myland, Fundamentals of Electrochemical Science, Academic Press, INC. 1994, PP193.

24. M.H.Atwan, Anode electrocatalysts for direct borohydride fuel cells. PHD dissertation, 2006, University of Windsor, Windsor, Ontario, Canada.

25. D.S.Scott, Inside fuelcells. Int.J.Hydrogen Energy, 29(2004)1203-1311.

26. F.Mighri, M.A.Huneault, and M.F.Champagne, Electrically conductive thermoplastic blends for injection and compression molding of bipolar plates in the fuel cell application. Polymer Engineering and Science, 44(2004)1755-1765.

27. G.Hoogers, Fuel Cell Technology Handbook, CRC Press, 2003, PP2-29.

28. F.Barbir, PEM Fuel Cells, Elsevier Academic Press, 2005, PP75-76.

29. U.Beuscher, S.J.C.Cleghorn and W.B.Johnson, Challenges for PEM fuel cell membranes. Int.J.Energy Research, 29(2005)1103-1112.

30. R.G.Rajendran, Polymer electrolyte membrane technology for fuel cells. MRS Bulletin, 30(2005)587-590.

31. S.Banerjee, D.E.Curtin, Nafion® perfluorinated membranes in fuel cells. J.Fluorine Chemistry, 125(2004)1211-1216.

32. L.J.M.J.Blomen and M.N.Mugerwa, Fuel Cell Systems, Plenum Press, 1993, PP66.

33. O.Savadago, Emerging membranes for electrochemical systems: (I) solid polymer electrolyte membranes for fuel cell systems. J.New Mat.Electrochem.Systems, 1(1998)47-66

34. B.Tazi, O.Savadogo, Parameters of PEM fuel-cells based on new membranes fabricated from Nafion, silicotungstic acid and thiophene. Electrochimica Acta, 45 (2000) 4329-4339.

35. A.E.Steck, C.Stone, Development of the BAM membrane for fuel cell applications. in Proceedings of the Second International Symposium on New Materials for Fuel-Cell Systems, Montréal, Canada, 1997, PP792-796.

36. A.E.Steck, Membrane Materials in Fuel Cells. in Proceedings of the First International Symposium on New Materials for Fuel-Cell Systems, Montréal, Canada, 1995, PP74-78.

37. N.P.Brandon, S.Skinner, and B.C.H.Steele, Recent advances in materials for fuel cells. Annu.Rev.Mater.Res, 33(2003)183-213.

38. H.Igarashi, T.Fujino, Y.Zhu, H.Uchida, M.Watanabe, CO Tolerance of Pt Alloy Electrocatalysts for Polymer Electrolyte Fuel Cells and the CO Detoxification Mechanism. Phys.Chem.Chem.Phys., 3(2001)306-314.

39. H.Yu, Z.Hou, B.Yi, Z.Lin, Composite anode for CO tolerance proton exchange membrane fuel cells. J.Power Souces, 105(2002)52-57.

40. A.Haug, R.E.White, J.W.Weidner, W.Huang, Development of a novel CO tolerant proton exchange membrane fuel cell anode. J.Electrochem Soc, 149(2002)A862-A867.

41. M.J.Escudero, E.Hontanon, S.Schwartz, M.Boutonnet, L.Daza, Development and performance characterisation of new electrocatalysts for PEMFC. J.Power Souces, 106(2002)206-214.

42. T.J.Schmidt, Z.Jusys, H.A.Gasteiger, R.J.Behm, U.Endruschat, H.Boennemann, On the CO tolerance of novel colloidal PdAu/carbon electrocatalysts. J.Electroanal. Chem, 501(2001)132-140.

43. K.A.Starz, E.Auer, T.H.Lehmann, R.Zuber, Characteristics of platinum-based electrocatalysts for mobile PEMFC applications. J.Power Sources, 84(1999)167-172.

44. M.C.Denis, G.Lalande, D.Guay, J.P.Dodelet, R.Schulz, High energy ball-milled Pt and Pt–Ru catalysts for polymer electrolyte fuel cells and their tolerance to CO. J.Appl.Electrochem, 29(1999)951-960.

45. P.Gouerec, M.C.Denis, D.Guay, J.P.Dodelet, R.Schulz, High Energy Ballmilled Pt-Mo Catalysts for Polymer Electrolyte Fuel Cells and Their Tolerance to CO. J.Electrochem.Soc, 147(2000)3989-3996.

46. J.P.Dodelet, M.C.Denis, P.Gouerec, D.Guay, R.Schulz, CO tolerant anode catalyst for fuel cell made by high energy ball milling. Fuel cell seminar (2000)51-54.

47. G.Hoogers, Fuel Cell Technology Handbook, CRC Press, 2003, PP6-12

48. S.Srinivasan, D.J.Manko, H.Koch, M.A.Enayetullah, Recent advances in solid polymer electrolyte fuel cell technology with low platinum loading electrodes. J Power Sources, 29(1990)367-387.

49. S.Mukerjee, S.Srinivasan, J.Appleby, Effect of sputtered film of platinum on low platinum loading electrodes on electrode kinetics of oxygen reduction in (PEMFCs). Electrochim Acta,38(1993)1661-1669.

50. G.S.Kumar, M.Raja, S.Parthasarathy, High performance electrodes with low platinum for polymer electrolyte fuel cell. Electrochim Acta, 40(1995)285-286.

51. F.N.Büchi, S.Srinivasan, Operating proton exchange membrane fuel cells without external humidification of the reactant gases. J Electrochem Soc, 144(1997)2767-2772.

52. E.Passalacqua. F.Lufrano, G.Squadrito, A.Patti, L.Giorgi, Influence of the structure in low-Pt loading electrodes for polymer electrolyte fuel cells. Electrochim Acta, 43(1998) 3665-3673.

53. L.Giorgi, E.Antolini, A.Pozio, E.Passalacqua, Influence of the PTFE content in the diffusion layer of low-Pt loading electrodes for polymer electrolyte fuel cells. Electrochim Acta, 43(1998)3675-3680.

54. K.Sopian, W.Ramli, W.Daud, Challenges and future developments in proton exchange membrane fuel cells. Renewable Energy, 31(2006)719-727.

55. R.Roshandel, B.Farhanieh, E.Saievar-Iranizad, The effects of porosity distribution variation on PEM fuel cell performance. Renewable Energy, 30(2005)1557-1572.

56. F.Barbir, PEM Fuel Cells, Elsevier Academic Press, 2005, PP93.

57. Y.Wang, C.Wang, K.Chen, Elucidating differences between carbon paper and carbon cloth in polymer electrolyte fuel cells. Electrochimica Acta, 52(2007)3965-3975.

58. T.R.Ralph, G.A.Hards, J.E.Keating, S.A.Campbell, D.P.Wilkinson, M.Davis, J.St-Pierre, M.C.Johnson, Low Cost Electrodes for Proton Exchange Membrane Fuel Cells. J.Electrochem. Soc, 144(11)(1997)3845-3857.

59.M.V Williams, E.Begg, L.Bonville, H.R.Kunz, J.M.Fenton, Characterization of Gas Diffusion Layers for PEMFC. J.Electrochem. Soc, 151(2004)A1173-A1180.

60. T.Frey, M.Linardi, Effects of membrane electrode assembly preparation on the polymer electrolyte membrane fuel cell performance. Electrochim.Acta, 50(2004)99-105.

61. A.Hermann, T.Chaudhuri, P.Spagnol, Bipolar plates for PEM fuel cells: A review. Int.Hydrogen Energy, 30(2005)1297-1302.

62. I.Bar-On, R.Kirchan, R.Roth, Technical cost analysis for PEM fuel cells, J. Power Sources, 109(2002)71 75.

63. H.Tsuchiya, O.Kobayashi, Mass production cost of PEM fuel cell by learning curve. Int.J.Hydrogen Energy, 29(2004)985-990.

64. C.A.Reiser, R.D.Sawyer, Solid polymer electrolyte fuel cell stack water management system. US Patent No. 4,769,297, 1988.

65. C.A.Reiser, Water and heat management in solid polymer fuel cell stack. US Patent No. 4,826,742, 1989.

66. X.Li, I.Sabir, Review of bipolar plates in PEM fuel cells: Flow-field designs. Int. J. Hydrogen Energy, 30(2005) 359-371.

67. A.Pollegri, P.M.Spaziante, Novel fuel cell fluid flow field plate. US Patent No. 4,197,178, 1980.

68. D.P.Wilkinson, G.J.Lamont, H.H.Voss, C.Schwab, Embossed fluid flow field plate for electrochemical fuel cells. US Patent No. 5,521,018,1996.

69. W.D.Ernst, G.Mittleman, PEM-type fuel cell assembly having multiple parallel fuel cell sub-stacks employing shared fluid plate assemblies and shared membrane electrolyte assemblies. US Patent No. 5,945,232, 1999.

70. A.Kazim, H.Liu, P.Forges, Modelling of performance of PEM fuel cell with conventional and interdigited flow fields. J.Applied Electrochemistry, 29(1999)1409-1416.

71. N.G.Vitale, Fluid flow plate for decreased density of fuel cell assembly US Patent No. 5,981,098, 1999.

72. V.Mehta, J.S.Cooper, Review and analysis of PEM fuel cell design and manufacturing. J.Power Sources, 114(2003)32-53.

73. R.L.Borup, N.E.Vanderborgh, Design and testing criteria for bipolar plate materials for PEM fuel cell applications. Mat.Res.Soc.Symp.Proc., 393(1995)151-155.

74. G.O.Mepsted and J.M.Moore, Performance and durability of bipolar plate materials, in: Handbook of Fuel Cells-Fundamentals, Technology and Applications, ed.

W Vielstich, H.A.Gasteigner and A.Lamm, John Wiley&Sons, Ltd., 2003, vol.3, PP286-293.

75. T.M.Besmann, J.W.Klett, J.J.Henry, E.Lara-Curzio, Carbon/carbon composite bipolar plate for proton exchange membrane fuel cells. J.Electrochem.Soc., 147(11) (2000)4083-4086

76. Los Alamos National Laboratory Home Page (1998). Available from World Wide Web: http://www.ott.doe.gov/pdfs/contractor.pdf. Last retrieved November 5, 2001.

77. J.Scholta, B.Rohland, V.Trapp, Investigations on novel low-cost graphite composite bipolar plates. J.Power Sources, 84(1999)231-234.

78. J.Scholta, N.Berg, P Wilde, L.Jörissen, J.Garche, Development and performance of a 10 kW PEMFC stack. J.Power Sources, 127(2004)206-212.

79. J.L.Acosta, L.González, C.Del Rio, C.Ojeda, A.Rodríguez, Elastomeric conducting systems based on ethylene-propylene-norbornene composites. J.Applied Polymer Science, 79(2001)2136-2145.

80. C. Del Rio, C. Ojeda, J.L. Acosta, M.J.Escudero, E.Hontañón, L.Daza, New polymer bipolar plates for polymer electrolyte membrane fuel cells: synthesis and characterization. J.Applied Polymer Science, 83(2002)2817-2822.

81. E.Middelman, W.Kout, B.Vogelaar, J.Lenssen, E. de Waal, Bipolar plates for PEM fuel cells. J.Power Sources, 118(2003)44-46.

82. E.A.Cho, U.-S.Jeon, H.Y.Ha, S.-A.Hong, I.-H.Oh, Characteristics of composite bipolar plates for polymer electrolyte membrane fuel cells. J.Power Sources, 125(2004)178-182.

83. A.Heinzel, F.Mahlendorf, O.Niemzig, C.Kreuz, Injection moulded low cost bipolar plates for PEM fuel cells. J.Power Sources, 131(2004)35-40.

84. H.Kuan, C.M.Ma, K.Chen, S.Chen, Preparation, electrical, mechanical and thermal properties of composite bipolar plate for a fuel cell. J.Power Sources, 134(2004)7-17.

85. M.H.Oh, Y.S.Yoon, S.G.Park, The electrical and physical properties of alternative material bipolar plate for PEM fuel cell system. Electrochimica Acta, 50(2004)777-780.

86. M.Wu, L.L.Shaw, A novel concept of carbon-filled polymer blends for applications in PEM fuel cell bipolar plates. Int.J. Hydrogen Energy, 30 (2005) 373-380.

87.M. Li, C.Zeng, S.Luo, J.Shen, H.Lin, C.Cao, Electrochemical corrosion characteristics of type 316 stainless steel in simulated anode environment for PEMFC. Electrochimica Acta, 48(2003)1735-1741.

88. H.Wang, M.A.Sweikart, J.A..Turner, Stainless steel as bipolar plate material for polymer electrolyte membrane fuel cells. J.Power Sources, 115(2003)243-251.

89. H.Wang, J.A.Turner, Ferritic stainless steels as bipolar plate material for polymer electrolyte membrane fuel cells. J.Power Sources, 128(2004)193-200.

90. H.Wang, G.Teeter, and J.Turner, Investigation of a Duplex Stainless Steel as Polymer Electrolyte Membrane Fuel Cell Bipolar Plate Material. J.Electrochemical Society, 152(3)B99-B104(2005).

91. D.P.Davies, P.L.Adcock, M.Turpin and S.J.Rowen, Bipolar plate materials for solid polymer fuel cells. J.Applied Electrochemistry, 30(2000)101-105.

92. A.M.Lafront, E.Ghali, A.T.Morales, Corrosion behavior of two bipolar plate materials in simulated PEMFC environment by electrochemical noise technique. Electrochimica Acta, 52(2007)5076-5085.

93. V V.Nikam, R.G.Reddy, Corrosion studies of a copper–beryllium alloy in a simulated polymer electrolyte membrane fuel cell environment. J.Power Sources, 152(2005)146-155.

94. V V.Nikam, R.G.Reddy, Copper alloy bipolar plates for polymer electrolyte membrane fuel cell. Electrochimica Acta, 51(2006)6338-6345.

95. R.Borup, N.Vanderborgh, Design and testing criteria for bipolar plate materials for PEM fuel cell applications, in: Proceedings of the Materials Research Society Symposium on the Materials for Electrochemical Energy Storage and Conversion I-Batteries, Capacitors and Fuel Cells, 393(1995)151-155.

96. J.Wind, R.Späh, W.Kaiser, G.Böhm, Metallic bipolar plates for PEM fuel cells. J.Power Sources, 105 (2002) 256-260.

97. M.Li, S.Luo, C.Zeng, J.Shen, H.Lin, C.Cao, Corrosion behavior of TiN coated type 316 stainless steel in simulated PEMFC environments. Corrosion Science, 46(2004)1369-1380.

98. E.A.Cho, U.-S.Jeon, S.-A.Hong, I.-H.Oh, S.-G.Kang, Performance of a 1 kW-class PEMFC stack using TiN-coated 316 stainless steel bipolar plates. J.Power Sources, 142(2005)177-183.

99. S.Lee, C.Huang, J.Lai, Y.Chen, Corrosion-resistant component for PEM fuel cells. J.Power Sources, 131(2004)162-168.

100. N.Cunningham, D.Guay, J.P.Dodelet, Y.Meng, A.R.Hlil, and A.S.Hay, New Materials and Procedures to Protect Metallic PEM Fuel Cell Bipolar Plates. J. Electrochem.Soc, 149(7)(2002)A905-A911.

101. H.Wang, M.P.Brady, G.Teeter, J.A.Turner, Thermally nitrided stainless steels for PEMFC bipolar plates. Part 1: Model Ni-50Cr and austenitic 349TM alloys. J.Power Sources, 138(2004)86-93.

102. H.Wang, M.P.Brady, K.L.More, H.M.MeyerIII, Thermally nitrided stainless steels for PEMFC bipolar plates. Part 2: Beneficial modification of passive layer on AISI446. J.A.Turner, J.Power Sources, 138(2004)79-85.

103. D.R.Hodgson, B.May, P.L.Adcock, and D.P.Davies, New lightweight bipolar plate system for polymer electrolyte membrane fuel cells. J.Power Sources, 96(2001)233-235.

104. P.L.Hentall, J.B.Lakeman, G.O.Mested, P.L.Adock, J.M.Moore, New materials for polymer electrolyte membrane fuel cell current collectors. J.Power Sources, 80 (1999)235-241.

105. K.M.El-Khatib, M.O.A.Helal, A.A.El-Moneim and H.Tawfik, Corrosion stability of SUS316L HVOF sprayed coatings as lightweight bipolar plate materials in PEM fuel cells. Anti-Corrosion Methods and Materials, 51(2004)136-142.

106. S.Lee, C.Huang, Y.Chen, Investigation of PVD coating on corrosion resistance of metallic bipolar plates in PEM fuel cell. J.Materials Processing Technology,140(2003)688-693.

107.M.P.Brady, K.Weisbrod, I,Paulauskas, R.A.Buchanan, K.L.More, H.Wang, M.Wilson, F.Garzon, L.R.Walker, Preferential thermal nitridation to form pin-hole free Cr-nitrides to protect proton exchange membrane fuel cell metallic bipolar plates. Scripta Mater., 50(2004)1017-1022.

59

CHAPTER 3

EXPERIMENTAL METHODS

3.1 Materials and electrode preparation

3.1.1 Materials

Six materials (ordered from OnlineMetals.com), including SS316L (Austenitic), SS347 (Austenitic), SS410 (Martensitic), pure Ti (grade2), Al6061 and A36 steel were examined. Their chemical compositions are given in Tables 3.1 and 3.2. The price of some metals is listed in Table 3.3.

Table 3.1. Chemical compositions of SS316L, SS347 and SS410 (wt%)

Metal	C	Mn	P	S	Si	Cr	Ni	Mo	Cu	Co	N	Al	Ti	Sn	Ta	Nb	Fe
SS316L	0 021	1 82	0 029	0 01	0 58	16 32	10 54	2 12	0 47	-	0 03		-				balance
SS347	0 04	1 58	0 029	0 0002	0 57	17 59	9 62	0 34	0 38		0 042				0 01	0 63	balance
SS410	0 135	0 36	0 018	0 001	0 4	12 22	0 21	0 03	0 1	0 01	0 012	0 001	0 001	0 011			balance

Table 3.2. Chemical compositions of Al6061 and A36 steel (wt%)

Metal	C	Mn	P	S	Si	Cr	Cu	V	Ti	B	Ca	Mg	Zn	Ga	Al	Fe
Al6061	_	_	_	_	0 70	0 18	0 25	_	_	_	_	1 12	0 02	0 02	balance	0 46
A36	0 06	0 12	0 004	0 005	0 09	0 02	0 01	0 003	0 003	0 0001	0 0019	_	_	_	0 047	balance

Table 3.3 Approximate price ($/lb) of some metals [1]

Aluminum	1.25	Nickel	9.53
Copper	3.57	Tin	9.89
Magnesium	2.4	Platinum	22720
Zinc	0.82	Gold	13117
Lead	0.85	Silver	215.5
Titanium	21		

3.1.2 Electrode preparation

The metal plates were cut into samples 1.5cmx1.5cm (area=2.25cm^2). An electrical contact was made to one side by means of nickel print (M.G. Chemicals Ltd) with the copper wire. Then the contact side and the edges of the metal sample were sealed with epoxy resin (Bondo), leaving one side for characterization [2, 3, 4]. After the epoxy resin totally dried, the sample could be taken out from the mold. In the corrosion testing of the uncoated metal, the samples were polished on 240, 320, 400, 600 and 800 grit silicon carbide papers (BUEHLER) and a final polish with 1.0μm alumina powder (BUEHLER). Then the polished sample was rinsed by ethanol and dried by hot air.

Fig 3.1 Preparation of the working electrode

3.2 Experimental cell set up

A typical three-electrode system was used in the experiments. The metallic electrode was the working electrode; a Pt electrode (Radiometer analytical) was the counter electrode; saturated Hg/HgCl$_2$ (Radiometer analytical) was the reference electrode. A Solartron 1285 Potentiostat was used for potentiodynamic, potentiostatic, galvanostatic, open circuit and cyclic voltammogram tests and a Solartron 1287 Electrochemical Interface was used for electrochemical impedance tests. A salt bridge was used to reduce the solution contact resistance and the pollution for the reference electrode. The working

electrode and the reference electrode can be placed in different containers using a salt bridge. This is very important in the electrochemical tests, since, otherwise, the solution in the reference electrode will exchange with that of the electrolyte, which can affect the accuracy of the reference electrode.
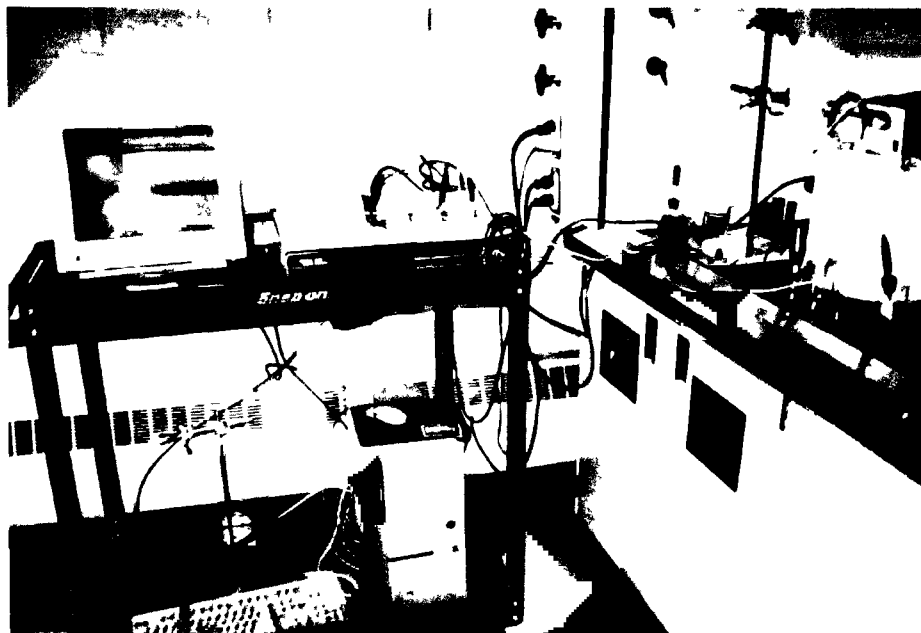
Fig 3.2 The experimental cell set up
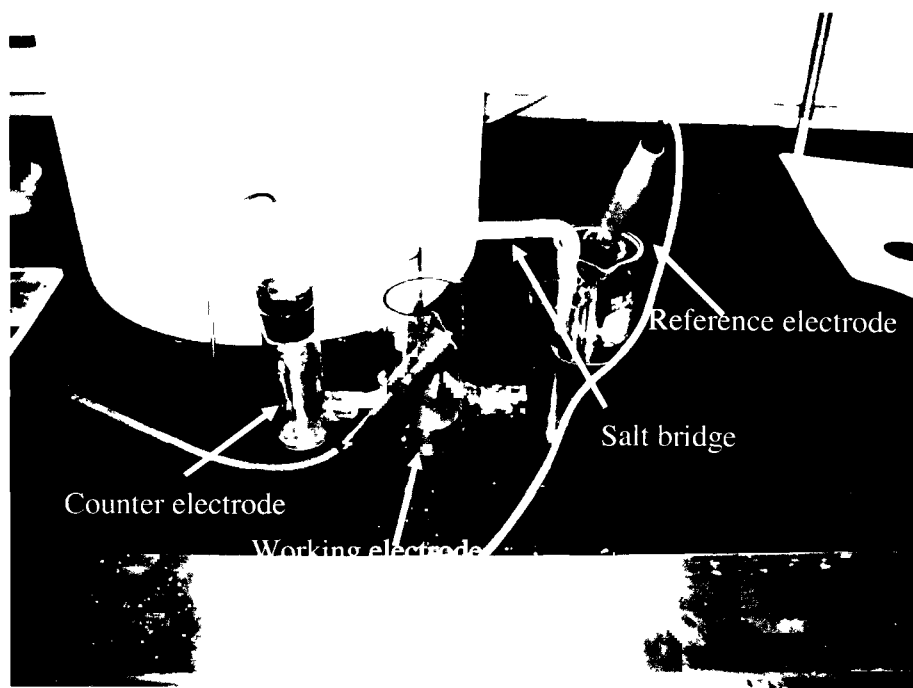
Fig 3.3 Three electrode system

3.2.1 Salt bridge preparation

1.5g Agar (Fisher Scientific Company) and 35g KCl (ACP) were added into 50g distilled water, mixed well, and then heated uniformly. After the solution reached boiling, the solution was poured into a U-shaped tube. The gel of agar and KCl filled tubes was then immediately placed in a saturated KCl solution to prevent shrinkage of the agar during cooling. When it was cool, any excess agar and KCl were removed from the outside of the bridge and the bridge examined for bubbles. Usable bridges were placed in a saturated KCl solution for long-term storage in order to avoid drying out. Salt bridges can be discarded after each use or reused several times. It is not difficult to remove the gel of agar and KCl from the glass tube and a new salt bridge can be made with the glass tube. It was always confirmed that there was no bubble in the salt bridge before using it.

3.2.2 Electrolyte preparation

The electrolyte was a 0.5M sulphuric acid solution for all the potentiodynamic, potentiostatic, open circuit, galvanostatic, cyclic voltammometric and electrochemical impedance tests. 50g 98% suphuric acid (EMD) was mixed with about 800mL distilled water. Then the solution was poured into a 1L volumetric flask and mixed well. The solution was stored in a cabinet for later use.

3.2.3 PVD coating of TiN

Before coating, the metal samples were polished on 240, 320, 400, 600 and 800 grit silicon carbide papers. The coating process was plasma enhanced reactive evaporation, in which Ti was evaporated in direct current (DC) plasma of nitrogen and argon. The process was conducted at about 450°C and the total coating time was about 12 hours. The samples was drilled a small hole at the edge and suspended over the evaporation from a wire. The PVD coating was done at Liburdi Turbine Services Inc., 400 Highway 6 North, Dundas, Ontario.

3.2.4 Polypyrrole coating

Both galvanostatic and cyclic voltammometric methods were used for the polypyrrole coating. In galvanostatic coating, different currents, coating times and concentration of

electrolyte were utilized to coat polypyrrole films. In cyclic voltammometric coating, the initial potential was -0.2VvsSCE, the final potential was 1.0VvsSCE and the scan rate was 5mV/sec. The number of cycles was 2, 4, 6, and 8. The electrochemical instrumentation used was a Solartron 1285 Potentiostat. All the polypyrrole coating were conducted at ambient temperature because the polypyrrole coating has its highest conductivity between 10 and 30°C [5].

3.3 Electrochemical measurement systems
3.3.1 Open circuit

This experiment was used to monitor the open circuit potential as a function of time. The experiment can be performed for a fixed duration or until a particular potential is reached [6]. In our tests, the setting time was 1 hour with 1 point/second measurement. The measurements were carried out at 70°C in order to simulate PEM fuel cell working conditions.

3.3.2 Potentiodynamic

A potential sweep between up to 4 separate potential setpoints is applied and the current response is measured. The sweep can be terminated or the sweep direction reversed if a particular current is reached. This can be configured to obtain either polarization resistance or Tafel data [6]. In the potentiodynamic tests, the initial potential was -0.1VvsOCP, and the final potential was 1.2VvsSCE and the scan rate was 1mV/sec. The measurements were carried out at temperatures of 20°C and 70°C. The polarization resistance was obtained from the polarization curves based on the linear polarization method:

$$R_p = \frac{\beta_a \beta_c}{2.3 i_{corr}(\beta_a + \beta_c)},$$

3.1

where β_a and β_c are the Tafel slopes of the anodic and cathodic reactions and i_{corr} is the corrosion current density [7].

3.3.3 Potentiostatic

This experiment applies a constant potential and monitors the current as a function of time. The experiment can be performed for a fixed duration or until a particular current is reached [6]. In PEM fuel cells, the anode and cathode are under different potentials. At the anode, the applied potential was -0.1VvsSCE purged with H_2 and at the cathode, the applied potential was 0.6VvsSCE purged with O_2. The setting time is 1 or 10 hours with 1 point/second measurement. The temperature for the potentiostatic test was 70°C.

3.3.4 Galvanostatic

A constant current is applied and the potential is monitored as a function of time. The experiment can be performed for a fixed duration or until a particular potential is reached [6]. Different applied current and different time were used in the galvanostatic tests.

3.3.5 Cyclic voltammogram

This experiment applies a potential sweep between up to 4 separate potential setpoints. If only 2 setpoints are used, multiple cycles may be performed [6].

3.3.6 Electrochemical impedance

This experiment uses the Zplot for Windows software package to perform impedance measurements. A ZplotW setup file must already have been created before beginning this experiment. A Solartron Electrochemical Interface (S1 1287) was used to conduct electrochemical impedance spectroscopy (EIS) measurements. The impedance measurements were performed at open circuit potential and the perturbation amplitude was 10mV The applied frequencies ranged from 1M to 10^{-1}Hz and the data were analyzed by both Zview and ZSmipWin [8] softwares.

3.3.7 Potential-pH diagrams

The potential-pH diagram may be thought of as a map showing conditions of solution oxidizing power (potential) and acidity of alkalinity (pH) for the various possible phases that are stable in an aqueous electrochemical system [7]. Boundary lines on the diagram dividing areas of stability for different phases are derived from the Nernst equation (3.2).

$$e = e^o - \frac{RT}{nF} \ln \frac{a(reduction)}{a(oxidation)}$$
<div align="right">**3.2**</div>

where e and e^o are the electrode potential and standard electrode potential; T is the absolute temperature; R is the universal gas constant; a is the chemical activities for the reduced and oxidized species respectively; F is the Faraday constant; n is the number of electrons transferred in the cell reaction.

First, the potential-pH diagrams for three metals including Al, Fe, Ti were drawn based on the Nerst equation. In our experiments, the pH of the electrolyte is about 0. For PEMFCs, at the anode, the potential is about –0.1V vs SCE and at the cathode, the potential is about 0.6V vs SCE. Therefore, we can determine which product is stable at the anode and cathode based on the potential-PH diagrams for different metals.

3.4 Characterization techniques
3.4.1 Optical microscopy

In order to observe any corrosion products on the metals, the surfaces of both non-polarized and polarized samples were examined using optical microscopy. A Buehler optical image analyzer 2002 system (Department of Mechanical, Automotive & Materials Engineering, University of Windsor) was used to determine the corrosion products on the specimens. The optical microscopy was performed using a Sony Exwavehad color video digital camera at 50 times magnification.

3.4.2 XRD

The PVD coated samples were examined by x-ray diffraction (XRD) using a Rigaku x-ray diffractometer operated at V=30KV, I=30mA and Cu Kα radiation (Department of Mechanical, Automotive & Materials Engineering, University of Windsor).

3.4.3 SEM and EDX

The surface morphologies and chemical analysis were characterized at high magnifications using scanning electron microscopy (SEM) and Energy Dispersive X-ray (EDX) analysis. In our work, two different SEMs were used. If only surface morphology was to be examined, a JEOL JSM-5800LV SEM (Department of Mechanical,

Automotive & Materials Engineering, University of Windsor) was used. The accelerating voltage was 15kV, while SEM images data were recorded on the floppy discs and images were printed on the 11x14cm sheet photograph papers. If both surface morphology and chemical analysis were required, an environmental scanning electron microscope (ESEM) facility equipped with EDX [FEI Quanta 200F with a solid state back scattered detector (BSD)] (Great Lakes Institute for Environmental Research, University of Windsor) was used. The accelerating voltage used was 15kV, while SEM image data were stored in a USB drive. The samples were viewed and photographed in the SEM at different magnifications including x500, x2000 and x5000.

3.4.4 AFM

When studying the nucleation and growth of polypyrrole, the detailed features of the surface microstructures were characterized at high magnifications using atom force microscopy (AFM) [Hysitron nanomechanical test instrument with AFM] (Department of Mechanical, Automotive & Materials Engineering, University of Windsor). In the AFM test, the contact tip of AFM moved over the sample surface. The AFM operating mode is constant load control mode and the tip used for nanoindentation is three-sided pyramid Berkovich tip with a radius of the tip curvature of ~100nm.

3.4.5 ICP-OES

Inductively coupled plasma optical emission spectrometry (ICP-OES) (IRIS #701776, Thermo Jarrell Ash Corporation) was used to investigate the metal ion concentrations in the electrolyte solution after corrosion. Liquid samples were introduced into the instrument via a Meinhard concentric glass nebulizer (TK-30-K2, JE Meinhard Associates Inc., California, USA) combined with a cyclonic spray chamber (Great Lakes Institute for Environmental Research, University of Windsor). The areosol was then introduced into a radial orientation argon plasma resulting in characteristic emission lines that are simultaneously resolved using argon purged echelle optics and a themostatted charge injection device detector.

3.4.6 ICP-MS

An ICP-MS (Thermo Instruments X-7 Inductively Coupled Plasma Mass-Spectrometer) technique was used to determine the metal ion concentration after 10 hours potentiostatic testing in both the simulated anode and cathode environments. Inductively coupled plasma mass spectrometry (ICP-MS) analyses were conducted using a high sensitivity (Great Lakes Institute for Environmental Research, University of Windsor). ThermoFisher Scientific (Mississauga, On, Canada) X series II quadrupole instrument. An ICP-MS can be thought of as four main processes, including sample introduction and aerosol generation, ionization by an argon plasma source, mass discrimination, and the detection system. For sample introduction, the aqueous solution was introduced via a Conikal nebulizer combined with Cyclonic spray chamber in the continuous flow mode using a SC-2 autosampler from ESI. After the sample entered the nebulizer, the liquid was broken up into a fine aerosol by the pneumatic action of Ar gas flow (~ 1L/min) dispersing the liquid into tiny droplets. Then, the spray chamber only allowed the small droplets to enter the plasma for dissociation, atomization, and finally ionization of sample's element components. In ICP-MS, a plasma consisting of ions, electrons and neutral particles is formed from Argon gas. Then the hot plasma is used to atomize and ionize the elements in a sample. The resulting ions that successfully pass through a series of apertures (cones) were first accelerated by a high voltage potential gradient and are then passed through a series of focusing lenses into the high vacuum quadrupole mass analyzer. The isotopes of the elements were identified by their mass-to-charge ratio (m/e) and the intensity of a specific peak in the mass spectrum is proportional to the amount of that isotope (element) in the original sample. The ion detector used in the ICP-MS system is the electron multiplier. ICP-MS analyses data reduction was conducted using Excel worksheets based programs/ macros written in Visual Basic. Multi elements calibration standards and internal standards have been used in the analyses.

3.4.7 FTIR

The polypyrrole coatings were characterized by Fourier Transform Infrared Spectroscopy (FTIR) [Bruker Vector 22] (Department of Chemistry and Biochemistry,

University of Windsor). A background peak was first acquired. The polypyrrole was mixed well with KBr. The peak for the polypyrrole was then obtained.

3.5 Surface roughness test

The roughness of the metal samples was characterized by a Mitutoyo SJ-201p stylus surface profiler, Japan (Department of Mechanical, Automotive & Materials Engineering).

3.6 Interfacial contact resistance

The interfacial contact resistance measurement method that was used in our experiments was based on other researchers' methods [2, 9]. All interfacial contact resistance measurements were carried out at room temperature. In our setup, shown in Fig3.4, two pieces of Toray conductive carbon paper (properties are shown in Table 3.4) (ordered from Fuel Cell Store) were sandwiched between the metal sample and the copper plates. A GW Instel GOM-802 milliohmmeter was used to measure the electrical resistance. While the compaction force was gradually increased, the contact resistance was gradually decreased. The compaction force was applied by means of a Tinus Olsen test machine (Department of Mechanical, Automotive & Materials Engineering, University of Windsor).

As can be seen in Fig 3.4, the total measured resistance (R_{T1}) is a resistance sum including two carbon paper/copper plate interfaces ($R_{C/Cu}$), two carbon paper/metal plate interfaces ($R_{C/M}$), the resistance of the metal (R_M), two carbon paper resistances (R_C) and two copper resistances (R_{Cu}). In order to calculate the contact resistance of carbon paper and metal plates, another experiment was set up as in Fig 3.5 (the total measured resistance is R_{T2}), which included two carbon paper/copper plate interfaces ($R_{C/Cu}$), one carbon paper/metal plates interface ($R_{C/M}$), the resistance of metal (R_M), one carbon paper resistance (R_C) and part of copper resistance (R_{Cu}).

$$R_{T1} = 2R_{C/Cu} + 2R_{C/M} + R_M + 2R_C + 2R_{Cu} \qquad \textbf{3.3}$$

$$R_{T2} = 2R_{C/Cu} + R_C + 2R_{Cu} \qquad \textbf{3.4}$$

Therefore, $R_{C/M} = \dfrac{R_{T1} - R_{T2} - R_M - R_C}{2}$ **3.5**

Since the resistances of the metal (Table 3.5) and the carbon paper are very small compared to the interfacial contact resistance, equation 3.3 can be rewritten as:

$R_{C/M} = \dfrac{R_{T1} - R_{T2}}{2}$ **3.6**

After this correction, halving the result gives the interfacial contact resistance for the carbon paper/metal ($R_{C/M}$) interface (assuming that the surfaces are homogeneous).

Table 3.4 The parameters of Toray carbon paper [10]

Unit	Thickness (mm)	Electrical resistivity mΩ·cm		Thermal conductivity W/(m·K)			Gas permeability ml·mm/ (cm²·hr·mmAq)	Porosity (100%)	Bulk Density (g/cm³)	Surface roughness (μm)	Coefficient of thermal expansion (in plane) (25~100°C) (x10⁻⁶/°C)	Flexural strength (MPa)	Flexural modulus (MPa)	Tensile Strength (kgf/cm)
		Through plane	In plane	Through plane(room temp.)	In plane (room temp.)	In plane (100°C)								
TGH-H-060	0.19	80	5.8	1.7	21	23	1900	78	0.44	8	-0.8	40	10	5

Table 3.5 The electrical resistance for metals

Metal	Electrical resistivity (nΩ·m)	Length (mm)	Area (cm²)	Electrical resistance (mΩ)
Copper	17.1	2	4	8.55×10^{-5}
Stainless steel	720	1	2.25	3.2×10^{-3}
Plain steel	180	1	2.25	8×10^{-4}
Aluminium	26.5	1	2.25	1.18×10^{-4}
Titanium	390	1	2.25	1.73×10^{-3}

Force

Plexisglass →

Copper plate →

Carbon paper →
Metal sample →
Carbon paper →

Copper plate →

Plexisglass →

Force
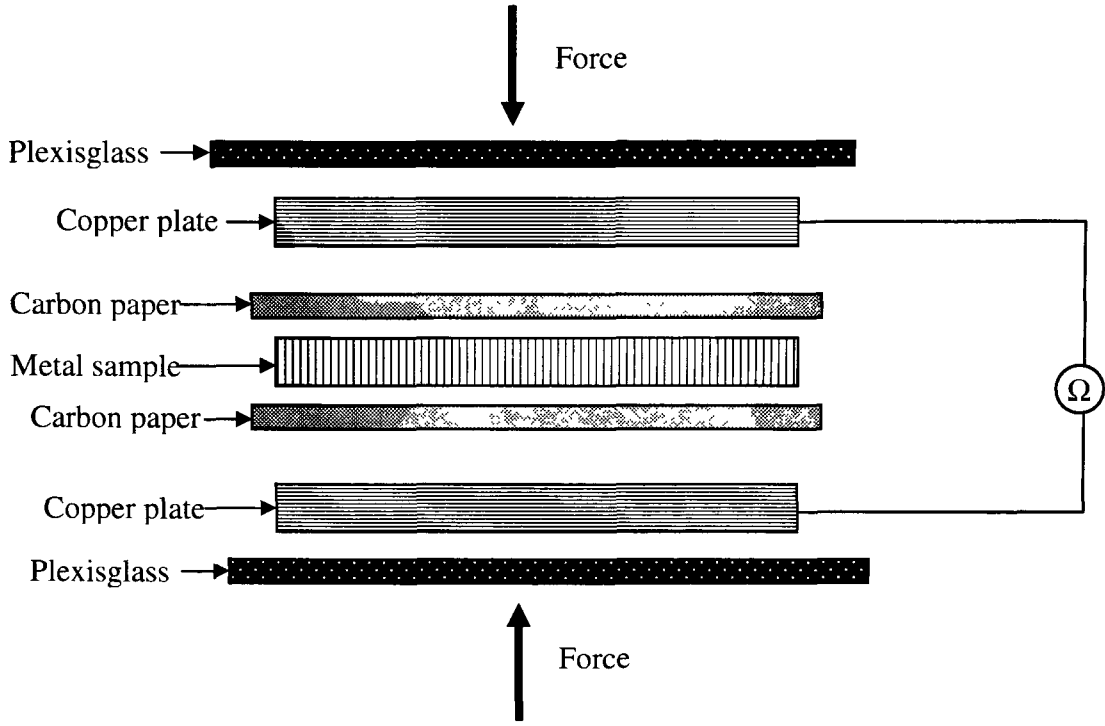
Fig 3.4 The setup of resistance1

Force

Plexisglass →

Copper plate →
Carbon paper →
Copper plate →

Plexisglass →

Force
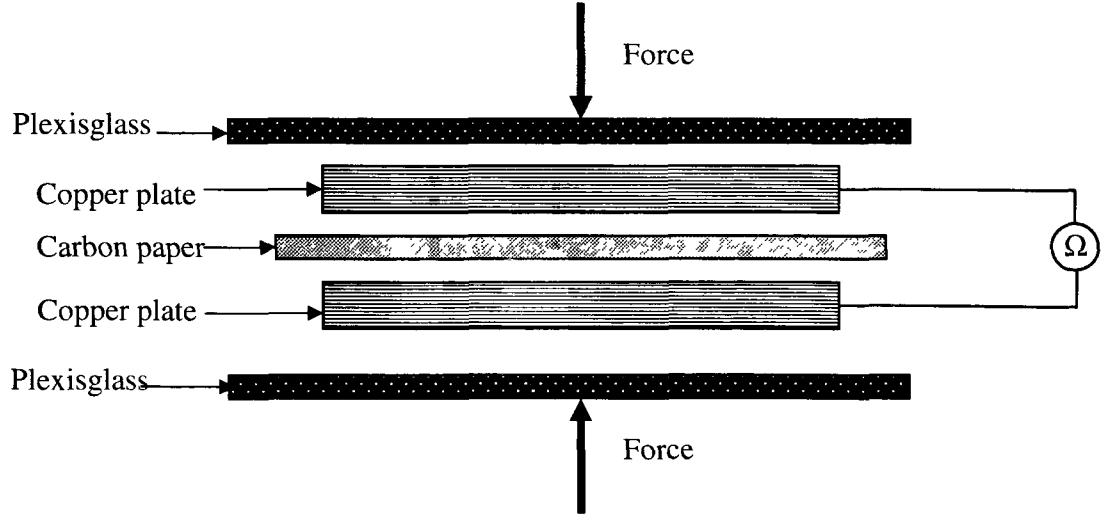
Fig 3.5 The setup of resistance 2

72

3.7 Summary

A summary of the experimental details is given in Table 3.6.

Table 3.6 Summary of experimental details

Base materials	SS316L, SS347, SS410, A36 steel, Al6061, Ti
Coating methods	PVD coating, Electrochemical coating
Coating materials	TiN, Polypyrrole
Electrochemical testing temperatures	20°C, 70°C
Electrochemical testing methods	Open circuit, Potentiodynamic, Potentiostatic, Galvanostatic, Cyclic voltammogram, Electrochemical impedance Potential-pH diagram
Electrochemical instrumentation	Solartron 1285 Potentiostat, Solartron 1287 Electrochemical Interface
Electrolyte	0.5M H_2SO_4
Characterization techniques	Optical microscopy, XRD, SEM with EDX, AFM, FTIR, ICP-OES, Interfacial contact resistance

References

1. http://www.metalprices.com/#. Last retrived on August 25, 2008.

2. H.Wang, M.A. Sweikart, J.A.Turner, Stainless steel as bipolar plate material for polymer electrolyte membrane fuel cells. J.Power Sources, 115(2003)243-251.

3. H.Wang, J.A.Turner, Ferritic stainless steel as bipolar plate material for polymer electrolyte membrane fuel cells. J.Power Sources, 128(2004)193-200.

4. H.Wang, G.Teeter, J.A.Turner, Investigation of a Duplex Stainless Steel as Polymer Electrolyte Membrane Fuel Cell Bipolar Plate Material. J.Electrochem Soc, 152(3)(2005)B99-B104.

5. A.Kassim, Z.Btebasar and H.Mahmud, Effects of preparation temperature on the conductivity of polypyrrole conducting polymer. Proc.Indian Acad.Sci., 114(2002)155-162.

6. Electrochemistry/Corrosion software operating manual, Version 1.4, 1996, Scribner Associates, Inc, Virginia.

7. D.A.Jones. Principles and Prevention of Corrosion, New York: Macmillan,1992.

8. http://www.echemsw.com/. Last retrieved on July 30, 2008.

9. D.P.Davies, P.L.Adcock, M.Turpin, S.J.Rowen, Bipolar plate materials for solid polymer fuel cells. J.Applied Electrochemisty, 30(2000)101-105.

10. http://www.torayca.com/properties/en/images/report_eng09_2.html. Last retrieved on July 30, 2008.

CHAPTER 4

POTENTIAL METALLIC BIPOLAR PLATE MATERIALS FOR PEM FUEL CELLS

Published in:

(1) Yan Wang, Derek O. Northwood, An investigation on metallic bipolar plate corrosion in simulated anode and cathode environments of PEM fuel cells using potential-pH diagrams, International Journal of Electrochemical Science, 1(2006)447-455.

(2) Yan Wang, Derek O. Northwood, An investigation of commercial Grade 2 titanium as a bipolar plate material for PEM fuel cells, ECS Transactions, 11(2008)53-60.

(3) Yan Wang, Derek O. Northwood, Life-limiting Aspects of the Corrosion of Metallic Bipolar Plates for PEM Fuel Cells, Advanced Materials Research, 41-42(2008)469-475.

(4) Yan Wang, Derek O. Northwood, An Electrochemical Investigation of Potential Metallic Bipolar Plate Materials for PEM Fuel Cells, submitted to International Journal of Hydrogen Energy.

Metallic materials have good mechanical stability, electrical conductivity and thermal conductivity and can be readily and consistently stamped to desired shape to accommodate the flow channels [1]. Unfortunately, metallic materials are prone to corrosion in the PEM fuel cell conditions. In this chapter, six metals, including SS316L, SS347. SS410, A36 steel, Al6061 and Grade 2 Ti, were investigated as potential bipolar plate materials. The corrosion behaviour and interfacial contact resistance for these metals were determined and a material selected for further investigation.

4.1 Polarization behavior of the metals

Figs 4.1-4.6 are the anodic polarization curves for the six different metals in a 0.5M H_2SO_4 solution at both ambient temperature and 70°C. From Fig4.1, we can see the

potentiodynamic polarization curve of SS316L can be divided into three regions. The first region is the active region from OCP to -0.15V, the second region is the passive region from -0.15 to 0.9V, and the third region is the transpassive region from 0.9V to 1.2V Comparing the two curves in Fig 4.1, the corrosion current density at the high temperature (70°C) is larger than that at ambient temperature. Thus, in PEMFC conditions, the corrosion rate is higher. Fig 4.2 presents the corrosion curves for SS347 We can see that they have almost the same shape as for SS316L. This is because both of the stainless steels are austenitic stainless steels and their chemical compositions are very similar. It is well known that the chromium content in a stainless steel determines the corrosion resistance because chromium forms a passive film that can prevent further corrosion. Also, nickel can play an important role in corrosion behavior of stainless steels. Nickel has a FCC crystal structure and nickel additions allow the stainless steel to retain a FCC structure at room temperature. Austenitic stainless steels normally have better corrosion resistance than ferritic and martensitic stainless steels because the carbides can be retained in solid solution by rapid cooling from high temperature [2].

Fig 4.3 presents the corrosion curves for SS410. At ambient temperature, SS410 has three areas: an active area, a passive area and a transpassive area. At the high temperature (70°C), SS410 has no passive region since SS410 does not form a dense film to prevent corrosion at high temperatures.

Fig 4.4 presents the corrosion curves for Al6061. There is no passive area in these curves. The corrosion current for Al6061 is large, being about $10^{-4}A/cm^2$ at ambient temperature and $10^{-3}A/cm^2$ at the high temperature (70°C).

Fig 4.5 presents the corrosion curves for A36. The corrosion current density can reach values as high as $0.1A/cm^2$ From Fig4.6, we can see that Grade2 Ti has good corrosion resistance because in the potentiodynamic tests, the current density is maintained at a very small value up to 1.2VvsSCE at 70°C.

Figs 4.7 and 4.8 compare the potentiodynamic polarization behaviour of the different metals at ambient temperature and high temperature (70°C), respectively. At ambient temperature, SS316L, SS347, SS410 and Ti exhibit very small corrosion currents in the passive area. The corrosion currents of Al6061 and A36 steel are very high. At the high temperature (70°C), SS316L, SS347 and Titanium all have a higher corrosion resistance

76

that other three metals. The other metals are readily corroded. Based on the linear polarization method (described in Section 3.3.2), we obtained the corrosion parameters summarized in Table 4.1 for the six metals at ambient and high temperatures. Compared the results in Table 4.1, we can see that the polarization resistance at ambient temperature is more than 10 times than that at high temperature for SS316L, SS347 and Ti. For other three metals, the polarization resistance at ambient temperature is only about 3 to 4 times than that at high temperature. This means that although SS316L, SS347 and Ti have higher polarization resistance than other three metals, they are more sensitive to the temperature. From the corrosion standpoint of view, SS316L, SS347 and Ti are more promising as bipolar plate materials.
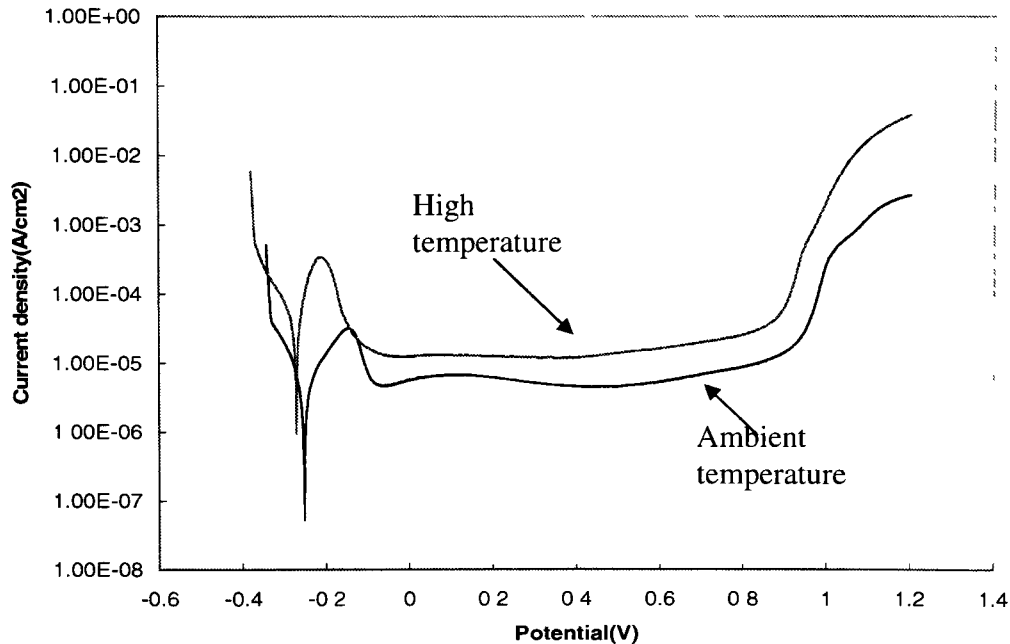
Fig 4.1. Potentiodynamic polarization curves of SS316L at ambient temperature and 70°C.
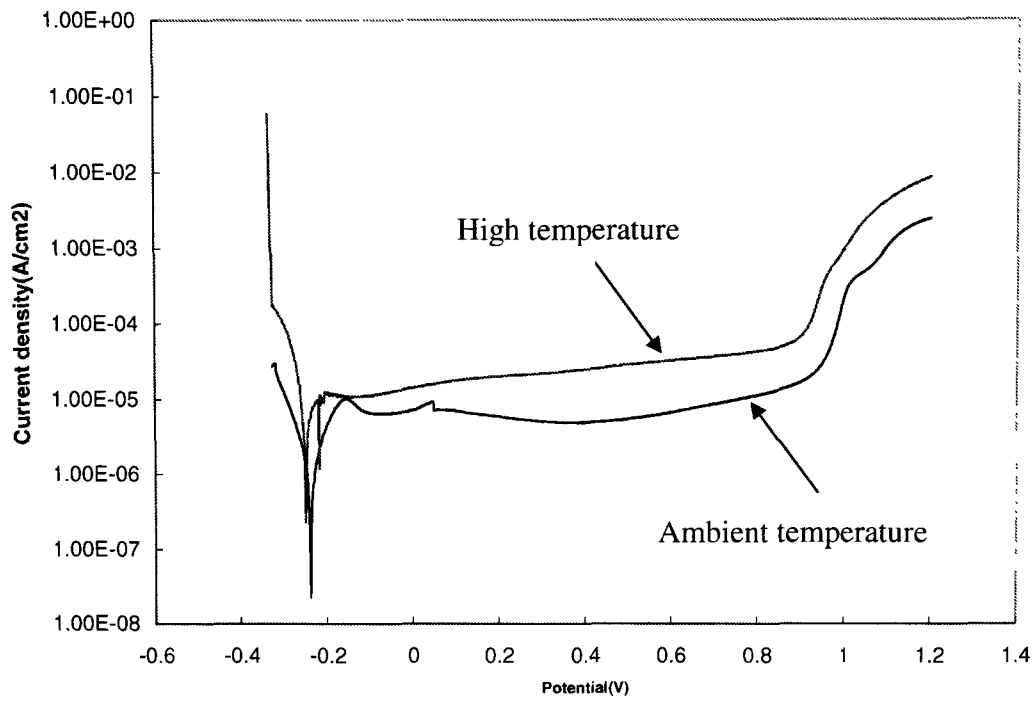
Fig 4.2. Potentiodynamic polarization curves of SS347 at ambient temperature and 70°C.
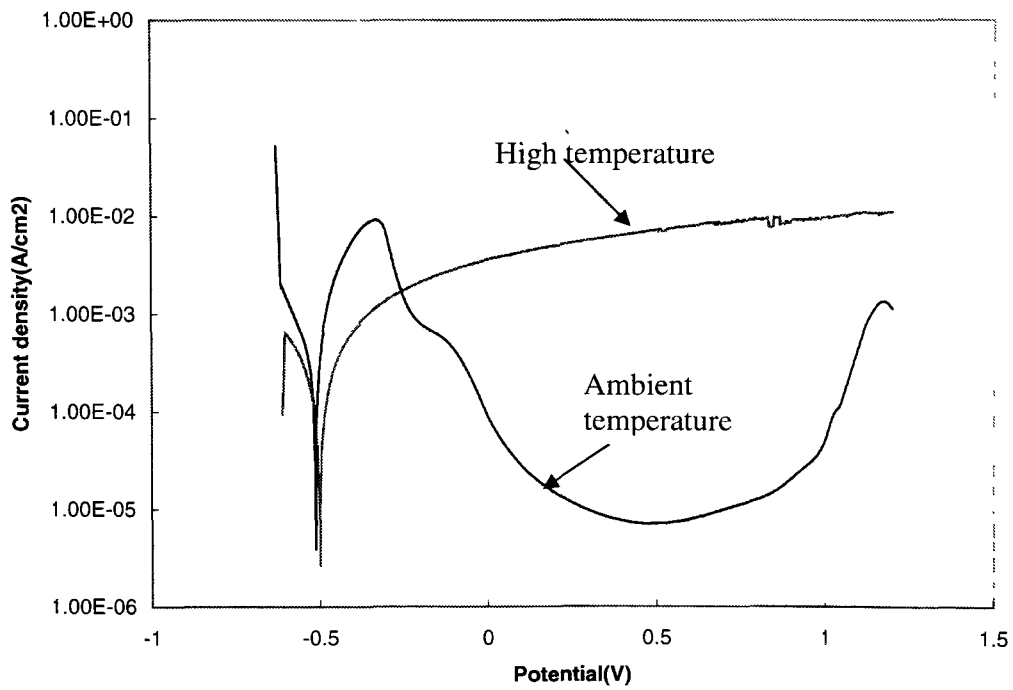
Fig 4.3. Potentiodynamic polarization curves of SS410 at ambient temperature and 70°C.
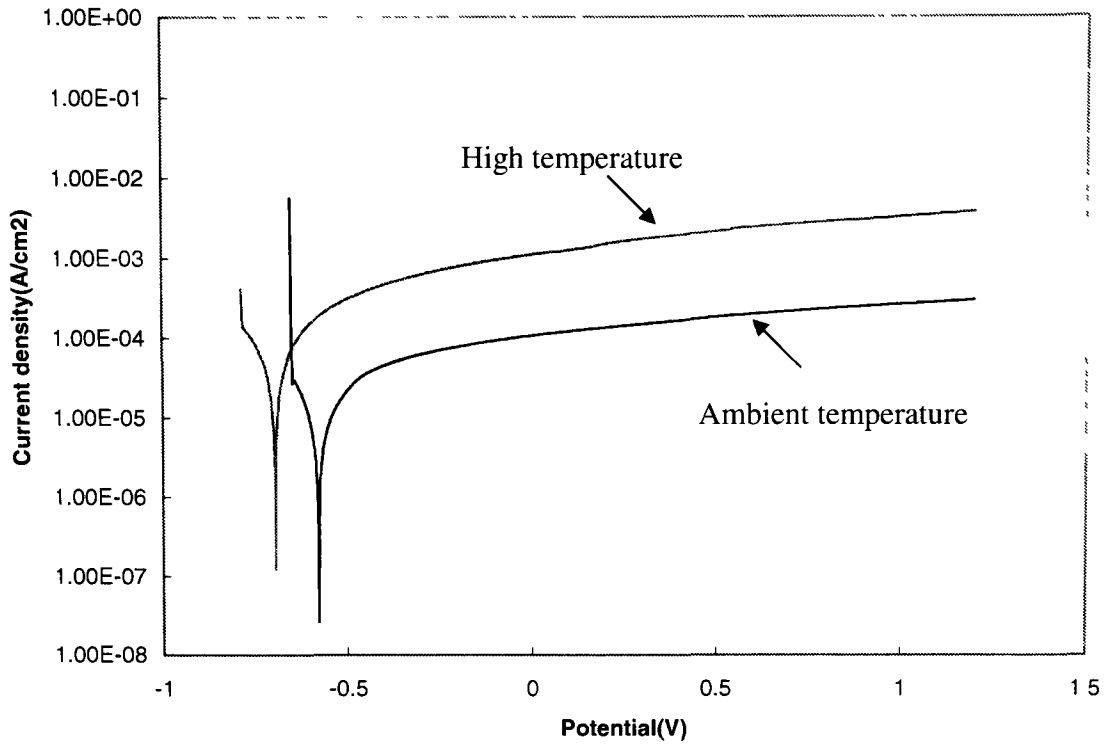
Fig 4.4. Potentiodynamic polarization curves of Al6061 at ambient temperature and 70°C.
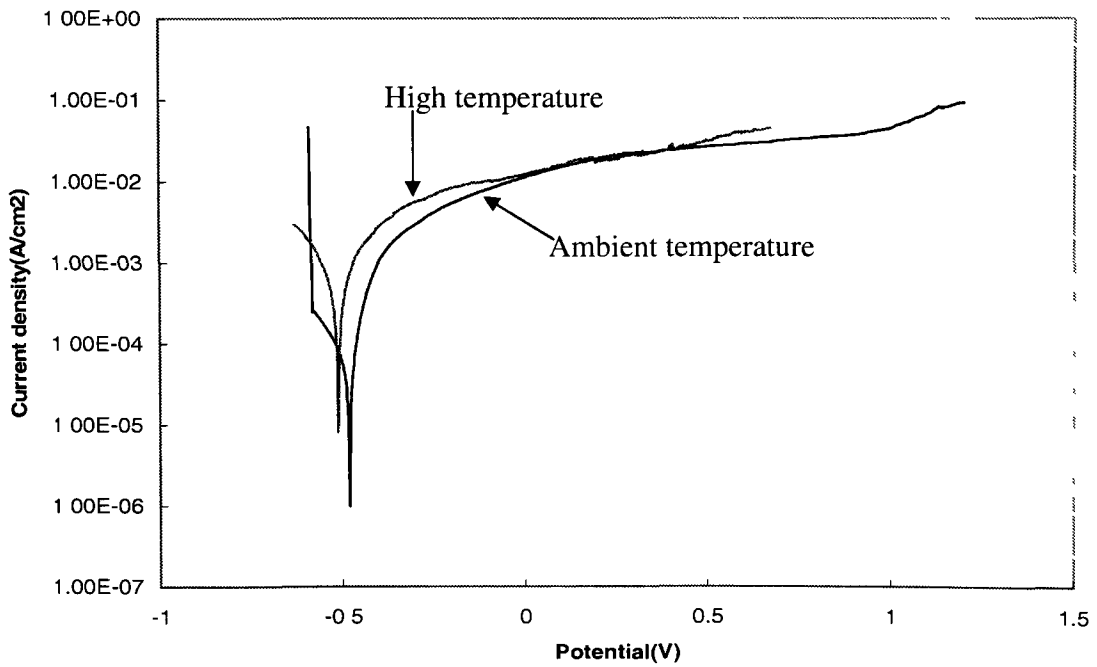
Fig 4.5. Potentiodynamic polarization curves of A36 steel at ambient temperature and 70°C.

79
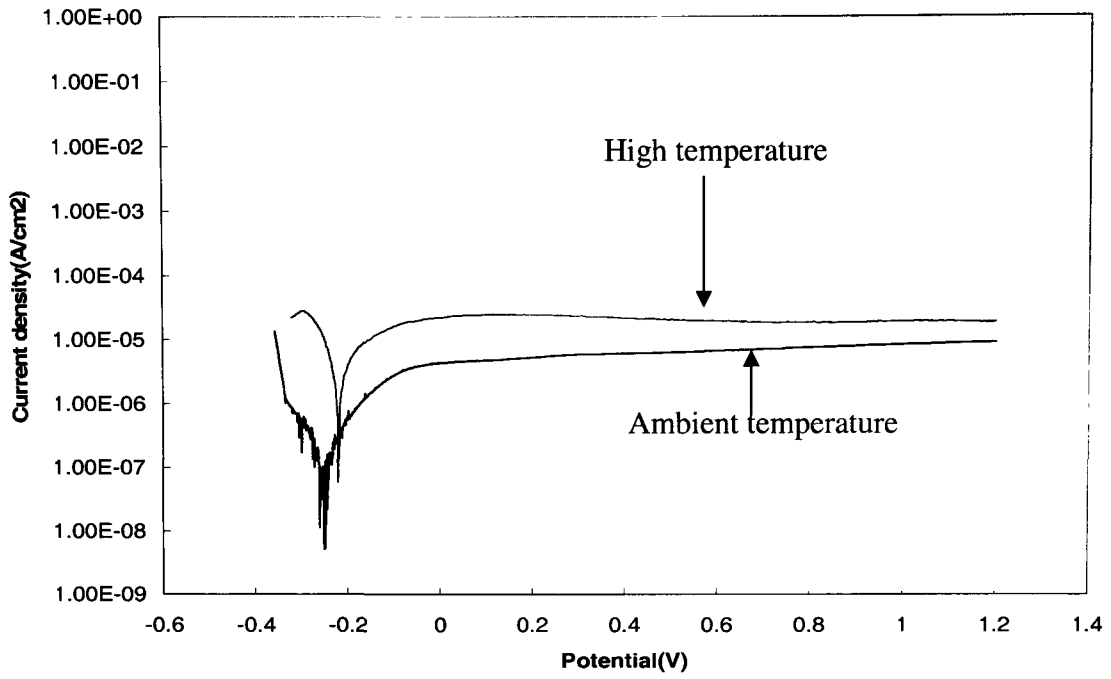
Fig 4.6. Potentiodynamic polarization curves of Grade 2 Ti at ambient temperature and 70°C
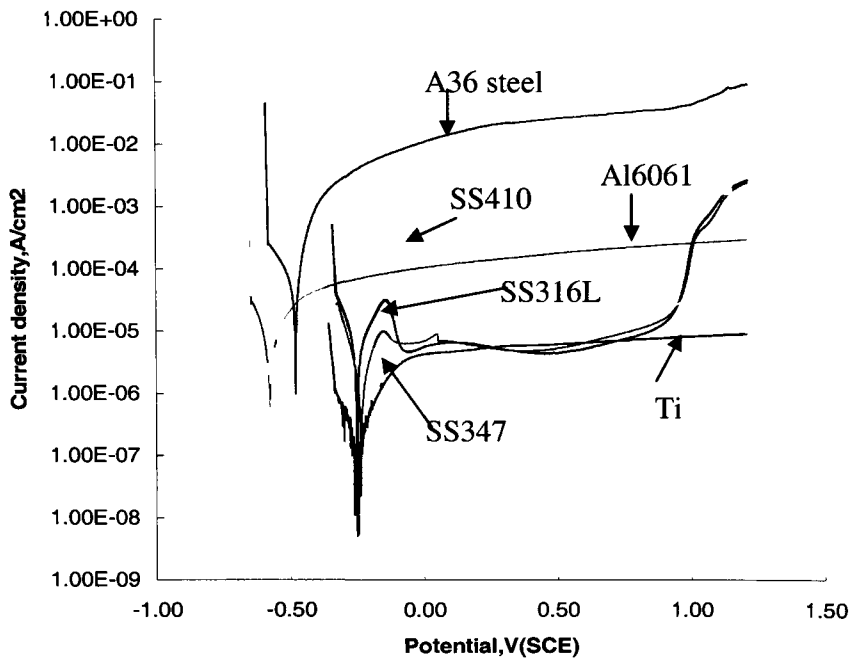
Fig 4.7. Potentiodynamic polarization curves of the six metals at ambient temperature

80
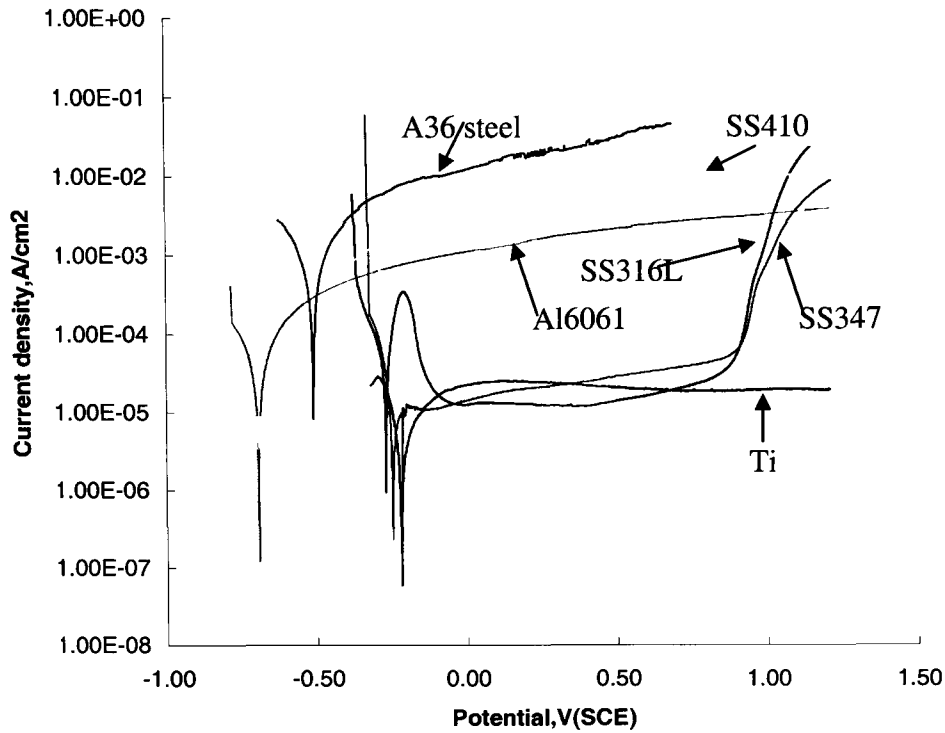
Fig 4.8. Potentiodynamic polarization curves of the six metals at a high temperature (70°C).

Table 4.1 The corrosion parameters of the various metals at 20°C and 70°C in 0.5M H_2SO_4 electrolyte.

Metal	Temperature/°C	β_a /V	β_c /V	E_{corr} /V	i_{corr} /(μA/cm^2)	R_p /(Ω•cm^2)
SS316L	20	0.118	0.085	-0.251	5.120	4196
SS316L	70	0.054	0.087	-0.277	37.774	384
SS347	20	0.086	0.069	-0.237	1.602	10390
SS347	70	0.110	0.091	-0.214	11.236	1927
SS410	20	0.060	0.119	-0.513	289.339	155
SS410	70	0.460	0.192	-0.557	380.935	60
Al6061	20	0.392	0.081	-0.611	13.511	2160
Al6061	70	0.334	0.143	-0.731	64.784	672
A36 steel	20	0.169	0.147	-0.504	151.281	226
A36 steel	70	0.235	0.183	-0.523	805.114	56
Ti	20	0.257	0.053	-0.304	0.437	43716
Ti	70	0.428	0.087	-0.236	7.649	4110

4.2 Corrosion in simulated anode and cathode conditions

In order to study the potential metallic bipolar plate materials in PEMFC working conditions, corrosion tests were conducted in the simulated anode and cathode conditions of a PEMFC. The simulated anode and cathode tests were -0.1VvsSCE purged with H_2 and 0.6VvsSCE purged with O_2. Since the corrosion potentials for the six metals range from -0.2V to -0.7VvsSCE (see Table 4.1), both the anode and cathode simulated corrosion tests are anodic polarization tests for all six metals.

Fig 4.9 presents the corrosion curves for SS316L in the simulated anode and cathode conditions. At the cathode, the corrosion current density gradually decreases and stabilizes at $8 \times 10^{-6} A/cm^2$ At the anode, the corrosion current decreases and becomes negative after about 100 seconds. This is in agreement with Wang et al's results on AISI446 [3]. The current density is maintained at about $-1 \times 10^{-5} A/cm^2$

From Fig 4.10, we can see the corrosion behavior of SS347 in the simulated anode and cathode conditions. In the anode condition, the corrosion current is $-6 \times 10^{-6} A/cm^2$ after 120 seconds. The corrosion current is $7 \times 10^{-6} A/cm^2$ in the cathode conditions. Comparing the curves for SS316L and SS347. we can see that they have almost the same corrosion behavior. As discussed in Section 4.1, this is because both the chemical composition and structure of these two metals are similar.

Fig 4.11 shows us the corrosion behaviour of SS410. The anodic corrosion current is $2.5 \times 10^{-2} A/cm^2$ and the cathodic corrosion current is $4 \times 10^{-3} A/cm^2$ In the anode corrosion, the current density suddenly dropped to $5 \times 10^{-3} A/cm^2$ after 1000 seconds because the applied potential cannot be maintained at -0.1V

Fig 4.12 presents the corrosion current densities for Al6061 in the simulated anode and cathode conditions. At the anode, the corrosion current is $4 \times 10^{-3} A/cm^2$ after 1 hour and at the cathode, the corrosion current is $1.5 \times 10^{-2} A/cm^2$, and after about 1000 seconds, the current density drops to $4 \times 10^{-3} A/cm^2$

Fig 4.13 shows the corrosion current densities for A36 steel. The anodic current density is $5 \times 10^{-3} A/cm^2$ and the cathodic current density is $2.5 \times 10^{-2} A/cm^2$ We can see that the current density drops suddenly for the anode of SS410 and the cathode of both Al6061 and the A36 steel. After the current density drops, it remains at about $4 \times 10^{-3} A/cm^2$ We can see that the corrosion current density is large for the anode of SS410 and

the cathode of both Al6061 and the A36 steel. Therefore, the corrosion reaction is first controlled by electrochemical polarization. After 1000 seconds, it is controlled by concentration polarization and there are insufficient H^+ ions to maintain a high current. Thus, the applied potential is reduced, and then the current density is also lowered.

Fig 4.14 presents the anodic and cathodic corrosion current densities in the simulated anode and cathode environments for Grade 2 titanium. At the anode, the current density is -8×10^{-6} A/cm^2 after 1 hour and at the cathode, the current density is 2×10^{-5} A/cm^2

Table 4.2 is a summary of all the measured anodic & cathodic current densities. From Table 4.2, we can see that SS316L, SS347 and Ti have a very small current density at both the anode and the cathode. Al6061 and ASTM-A36 have small current densities at the cathode side, but these metals have large current densities at the anode side. SS410, a martensitic stainless steel, has a larger current density at the anode than that at the cathode, and the current densities are much higher than for the austenitic stainless steels, 316L and 347.

Table 4.2. Anodic and cathodic current densities of the six alloys in simulated PEMFC working conditions

Metal	Anodic current density (A/cm^2)	Cathodic current density (A/cm^2)
SS316	-1×10^{-5}	8×10^{-6}
SS347	-6×10^{-6}	7×10^{-6}
SS410	2.5×10^{-2}, then changes to 4×10^{-3}	4×10^{-3}
Aluminium6061	4×10^{-3}	1.5×10^{-2}, then changes to 4×10^{-3}
ASTM-A36	5×10^{-3}	2.5×10^{-2}, then changes to 4×10^{-3}
Ti	-8×10^{-6}	2×10^{-5}
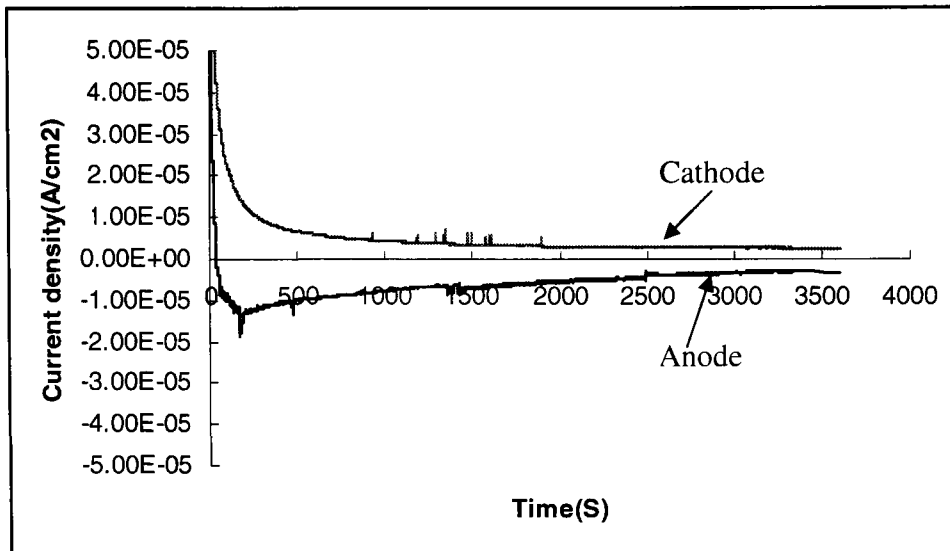
Fig 4.9. Current density vs. time for SS316L at -0.1V purged with H_2 (anode) and 0.6V

purged with O_2 (cathode) at 70°C
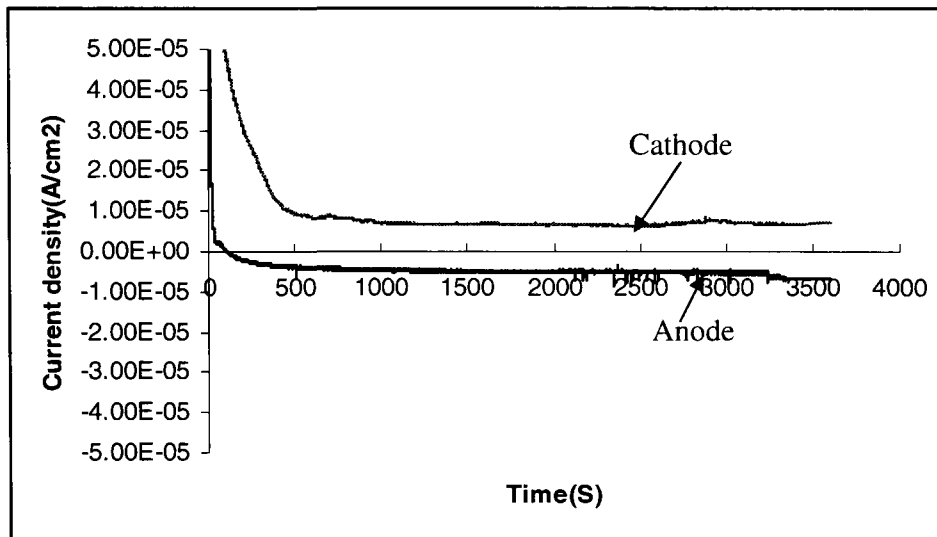
Fig 4.10. Current density vs. time for SS347 at -0.1V purged with H_2 (anode) and 0.6V

purged with O_2 (cathode) at 70°C
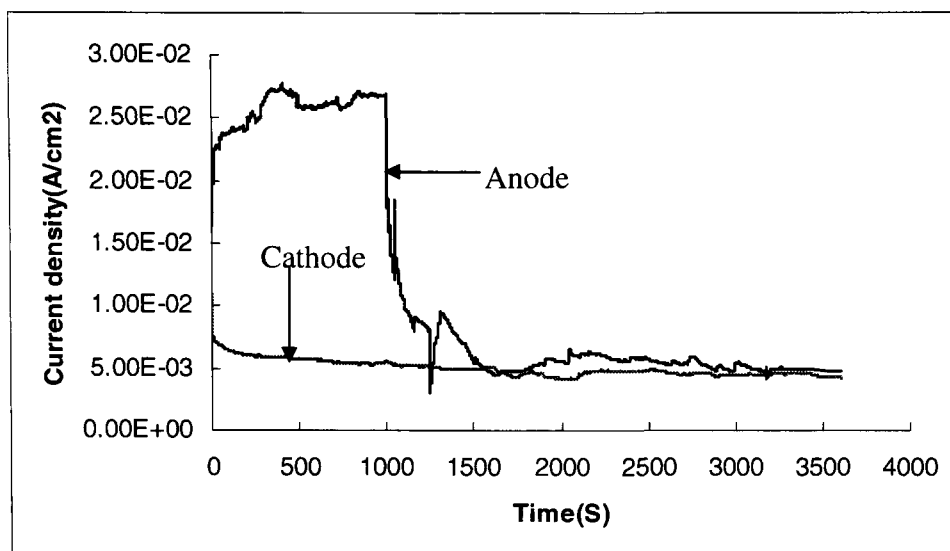
Fig 4.11. Current density vs. time for SS410 at -0.1V purged with H_2 (anode) and 0.6V

purged with O_2 (cathode) at 70°C
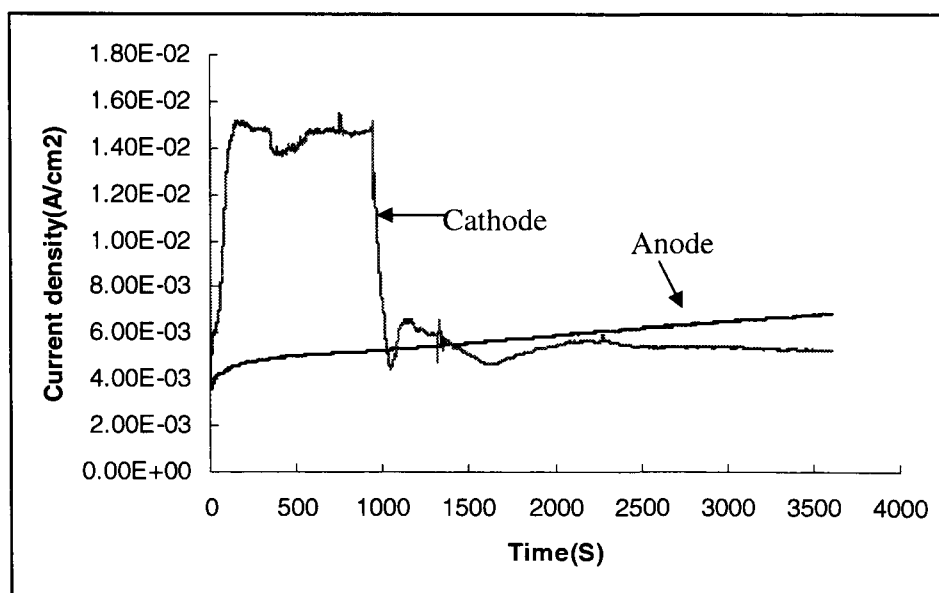
Fig 4.12. Current density vs. time for Aluminium6061 at -0.1V purged with H_2 (anode)

and 0.6V purged with O_2 (cathode) at 70°C
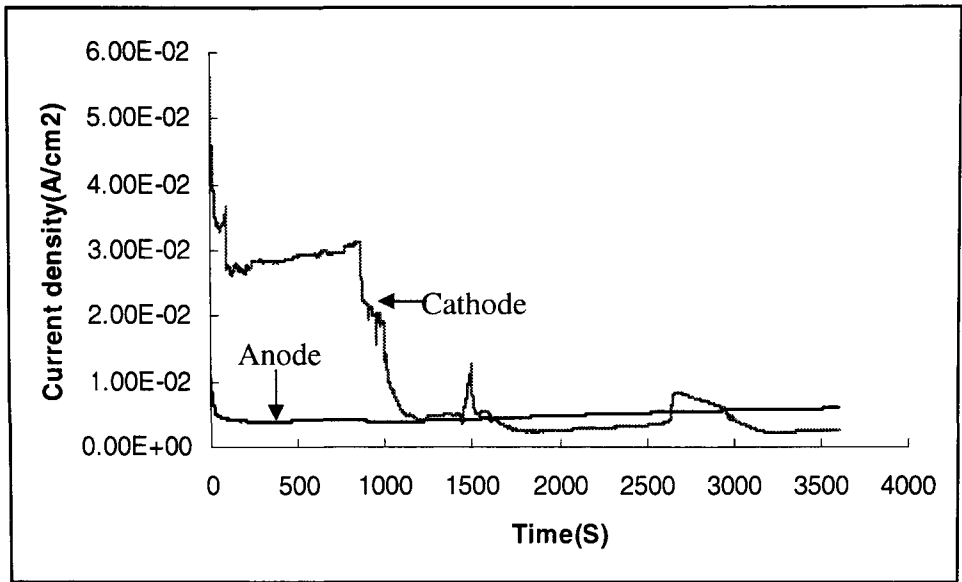
Fig 4.13. Current density vs. time for A36 steel at -0.1V purged with H_2 (anode) and
0.6V purged with O_2 (cathode) at 70°C
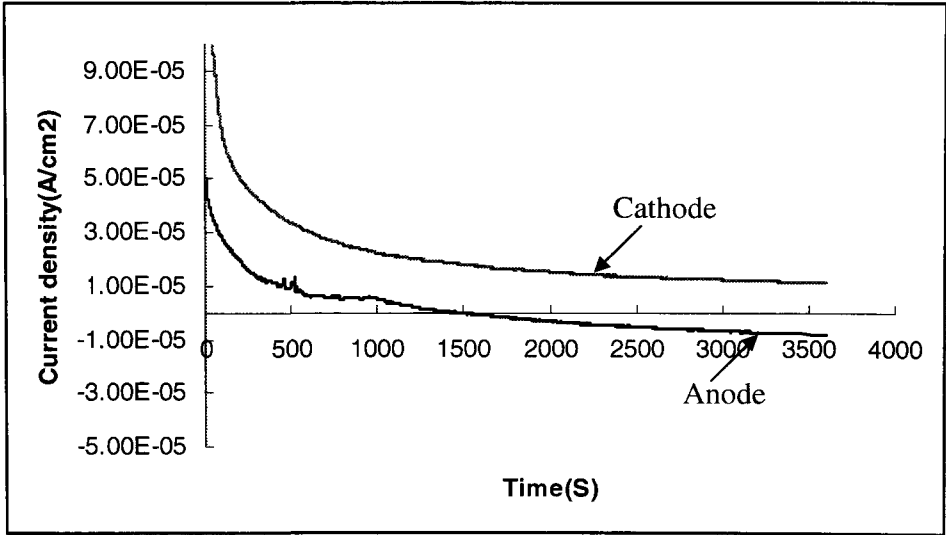
Fig 4.14. Current density vs. time for Grade2 Ti at -0.1V purged with H_2 (anode) and
0.6V purged with O_2 (cathode) at 70°C

As mentioned before, the current densities of SS316L, SS347 and Ti are negative at the
anode. The negative current is due to the following reactions:

86

$$2H^+ + 2e^- \rightarrow H_2 \quad \text{or} \quad 4H^+ + O_2 + 4e^- \rightarrow 2H_2O \qquad \textbf{Metal electrode} \qquad \textbf{4.1}$$

$$2H_2O \rightarrow 4H^+ + O_2 + 4e^- \qquad\qquad\qquad\qquad \textbf{Platinum electrode} \qquad \textbf{4.2}$$
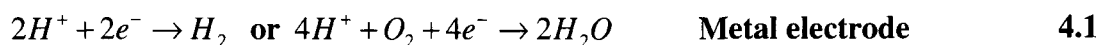
When metals corrode at the anode ($M - 2e^- \rightarrow M^{2+}$), the current is positive. This means that there are electrons produced on the metal electrode. In the standard electrode system, the electrons will flow from the metal electrode to the counter electrode (Pt electrode). In this case, the current is positive (Fig 4.15).
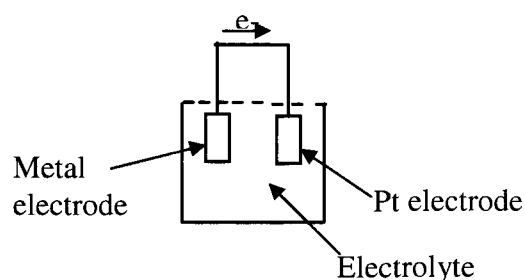
Fig 4.15. Electron flow during corrosion

However, when the current is negative, electrons should flow from the Pt electrode to the metal electrode (Fig 4.16). On the metal electrode, there is a good supply of H^+ ions. Thus, two reactions including $2H^+ + 2e^- \rightarrow H_2$ and $4H^+ + O_2 + 4e^- \rightarrow 2H_2O$, are possible on the metal electrode. In order to determine which of these reactions was taking place, we performed a series of potentiostatic tests at different potentials (-0.1V~-0.5V) for SS316 at ambient temperature. The results are summarized in Table 4.3.
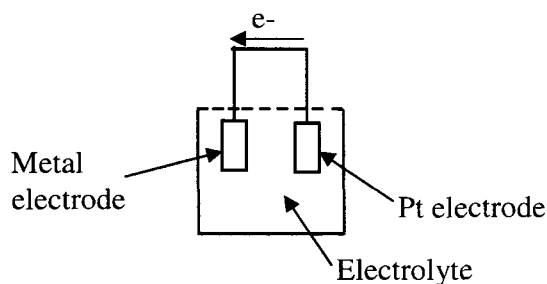
Fig 4.16. Electron flow when there is no corrosion

Table 4.3. Current densities at different applied potentials for SS316L at ambient temperature

Applied Potential (V)	Current Density (A/cm^2)	Bubbles evolved at electrodes
-0.1	-1.6×10^{-6}	no
-0.2	-2×10^{-5}	no
-0.3	-2×10^{-4}	no
-0.4	-4×10^{-3}	Bubbles at both electrodes
-0.5	-2×10^{-2}	Bubbles at both electrodes

From Table 4.3, we can see that the current density increases when the applied potential becomes more negative. When the applied potential reaches -0.4V, there are bubbles formed at both electrodes. The bubbles on the metal electrode are hydrogen and the bubbles on the Pt electrode are oxygen. Even if the current density is $-2 \times 10^{-2} \text{A/cm}^2$, there is no corrosion on the metal surface. We then need to determine which reaction occurs on the metal electrode. Because the potential of the $4H^+ + O_2 + 4e^- \rightarrow 2H_2O$ reaction is more positive than that of the $2H^+ + 2e^- \rightarrow H_2$ reaction, the $4H^+ + O_2 + 4e^- \rightarrow 2H_2O$ reaction will take place first. However, the concentration of O_2 is very low because we purge with H_2 for about one hour and there is a high concentration of H^+ ions and the exchange current density of the $2H^+ + 2e^- \rightarrow H_2$ reaction is larger than that of the $4H^+ + O_2 + 4e^- \rightarrow 2H_2O$ reaction. Therefore, we believe, the reaction is mainly $2H^+ + 2e^- \rightarrow H_2$ on the metal electrode.

4.3 Optical microscopy of surfaces of corroded samples

Figs 4.17-4.22 are optical micrographs of the surfaces of the six alloys before corrosion, after high temperature potentiodynamic testing, and after potentiostatic tests purged with hydrogen or oxygen.

From Figs 4.17 and 4.18, we can see that the grain boundaries are corroded after high temperature corrosion for both SS316L and SS347. Chromium carbides ($Cr_{23}C_6$) can precipitate at the grain boundaries when the carbon content is over 0.02wt%. When the chromium carbides form at the grain boundaries, they deplete the regions adjacent to the

boundaries of chromium so that the chromium level in these areas is decreased below the 12 percent chromium level necessary for passive behaviour. These areas become anodic to the rest of the grain bodies, which are cathodic, thereby creating galvanic couples [4]. When SS316L and SS347 are potentiostatically corroded in the simulated anode conditions, we do not see a corrosion product. This is because the cathodic current provides cathodic protection for the metal. After cathode corrosion, we also can not see a corrosion product on the metal surface. However, this does not mean that there is no corrosion on the metal surface because we observed a corrosion current in the potentiostatic tests.

SS410 and A36 steel were uniformly corroded in all three conditions. Aluminum6061 is uniformly corroded after the potentiodynamic tests. However, in the simulated anode and cathode conditions, we could see grain boundary corrosion and pitting corrosion. Moreover, the pitting is more extensive in the simulated cathode condition because the polarization potential is larger. For Grade 2 Ti, in the simulated anode conditions, there is no corrosion. In the simulated cathode conditions and the potentiodynamic test, corrosion is not very severe because the corrosion current is very small.

For bipolar plates, the goal for corrosion rate is that it should be less than $1.6 \times 10^{-5} A/cm^2$ [5]. Strictly this is only applicable to graphite and composite bipolar plates because when these types of bipolar plates are corroded, the product is CO_2 and it will vent with residual H_2 and O_2. From the data that we obtained, it seems that SS316L, SS347 and Grade 2 Ti could be suitable materials for bipolar plates based on the corrosion criteria. However, some researchers [6, 7] have reported that metals ions can migrate to the membrane, and that levels as low as 5~10ppm can degrade the membrane performance. Furthermore, PEM fuel cells should have operating lifetimes over 5000h for transportation application [8]. A detailed calculation of the metal ion concentrations was as follows.

Calculation of metal ion concentrations for PEM fuel cell after 5000h operation

Suppose $i_{corr} = 10^{-5} A/cm^2$

The electrode area is 2.25 cm^2

$I = iA = 10^{-5} \times 2.25 = 2.25 \times 10^{-5} A$ **4.3**

$C = It = 2.25 \times 10^{-5} \times 5000 = 0.1125 Ah$ **4.4**

$0.1125/26.8 = 0.004198 F$

Suppose Fe changes to Fe^{2+}, $0.004198 \times 29/58 = 0.002099$mol   [for all Fe-based alloys]

Al changes to Al^{3+}, $0.004198 \times 9/27 = 0.0014$mol   [for Al 6061]

Ti changes to Ti^{2+}, $0.004198 \times 24/48 = 0.002099$mol   [for Grade 2 Ti]

The volume of solution is about 0.1L

Based on Bontha and Pintauro's research results [9], about 6 percent of these metal ions will remain in solution in the PEM fuel cell stack. Assuming 5 percent remain in solution:

Wt of Fe^{2+} in the solution after 5000h is $(2.099 \times 10^{-3} \times 58/0.1) \times 0.05 = 0.6 \times 10^{-1}$g/L ≈ 60ppm

Wt of Al^{3+} in the solution after 5000h is $(1.4 \times 10^{-3} \times 27/0.1) \times 0.05 = 1.85 \times 10^{-2}$g/L ≈ 18.5ppm

Wt of Ti^{2+} in the solution after 5000h is $(2.099 \times 10^{-3} \times 48/0.1) \times 0.05 = 0.5 \times 10^{-1}$g/L ≈ 50ppm

From such a calculation, we can see that the concentration after 5000h is 60ppm for Fe^{2+}, 18.5ppm for Al^{3+} and 50ppm for Ti^{2+} All these concentrations are much higher than 5~10ppm. Therefore, even if the corrosion rate is 10^{-5}A/cm^2, these metals cannot meet the requirement that the concentration of metal ions is less than 5~10ppm. Therefore, these metals can probably not be used as bipolar plates, but would require coating to increase their corrosion resistance.
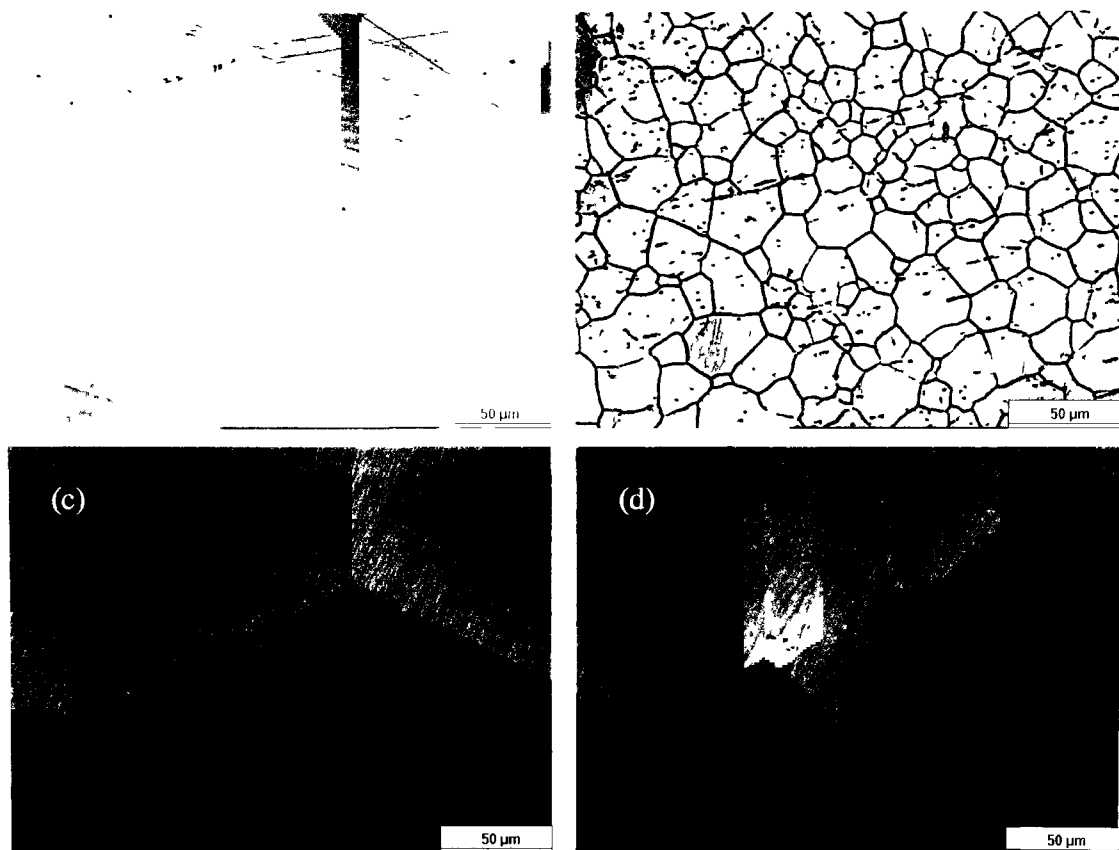
Fig 4.17 Optical micrographs of surface of SS316L before and after potentiodynamic tests at 70°C and potentiostatic tests at 70°C (a) before tests, (b) after potentiodynamic tests at 70°C, (c) after potentiostatic tests at 70°C purged with hydrogen, (d) after potentiostatic tests at 70°C purged with oxygen
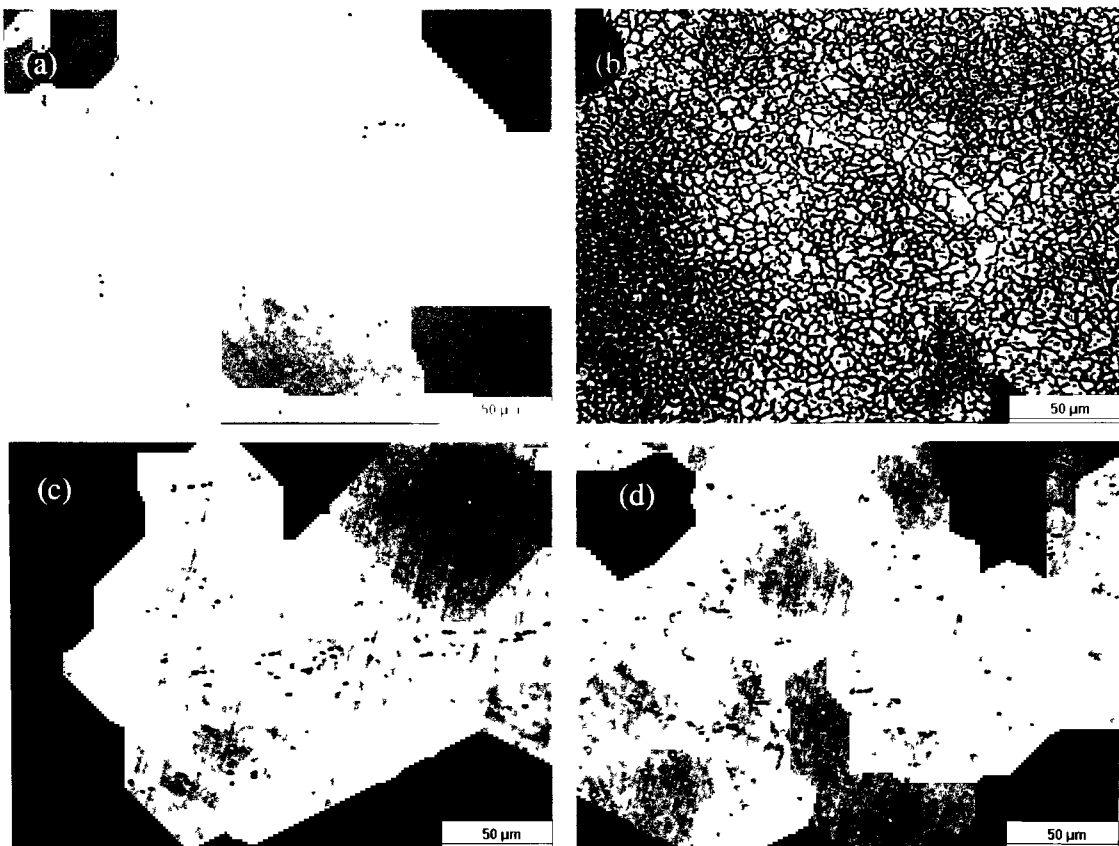
Fig 4.18 Optical micrographs of surface of SS347 before and and after potentiodynamic tests at 70°C and potentiostatic tests at 70°C (a) before tests, (b) after potentiodynamic tests at 70°C, (c) after potentiostatic tests at 70°C purged with hydrogen, (d) after potentiostatic tests at 70°C purged with oxygen
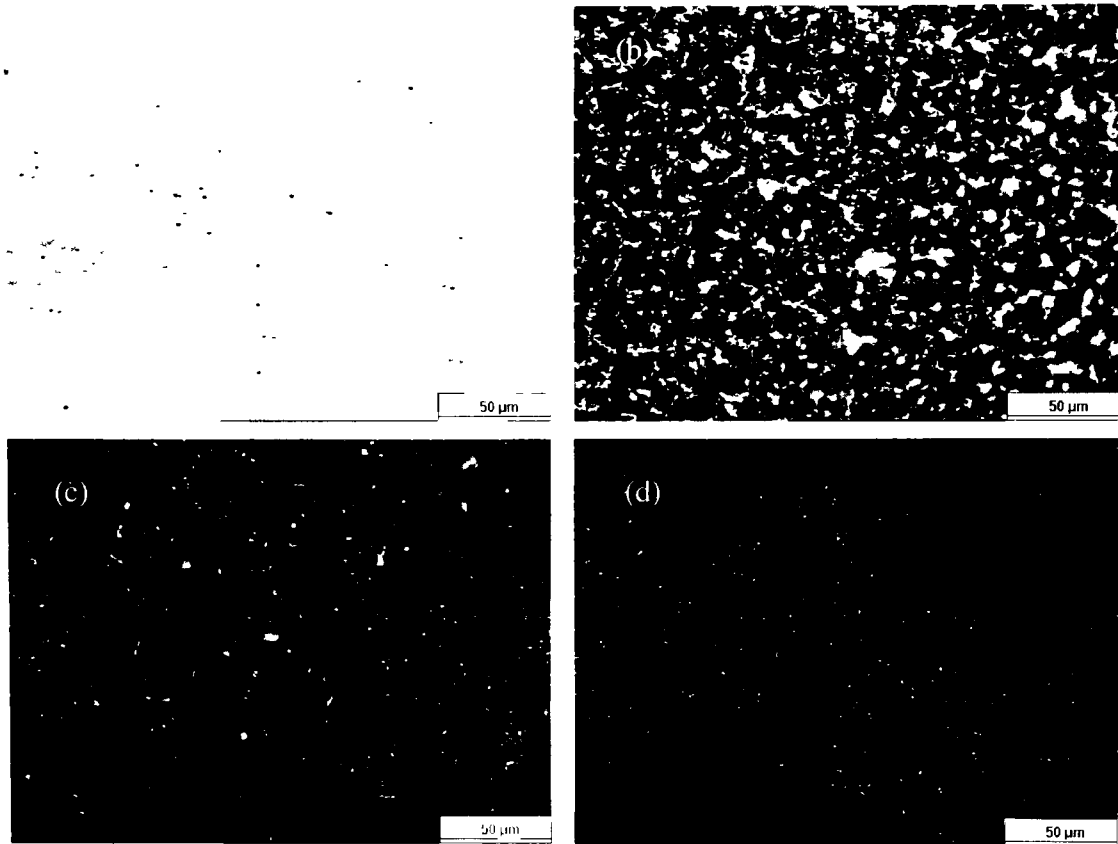
Fig 4.19 Optical micrographs of surface of SS410 before and and after potentiodynamic tests at 70°C and potentiostatic tests at 70°C (a) before tests, (b) after potentiodynamic tests at 70°C, (c) after potentiostatic tests at 70°C purged with hydrogen, (d) after potentiostatic tests at 70°C purged with oxygen

Fig 4.20 Optical micrographs of surface of Al6061 before and and after potentiodynamic tests at 70°C and potentiostatic tests at 70°C (a) before tests, (b) after potentiodynamic tests at 70°C, (c) after potentiostatic tests at 70°C purged with hydrogen, (d) after potentiostatic tests at 70°C purged with oxygen

Fig 4.21 Optical micrographs of surface of A36 steel before and and after
potentiodynamic tests at 70°C and potentiostatic tests at 70°C (a) before tests, (b) after
potentiodynamic tests at 70°C, (c) after potentiostatic tests at 70°C purged with
hydrogen, (d) after potentiostatic tests at 70°C purged with oxygen

95

Fig 4.22 Optical micrographs of surface of Ti before and and after potentiodynamic tests at 70°C and potentiostatic tests at 70°C (a) before tests, (b) after potentiodynamic tests at 70°C, (c) after potentiostatic tests at 70°C purged with hydrogen, (d) after potentiostatic tests at 70°C purged with oxygen

4.4 SEM examination

Figs 4.23-4.28 are scanning electron microscopy (SEM) micrographs of SS316L, SS347, SS410, Al6061, A36 steel and Grade 2 Ti. From Figs 4.23 (SS316L) and 4.24 (SS347), we can see that the grain boundaries are corroded after high temperature potentiodynamic tests. The grain size for SS316L is the range of 5-20μm and the grain size for SS347 is about 5μm. However, we can not see the corrosion products after potentiostatic tests purged with O_2 and H_2 for both SS316L and SS347 because the corrosion rate is very slow. This is similar to what was observed using optical microscopy.

From the SEM micrographs of SS410 (Fig 4.25), we can clearly see the corrosion products. SS410 has a porous surface structure after high temperature potentiodynamic tests (Fig 4.25(a), (b)). However, after potentiostatic tests purged with H_2 (Fig 4.25(c), (d) and O_2 (Fig 4.25(e), (f), the corrosion products are layered and needle shape, respectively.

Fig 4.26 are SEM micrographs showing the corrosion products formed on Al6061. We can see that Al6061 was severely corroded in all conditions. Grain boundary and pitting corrosion are the main corrosion types for Al6061. From Fig 4.26(d), we can see two large holes after the potentiostatic tests with O_2 (diameters are about 500μm.). Comparing the corrosion products after potentiostatic tests with H_2 and O_2, we can see that corrosion is more severe in the simulated cathode condition than in the simulated anode condition.

Fig 4.27 shows us the corrosion products formed on A36 steel. A36 was severely corroded in all conditions. Also the corrosion products for these conditions had almost the same morphology for all corrosion conditions.

In Fig 4.28, we cannot see the corrosion products for Ti for all the conditions because the corrosion rate is very slow. The SEM metallography thus confirmed the electrochemical testing results, ie SS316L, SS347 and Grade 2 Ti have the best corrosion performance of the alloys tested.
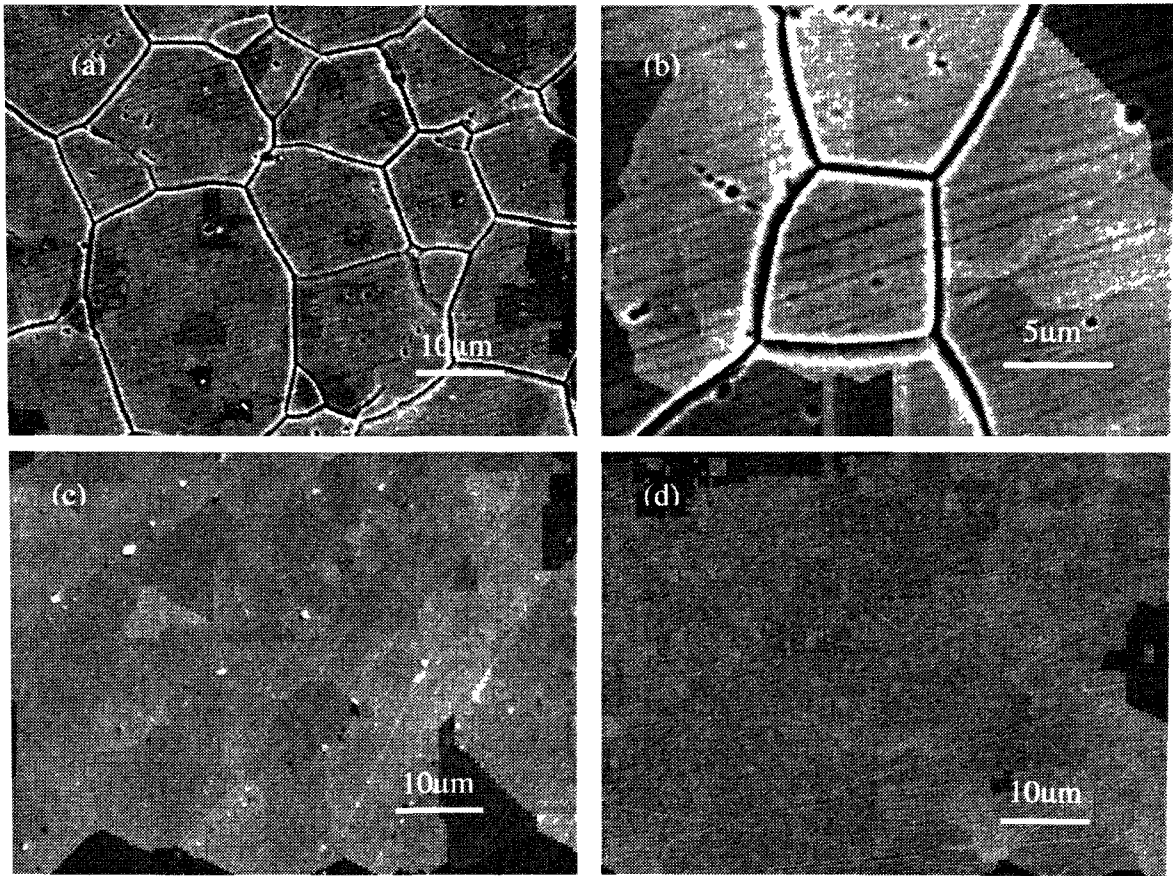
Fig 4.23 SEM micrographs of surface of SS316L after corrosion, (a),(b) after high temperature corrosion, (c) purged with hydrogen, (d) purged with oxygen
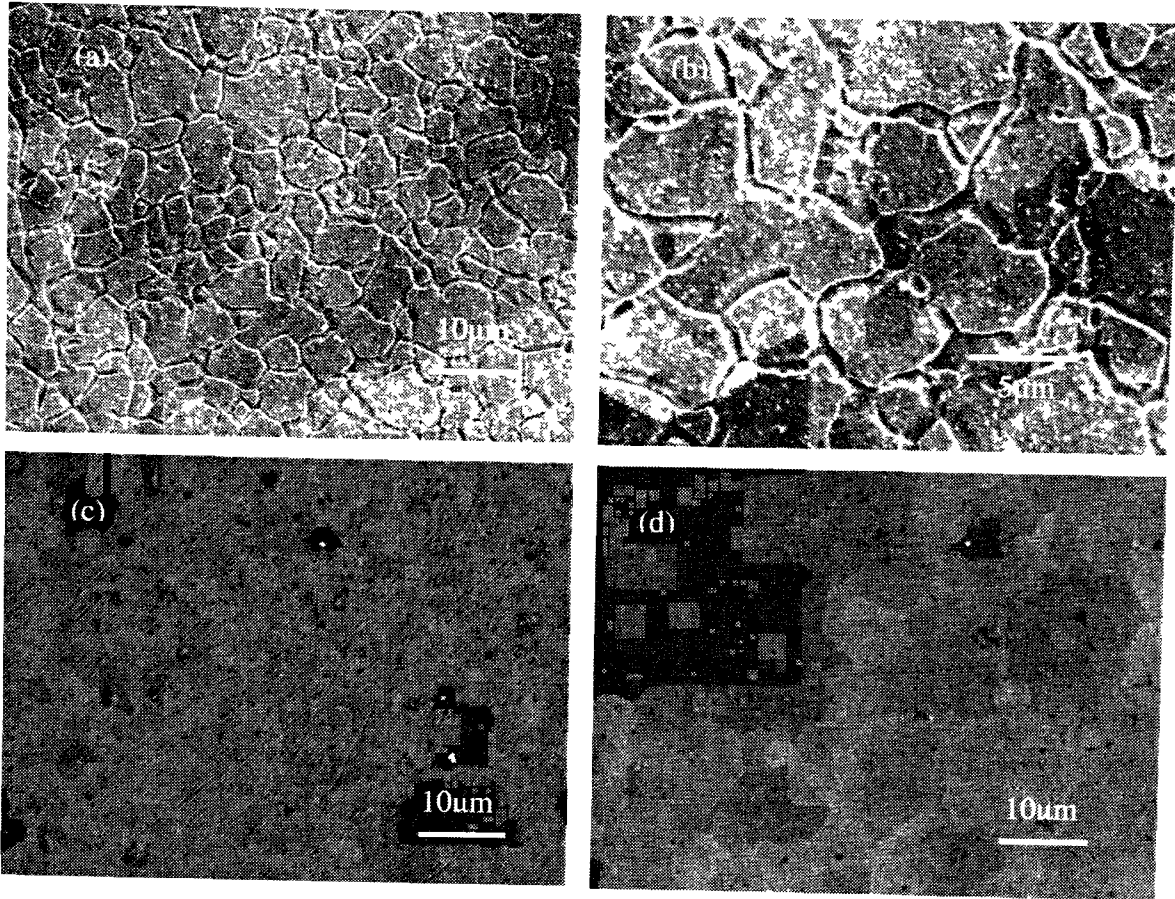
Fig 4.24 SEM micrographs of surface of SS347 after corrosion, (a), (b) after high temperature corrosion, (c) purged with hydrogen, (d) purged with oxygen
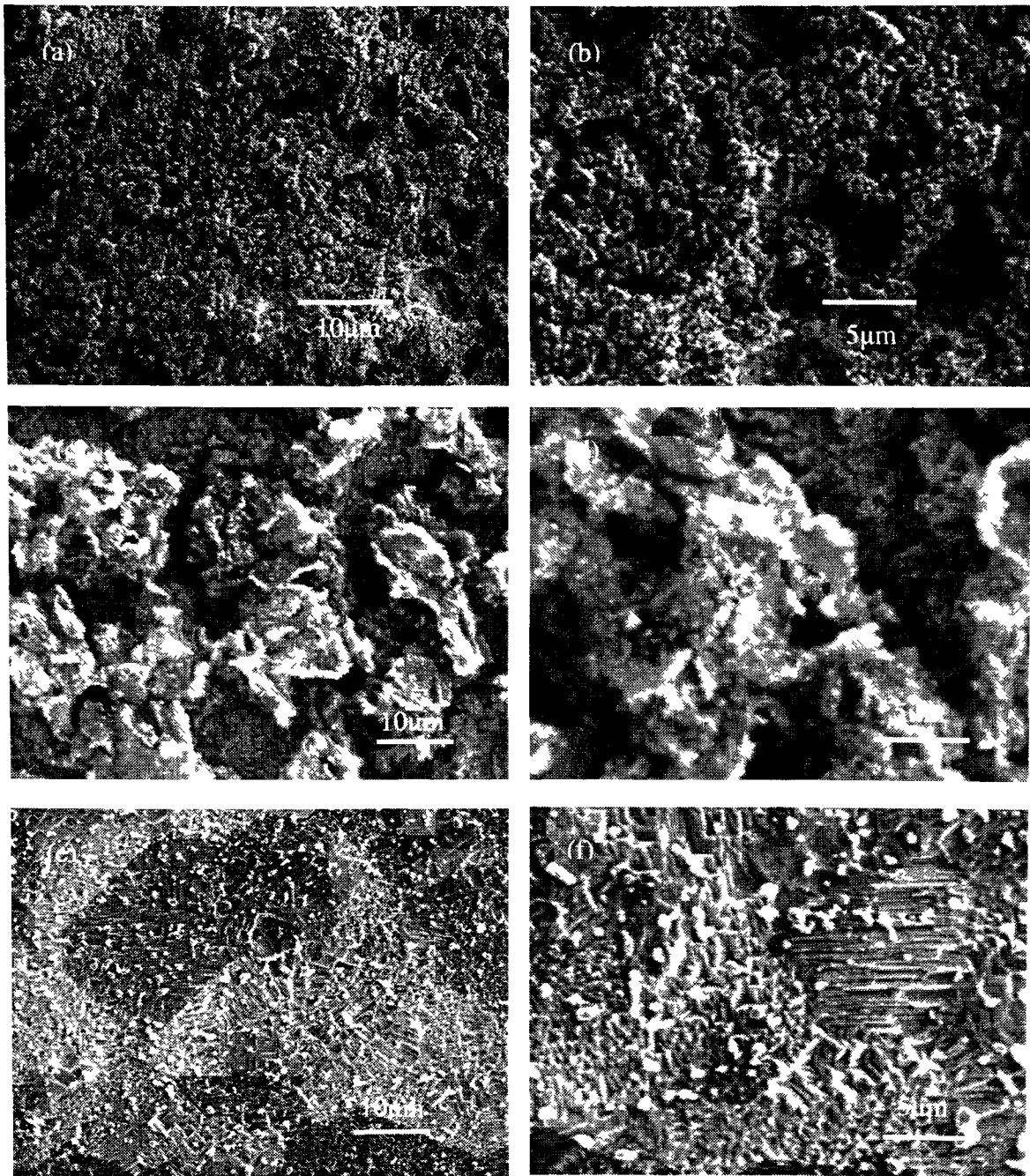
Fig 4.25 SEM micrographs of surface of SS410 after corrosion, (a), (b) after high temperature corrosion, (c), (d) purged with hydrogen, (e), (f) purged with oxygen

100
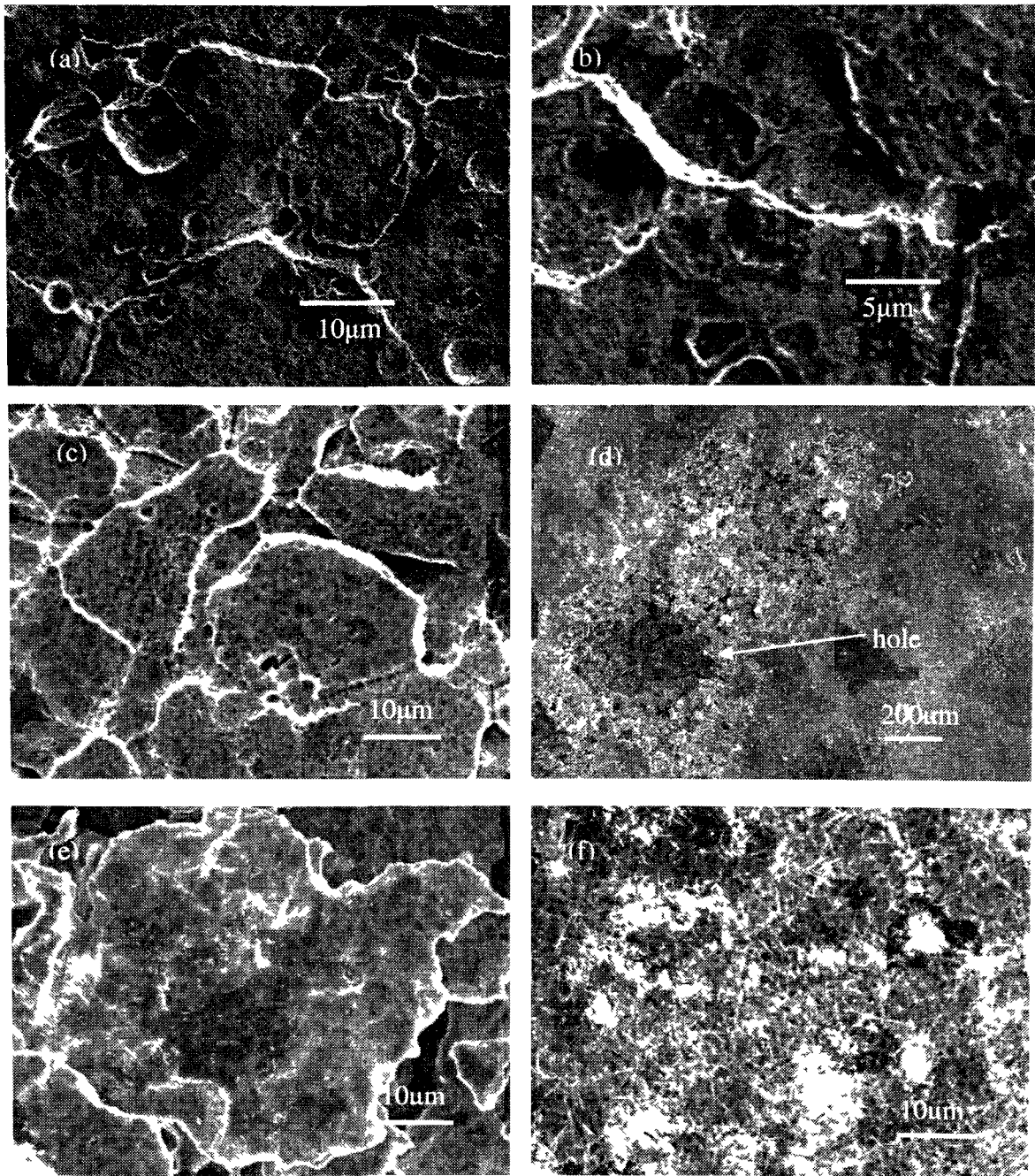
Fig 4.26 SEM micrographs of surface of Al6061 after corrosion, (a), (b) after high
temperature corrosion, (c) purged with hydrogen, (d) purged with oxygen, (e) hole area
purged with oxygen, (f) other area except hole area purged with oxygen

101
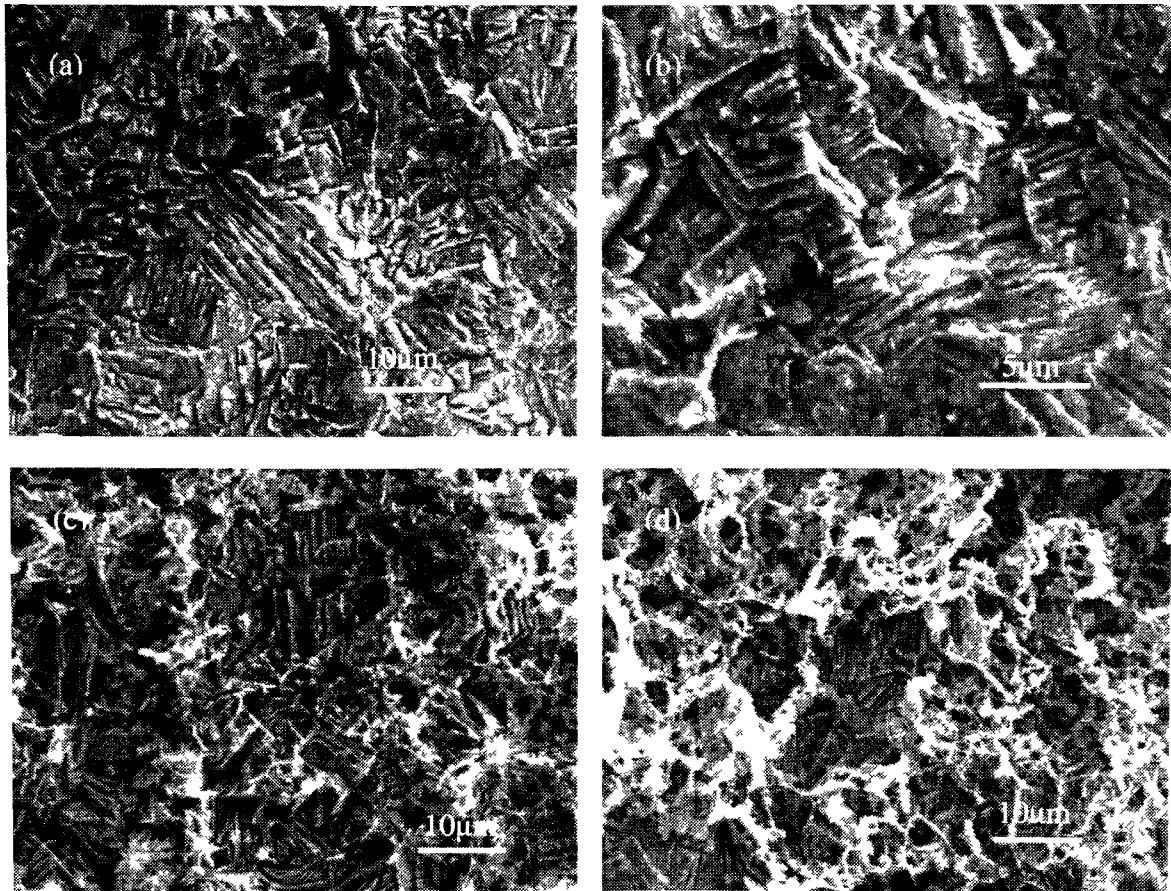
Fig 4.27 SEM micrographs of surface of A36 steel after corrosion, (a), (b) after high temperature corrosion, (c) purged with hydrogen, (d) purged with oxygen
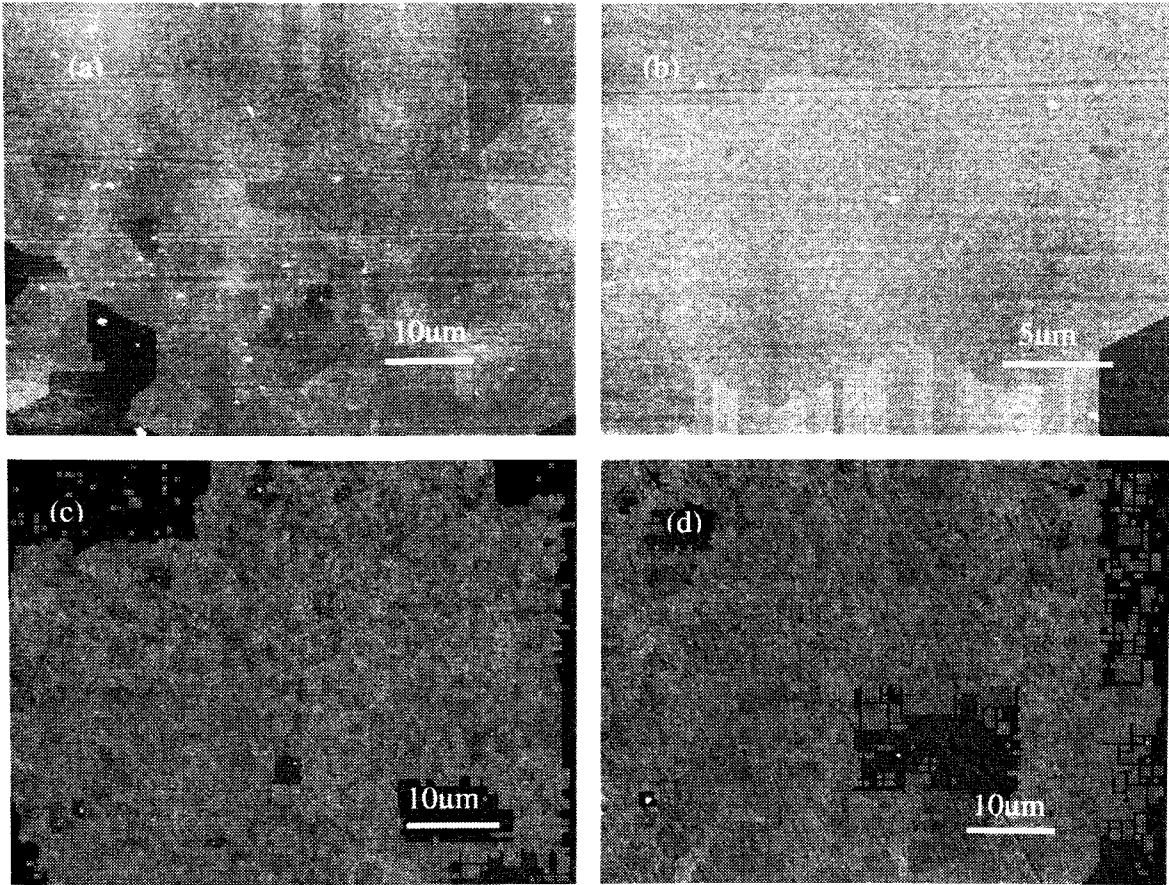
Fig 4.28 SEM micrographs of surface of Ti after corrosion, (a), (b) after high temperature corrosion, (c) purged with hydrogen, (d) purged with oxygen

4.5 EIS

Figs 4.29-4.34 presents the electrochemical impedance spectra for the six metals. For SS316L (Fig 4.29) and SS347 (Fig 4.30), the EIS spectra are part of a circle, which is because of the activation polarization. For Grade 2 Ti (Fig 4.34), we can see that the EIS spectra are divided into two parts including some part of a circle and a straight line. The circle is because of activation polarization and the straight line is because of concentration polarization. For SS410 (Fig 4.31), Al6061 (Fig 4.32) and A36 steel (Fig 4.33), the EIS spectra are divided into two semicircles, which mean that there are two reactions involved in the SS410, Al6061 and A36 steel corrosion. An interesting feature of the impedance for SS410 is that the first semicircle is a negative Faradic impedance in the real component, which suggests the presence of an inductive component because the inductance current is 180° off the capacitive current phase [10, 11]. From these electrochemical impedance spectra, we can deduce that SS316L, SS347, Ti and Al6061 have a higher impedance than A36 and SS410.
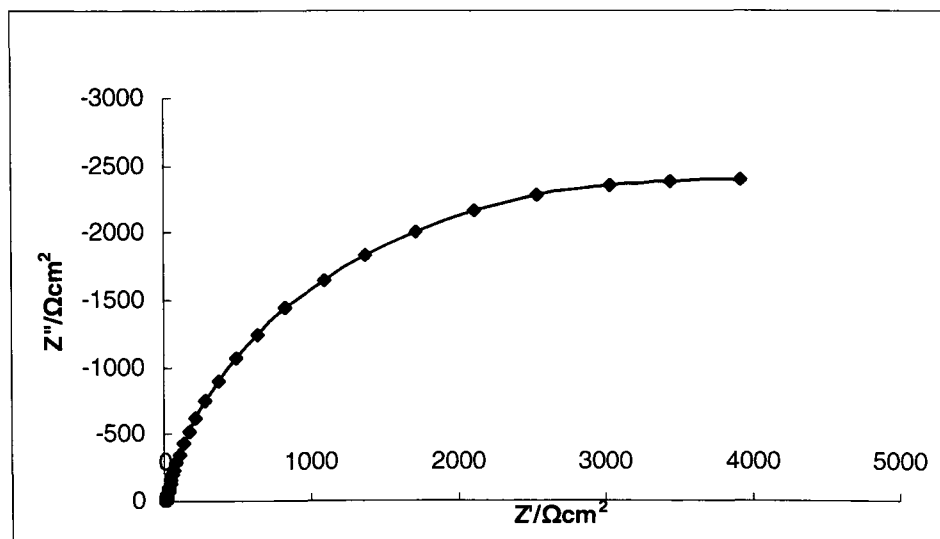
Fig 4.29 Impedance spectra for SS316L in a 0.5M H_2SO_4 solution at 20°C
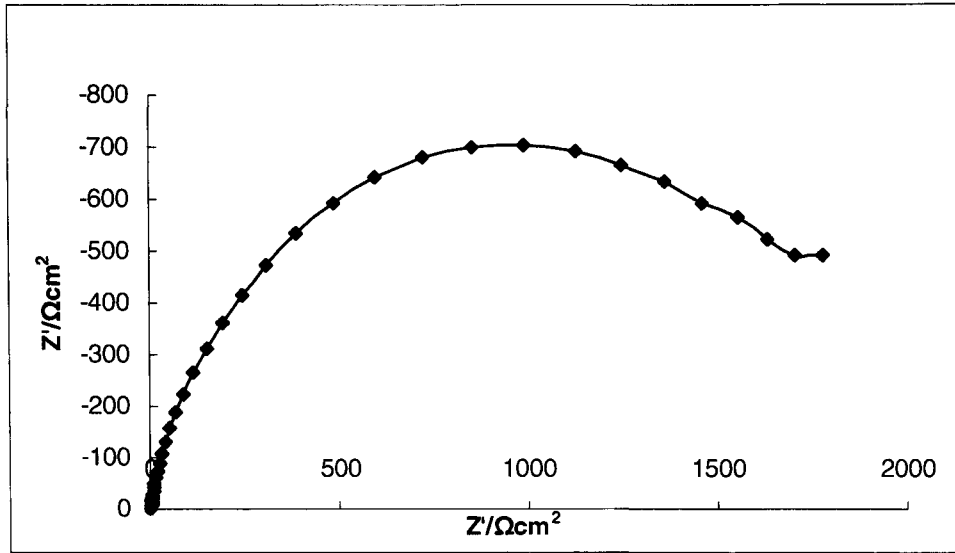
Fig 4.30 Impedance spectra for SS347 in a 0.5M H_2SO_4 solution at 20°C
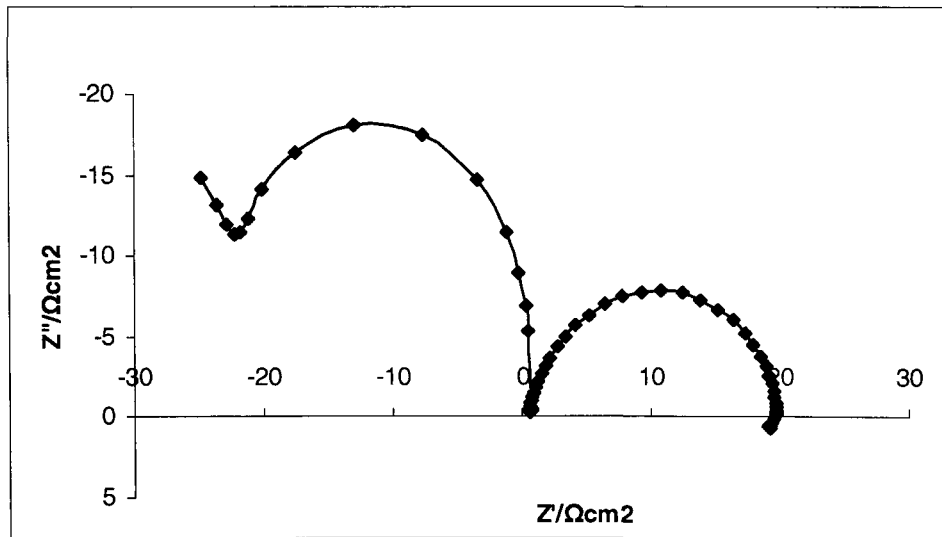
Fig 4.31 Impedance spectra for SS410 in a 0.5M H_2SO_4 solution at 20°C

105
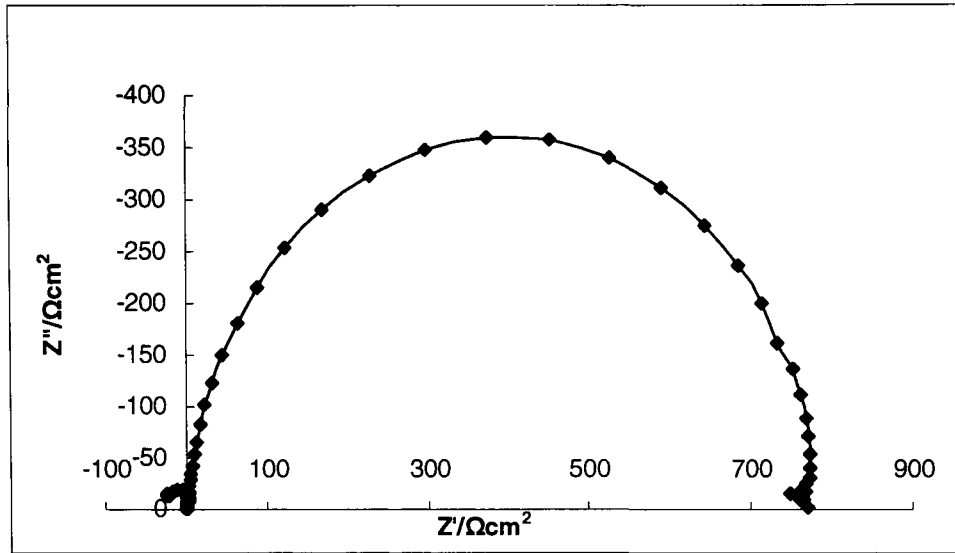
Fig 4.32 Impedance spectra for Al6061 in a 0.5M H_2SO_4 solution at 20°C
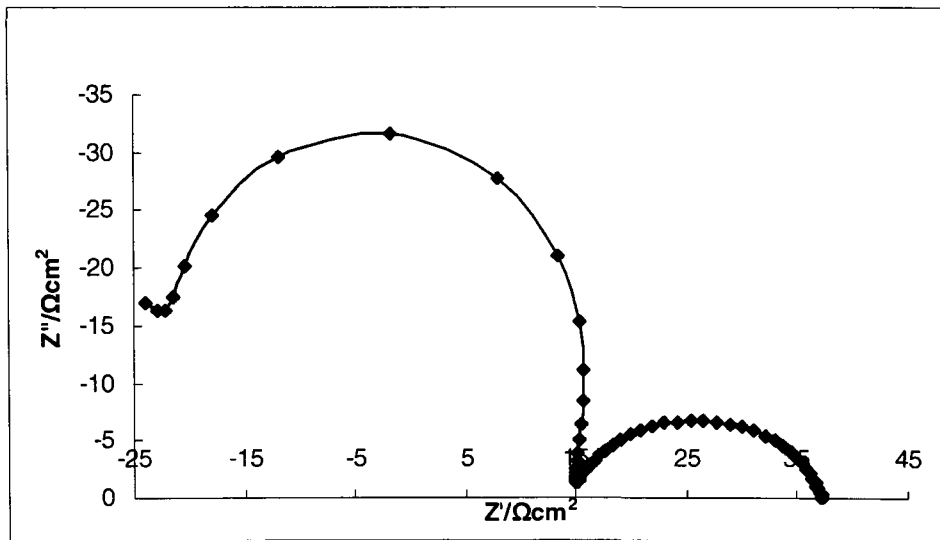
Fig 4.33 Impedance spectra for A36 steel in a 0.5M H_2SO_4 solution at 20°C
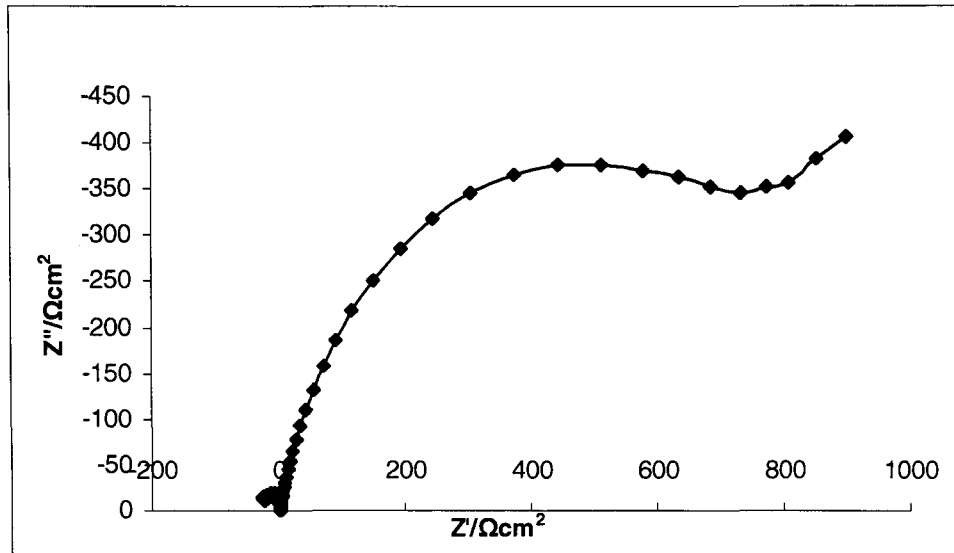
Fig 4.34 Impedance spectra for Grade 2 Ti in a 0.5M H₂SO₄ solution at 20°C

4.6 Potential-pH diagrams

As discussed in Section 4.2, the anode and cathode are at different potentials, which is different from open circuit corrosion. Potential-pH diagrams are an excellent tool to research metal corrosion at different pH values and potentials. Pourbaix diagrams show the reactions and reaction products that will be present when equilibrium has been attained, assuming that all appropriate reactions have been included. The collection of such diagrams by Pourbaix gives rather complete equilibria for most possible chemical reactions in pure water. Of special interest are conditions in which corrosion is thermodynamically impossible. Thus, potential and/or pH can in some cases be adjusted to prevent corrosion thermodynamically.

For the usual conditions in areas on the Pourbaix diagram where corrosion is possible, no predictions can be made as to corrosion rates, which may be fast or slow at the relatively low temperatures present in liquid aqueous solutions. Thermodynamics is generally more useful at high temperatures, where rates are higher and equilibrium is reached relatively rapidly. Although the Pourbaix diagram gives the stable phases for given conditions of potential and pH, other thermodynamically unstable phases formed in the past may still be present because they are slow to decompose. As a general statement,

107

thermodynamics, and the Pourbaix diagrams derived therefrom, give no information about the rates of the reactions they describe [10].

Because 5~10ppm metal ions can affect the ionic conductivity of the membrane, and thus the performance of the fuel cell stack [6, 7], we assume a metal ion concentration of 10ppm in the simulated PEMFC environments when drawing the potential-pH diagrams. Based on the Nernst equation (Section3.3.7) and assumption that the three alloys (Al6061, A36 steel, Grade 2 Ti) are essentially Al, Fe and Ti, potential-pH diagrams have been constructed and are shown in Figures 4.35-4.37 [12,13]. In the PEMFC working environment, pH is in the range 0~3.5 [14, 15]. At the anode, the potential of the bipolar plates is -0.1VvsSCE and at the cathode, the potential of the bipolar plates is 0.6VvsSCE. This information can be used to predict the behavior of Al6061, A36 steel and Grade 2 Ti as metallic bipolar plates in PEM fuel cells.

The reactions and Nernst equations for the Al potential-pH diagram [16] are:

$$Al \rightarrow Al^{3+} + 3e^-$$
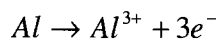
$$e_{Al/Al^{3+}} = -1.66 + \frac{0.059}{3}\log Al^{3+} \qquad \textbf{4.6}$$

$$Al + 3H_2O \rightarrow Al_2O_3 + 6H^+ + 6e^-$$
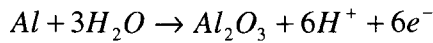
$$e_{Al/Al_2O_3} = -1.55 - 0.059 pH \qquad \textbf{4.7}$$

$$Al + 2H_2O \rightarrow AlO_2^- + 4H^+ + 3e^-$$
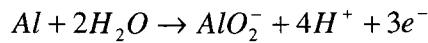
$$e_{Al/AlO_2^-} = -1.262 + 0.020\log AlO_2^- - 0.079 pH \qquad \textbf{4.8}$$

$$2Al^{3+} + 3H_2 \rightarrow Al_2O_3 + 6H^+$$
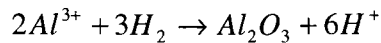
The equilibrium pH where lines (1) and (2) intersect may be calculated from the known value of the equilibrium constant of $K=(H^+)^6/(Al^{3+})^2=10^{-11.4}$ for line 4. For $(Al^{3+})=10^{-5}$,

Log K=6log (H^+)-2log(Al^{3+})=-6pH-2log(Al^{3+})

pH=-logK/6-log(Al^{3+})/3=11.4/6+5/3=3.57

pH=3.57 $\qquad$ **4.9**

$$Al_2O_3 + H_2O \rightarrow AlO_2^- + 2H^+$$
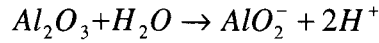
The equilibrium pH where lines (2) and (3) intersect may be calculated from the known value of the equilibrium constant of $K=(AlO_2^-)(H^+)^2=10^{-24.2}$ for line 5. For $(AlO_2^-)=10^{-5}$,

Log K=log (AlO_2^-)+2log(H^+)= log (AlO_2^-)-2pH

pH= log (AlO_2^-)/2-log(K)/2=-5/2+24.2/2=9.6

pH=9.6   **4.10**

The reactions and Nernst equations for the Fe potential-pH diagram [17] are:

$$Fe \rightarrow Fe^{2+} + 2e^-$$
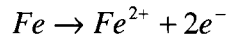
$$e_{Fe/Fe^{2+}} = -0.440 + 0.0295 \log Fe^{3+}$$ **4.11**

$$Fe + 2H_2O \rightarrow Fe(OH)_2 + 2H^+ + 2e^-$$
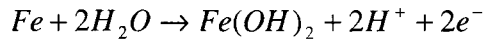
$$e_{Fe/Fe(OH)_2} = -0.0470 - 0.0591 pH$$ **4.12**

$$Fe + 2H_2O \rightarrow HFeO_2^- + 3H^+ + 3e^-$$
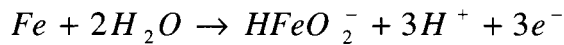
$$e_{Fe/HFeO_2^-} = 0.493 - 0.0886\ pH + 0.0295\ \log(HFeO_2^-)$$ **4.13**

$$Fe^{2+} + 2H_2O \rightarrow Fe(OH)_2 + 2H^+$$
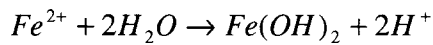
$$pH = 6.65 - 0.5 \log Fe^{2+}$$

Assuming $(Fe^{2+})=10^{-5}$

$$pH = 9.15$$ **4.14**

$$Fe(OH)_2 \rightarrow HFeO_2^- + H^+$$
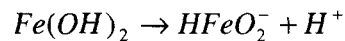
$$pH = 18.30 + \log(HFeO_2^-)$$

Assuming $(HFeO_2^-)=10^{-5}$

$$pH = 13.3$$ **4.15**

$$Fe^{2+} + 3H_2O \rightarrow Fe(OH)_3 + 3H^+ + 3e^-$$
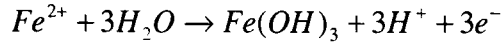
$$e_{Fe^{2+}/Fe(OH)_3} = 1.057 - 0.1773pH - 0.0591\log Fe^{2+} \qquad \textbf{4.16}$$

$$Fe^{3+} + 3H_2O \rightarrow Fe(OH)_3 + 3H^+$$
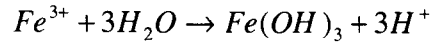
$$pH = 1.613 - \frac{1}{3}\log Fe^{3+}$$

Assuming $(Fe^{3+}) = 10^{-5}$

$$pH = 3.28 \qquad \textbf{4.17}$$
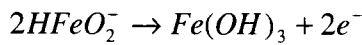
$$2HFeO_2^- \rightarrow Fe(OH)_3 + 2e^-$$

$$e_{HFeO_2^-/Fe(OH)_3} = -0.810 - 0.0591\log(HFeO_2^-) \qquad \textbf{4.18}$$

The reactions and Nernst equations for the Ti potential-pH diagram [18] are:

$$Ti^{3+} + 2H_2O \rightarrow TiO_2 + 4H^+ + e^-$$
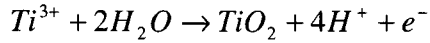
$$e_{Ti^{3+}/TiO_2} = -0.666 - 0.2364pH - 0.0591\log Ti^{3+} \qquad \textbf{4.19}$$

$$Ti^{2+} + 2H_2O \rightarrow TiO_2 + 4H^+ + 2e^-$$
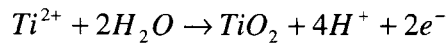
$$e_{Ti^{2+}/TiO_2} = -0.502 - 0.1182pH - 0.0295\log Ti^{3+} \qquad \textbf{4.20}$$

$$2Ti^{2+} + 3H_2O \rightarrow Ti_2O_3 + 6H^+ + 2e^-$$
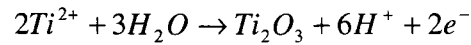
$$e_{Ti^{2+}/Ti_2O_3} = -0.478 - 0.1773pH - 0.0591\log Ti^{2+} \qquad \textbf{4.21}$$

$$Ti \rightarrow Ti^{2+} + 2e^-$$
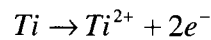
$$e_{Ti/Ti^{2+}} = -1.630 - 0.0295\log Ti^{2+} \qquad \textbf{4.22}$$

$$Ti + H_2O \rightarrow TiO + 2H^+ + 2e^-$$
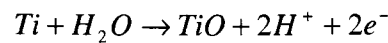
$$e_{Ti/TiO} = -1.306 - 0.0591pH \qquad \textbf{4.23}$$

110

$$2TiO + H_2O \rightarrow Ti_2O_3 + 2H^+ + 2e^-$$
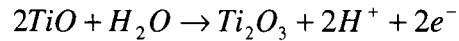
$$e_{TiO/Ti_2O_3} = -1.123 - 0.0591pH \qquad \textbf{4.24}$$

$$Ti_2O_3 + H_2O \rightarrow 2TiO_2 + 2H^+ + 2e^-$$
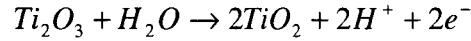
$$e_{Ti_2O_3/TiO} = -0.556 - 0.0591pH \qquad \textbf{4.25}$$

From Fig 4.35, we can see that Al^{3+} is the stable form for Al at -0.1V when the PH is 0~3.5. Thus, at the anode, Al will corrode and form Al^{3+} At the cathode, we can see that Al^{3+} is also the stable form for Al. Therefore, whether it is the anode or the cathode side as metallic bipolar plates, Al is always corroded and the corrosion product is Al^{3+} Therefore, Al is prone to corrode in the PEMFC working conditions and can not be used as bipolar plates without some form of protective coating.

From Fig 4.36, we can see that Fe^{2+} is the stable form at the anode when PH is 0~3.5. At the cathode Fe^{3+} is the stable form at PH 0~3.28 and $Fe(OH)_3$ can be formed between PH 3.28 and 3.5. Thus, Fe is corroded at both the anode and cathode. However, Fe^{2+} is the corrosion product at the anode and Fe^{3+} is the corrosion product at the cathode. When the PH value is higher than 3.28, $Fe(OH)_3$ will be formed.

For Ti in Fig 4.37, there is no accurate equation for line 8. The yellow peroxide, $TiO_3 \cdot 2H_2O$, whose conditions for thermodynamic stability have been represented diagrammatically in Fig 4.37 is an oxidizing substance, unstable in the presence of water and much more soluble than TiO_2 or $TiO_2 \cdot H_2O$; it dissolves in acid solutions with the formation of yellow to red pertitanyl ions TiO_2^{2+}, and in alkaline solution with the formation of titanate ions $HTiO_3$ and/or colourless pertitanate ions $HTiO_4-$ and TiO_4^{2-}

By the action of hydrogen peroxide on very acid solutions of tri- or tetravalent titanium, a solution of peroxidized TiO_2^{2+} ions is obtained, which deposits a precipitate of peroxide, $TiO_3 \cdot 2H_2O$, on increase in pH. The oxidizing power of $TiO_3 \cdot 2H_2O$ is similar to that of hydrogen peroxide. This peroxide can also be formed by the action of hydrogen peroxide on the oxide $TiO_2 \cdot H_2O$ [12].

We can see that TiO_2 is the stable form of Ti at the anode and TiO_2 is also the stable form of Ti at the cathode. Ti will be oxidized in the PEMFC conditions and there is no

corrosion of Ti bipolar plates. However, even if there is no corrosion on the Ti surface, TiO_2 can affect the performance of the bipolar plates because the oxide will increase the contact resistance between the Ti bipolar plates and gas diffusion layers.

In summary, Al will corrode at the anode and the cathode in a PEMFC working environment and the corrosion product is Al^{3+} ions. Fe corrodes at the anode and the cathode in a PEMFC working environment and the corrosion product is Fe^{2+} ions at the anode and Fe^{3+} ions at the cathode. Ti is oxidized at the anode and cathode rather than corroded and the product is TiO_2. However, in a 'real' PEMFC, the working potential can fluctuate over a potential range. For example, the short-term local voltage can exceed 1V under start conditions if oxygen gains access to the anode side of the fuel cell [19, 20]. If the working potential is below to -0.113V, Ti will corrode to form Ti^{3+} ions.
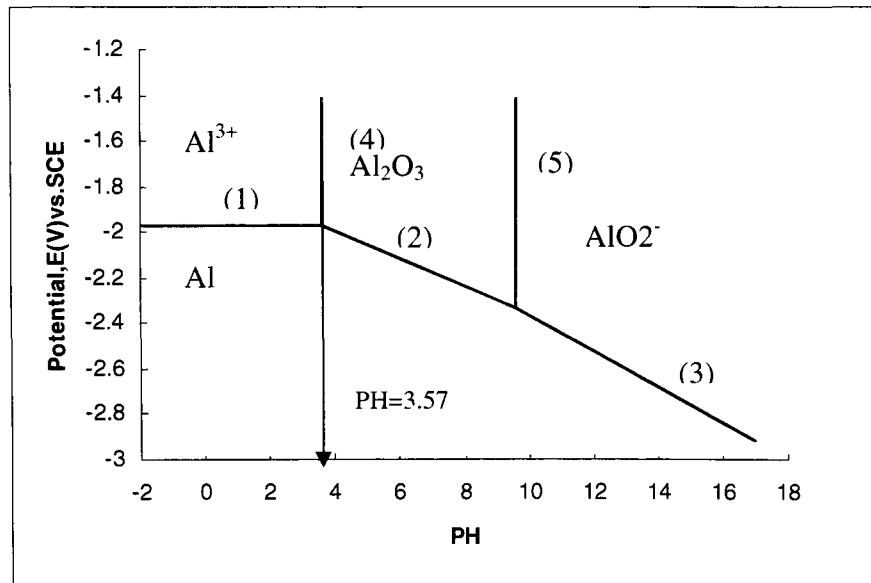
Fig 4.35: Potential-PH diagram for Al

112
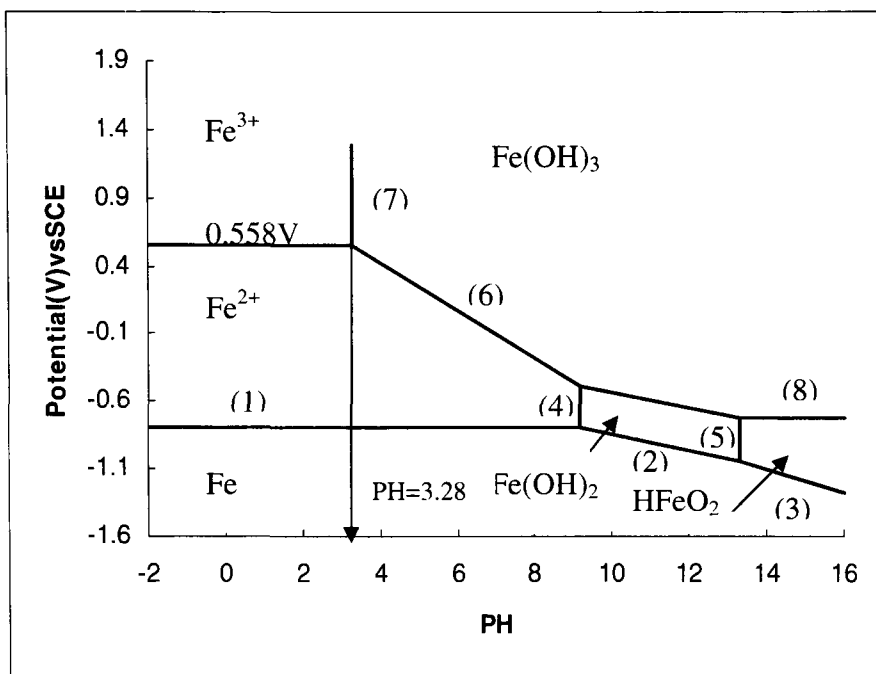
Fig 4.36: Potential-PH diagram for Fe
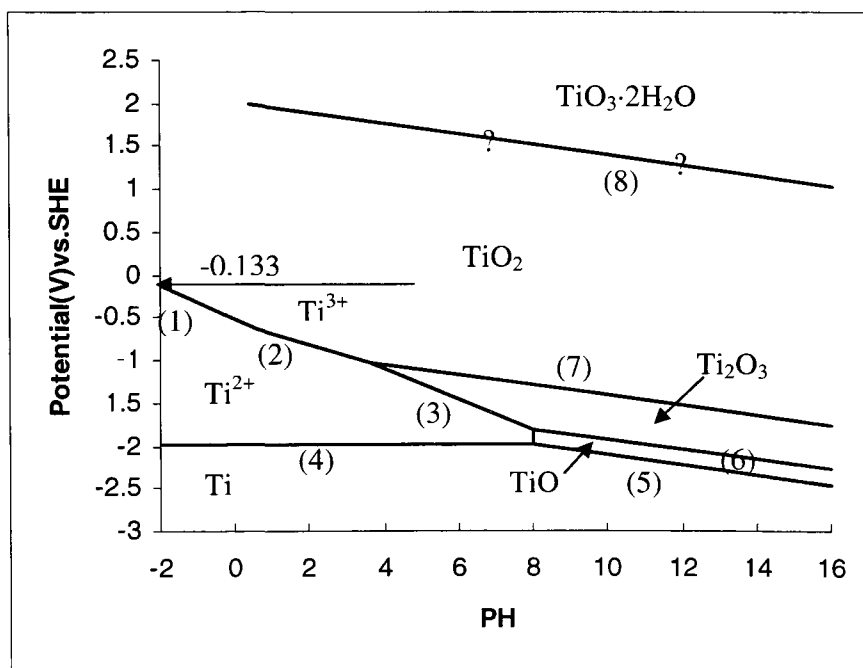
Fig 4.37: Potential-PH diagram for Ti

113

4.7 Interfacial contact resistance test

Fig 4.38 presents the interfacial contact resistance results for the six metals with an air-formed oxidization film. Before performing the interfacial contact resistance tests, we could see that the A36 steel was covered by a thick dark oxide layer and the other metals had a metallic lustre. From Fig 4.38, we can see that A36 steel has the highest contact resistance with carbon paper. Al6061 has the smallest contact resistance with carbon paper and therefore, the oxide film on Al is more conductive. At a low compaction force, SS316L, SS347, SS410 and Ti have different contact resistances with the carbon paper. However, at high compaction forces, they have the almost the same contact resistances with the carbon paper. Therefore, the metal contact resistance with carbon paper is in the order of A36steel>SS410>SS347>SS316L>Ti>Al6061.

Fig 4.39 presents the interfacial contact resistance results for the six metals after polishing with 240, 320, 400, 600, 800 grit silicon papers. SS410 has the highest contact resistance with carbon paper. SS316L, SS347 and A36 steel has almost the same contact resistance with carbon paper. Al6061 still has the lowest contact resistance with carbon paper. The metal (after polishing) contact resistance with carbon paper is in the order of SS410>SS316L, SS347, A36 steel>Ti>Al6061.

Comparing the data in Figs 4.38 and 4.39, we see that metal contact resistance with carbon paper increased after polishing except for A36 steel. There are two main factors which can affect the interfacial contact resistance with carbon paper. One is the conductivity of the material surface or the thickness of oxide film. If the surface has a higher conductivity or thinner oxide film, the contact resistance with carbon paper is lower. After polishing, the oxide film is removed and the surface is more conductive, so the contact resistance should be lower. The other factor is the surface area. As we know, the surface is smoother after polishing. So there is a higher contact area with the carbon paper in the contact resistance tests, which thus increases the contact resistance. For A36 steel, the conductivity of oxide film is very low or the oxide film is thick; therefore, the conductivity of the A36 steel surface is increased significantly and the interfacial contact resistance is decreased after polishing, even though the contact area is increased. However, for the other five metals, the conductivity of the oxide film is higher compared

114

to A36 steel and contact area is the main factor affecting the contact resistance. Therefore, the metal contact resistance is increased after polishing.

We also should note that there are no flow channels in our samples and there is more contact area in the interfacial contact resistance tests. However, in the real fuel cells, metallic bipolar plates require machined channels so that the gas can diffuse to the electrode. These channels can reduce the contact area between the bipolar plates and the gas diffusion layer. Therefore we can predict that our measured interfacial contact resistance is larger than that in the real bipolar plates made with the same materials.
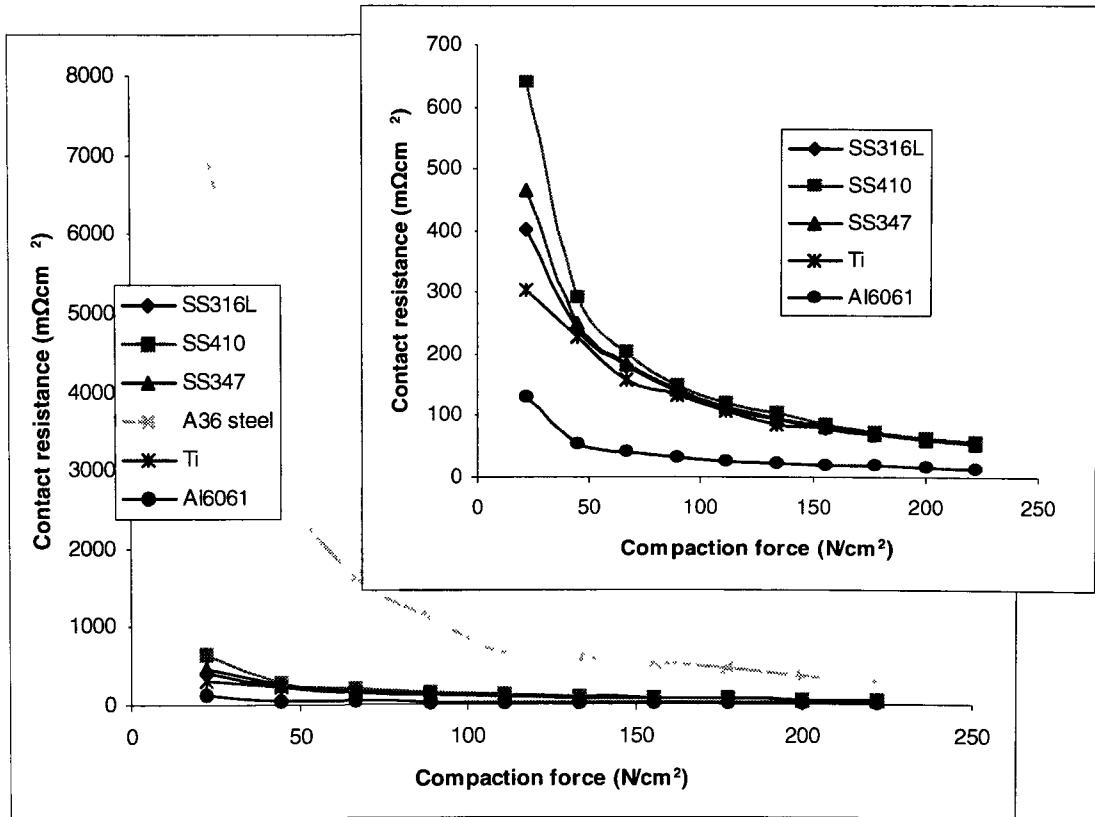
Fig 4.38 Interfacial contact resistances for different unpolished metals and carbon paper at different compaction forces, (a) including A36 steel results, (b) expanded view without A36 steel results

2500

2000

Contact resistance (mΩcm^2)

1500

—◆—SS316L
—■—SS410
—▲—SS347
A36 steel
—✱—Ti
—●—Al6061

1000

500

0

0   50   100   150   200   250
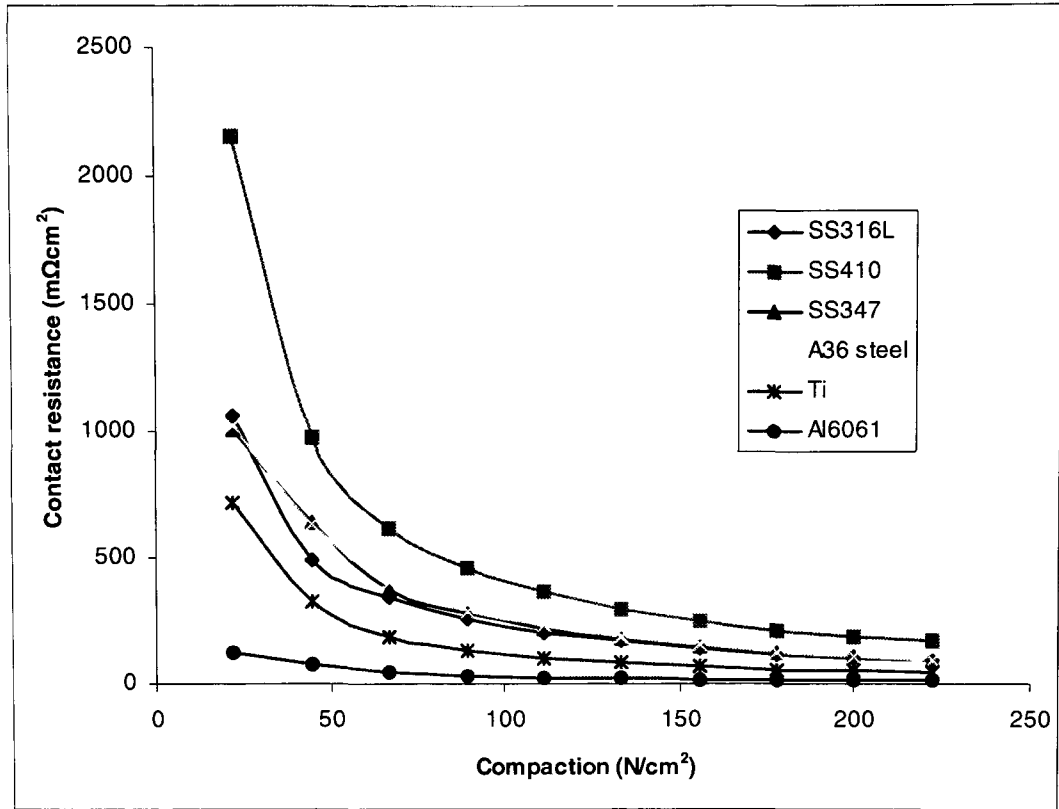
Compaction (N/cm^2)

Fig 4.39 Interfacial contact resistances for different polished metals and carbon paper at different compaction forces

4.8 Summary

From a corrosion criteria standpoint, SS316L, SS347 and Ti are more promising bipolar plate candidate materials than SS410, Al6061 and A36 steel. From an interfacial contact resistance standpoint, Al6061 is the best material. The interfacial contact resistances of SS316L, SS347. SS410 and Ti are still in an acceptable range. A36 steel has the highest contact resistance. Therefore, based on the corrosion and interfacial contact resistance results, SS316L, SS347 and Ti are the most promising bipolar plate materials. Ti is more expensive compared to stainless steel. Comparing the two stainless steels, SS347 has a similar structure and composition to SS316L, but is more expensive. Therefore, in our subsequent work, SS316L was chosen as the candidate bipolar plate material and various methods were examined to increase the corrosion resistance of SS316L in order to meet the requirements for a bipolar plate material.

116

References

1. A.Hermann, T.Chaudhuri, P.Spagnol, Bipolar plates for PEM fuel cells: A review. Int.J.Hydrogen Energy, 30(2005)1297-1302.

2. W.F.Smith, Foundations of Materials Science and Engineering, New York, Third Edition, McGraw-Hill, 2004, PP497

3. H.Wang, M.A.Sweikart, J.A.Turner, Stainless steel as bipolar plate material for polymer electrolyte membrane fuel cells. J.Power Sources 115(2003)243-251.

4. W.F.Smith, Foundations of Materials Science and Engineering, New York, Third Edition, McGraw-Hill, 2004, PP702.

5. R.L.Borup, N.E.Vanderborgh, Design and testing criteria for bipolar plate materials for PEM fuel cell applications. Mat.Res.Soc.Symp.Proc., 393(1995)151-155.

6. L.Ma, S.Warthesen, D.A.Shores, Evaluation of materials for bipolar plates in PEMFCs. J New Mater Electrochem Syst., 3(2000)221-228.

7. M.P.Brady, K.Weisbrod, I.Paulauskas, R.A.Buchanan, K.L.More, H.Wang, M.Wilson, F.Garzon, L.R.Walker, Preferential thermal nitridation to form pin-hole free Cr-nitrides to protect proton exchange membrane fuel cell metallic bipolar plates. Scripta Mater., 50(2004)1017-1022.

8. R.G.Rajendran, Polymer electrolyte membrane technology for fuel cells. MRS Bulletin, 30(2005)587-590.

9. J.R.Bontha, P.N.Pintauro, Water orientation and ion solvation effects during multicomponent salt partitioning in a Nafion cation exchange membrane, Chem. Eng. Sci., 49(1994)3835-3843.

10. W.Chen, J. Kim, S.Sun, and S.Chen, Electro-oxidation of formic acid catalyzed by FePt nanoparticles. Physical Chemistry Chemical Physics, 23(2006)2779-2786.

11. G.Markovich, C.P.Collier, and J.R.Heath, Reversible Metal-Insulator Transition in Ordered Metal Nanocrystal Monolayers Observed by Impedance Spectroscopy Physical Review Letters, 80(1998)3807-3810.

12. M.Pourbaix, Atlas of Electrochemical Equilibria in Aqueous Solutions, Second Edition, National Association of Corrosion Engineers, 1974, PP221.

13. D.A.Jones, Principles and Prevention of Corrosion, Macmilian, New York, 1992, PP147.

14. S.Lee, C.Huang, J.Lai, Y.Chen, Corrosion-resistant component for PEM fuel cells. J.Power Sources, 131(2004)162-168.

15. ASTM G5-94, Standard Reference Test Method for Marking Potentiostatic and Potentiodynamic Anodic Polarization Measurements, American Society for Testing and Materials, Philadelphia, 1995.

16. D.A.Jones, Principles and Prevention of Corrosion, Macmillan, New York, 1992, PP53-56.

17. D.A.Jones, Principles and Prevention of Corrosion, Macmillan, New York, 1992, PP57-58.

18. D.A.Jones, Principles and Prevention of Corrosion, Macmillan, New York, 1992, PP63.

19. C.A.Reiser, L.Bregoli, T W.Patterson, J.S.Yi, J.D.Yang, M.L.Perry, T.D.Jarvi, A Reverse-Current Decay Mechanism for Fuel Cells. Electrochemical and Solid State Letters, 8(6)(2005)A273-A276.

20. M.P.Brady, B.Yang, H.Wang, J.A.Turner, K.L.More, M.Wilson, and F.Garzon, The Formation of Protective Nitride Surfaces for PEM Fuel Cell Metallic Bipolar Plates. J.the Minerals, Metals & Materials Society, 58(8)(2006)50-57

CHAPTER 5

EFFECT OF O_2 AND H_2 ON THE CORROSION OF SS316L METALLIC BIPOLAR PLATE MATERIALS IN SIMULATED ANODE AND CATHODE ENVIRONMENTS OF PEM FUEL CELLS

Increasing attention is being paid to the use of metallic materials as a replacement for non-porous graphite bipolar plates (BPs) for polymer exchange membrane (PEM) fuel cells. Although there has been a fair body of research work on uncoated and coated SS316 as a potential metallic bipolar plate material, there had been little work done on the effects of O_2 and H_2 on the corrosion of SS316 in simulated anode and cathode environments of PEM fuel cells. Also as noted, there have been differing opinions as to whether SS316 can be used as a bipolar plate material in the uncoated condition. This part of research was designed to investigate the electrochemical corrosion characteristics of SS316, and to examine how O_2 and H_2 can affect the corrosion characteristics of SS316 in simulated PEMFC environments.

5.1 Open circuit potential (OCP) of SS316L

Fig 5.1 presents the open circuit potential vs time data for SS316L in the anode and cathode environments at 70°C. We can see that the OCP of SS316L in the O_2-containing environment is higher than that in the H_2-containing environment. A detailed explanation of this behavior can be obtained using mixed potential theory.

In the solution bubbled with H_2, reactions 5.1 and 5.2 are occurring. Each reaction has its own half-cell electrode potential and exchange current density. However, the two electrode potentials $e_{Fe/Fe^{2+}}$ and e_{H^+/H_2} can not coexist separately on an electrically conductive surface. Each must polarize, or change potential, to a common intermediate value, Ecorr, which is called the corrosion potential [1].

$$2H^+ + 2e^- \rightarrow H_2 \qquad\qquad\qquad\text{5.1}$$

$$Fe - 2e^- \rightarrow Fe^{2+} \qquad\qquad\qquad\text{5.2}$$

However, in the solution bubbled with O_2, reactions 5.3 and 5.4 are occurring and the mixed potential theory can also be applied.

$$O_2 + 4H^+ + 4e^- \rightarrow 2H_2O \qquad\qquad\qquad\text{5.3}$$

$$Fe - 2e^- \rightarrow Fe^{2+} \qquad\qquad\qquad\text{5.4}$$

The test system is open and the concentration of H^+ is 1mol/L. Assuming the pressure of H_2 and O_2 in the solution is 1atm, respectively, we can get e_{H^+/H_2} and e_{O_2/H_2O} using the NERNST equation.

$$e = e^o - \frac{RT}{nF} \ln \frac{a(reduction)}{a(oxidation)} \qquad\qquad\qquad\text{5.5}$$

The potentials of e_{H^+/H_2} and e_{O_2/H_2O} are the same as the standard potentials, which are 0VvsSHE and 1.229VvsSHE. When we use the mixed potential theory to obtain the corrosion potential of SS316L in the solutions bubbled with H_2 and O_2, the corrosion potential in the solution with O_2 is higher because the half-cell potential of e_{O_2/H_2O} is higher. As is well known, a higher potential means that corrosion is retarded. Therefore, we can say that at the open circuit potential, corrosion more readily occurred in the H_2-containing environment than that in the O_2-containing environment.
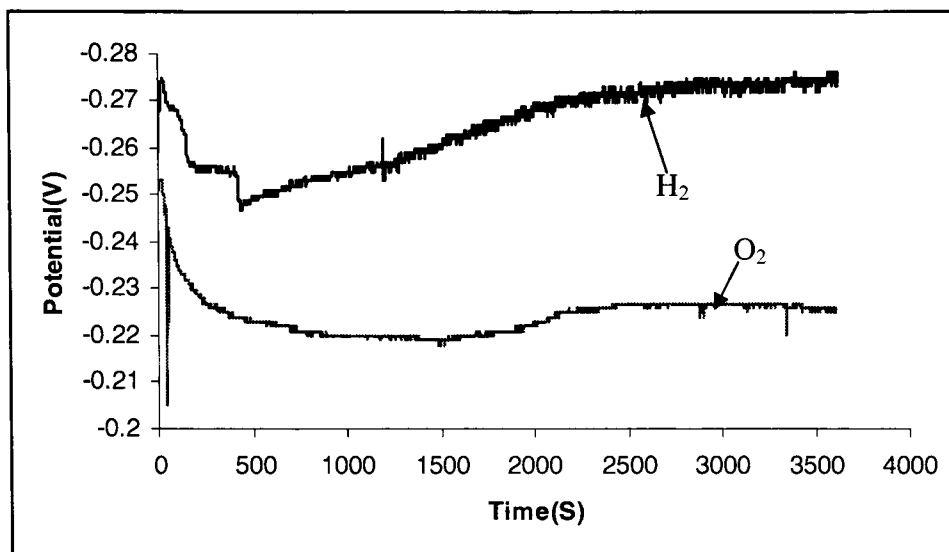
Fig 5.1. Open circuit potential of SS316L in 0.5M H_2SO_4 at 70°C bubbled with O_2 or H_2

5.2 Potentiodynamic tests with O_2 and H_2

In a PEM fuel cell, the anode is bubbled with H_2 and the cathode is bubbled with O_2 or air. In order to investigate the corrosion characteristics of SS316L in the anode and cathode conditions, the potentiodynamic tests were done in H_2-containing and O_2-containing environments, respectively. Fig 5.2 presents the potentiodynamic curves of SS316L in the H_2 and O_2 environments. Both of the curves can be divided into three areas, namely, active, passive and transpassive. Comparing the two curves, we find that the corrosion potential of SS316L in 0.5M H_2SO_4 bubbled with O_2 is higher than that in H_2SO_4 bubbled with H_2, which is the same behavior as in the OCP tests. The increased corrosion potential retards corrosion of SS316L in the O_2-containing environment. Also, the corrosion current density for SS316L in 0.5M H_2SO_4 bubbled with O_2 is slightly lower than that in 0.5M H_2SO_4 bubbled with H_2. However, in the transpassive area, the two curves are almost identical. Using the linear polarization method, we can obtain the corrosion parameters for SS316L in both environments: these are given in Table5.1. The polarization resistance was calculated using the linear polarization method (described in Section 3.3.2).

We can see that the polarization resistance and corrosion current density in the H_2-containing environment are 975 Ω•cm^2 and 9.145 $\mu A/cm^2$, respectively. However, in the

121

O_2-containing environment the polarization resistance and corrosion current density are 5361 $\Omega \cdot cm^2$ and 2.426 $\mu A/cm^2$, respectively. The polarization resistance of SS316L in 0.5M H_2SO_4 bubbled with O_2 is about 6 times than that in 0.5M H_2SO_4 bubbled with H_2, and the corrosion current density in the O_2-containing environment is only about ¼ of that in the H_2-containing environment. SS316L has a higher corrosion resistance and a lower corrosion current density in the O_2-containing environment because it is more readily passivated than in an H_2-containing environment, and the passive layer is both more stable and thicker.
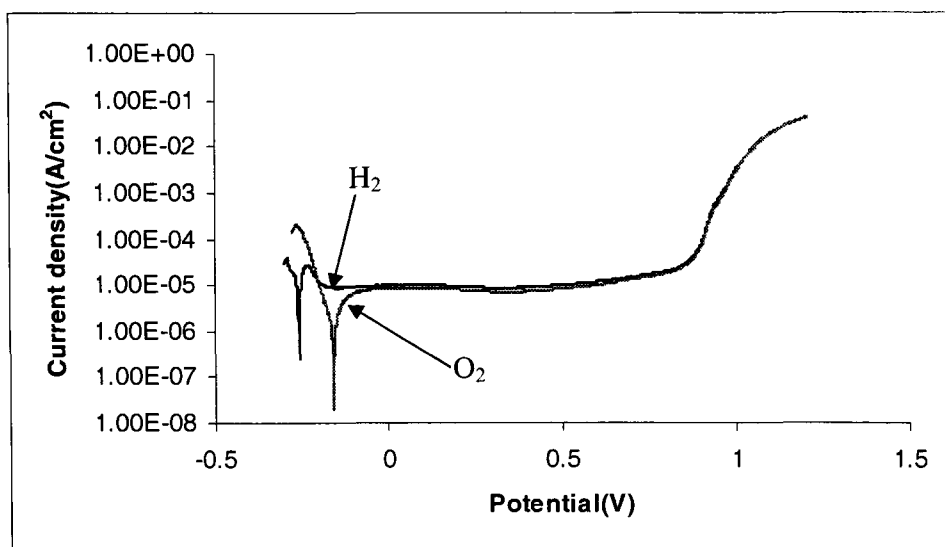
Fig5 .2. Potentiodynamic curves for SS316L at 70°C in 0.5M H_2SO_4 bubbled with H_2 or O_2

Table 5.1. Polarization parameters of SS316L at 70°C in 0.5M H_2SO_4 bubbled with either H_2 or O_2

Environment	β_a/V	β_c/V	E_{corr}/V	i_{corr}/($\mu A/cm^2$)	R_p/($\Omega \cdot cm^2$)
H_2	0.029	0.070	-0.255	9.145	975
O_2	0.177	0.036	-0.198	2.426	5361

122

5.3 Potentiostatic tests in simulated anode and cathode environments

In the real PEMFC working conditions, the anode and cathode are about at -0.1VvsSCE(0.131VvsSHE) bubbled with H_2 and 0.6VvsSCE(0.831VvsSHE) bubbled with O_2, respectively [2, 3, 4]. Therefore, the anode and cathode are undergoing corrosion at an applied potential which is different from the free potential corrosion. Potentiostatic tests were therefore performed under the specific conditions of the anode and cathode.

Fig 5.3 presents the potentiostatic curves of SS316L in these simulated anode and cathode conditions. Although the total test time was 10 hours for the potentiostatic tests, the software used could only store 16800 points (about 4.67hours) at 1point/second speed. Therefore, Fig 5.3 shows only a part of the total curve. In the simulated anode conditions, the stable current density is negative because H^+ changes to H_2 through the following reactions [5, 6].

Ionic reduction: $H^+ + e^- \rightarrow H_{ads}$ **5.6**

Combination (desorption) process: $H_{ads} + H_{ads} \rightarrow H_2$ **5.7**

And/or: $H_{ads} + H^+ + e \rightarrow H_2$ **5.8**
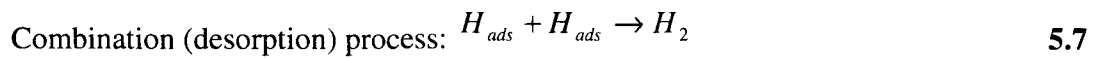
H_{ads} is the adsorbed hydrogen atom on the electrode surface and represents an intermediate state prior to desorption or diffusion into the metal. The current densities in the simulated anode and cathode conditions stabilized at about $-7 \times 10^{-7} A/cm^2$ and 5×10^{-6} A/cm^2, respectively. The negative current can provide cathodic protection for SS316L, and the positive current arises because of corrosion of the metal.
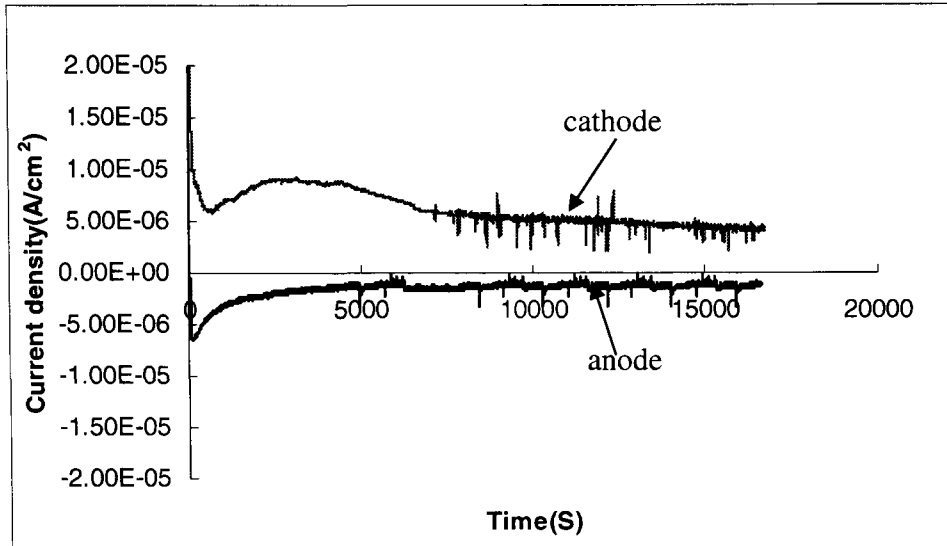
Fig 5.3. Potentiostatic curves for SS316L at -0.1VvsSCE bubbled with H_2 and 0.6VvsSCE bubbled with O_2 at 70°C

5.4 Optical microscopy of specimens after potentiodynamic or potentiostatic testing

Optical micrographs of SS316L after potentiodynamic and potentiostatic testing are shown in Fig 5.4. Intergranular corrosion occured after potentiodynamic testing for both the H_2-containing and O_2-containing environments; Figs 5.4(a) and 5.4(b). In austenitic stainless steels, chromium carbides ($Cr_{23}C_6$) can precipitate at the grain boundaries, and deplete the regions adjacent to the boundaries of chromium so that the chromium level in these areas is decreased below the 12 percent chromium level necessary for passive behaviour. These areas become anodic to the rest of the grain interiors, which are cathodic, thereby creating galvanic couples [7]. It should be noted, however, that SS316L with its much lower carbon content than SS316, should be less susceptible to the carbide precipitation, and hence, chromium depletion. In the simulated anode conditions for the potentiostatic tests, very little corrosion is evident: Fig 5.4(c). However, in the simulated cathode conditions for the potentiostatic tests, SS316L became covered with a layer of corrosion products which were brown in colour: Fig 5.4(d).

124
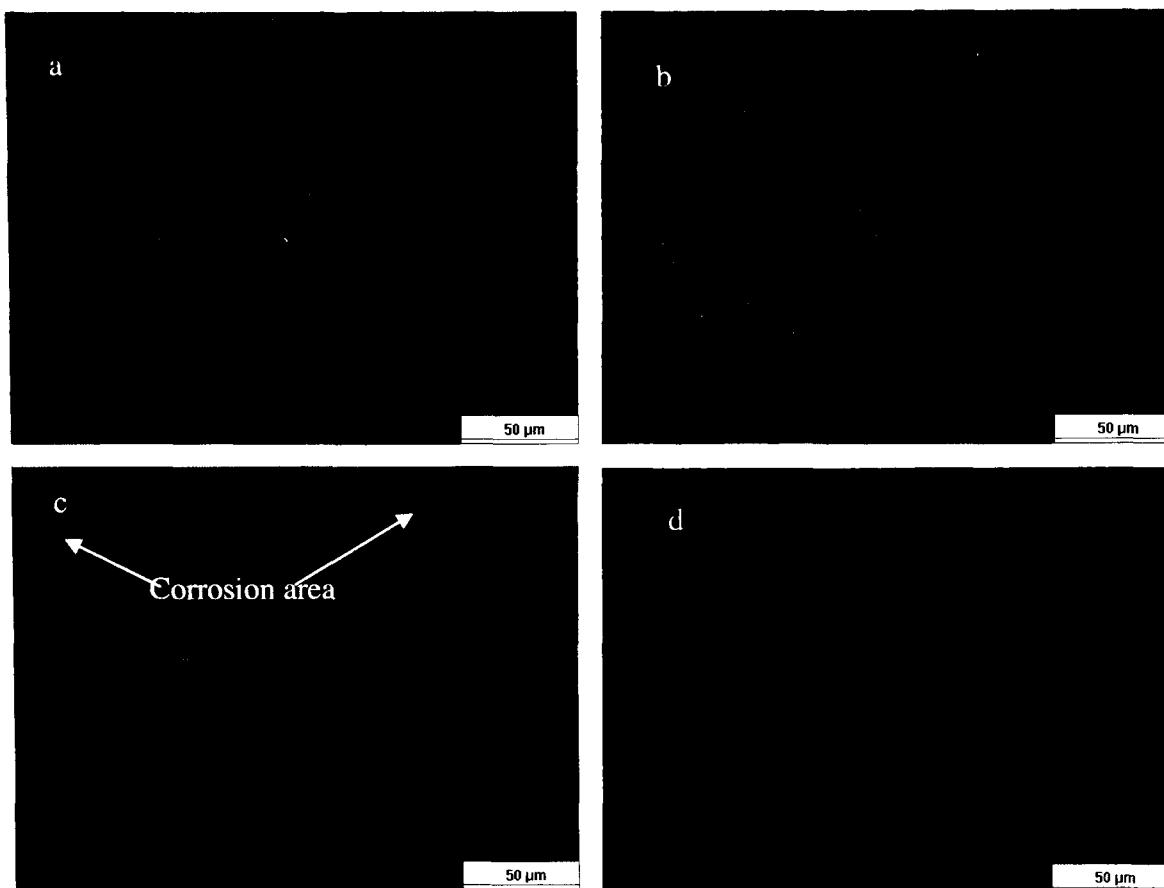
Fig 5.4. Optical micrographs of SS316L after corrosion: (a) potentiodynamic test with H₂, (b) potentiodynamic test with O₂, (c) potentiostatic test at -0.1VvsSCE with H₂, (d) potentiostatic test at 0.6VvsSCE with O₂

5.5 SEM metallography of specimens after potentiodynamic and potentiostatic testing

SEM micrographs of SS316L which had undergone potentiodynamic testing, Figs 5.5(a) and (b), showed both intergranular corrosion and pitting corrosion. The pitting corrosion is because of local breakdown of the passive film at isolated sites [8]. The pitting corrosion begins at the pitting corrosion potential in the potentiodynamic curve. There were no significant differences between the samples that had undergone potentiodynamic testing in O_2-containing or H_2-containing environments. In the potentiostatic tests in the simulated anode conditions, little corrosion is evident, Fig 5.5(c). However, in the simulated cathode conditions, a porous corrosion product could be readily seen, Fig 5.5(d).
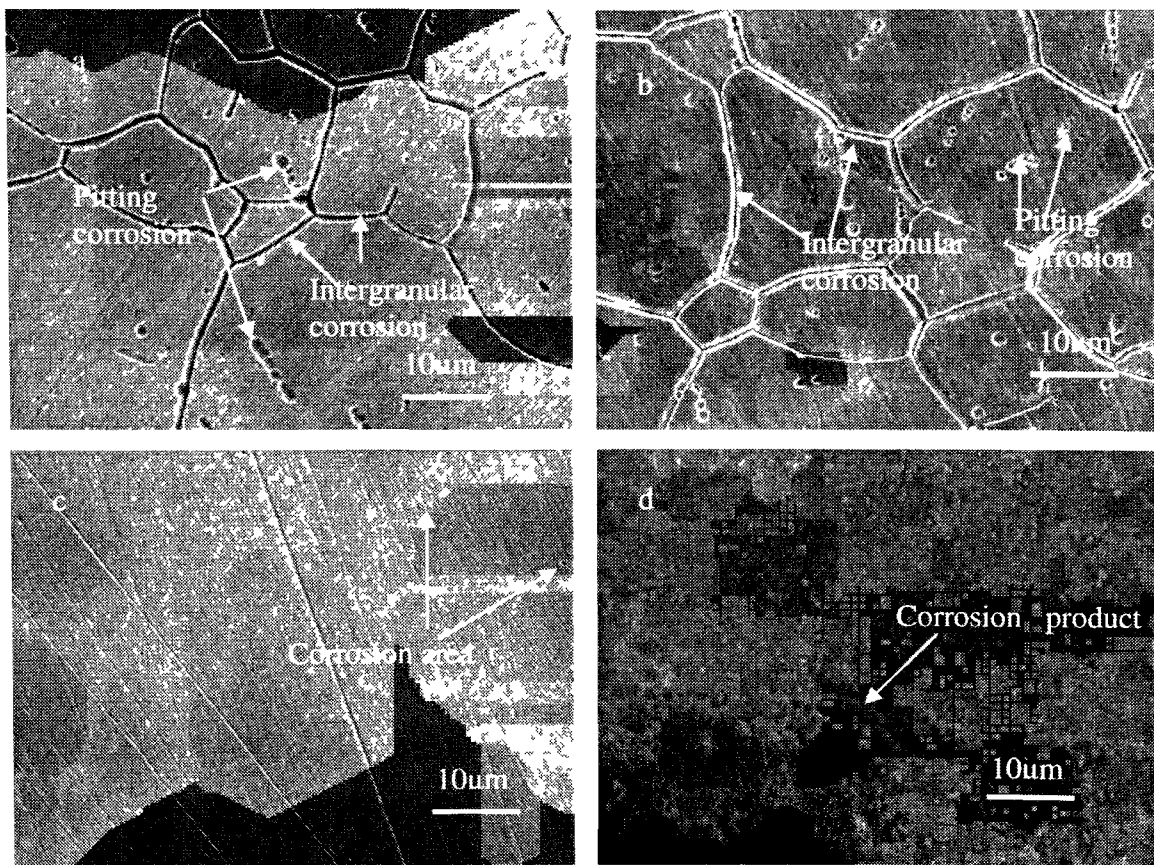
Fig 5.5. SEM of SS316L after corrosion: (a) potentiodynamic test with H_2, (b) potentiodynamic test with O_2, (c) potentiostatic test at -0.1VvsSCE with H_2, (d) potentiostatic test at 0.6VvsSCE with O_2

126

5.6 ICP-OES determination of metal ion concentrations after corrosion

In a 'real' PEM fuel cell environment, metal ions generated from the corrosion reaction(s) can migrate to the membrane and, it has been suggested that, levels as low as 5-10ppm can degrade the membrane performance [9, 10]. Therefore, metal ion concentration, generated by corrosion, in solution is a very important parameter for gauging the performance of metallic bipolar plate materials. Table 5.2 summarises the metal ion concentrations measured in the electrolyte after potentiostatic testing in simulated anode and cathode conditions. From Table 5.2, we can see that metal ion concentration in solution at the cathode is much higher (by a factor of 1.7) than that in solution at the anode for all metal ions measured. Therefore, based on these ICP-OES results, metal corrosion is more severe at the cathode environment, which is consistent with the potentiostatic test results. On the other hand, the measured metal ion concentrations do not seem consistent with the potentiostatic tests since the negative current at the anode should provide cathodic protection for SS316L. However, the cathodic protection at the anode is partial and corrosion of the SS316L still takes place. Therefore, SS316L corrodes in both the anode and cathode environments, but corrosion levels are much higher at the cathode.

It is generally considered that PEM fuel cells should have operating lifetimes over 5000h for transportation applications [11]. If, indeed, metal ion concentration levels of 10ppm can adversely affect membrane performance, then metal ion concentration build-up must not exceed 1ppm/500hr. However, in our test results, after a 10 hour experiment the total metal ion concentrations have reached levels of 1 to 1.7ppm. If the corrosion rate remains the same for the 5000h lifetime of the fuel cell, Fe, Cr, Ni, Mn ion concentrations will be at 375, 64.5, 40.4, 9.1ppm at the anode, and 613, 115, 90.1, 18.2ppm at the cathode after 5000h. Let us suppose that 5% percent of the metal ions remain in solution. Then, the total metal ion concentrations will be 24.5 and 41.8ppm at the anode and cathode, respectively. Such levels of metal ion concentration are still too high for satisfactory PEM fuel cell performance.

127

Table 5.2. Metal ion concentration after potentiostatic tests at -0.1VvsSCE bubbled with

H$_2$ and 0.6VvsSCE bubbled with O$_2$ at 70°C

Environment	Dissolved metal ion concentration(µg/L)				Total concentration of metal ions (µg/L)
	Fe	Cr	Ni	Mn	
Base solution	20.71	<IDL	<IDL	1.36	22.07
Anode side	770.90	129.00	80.88	19.58	1000.34
Cathode side	1245.79	230.34	180.27	36.38	1692.78

*Note: IDL is the identification limit.

5.7 Summary

The effects of O$_2$ and H$_2$ for SS316L in the simulated anode and cathode environments of PEMFCs have been investigated in this chapter. The results show that the OCP of SS316L is higher in an O$_2$-containing environment than in a H$_2$-containing environment because e_{O_2/H_2O} is higher than e_{H^+/H_2}. Metal ion concentrations are about 25 and 42ppm at the anode and cathode, respectively, after 5000 hour potentiostatic tests. These metal ion concentrations will affect the performance of the PEMFCs. Therefore, SS316L must be coated in order to reduce corrosion to levels acceptable for use of SS316L as a bipolar plate material in PEM fuel cells.

References

1. D.A.Jones, Principles and Prevention of Corrosion, First ed., New York, Macmillan, 1992, PP86.

2. H.Wang, J.A.Turner, Ferritic stainless steels as bipolar plate material for polymer electrolyte membrane fuel cells. J.Power Sources, 128(2004)193-200.

3. H.Wang, M.A.Sweikart, J.A.Turner, Stainless steel as bipolar plate material for polymer electrolyte membrane fuel cells. J.Power Souces, 115(2003)243-251.

4. H.Wang, J.A.Turner, Investigation of a Duplex Stainless Steel as Polymer Electrolyte Membrane Fuel Cell Bipolar Plate Material. J.Electrochem Soc., 152(3)(2005) B99-B104.

5. M.Li, C.Zeng, S.Luo, J.Shen, H.Lin, C.Cao, Electrochemical corrosion characteristics of type 316 stainless steel in simulated anode environment for PEMFC. Electrochimica Acta, 48(2003)1735-1741.

6. A.A.Hermas, M.S.Morad, K.Ogura, A correlation between phosphorous impurity in stainless steel and a second anodic current maximum in H_2SO_4, Corrosion Science, 41(1999)2251-2266.

7. W.F.Smith, Foundations of Materials Science and Engineering, New York, Third Edition, McGraw-Hill, 2004, PP702.

8. D.A.Jones, Principles and Prevention of Corrosion, First ed., New York, Macmillan, 1992, PP15.

9. D.A.Davies, P.L.Adcock, M.Turpin and S.J.Rowen, Bipolar plate materials for solid polymer fuel cells. J.Applied Electrochemistry, 30(2000)101-105.

10. M.P.Brady, K.Weisbrod, I.Paulauskas, R.A.Buchanan, K.L.More, H.Wang, M.Wilson, F.Garzon, L.R.Walker, Preferential thermal nitridation to form pin-hole free Cr-nitrides to protect proton exchange membrane fuel cell metallic bipolar plates. Scripta Mater., 50(2004)1017-1022.

11. R.G.Rajendran, Polymer electrolyte membrane technology for fuel cells. MRS Bulletin, 30(2005)587-590.

CHAPTER 6

PVD COATINGS

Physical vapor deposition (PVD) is one of the most promising coating technologies and is widely used for the improvement of the mechanical and corrosion properties of metallic materials [1]. TiN coatings have been used in many applications, e.g. cutting tools, because of their high wear resistance, hardness and low friction coefficient characteristics [2]. TiN coatings also have potential application to metallic bipolar plates because of TiN's excellent corrosion resistance and metal-like electrical conductivity [3]. However, little attention has been paid to determining the corrosion performance of TiN coatings on a metallic substrate under actual PEM fuel cell working conditions. In this section of the research, TiN was coated on SS316L using a PVD technology (plasma enhanced reactive evaporation) to increase the corrosion resistance of the base SS316L. XRD, SEM and electrochemical methods were used to characterize the TiN-coated SS316L.

6.1 XRD for the uncoated and TiN coated SS316L

The coating process was plasma enhanced reactive evaporation, in which Ti is evaporated in a DC plasma of nitrogen and argon. Fig 6.1 presents the XRD results for (a) the uncoated and (b) TiN-coated SS316L. Both the SS316L and TiN have a FCC structure. Comparing Figs 6.1a and 6.1b, we can see that there are no SS316L peaks for the coated sample since the penetration depth of the x-rays is less than the thickness of the TiN coating. The $(111)_{TiN}$ diffraction peak is the strongest. In the standard TiN

diffraction pattern [4], (200) is the strongest peak and the intensity ratio between I_{111} and I_{200} is 0.72. However, the intensity ratio between I_{111} and I_{200} in our samples is 2.04. Thus, the growth orientation of TiN is mainly in the <111> direction, which is consistent with other reports [5, 6], where the coatings have a columnar structure.
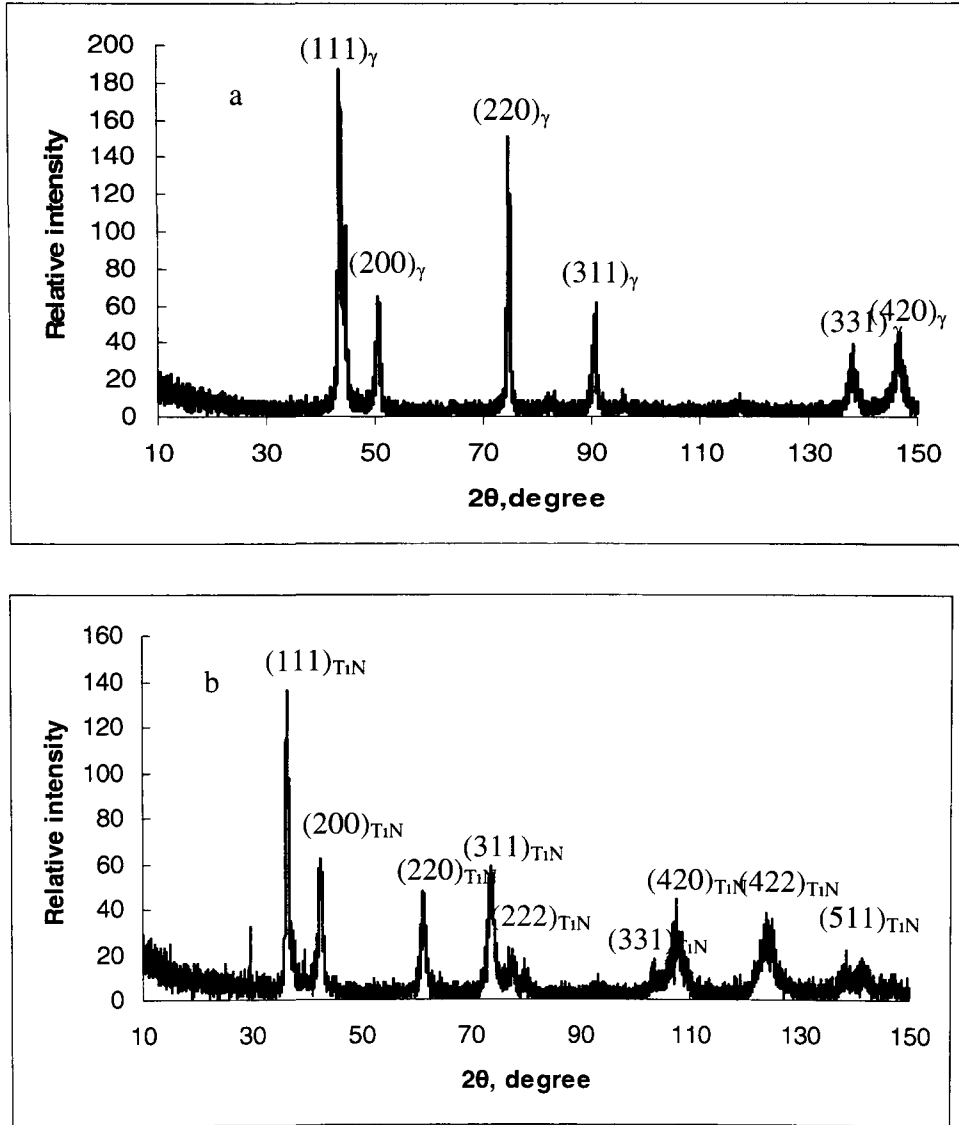
Fig 6.1 XRD patterns for uncoated and coated SS316L, (a) uncoated SS316, (b) coated SS316

6.2 SEM characterization of TiN coatings

Fig 6.2 are SEM micrographs of the TiN coatings on the SS316L surface. Fig 6.2a shows that TiN coating surface has a 'dented' appearance, due to the columnar growth of the TiN during the coating process. Fig 6.2b is a cross-sectional view of the TiN coating, which is 15μm thick. It is evident from Fig6.2b that the coating is multilayered. This layering has arisen because of regular modulation of the N_2 flow and irregular oscillations of the Ti from the e-beam pool during the commercial coating process. These layers overlap and result in an irregular structure.
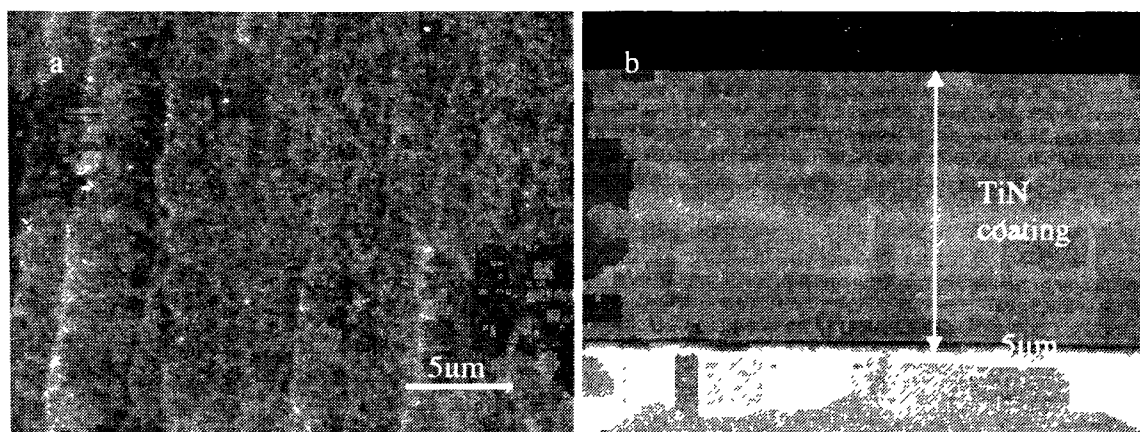
Fig 6.2 TiN coated SS316L, (a) TiN coating surface (secondary electron image), (b) Cross-sectional view of TiN coating on SS316L (back-scattered electron image)

6.3 Potentiodynamic testing

Fig 6.3 presents the potentiodynamic results for uncoated and coated SS316L. The open circuit potential of the base SS316L is -0.26VvsSCE. However, the open circuit potential of the TiN-coated SS316L increased to 0.16VvsSCE. Thus, the increased potential retards corrosion of the base SS316L. Comparing the two curves in Fig 6.3, we can see that the base SS316L shows a typical potentiodynamic curve for an austenitic stainless steel, in that it is divided into three regions, namely active, passive and transpassive. However, the corrosion curve for TiN-coated SS316L has no visible transpassive region. Based on the linear polarization method [7], we can obtain the polarization resistance of uncoated and TiN-coated SS316L at 70°C:

From Table 6.1, we can see that by coating with TiN, the polarization resistance of SS316L is increased by about 30 times, and the corrosion rate is decreased by about 40 times.
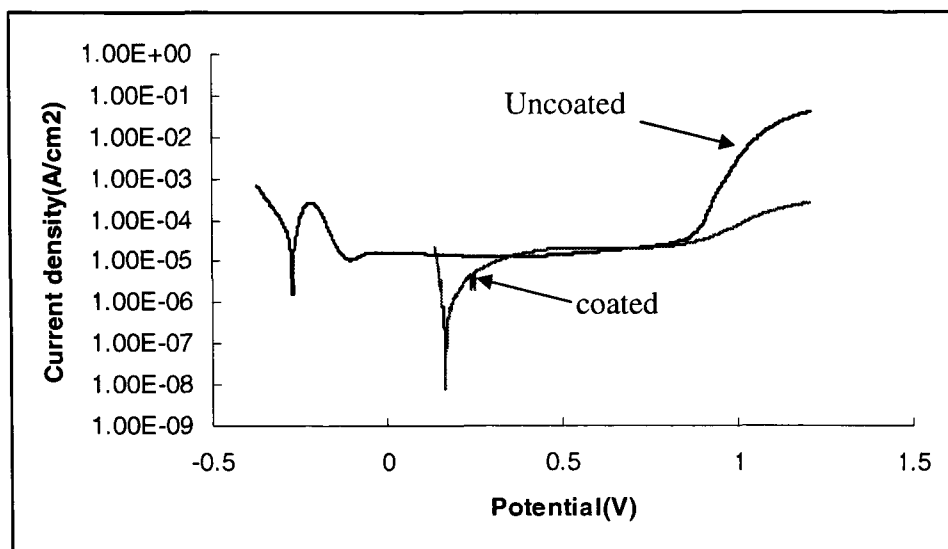
Fig 6.3. Potentiodynamic tests for uncoated and TiN-coated SS316L in 0.5M sulphuric acid at 70°C

Table 6.1. Polarization parameters of uncoated and coated SS316L in a 0.5M sulphuric acid solution at 70°C

Metal	β_a/V	β_c/V	E_{corr}/V	i_{corr}/(μA/cm^2)	R_p/($\Omega \cdot$cm^2)
Uncoated SS316L	0.055	0.074	-0.268	40.318	340
Coated SS316L	0.224	0.026	0.160	1.020	9930

Fig 6.4 presents SEM micrographs for both uncoated and TiN-coated SS316L after the potentiodynamic tests. From Fig6.4a, we can see that the uncoated SS316L corrodes by grain boundary (intergranular) corrosion. However, from Fig6.4b, we can see that there is no evidence of grain boundary corrosion for the TiN-coated SS316L.
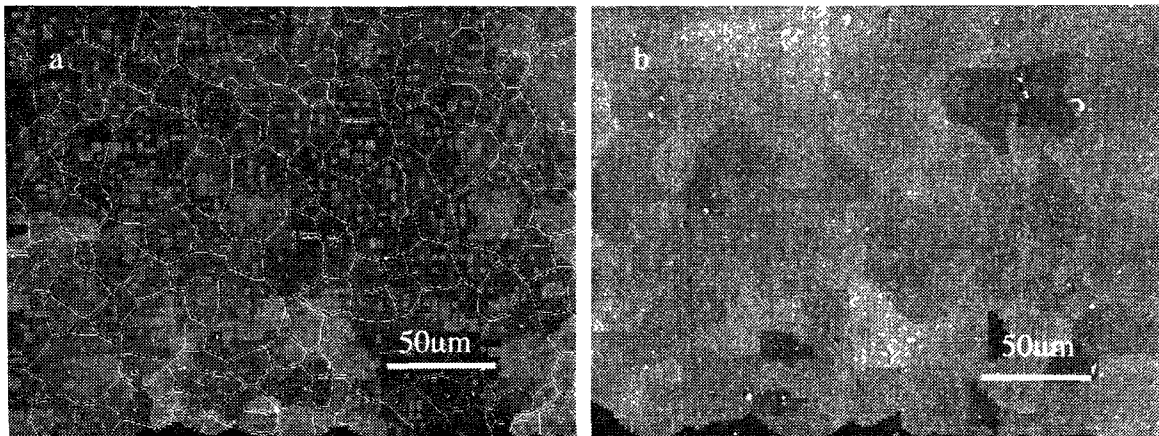
Fig 6.4. SEM micrographs for (a) uncoated, and (b) TiN-coated SS316L after potentiodynamic testing

6.4 Impedance tests

Fig 6.5 presents the EIS spectra for uncoated and TiN-coated SS316L. Comparing the two curves in Fig 6.5, we can see that the impedance value for TiN-coated SS316L is much higher than that for the uncoated SS316L over the complete curve. This is consistent with the values for the polarization resistance that were obtained in the potentiodynamic tests.
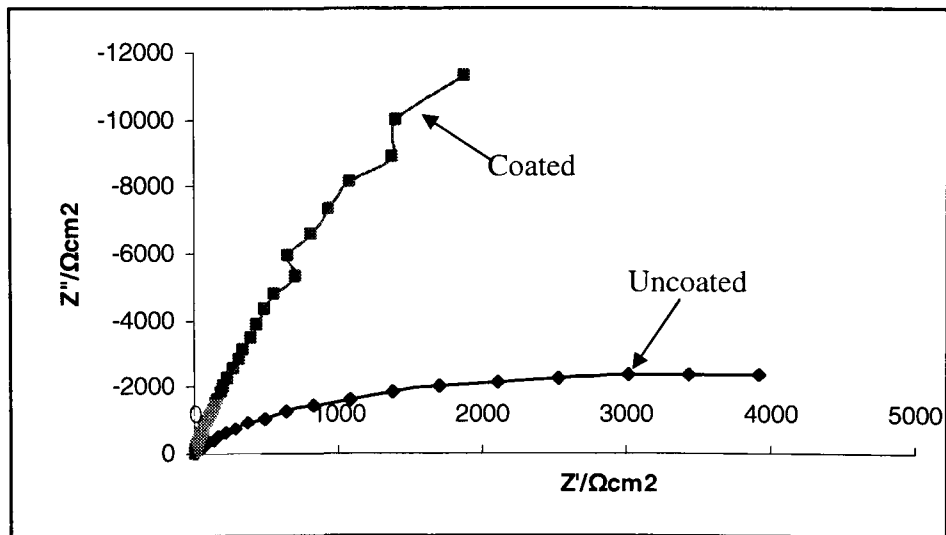
Fig 6.5 Electrochemical impedance spectra for the uncoated and TiN-coated SS316L

6.5 Potentiostatic testing in simulated anode and cathode conditions

In actual PEMFC working conditions, the anode is at a potential of about -0.1VvsSCE and the cathode is at a potential of about 0.6VvsSCE [8]. Because the open circuit potentials of uncoated and TiN-coated SS316L are -0.26VvsSCE and 0.16VvsSCE, respectively, the simulated anode potential is anodic to uncoated SS316L and cathodic to TiN-coated SS316L. The simulated cathode potential is anodic to both uncoated and TiN-coated SS316L. Under these PEMFC conditions, any corrosion that takes place is not the same as the free potential corrosion. In order to study the corrosion behavior of metallic bipolar plates in actual PEMFC working conditions, potentiostatic tests were conducted at -0.1VvsSCE purged with H_2 to simulate the anode working conditions and at 0.6VvsSCE purged with O_2 to simulate the cathode working conditions. The test results are shown in Figs 6.6 and 6.7, for both the simulated cathode and anode conditions.

From Fig 6.6, which is the simulated anode working conditions, we can see that the current density of the uncoated SS316L stabilizes at about $-1 \times 10^{-5} A/cm^2$ For the TiN-coated samples, the current density stabilizes at about $-4 \times 10^{-5} A/cm^2$ This implies that H^+ ions can form H_2 more easily on the TiN-coated surface because TiN has a more positive potential than SS316L. Also, the corrosion current of TiN-coated SS316L became negative immediately after the start of the experiments. However, it took about 50 seconds for the corrosion current for the base SS316L to become negative. Thus, in the first 50 seconds, SS316L can corrode in the simulated anode environment. The corrosion current density of TiN-coated SS316L is negative at all times. This negative current provides cathodic protection for both the uncoated and TiN-coated SS316L. Therefore, the TiN-coated SS316L undergoes less corrosion in the simulated anode environment of PEM fuel cells.

Fig 6.7 presents the potentiostatic test results for the simulated cathode working conditions. For uncoated samples, the current density is $8 \times 10^{-6} A/cm^2$, and for the coated samples, the current density stabilizes at about $2.5 \times 10^{-5} A/cm^2$ It is somewhat surprising that the corrosion current density increased by a factor of about 3 after coating with TiN. This is because the base SS316L is in the passive region in the simulated cathode environment. Also, the thin TiN coatings, such as those produced by plasma enhanced reactive evaporation, are not 'perfect' and typically contain defects such as pinholes,

135

which can give rise to pitting corrosion [6, 9,10]. The incidence of these pinhole defects can potentially be reduced through modification of the processing parameters for the plasma enhanced reactive evaporation. Such processing parameter modification would lead to changes in the thickness and chemistry of the TiN-layer. An alternative approach is the use of direct nitriding process, such as plasma nitriding, to produce a dense nitrogen-rich austenitic layer on the surface of the stainless steel [11].
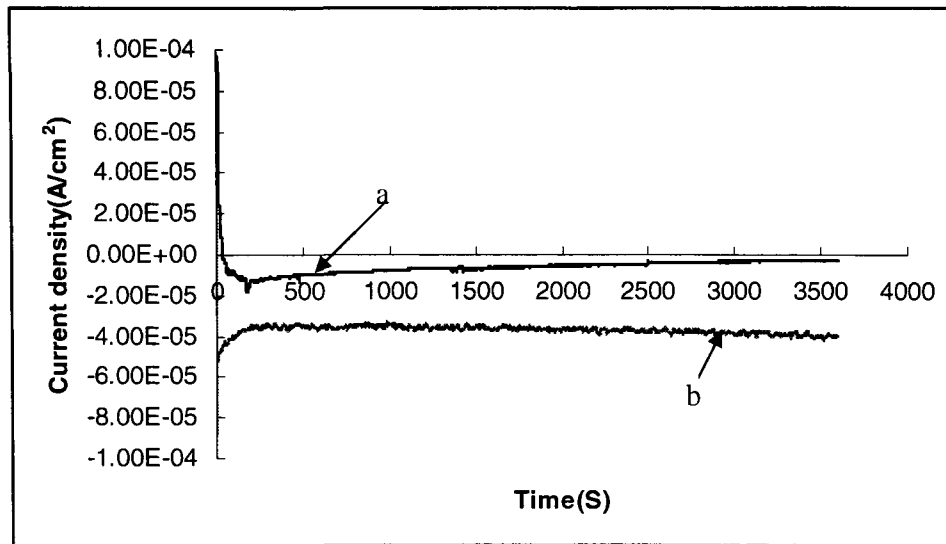
Fig 6.6. Potentiostatic tests for the uncoated and TiN-coated SS316L in simulated anode conditions, (a) uncoated, (b) coated
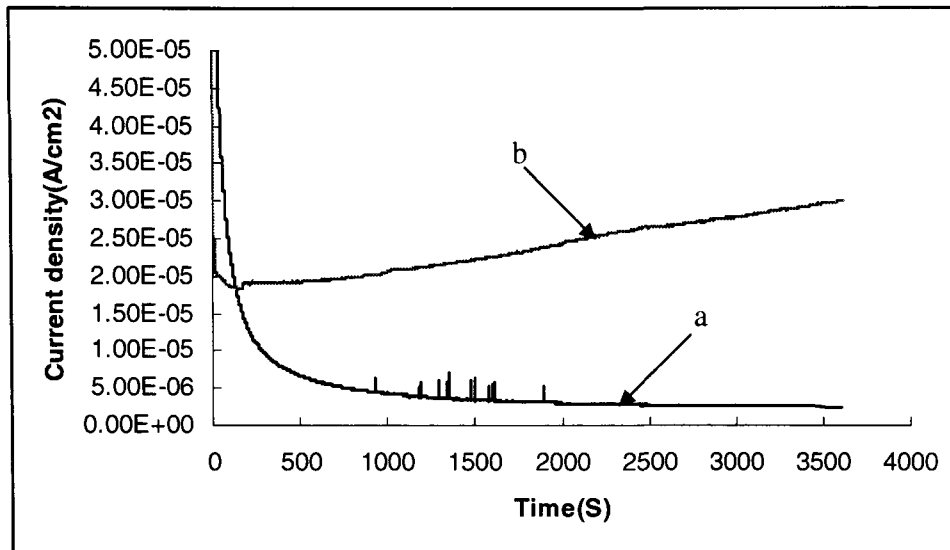
Fig 6.7 Potentiostatic tests for the uncoated and TiN-coated SS316L in simulated cathode conditions, (a) uncoated, (b) coated

6.6 SEM examination of coated SS316L surfaces after potentiostatic tests in simulated anode and cathode conditions

Fig 6.8 presents the SEM micrographs of TiN coated SS316L after potentiostatic testing in the simulated PEM fuel cell working environments. From Fig 6.8a, we can see that there is no evidence of corrosion at the anode side. However, there is pitting corrosion at the cathode side: see Fig 6.8b. So, if TiN-coated SS316L, fabricated using plasma enhanced reactive evaporation, is used as the bipolar plates of PEMFCs, there will be corrosion problems at the cathode. Methods should be developed to produce improved, ie defect-free, TiN coatings to prevent pitting corrosion.

137
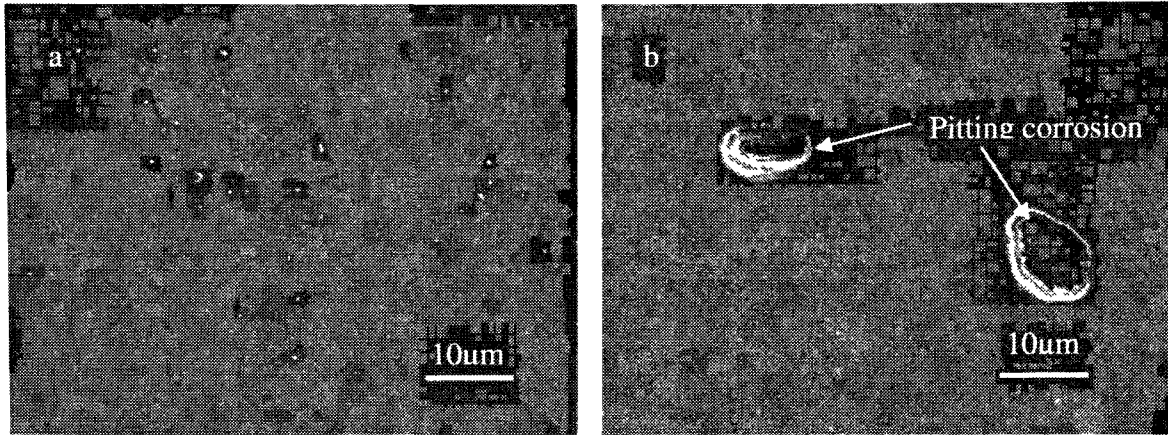
Fig 6.8. SEM micrographs for the coated SS316L after potentiostatic tests in the simulated anode and cathode conditions, (a) anode side, (b) cathode side

6.7 Metal ion concentration after 10 hours potentiostatic tests

Table 6.2 summarizes the metal ion concentrations after 10 hours potentiostatic tests in the simulated anode and cathode conditions for a PEM fuel cell. Comparing the data in the Table 6.2, we find that metal ion concentration at the cathode is much higher than that at the anode for all the elements analyzed for both uncoated and TiN-coated samples. Also, comparing the results of uncoated and TiN-coated SS316L, we find that the metal ion concentration in solution for TiN-coated SS316L is only about half that for the uncoated samples in the simulated anode conditions. However, in the simulated cathode conditions, there are more metal ions in the solution for TiN-coated SS316L. Therefore, based on our research results, metal corrosion is more severe in the cathode environment, which is consistent with the potentiostatic test results. The metal ion concentrations measured in the simulated anode conditions seems at odds with the potentiostatic tests because the negative current should provide cathodic protection for SS316L. The reason why we still get a relatively high metal ion concentration at the anode is that the negative protection is only partial and it can not provide the full protection for SS316L.Therefore, SS316L can be corroded in both the anode and cathode environments, and corrosion in the cathode environment is the hot spot.

If the corrosion rate remains the same for the 5000h lifetime of the fuel cell, Fe, Cr, Ni, Mn ion concentrations will reach 375, 64.5, 40.4, 9.1ppm at the anode, and 613, 115, 90.1, 18.2ppm at the cathode after 5000h for uncoated SS316L. Fe, Cr, Ni, Mn metal ion concentrations will reach 185, 25, 30, 5ppm at the anode, and 950, 145, 35, 55ppm at the cathode after 5000h for TiN-coated SS316L. Let us suppose that 5% percent of metal ions remain in solution, and then the total metal concentrations are 24.5 and 41.8ppm at the anode and cathode for uncoated SS316L, respectively, and 12.3ppm at the anode and 59.3ppm at the cathode, respectively, after 5000h for TiN-coated SS316L. The metal ion concentration in the simulated anode condition is approaching the satisfactory levels for the TiN-coated SS316L; however, the metal ion concentration is still too high in the simulated cathode conditions.

Table 6.2 Metal ion concentration in solution after potentiostatic tests

Different coatings	Dissolved metal concentration (μg/L)				Total concentration of metal ions (μg/L)
	Fe	Cr	Ni	Mn	
Base solution	20.71	<IDL	<IDL	1.36	22.07
Uncoated SS316L at anode side	770	129	80	19	998
Uncoated SS316L at cathode side	1245	230	180	36	1691
PVD coated SS316L at anode side	370	50	60	10	490
PVD coated SS316L at cathode side	1900	290	70	110	2370

IDL is the identification limit.

6.8 Contact resistance tests

Fig 6.9 shows the contact resistance of SS316L and TiN coated SS316L at different compaction pressures. With increasing compaction pressure from 20N/cm^2 to 220N/cm^2, the contact resistance decreased rapidly at low compaction pressures and then decreased more gradually, probably due to a decrease in interfacial resistance [12]. Comparing the two curves in Fig 6.9, we can see that the contact resistance of TiN coated SS316L has a lower contact resistance than that of SS316L. However, the difference is significantly reduced with increasing compaction pressure, i.e., at a compaction pressure of 200N//cm^2, the contact resistance has almost the same value. These results show that TiN coated SS316L is a better material compared to SS316L from a contact resistance point of view.
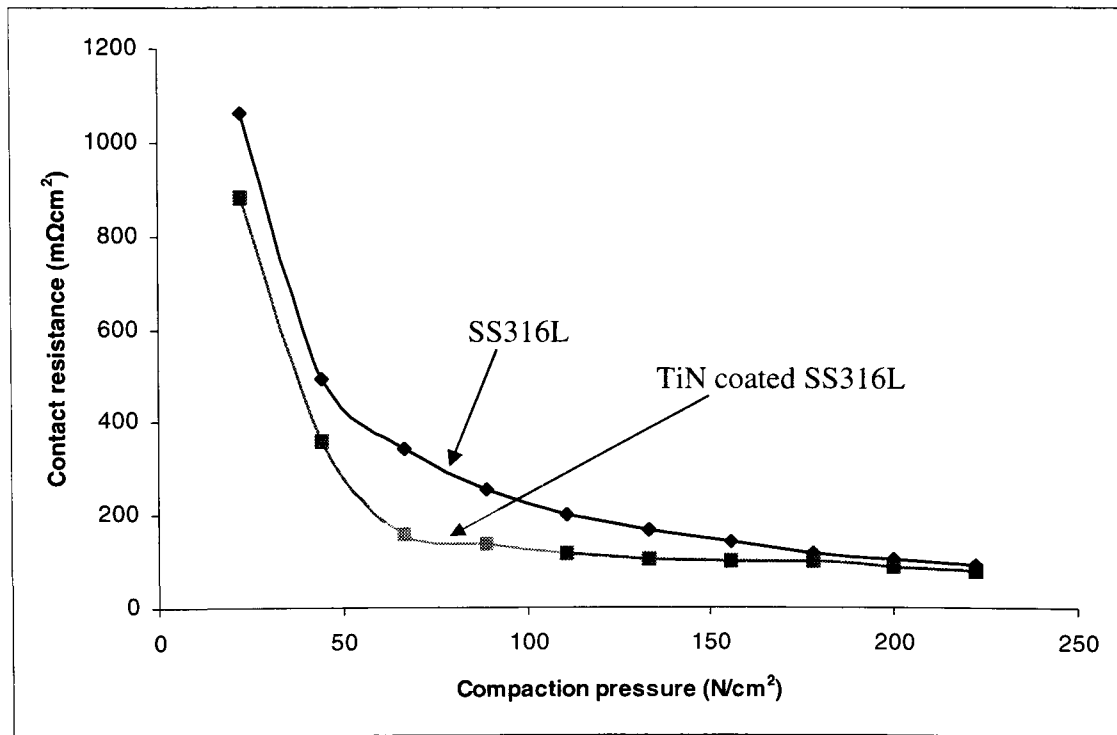
Fig 6.9 Interfacial contact resistances for SS316L and TiN coated SS316L

6.9 Summary

TiN was coated on SS316L using PAPVD coating technology. Potentiodynamic tests and electrochemical impedance measurements show that the corrosion resistance of TiN-coated SS316L has been increased compared to uncoated SS316L. However, in the

140

simulated PEMFC conditions, the cathode side will have more severe corrosion problems if TiN-coated SS316L is used for the bipolar plates of PEM fuel cells.

References

1. L.A.Dobrzański, K.Lukaszkowicz, A.Zarychta, L.Cunha, Corrosion resistance of multilayer coatings deposited by PVD techniques onto the brass substrate. J.Materials Processing Technology, 164-165(2005)816-821.

2. Y.Li, L.Qu, F Wang, The electrochemical corrosion behavior of TiN and (Ti,Al)N coatings in acid and salt solution, Corrosion Science, 45(2003)1367-1381.

3. M.Li, S.Luo, C.Zeng, J.Shen, H.Lin, C.Cao, Corrosion behavior of TiN coated type 316 stainless steel in simulated PEMFC environments. Corrosion Science, 46(2004)1369-1380.

4. W.Wong, H.McMurdie, B.Paretzkin, C.Hubbard, A.Dragoo, Standard x-ray diffraction powder patterns of sixteen ceramic phases. Powder Diffraction. 2(1987)191-202.

5. C.Hsu, M.Chen, K.Lai, Corrosion resistance of TiN/TiAlN-coated ADI by cathodic arc deposition, Materials Science and Engineering A, 421(2006)182-190.

6. H.C.Barshilia, M.S.Prakash, A.Poojari, K.S.Rajam, Corrosion behavior of nanolayered TiN/NbN multilayer coatings prepared by reactive direct current magnetron sputtering process, Thin Solid Films, 460(2004)133-142.

7. D.A.Jones, Principles and Prevention of Corrosion, First ed, New York, Macmillan, 1992, PP147

8. H.Wang, J.A.Turner, Ferritic stainless steels as bipolar plate material for polymer electrolyte membrane fuel cells. J.Power Sources, 128(2004)193-200.

9. F.Lang, Z.Yu, The corrosion resistance and wear resistance of thick TiN coatings deposited by arc ion plating, Surface and Coatings Technology, 145(2001)80-87

10. H.A.Jehn, Improvement of the corrosion resistance of PVD hard coating–substrate systems, Surface and Coatings Technology, 125(2000)212-217

11. R.Tian, J.Sun, L.Wang, Plasma-nitrided austenitic stainless steel 316L as bipolar plate for PEMFC Int.J.Hydrogen Energy, 31(2006)1874-1878.

12. E.A.Cho, U.S.Jeon, S.A.Hong, I.H.Oh, S.G.Kang, Performance of a 1 kW-class PEMFC stack using TiN-coated 316 stainless steel bipolar plates. J.Power Sources, 142(2005)177-183.

CHAPTER 7

POLYPYRROLE COATINGS

Conductive polymers are a new type of material, which has a high redox potential, and properties of both metals and plastics. Electrochemical polymerization of conductive polymers has received wide attention because of its simplicity and the fact that it is a one-step process [1]. Polymers have been deposited on aluminium and stainless steel to improve the corrosion resistance of the metals [2-6]. Polypyrrole is one of the most researched conductive polymers that have been deposited on metal surfaces. In this research work, polypyrrole was coated on SS316L in order to increase the corrosion

143

resistance of the base material. The nucleation and growth mechanisms of polypyrrole on SS316L were studied by an electrochemical method. The polypyrrole coating parameters were optimized using a Taguchi DOE method. In order to further lower the metal ion concentration in the solution, polypyrrole was coated on an Au-coated SS316L surface.

7.1 An investigation into polypyrrole coated 316L stainless steel as a bipolar plate material for PEM fuel cells

7.1.1 Effect of roughness on polarization resistance

In corrosion tests, surface inhomogeneity arising from polishing of the working electrode can lead to different corrosion results [7]. Because different grit silicon carbide papers were used to prepare specimens for the potentiodynamic tests and polymerization, potentiodynamic tests were conducted for different surface roughnesses (R_a) in order to determine the effect of surface roughness on the polarization resistance. The results are shown in Table 7.1. From the results, we can see that the corrosion current density and polarization resistance are almost the same for the different surface roughness samples in our experiments.

Table 7.1 Polarization parameters of SS316L with different surface roughnesses at 70°C

Polishing media	$R_a/\mu m$	β_a/V	β_c/V	E_{corr}/V	i_{corr}/($\mu A/cm^2$)	R_p/($\Omega \cdot cm^2$)
240 grit	-------	0.052	0.072	-0.259	38.981	337
240 grit	-------	0.054	0.074	-0.268	38.074	356
240 grit	-------	0.057	0.075	-0.271	42.502	331
Average	0.12	--------	--------	-0.266	39.852	341
Alumina powder 1.0	-------	0.057	0.071	-0.267	41.273	333
Alumina powder 1.0	-------	0.053	0.071	-0.270	40.012	328
Alumina powder 1.0	-------	0.055	0.074	-0.268	40.318	340
Average	0.05	--------	--------	-0.268	40.534	334

7.1.2 Electrochemical polymerization

Fig 7.1 presents galvanostatic coating curves for polypyrrole on SS316L. We can see that when different currents are used to coat polypyrrole on SS316L, it gives rise to different coating potentials. When the applied current is 0.0001A, the potential increases to about 0.36V after a short time and then stabilizes. When the applied current is 0.0002A, the potential is about 0.6V after 100 seconds and then stabilizes. When the applied current is 0.0005A, the potential first increases to 0.8V and it then takes about 700 seconds to reach a stable potential (1.5V). When the current is further increased to 0.001A and 0.005A, it takes less time to reach the stable potential. However, the stable potentials are almost the same for applied currents of 0.0005A, 0.001A and 0.005A. This is because water begins to dissociate on the SS316L surface at 1.5VvsSCE and we observed some bubbles on the metal surface.
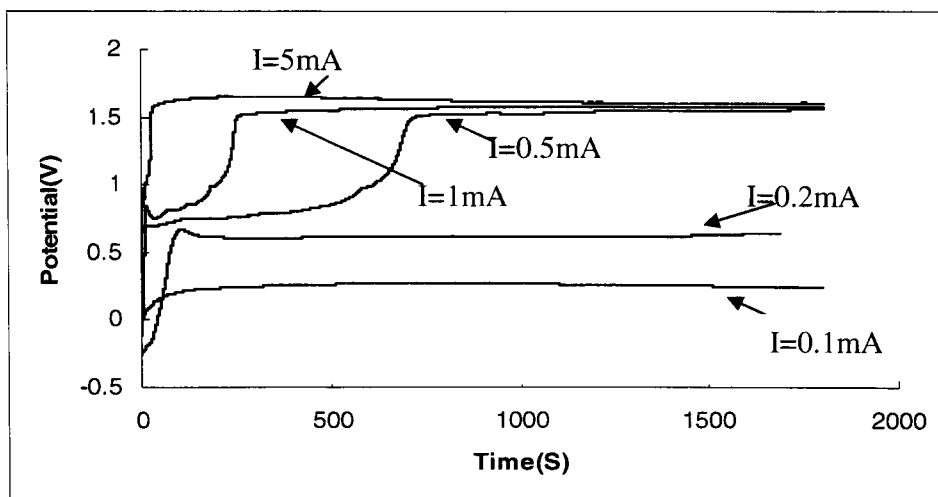
Fig7.1. Galvanostatic coating of polypyrrole on SS316L

Fig 7.2 presents the cyclic voltammometric coating curves for polypyrrole on SS316L. In the first cycle, the current density is very low from -0.2V to 0.7V At 0.7V, the current density begins to rapidly increase and reaches $1.0 \times 10^{-3} A/cm^2$ at which time polypyrrole begins to form in significant amounts on the SS316L surface. In the second cycle, the maximum current density is only about $4.0 \times 10^{-4} A/cm^2$ Thus, there is less polypyrrole formed in the second cycle. Moreover, in the second cycle, we find that there is a wide peak at 0.7V From Fig 7.2b, we can also see a peak at 0.7V in the third and fourth cycles. With increasing number of cyles, the peak becomes smaller. This peak at about

145

0.7V is due to the oxidation of the polypyrrole. Therefore, in the first cycle of a multi-cycle coating process, polypyrrole is formed first. In subsequent cycles, some of the polypyrrole is oxidized at about 0.7V The oxidation of polypyrrole helps protect the SS316L from corroding.
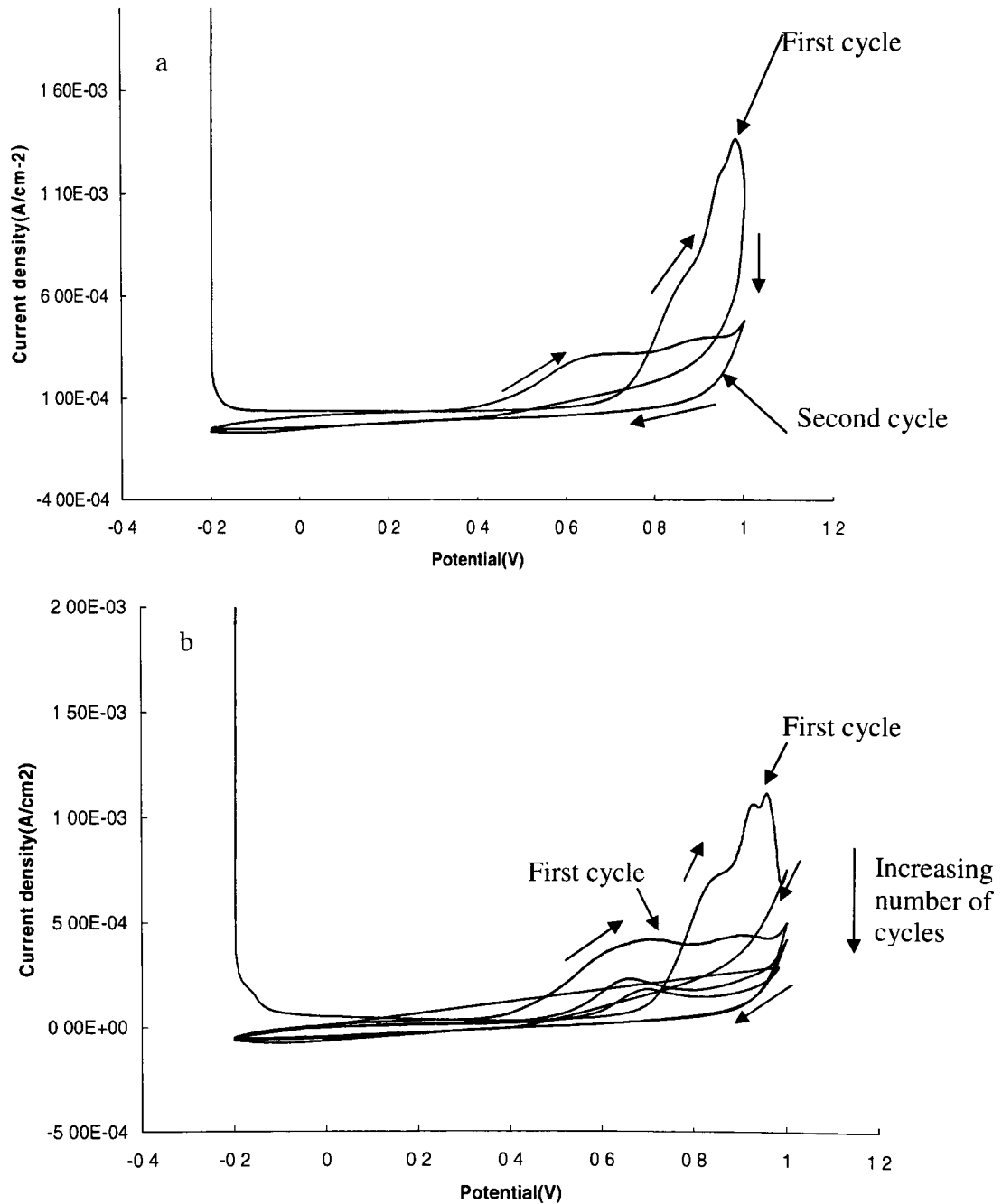
Fig 7.2. Cycle voltammometric coating of polypyrrole on SS316L: (a) 2 cycles, (b) 4 cycles

7.1.3 SEM of polypyrrole-coated materials

SEM micrographs of polypyrrole-coated SS316L produced at different applied currents and number of cycles are shown in Figs 7.3 and 7.4. Figs 7.3a and 7.3b show the samples produced using the galvanostatic method and applied currents of 0.0001A and 0.0002A, respectively. The polypyrrole film is quite thin and the polishing marks from the 240 grit polishing of the SS316L are still visible. When the applied current is increased to 0.0005A and 0.001A, polypyrrole particles are seen on the SS316L surface. Most of the polypyrrole particles are smaller than $1\mu m$ for an applied current of 0.0005A, Fig 7.3c. The polypyrrole particle size increases to 2 to 3 μm for an applied current of 0.001A, Fig 7.3d. When the applied current is increased to 0.005A, the individual particle morphology can no longer be seen in the polypyrrole coating, Fig 7.3e. Cracks were seen in the polypyrrole coating, Fig 7.3f. The cracks are the result of gases being produced under the polypyrrole coating, which generate sufficient pressure to fracture the coating. Because it is an oxidation reaction, the gases should be oxygen.

The morphology of the polypyrrole coatings produced using the cyclic voltammometric method are different from those produced using the galvanostatic method; compare Fig 7 4 with Fig 7.3. The polypyrrole particle size is larger for the cyclic voltammometric-produced coatings. The polypyrrole particle increases with increasing number of cycles. Again, the influence of the 240 grit polishing can be seen in the surface morphology, particularly at a lower number of cycles (similar to a lower applied current).
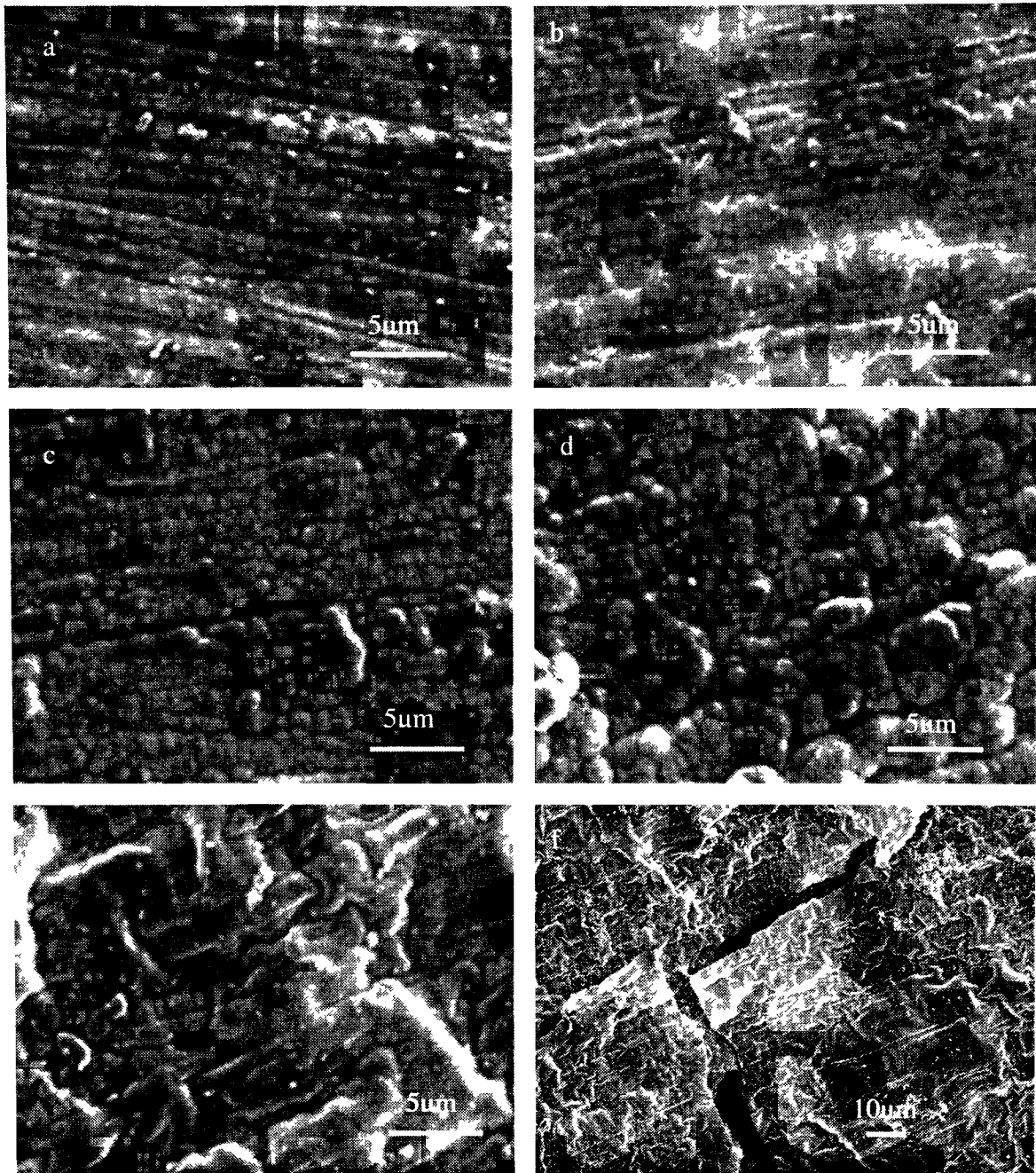
Fig 7.3. SEM micrographs of SS316L coated with polypyrrole using galvanostatic method and different applied currents, (a) 0.0001A, (b) 0.0002A, (c) 0.0005A, (d) 0.001A, (e) and (f) 0.005A
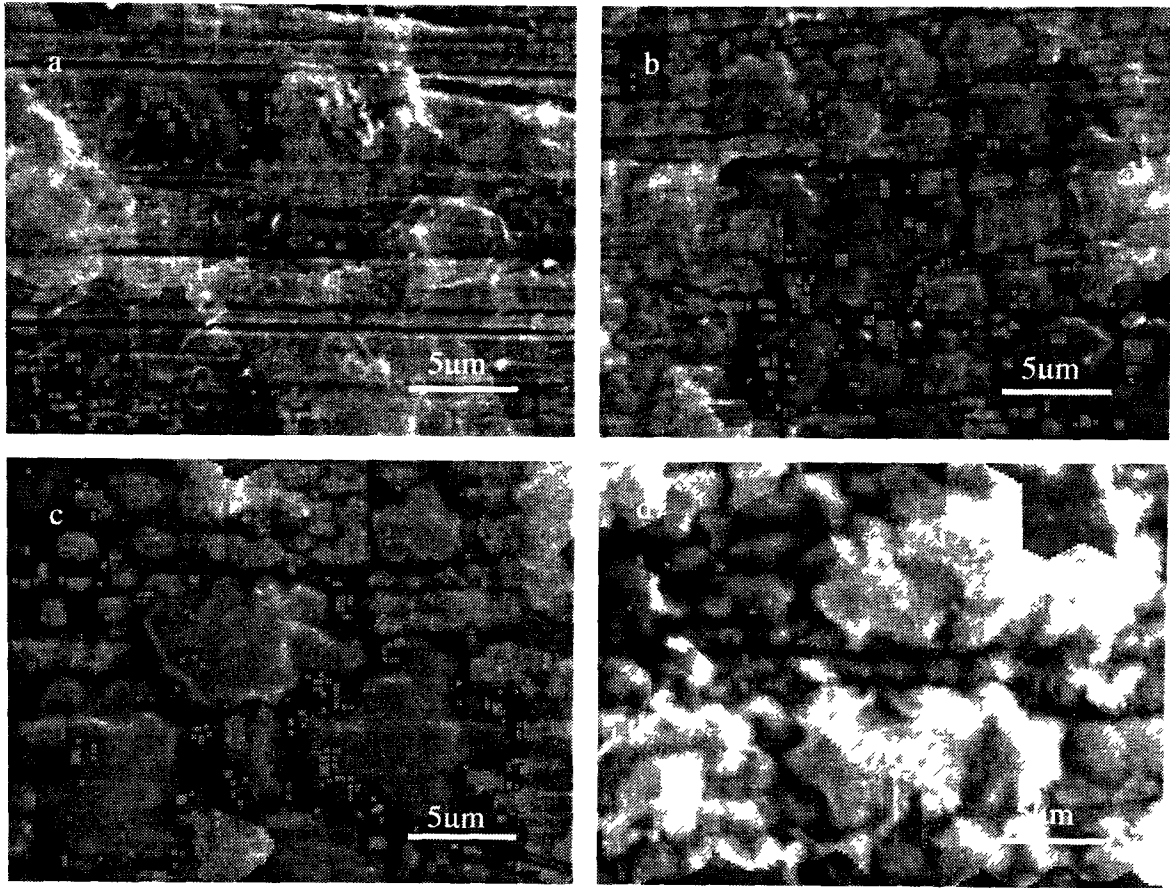
Fig 7 4. SEM micrographs of SS316L coated with polypyrrole using a cyclic voltammometric method, (a) 2-cycle coating, (b) 4-cycle coating, (c) 6-cycle coating, (d) 8-cycle coating

7.1.4 FTIR

Fig 7.5 is the IR spectra of polypyrrole. Before the test, polypyrrole is completely mixed with KBr, and KBr is used to record the background spectrum. The peak at 1700cm^{-1} is the C=O peak, and the peaks in the range of 1580~1390 and 1210cm^{-1} are due to C=C and C=N in plane vibrations. Peaks at 1045, 926, 800cm^{-1} are due to ring vibrations of pyrrole. The peaks in the 600-680cm^{-1} are due to N-H bond [2, 6].
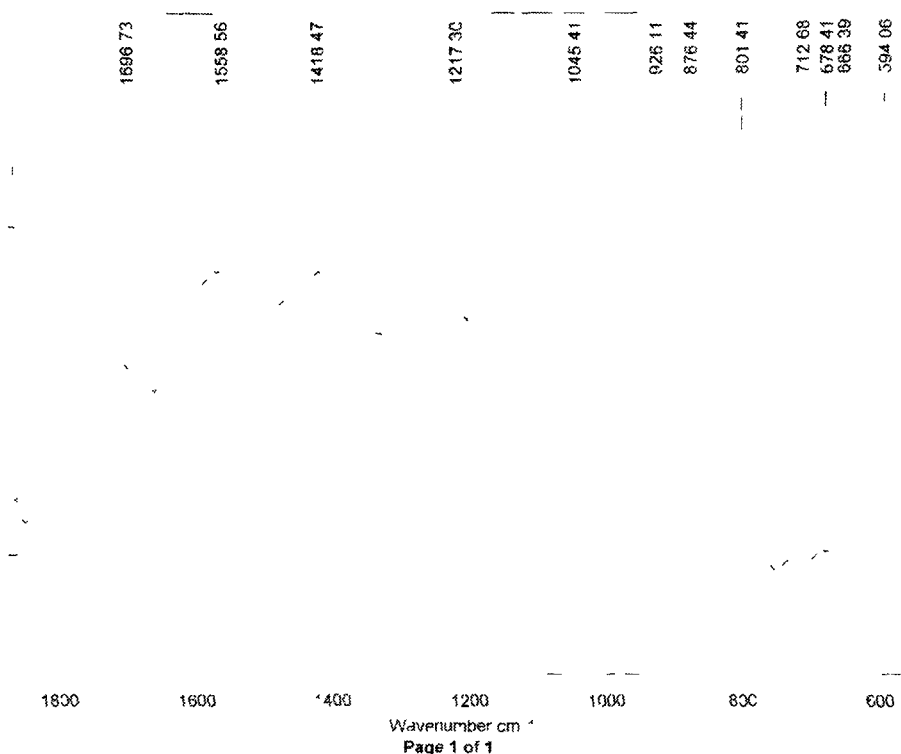
Fig 7.5 FTIR spectra of polypyrrole

7.1.5 Potentiodynamic polarization testing after coating with polypyrrole

In order to determine the polarization resistance after coating with polypyrrole, potentiodynamic polarization tests were conducted on the 4-cycle voltammometric coated sample, Fig 7.6. The polypyrrole coating results in an elevated (more positive) corrosion potential for SS316L and a lower corrosion current density: see Fig 7.6 and Table 7.2. From the linear polarization data, the polarization resistance after polypyrrole coating is more than 10 times higher than for the uncoated samples. Comparing the data in Table

7.2, we can find that the polarization resistance and corrosion current density after coating at high temperature are the same order as those of the uncoated SS316L at ambient temperature. Comparing the corrosion current densities in our work with Joseph et al's results [5], we find that the corrosion current density ($\sim$2.4μA/cm^2) in our tests is higher than that found by Joseph et al (1μA/cm^2). There are at least two possible reasons for this. First, our experiments were conducted at 70°C, whereas Joseph et al [5] appear to have conducted their tests at ambient temperature. The other main reason is that we used a higher concentration electrolyte for the potentiodynamic tests, 0.5M H$_2$SO$_4$ VS. 0.1M H$_2$SO$_4$. From Fig 7.6, we can also see that the current density is lower for coated SS316L below 0.6V, but from 0.6V$\sim$1.0V the coated SS316L has a higher current density because polypyrrole can be oxidized, thus generating a current. Above 1.0V, uncoated and coated SS316L exhibit almost the same current densities.
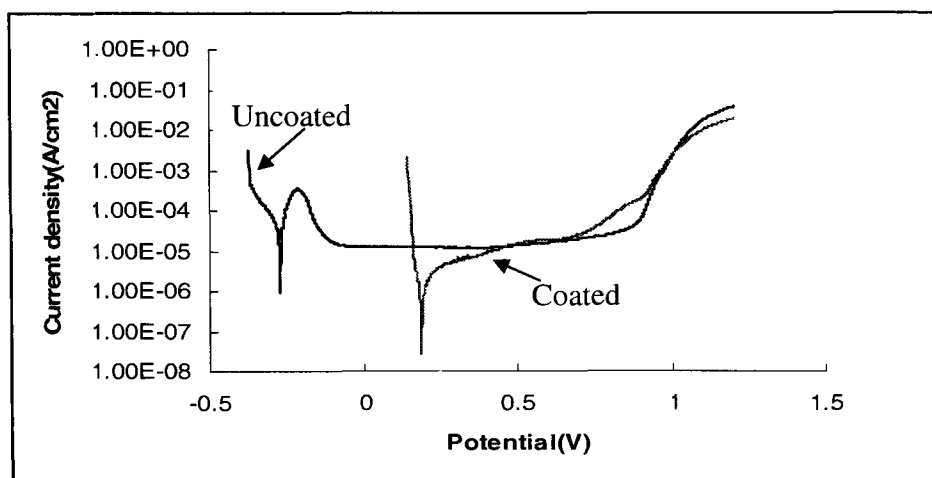
Fig 7.6 Potentiodynamic polarization curve for uncoated and 4-cycle voltammometric
coated SS316L at 70°C

Table 7.2 Polarization resistance of uncoated and polypyrrole-coated SS316L at 70°C

Samples	β_a/V	β_c/V	E_{corr}/V	i_{corr}/μA	R_p/(Ω·cm^2)
Uncoated SS316L at 20°C	0.114	0.081	-0.251	4.891	4198
Uncoated SS316L at 70°C	0.053	0.071	-0.270	40.012	328
Coated-SS316L	0.399	-0.020	0.171	2.379	3459

From Fig 7.7, which is an optical micrograph of a polypyrrole-coated SS316L sample after potentiodynamic testing, we can see that some intergranular corrosion has occurred. Thus, the polypyrrole coating can not completely prevent corrosion. However, comparing this sample with the uncoated SS316L (Fig 4.17(b)), there is less corrosion evident after polypyrrole coating.
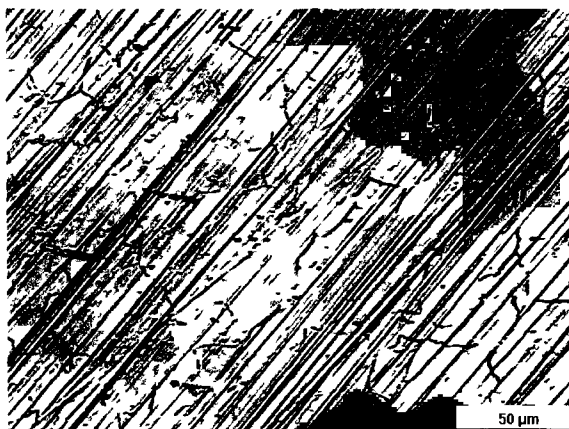
Fig 7.7 Optical micrograph of 4-cycle voltammometric coated SS316L after potentiodynamic testing at 70°C

7.1.6 Potentiostatic tests simulating the PEMFC working conditions

Figs 7.8 and 7.9 present the potentiostatic tests in the simulated cathode and anode conditions, respectively. From Fig 7.8, which is the simulated cathode working conditions, we can see that the current density of uncoated SS316L stabilizes at about $4 \sim 5 \times 10^{-6} A/cm^2$ after 500 seconds, but that it takes more time for polypyrrole-coated SS316L to obtain a stable current density. For the coated samples, the current density gradually decreased to about $1.0 \times 10^{-5} A/cm^2$ after 2 hours. It seems surprising that the corrosion current increases after coating with polypyrrole, but this is because the polypyrrole coating is oxidized at 0.6VvsSCE, which is consistent with Garcia and Smit's findings [6]. This is similar to the results from the potentiodynamic tests (Fig 7.6). Also from Fig 7.8, we can see the polypyrrole coatings produced using the different methods and processing parameters exhibit almost the same corrosion current densities. The possible reason is that some polypyrrole is oxidized to maintain such a small current density.
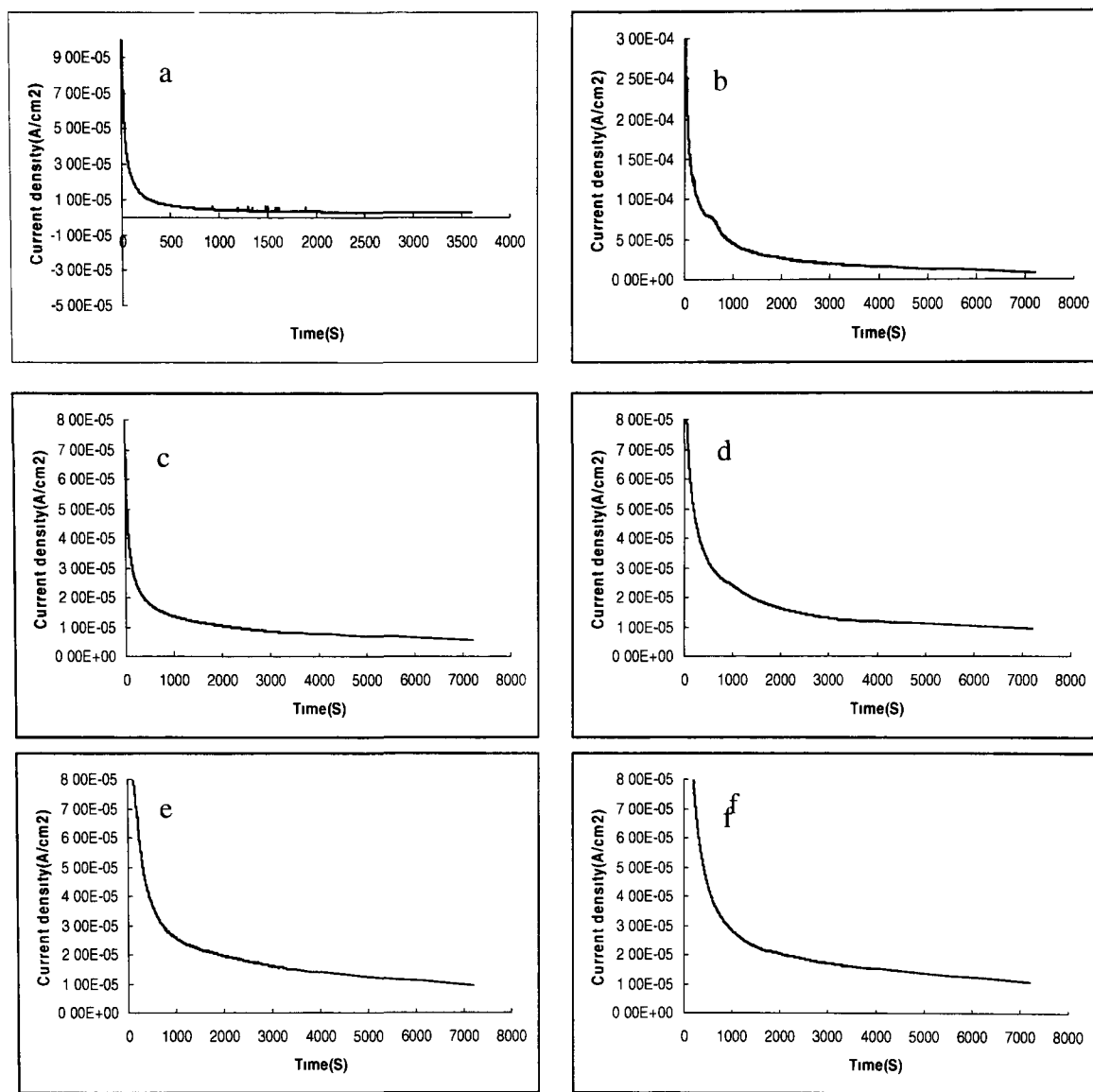
Fig 7.8 Potentiostatic curves for uncoated and polypyrrole-coated SS316L at 0.6V purged

with O₂. (a) uncoated SS316L, (b) 0.0002A coated SS316L, (c) 0.001A coated SS316L,

(d) 4-cycle coated SS316L, (e) 6-cycle coated SS316L, (f) 8-cycle coated SS316L

Fig 7.9 presents the potentiostatic testing results for the simulated anode conditions. For uncoated samples, the current density becomes negative after 50 seconds. However, for the coated samples, the current density is negative right from the start of the potentiostatic tests and stabilizes at about $-1.0 \times 10^{-5} \sim -2.0 \times 10^{-5} A/cm^2$ The current density for polypyrrole-coated SS316L becomes negative right away because the corrosion

153

potential is increased after coating with polypyrrole. This negative current density can provide cathodic protection for the metallic bipolar plate material.
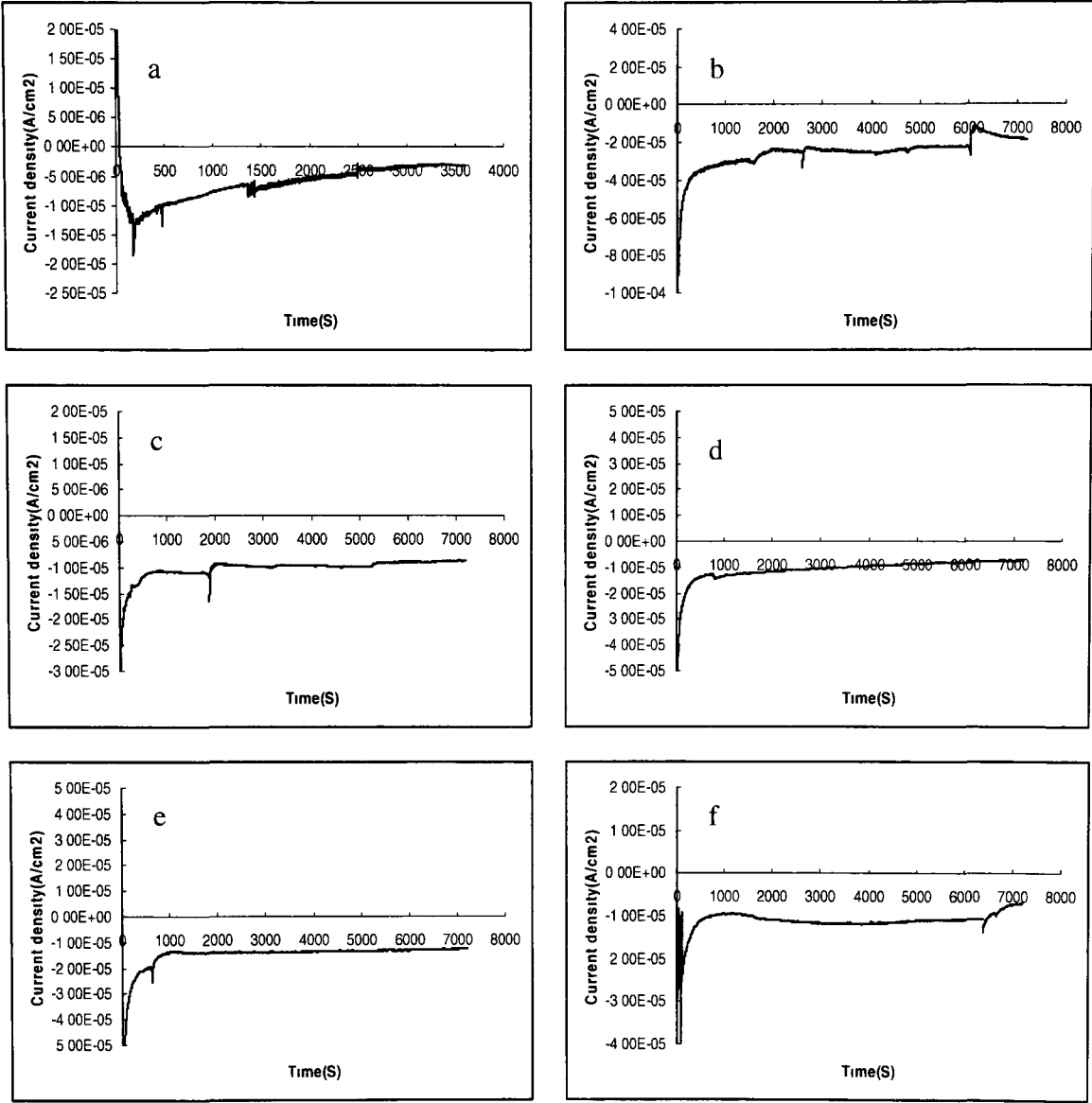
Fig 7.9 Potentiostatic curves for uncoated and coated SS316 at -0.1V purged with H_2. (a) uncoated SS316L, (b) 0.0002A coated SS316L, (c) 0.001A coated SS316L, (d) 4-cycle coated SS316L, (e) 6-cycle coated SS316L, (f) 8-cycle coated SS316L

7.2 An investigation into the nucleation and growth of an electropolymerized polypyrrole coating on a 316L stainless steel surface

7.2.1 Electropolymerization of polypyrrole

Fig 7.10 presents the chronoamperometric curves of polypyrrole deposited on SS316L at different potentials. Comparing the curves in Fig 7.10, we can see that the nucleation current density is very small at 0.6 V, and therefore there is very little polypyrrole formed. At 0.8 V, the current density increased with time and reached the highest current density of 8.6×10^{-1} mA/cm^2 at 45 s to 48 s. When the applied potential increased to 1.0 V, we can see that there was an apparent peak current density of 2.89 mA/cm^2 at times from 4.5 s to 5.0 s. When the applied potential increased to 1.2 V, the peak current density reached 4.6 mA/cm^2 at 2.05 s to 2.15 s. Comparing these curves, we can see that the peak current density increased with increasing potential. However, the incubation time, the peak current time, and the width of peak current density, decreased because of the severe oxidation of polypyrrole at a higher potential.
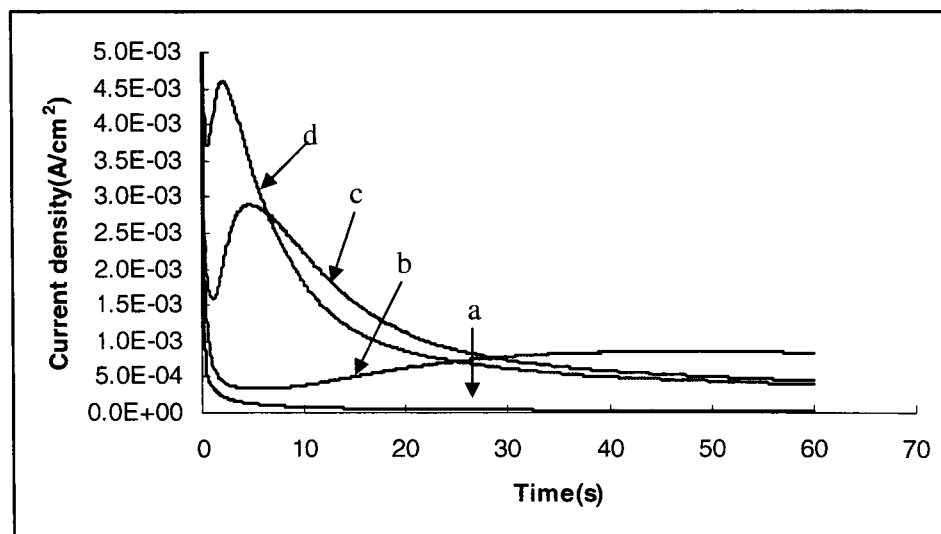
Fig 7.10. Chronoamperometric curves of polypyrrole deposited on SS316L at different potentials, (a) 0.6V, (b) 0.8V, (c) 1.0V, (d) 1.2V

As it is well known, there are two kinds of nucleation, i.e. instantaneous and progressive, and two kinds of growth, i.e. 2-D and 3-D. The number of nuclei in the instantaneous nucleation mechanism is constant, and they grow from their former

155

positions on the bare substrate surface without the formation of new nuclei. Hence the radii of the nuclei are larger and the surface morphology is rougher. In progressive nucleation, the nuclei not only grow from their former positions on the bare substrate surface but also from new nuclei forming smaller nuclei particles, and the surface morphology is flatter. In 3-D growth, the growth rates of nuclei are essentially equal or comparable in the directions parallel, or perpendicular, to the electrode surface. However, in 2-D growth, the nuclei grow more quickly in the parallel direction than in the perpendicular direction until they impinge on each other [8].

In Figure 7.11, the nucleation and growth curves can be divided into three stages [9-11]. It can be seen that the initial current fell to a value after a very short time (incubation period, first stage) and then increased until it reached a maximum (the second stage) followed by a decrease (the third stage) for 0.8 V, 1.0 V and 1.2 V The first stage is the incubation period, which increased when the polarization potential decreased. The incubation period arises because of monomer oxidation. Then, the oxidized monomers diffuse towards the interface where oligomerization takes place. When the oligomeric high density region is built, the oligomers precipitate upon the electrode surface, and bring about generation of the deposit [9-12]. In general, the incubation process is very rapid, e.g. the incubation time is 0.64 s at 1.2 V The second stage and third stage represent the typical nucleation and growth curves. Comparing the nucleation and growth curves with the theoretical 2-D and 3-D nucleation and growth curves derived by Harrison and Thirsk for nucleation from current-time relations [13], we find that in the second stage, the nucleation and growth curves (curves e, f, g) are consistent with those for instantaneous nucleation with either 2-dimensional or 3-dimensional growth. Therefore the second stage is possibly a combination of instantaneous nucleation and 2-dimensional growth and instantaneous nucleation and 3-dimensional growth models. In the third stage, the nucleation and growth curves lie between those predicted by the instantaneous nucleation and 3-dimensional growth and progressive nucleation and 3-D growth, and is thus possibly a combination of the instantaneous nucleation and 3-dimensional growth and progressive nucleation and 3-D growth processes. Therefore, we propose that the nucleation and growth of polypyrrole on SS316L is divided into three stages. The first stage is the incubation period. The second stage is possibly a

combination of instantaneous nucleation and 2-dimensional growth and instantaneous nucleation and 3-dimensional growth. The third stage is possibly a combination of instantaneous nucleation and 3-dimensional growth and progressive nucleation and 3-D growth. In order to provide further evidence for this posit, optical microscopy and atomic force microscopy were used to observe the nucleation and growth of polypyrrole on the SS316L surface.
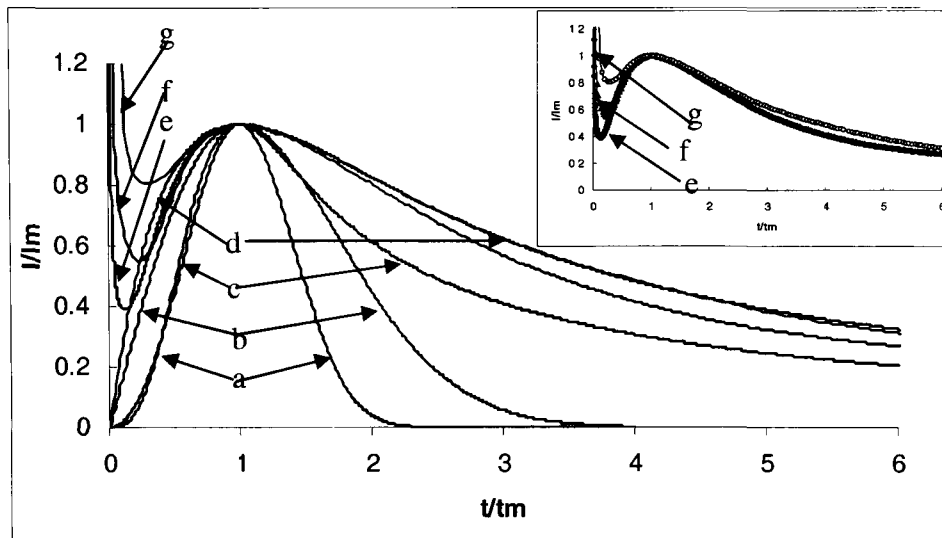
Fig 7.11. Dimensionless plot of current maximum shown in Fig7.10 compared with theoretical curves for 2-D and 3-D instantaneous and progressive model, (a) theoretical 2-D progressive model, (b) theoretical 2-D instantaneous model, (c) theoretical 3-D progressive model, (d) theoretical 3-D instantaneous model, (e) nucleation at 0.8V, (f) nucleation at 1.0V, (g) nucleation at 1.2V

7.2.2 Optical microscopy characterization of polypyrrole

Fig 7.12 presents optical micrographs of polypyrrole coatings produced at different applied potentials. The total coating time was 60 s. We can see that the coating surface is different because of the different oxidation potential. For all coatings produced at the different potentials, the surface of SS316L was completely covered by polypyrrole after 60 s coating time. If we observe these coating surfaces carefully, we can see some

157

polypyrrole particles, which are shown by arrows in Fig 7.12. Also, we can see that the size of the nucleation particles increased with increasing potential.

Fig 7.13 presents optical micrographs of the polypyrrole coatings produced at 1.0 V for different coating times. From Fig 7.13(a), after a 1 s coating time, we can see some small dark spots on the SS316L surface, which are some small polypyrrole particles. Then after a 5 s coating time (Fig 7.13(b)), we can see that the size of these particles increases. A very thin layer of polypyrrole covers the surface of SS316L and the color of the surface became golden. Comparing Figs 7.13(a) and 7.13(b), we find that the number of polypyrrole particles is approximately constant. Therefore, we deduce that it is mainly instantaneous nucleation before 5 s. After a 15 s coating time, there was a marked increase in the amount of polypyrrole and in Fig 7.13(c), we can see some large particles. With further increase in coating time, the particle size continues to increase and the polypyrrole particles become readily visible. Comparing Figs 7.13(c) and 7.13(d), the particles have different sizes, and therefore, we assume that there must have been progressive nucleation.

158
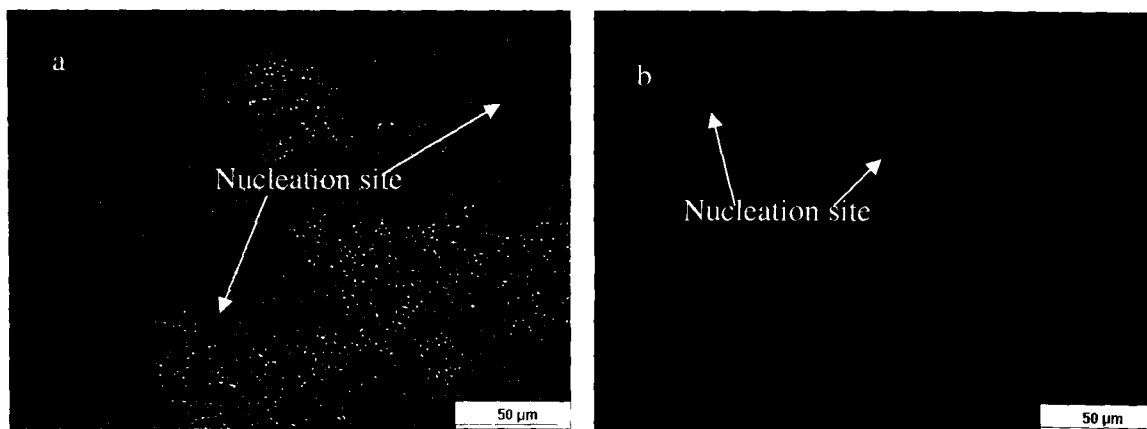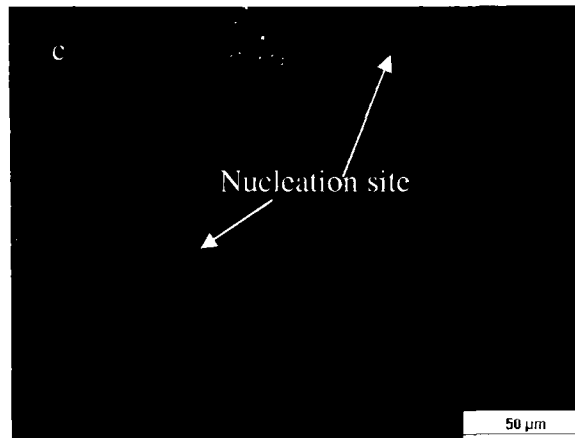
Fig 7.12. Optical microscopy of polypyrrole coatings produced at different applied
potential for a 60s coating time (a) 0.8V, (b) 1.0V, (c) 1.2V
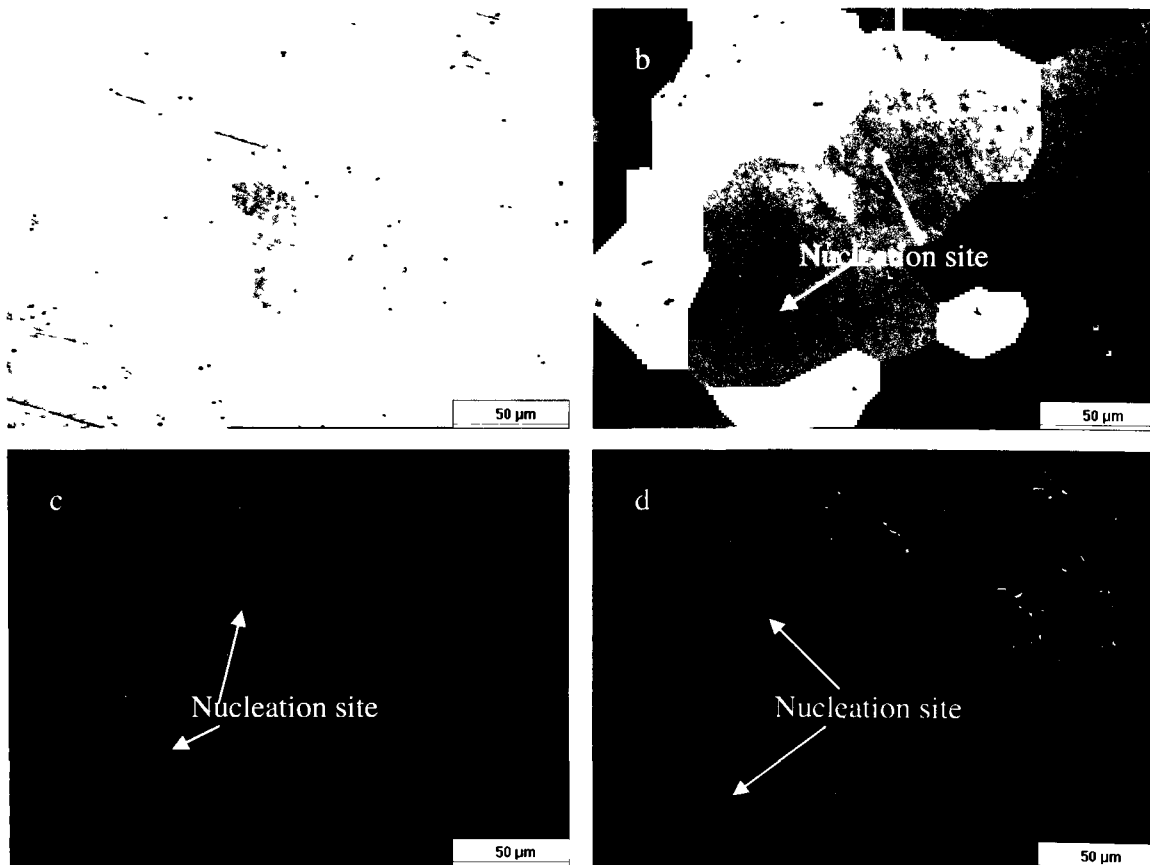
Fig 7.13. Optical microscopy of polypyrrole coatings produced at 1.0V for different
coating times (a) 1s, (b) 5s, (c) 15s, (d) 30s

159

7.2.3 AFM characterization of polypyrrole

Figs 7.14(a), 7.14(b) and 7.14(c) present AFM images of the polypyrrole coatings produced at different applied potentials. After a 60 s coating time, a thin layer of polypyrrole coats the surface of SS316L. We can also see that the shape of the polypyrrole particles is approximately circular and that the size of the polypyrrole particles is increasing with increased potential.

Figs 7.14(d), 7.14(e) and 7.14(f) present AFM images of polypyrrole coatings produced at 1.0 V for different coating times. We did not generate an AFM image of the polypyrrole coating for 1 s coating time because it was difficult to locate the particles with so few polypyrrole particles being present. The height of the surface in the AFM images increases with increasing coating time, for example, the height of the surface (Table 7.3) is 10.9 nm, 19.1 nm, 30.5 nm and 40.4 nm after 1 s, 5 s, 15 s and 60 s coating, respectively. This is an indication of polypyrrole growing in the vertical direction. The height of the surface also increases with increased coating potential, which is consistent with the current density curves. Moreover, we can see that the average diameter of polypyrrole particles increases with increasing coating time in the parallel direction. Therefore, there must have been a 3-dimensional growth process for polypyrrole on a SS316L substrate.

160
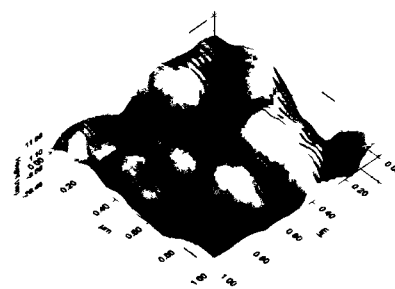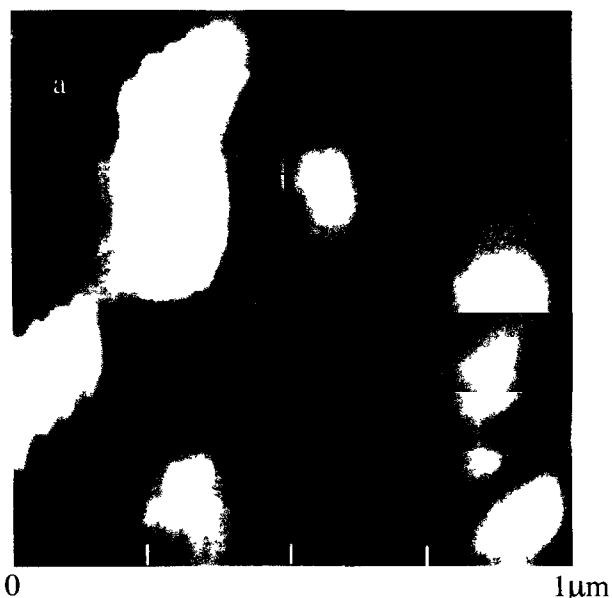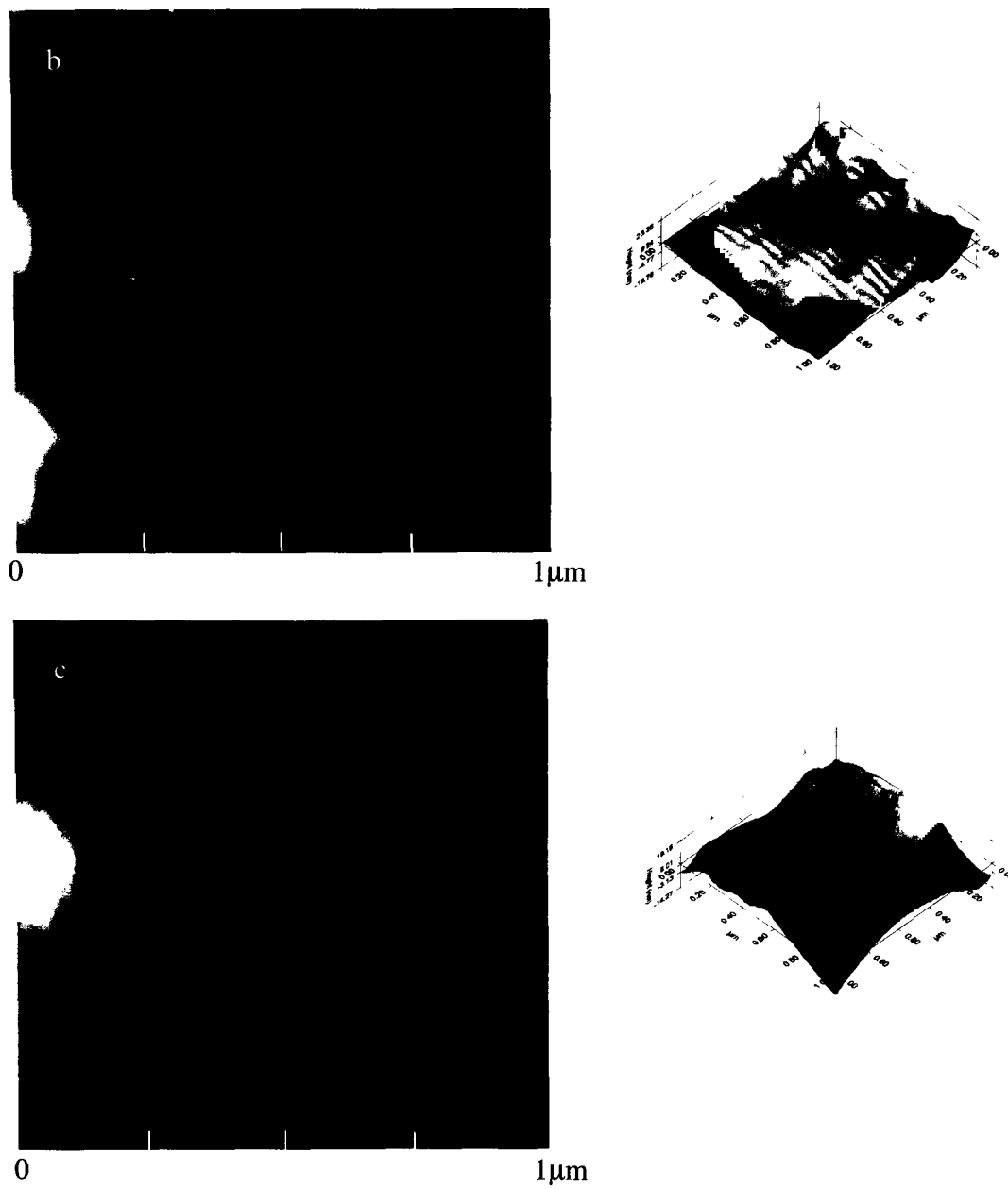
Fig 7.14. AFM images of the polypyrrole coatings on SS316L produced at different applied potentials (a) 0.8V, (b) 1.0V, (c) 1.2V
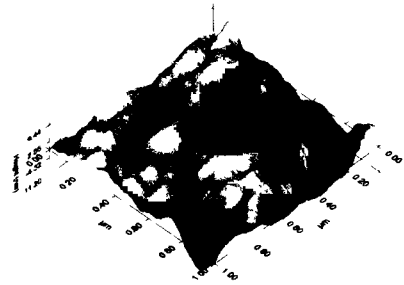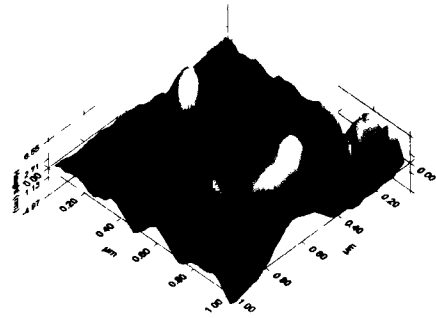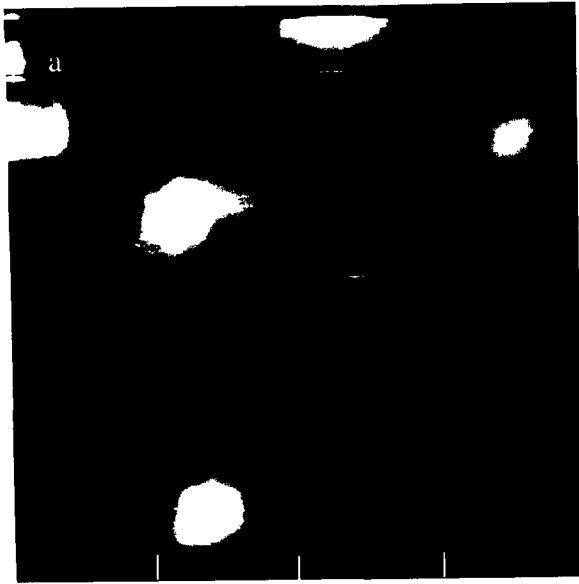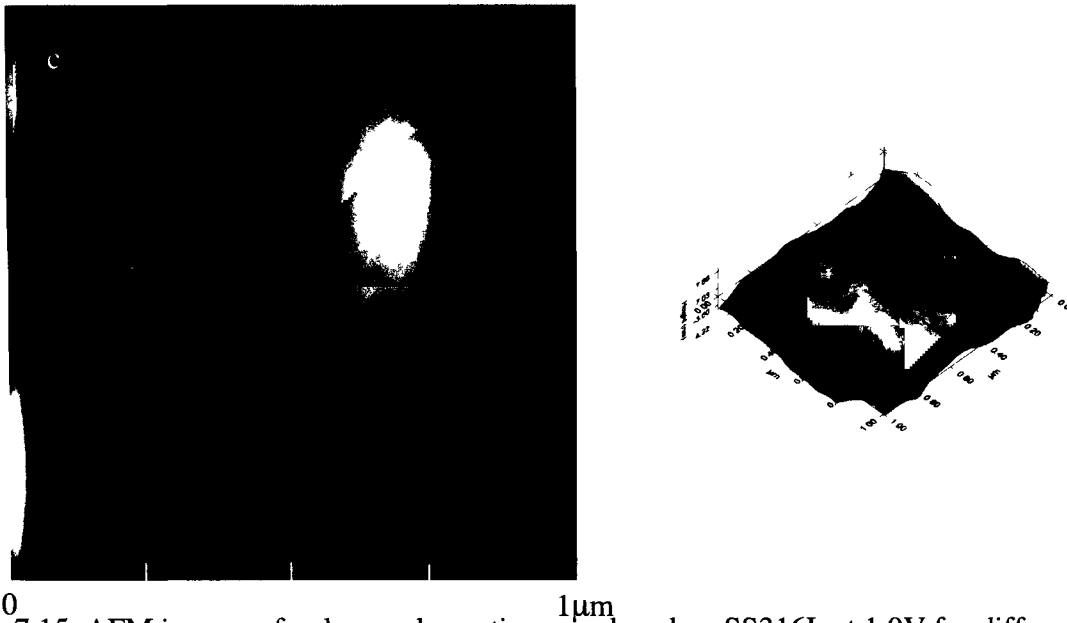
0   1μm
Fig 7.15. AFM images of polypyrrole coatings produced on SS316L at 1.0V for different

coating times (a) 1s, (b) 5s, (c) 15s

Table 7.3 The height of the surface of the polypyrrole coating at different coating times

Coating time (s)	1	5	15	60
Height of the surface (nm)	10.9	19.1	30.5	40.4

Note: X-Y Resolution 0.7nm, Z resolution 0.07nm.

7.3 Optimization of the Polypyrrole-coating Parameters for PEM Fuel Cell Bipolar Plates using the Taguchi Method

A classical optimization method would design experiments that identify all possible combinations for a given set of variables. This approach is called the full factorial design and it takes into account a large number of experiments, which can be costly and time consuming. Taguchi [14] proposed a design of experiment method, which minimizes the number of experiments to a practical level for optimization processes. Taguchi's parameter design has proved to be an effective approach producing high quality products at a relatively low cost.

163

7.3.1 Taguchi design of experiment

The Taguchi method uses a special of orthogonal arrays to study all the designed factors with a minimum of experiments. Orthogonality means that factors can be evaluated independently of one another; the effect of one factor does not interfere with the estimation of the influence of another factor [14]. Four factors (applied current(A), time(B), the concentration of polypyrrole(C), the concentration of H_2SO_4(D)) with three levels were selected as shown in Table 7.4. The factors and levels were used to design a experimental layout using a $L_9(3^4)$ array. The experiments were repeated 3 times in order to ensure reliability. For the applied current, levels of 0.0002A (1), 0.0005A (2), 0.001A (3) were used. For coating time, levels of 10min (1), 30min (2), 60min (3) were used. For the concentration of polypyrrole, levels of 0.05mol/L (1), 0.1mol/L (2), 0.2mol/L (3) were used. For the concentration of H_2SO_4, levels of 0.05mol/L (1), 0.1mol/L (2), 0.2mol/L (3) were used.

Table 7.4. Experimental layout using a L9 orthogonal array

Column number / Experiment number	A(applied current)	B (Time)	C(Concentration of polypyrrole)	D (Concentration of H_2SO_4)
1	1	1	1	1
2	1	2	2	2
3	1	3	3	3
4	2	1	2	3
5	2	2	3	1
6	2	3	1	2
7	3	1	3	2
8	3	2	1	3
9	3	3	2	1

7.3.2 SEM of polypyrrole-coated materials

Figs 7.16(a)-(i) are SEM micrographs of polypyrrole-coated SS316L produced at different process conditions. Two types of polypyrrole structure can be seen. In Figs 7.16(a), (b), (d), (g), the polypyrrole film is quite thin and the polishing marks from the 240 grit polishing of the SS316L are still visible. In Figs 7.16(c), (e), (f), (h), (i), we can see polypyrrole particles, which are between 1~3µm in size. Comparing the particle sizes in the different coatings, it was found that the polypyrrole particle size increased with both increasing coating current and coating time.
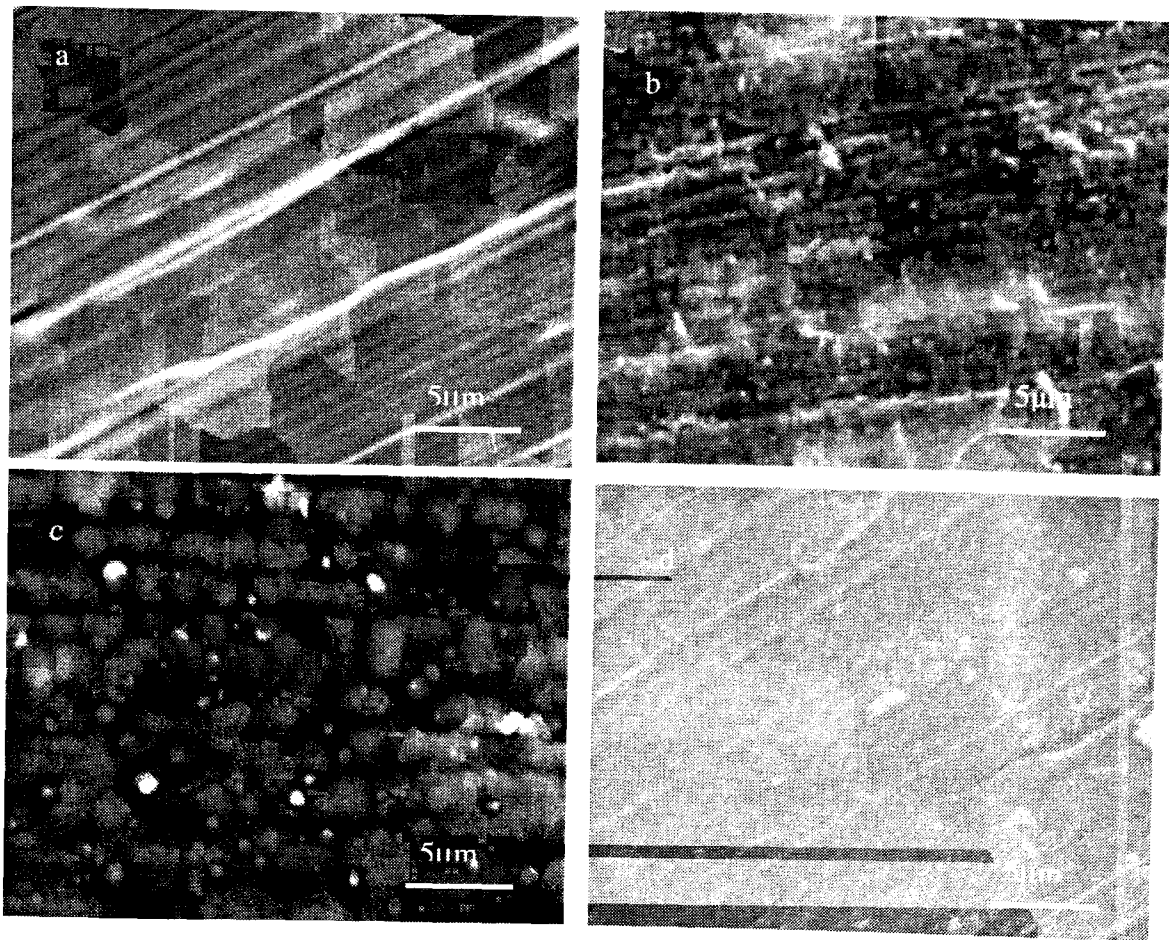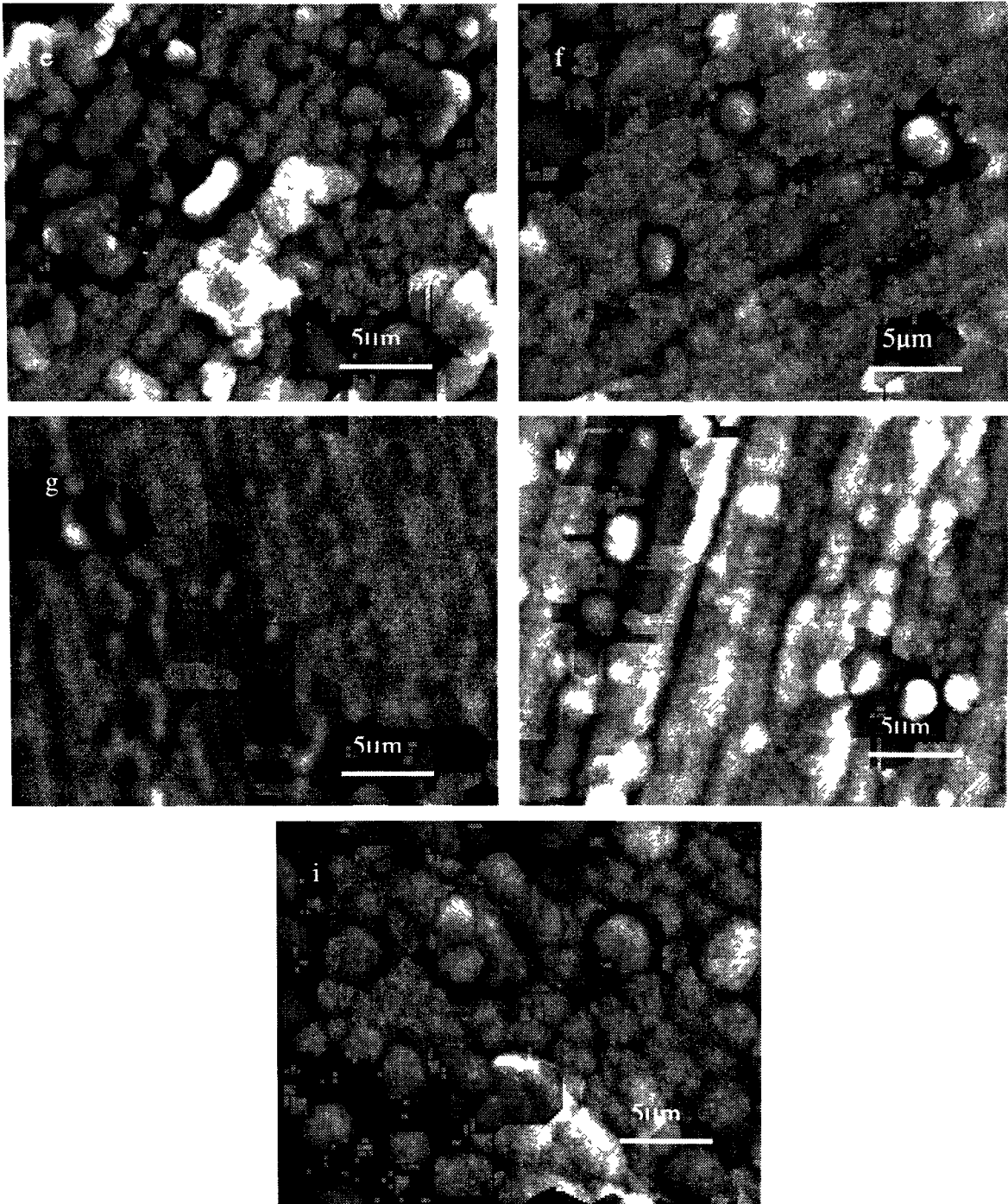
Fig 7.16 SEM micrographs of SS316L coated with polypyrrole: (a) experiment 1, (b) experiment 2, (c) experiment 3, (d) experiment 4, (e) experiment 5, (f) experiment 6, (g) experiment 7. (h) experiment 8, (i) experiment 9 (For process parameters, see Table 7.4)

From cross-sectional micrographs, we determined the thickness of the polypyrrole coating for different coating conditions, and these are given in Table 7.5. We can see that

166

the polypyrrole coatings have different thickness with different coating conditions. The thickness of polypyrrole coatings for coating conditions 1, 2, 4, 7 are relatively thin (less than 30 μm) compared to coating conditions 3, 5, 6, 8, 9 (more than 30 μm). Therefore, in general, the coating thickness increased with increased coating time, coating current and polypyrrole concentration.

Table 7.5. The thickness of polypyrrole coating with different coating conditions

Coating condition	1	2	3	4	5	6	7	8	9
Coating thickness/μm	7±0.5	21±0.5	46±0.5	18±0.5	43±0.5	50±0.5	25±0.5	43±0.5	54±0.5

7.3.3 Corrosion resistance of polypyrrole coatings

The corrosion potential increased and the corrosion current density decreased after coating polypyrrole on SS316L: see Table 7.6. In our earlier studies, the polarization resistance and corrosion current density of uncoated SS316L were found to be 328 Ω•cm^2 and 40 μA/cm^2 at 70°C, respectively, for the same test conditions. From the linear polarization data, the polarization resistance for the thin (less than 30μm) polypyrrole coatings (Figs 7.16(a), (b), (d), (g)) was around 1500 Ω•cm^2, which is about 5 times higher than for the uncoated samples. Also, the polarization resistance of relatively thick (more than 30μm) polypyrrole coating (Figs 7.16(c), (e), (f), (h)) is about 3500 Ω•cm^2, which increased the polarization resistance of SS316L by more than 10 times. The polarization resistance and corrosion current density for uncoated SS316L are about 4200 Ω•cm^2 and 5 μA/cm^2 at 20°C, respectively. Therefore, the polarization resistance and corrosion current density for a relatively thick polypyrrole coated material at high temperature (70°C) are of the same order as those of the uncoated SS316L at ambient temperature (20°C).

Table 7.6. Polarization resistance of polypyrrole-coated SS316L at 70°C

Results \ No.		1	2	3	4	5	6	7	8	9
β_a/V	Test 1	0.128	0.179	0.204	0.173	0.067	0.247	0.322	0.159	0.152
	Test 2	0.163	0.163	0.141	0.259	0.192	0.265	0.137	0.208	0.163
	Test 3	0.185	0.189	0.113	0.192	0.123	0.467	0.178	0.191	0.185
β_c/V	Test 1	0.107	0.050	0.025	0.051	0.027	0.021	0.056	0.018	0.023
	Test 2	0.126	0.058	0.051	0.050	0.025	0.027	0.063	0.017	0.026
	Test 3	0.118	0.049	0.031	0.054	0.027	0.021	0.054	0.018	0.029
E_{corr}/V	Test 1	0.129	0.137	0.145	0.142	0.146	0.154	0.158	0.171	0.233
	Test 2	0.128	0.129	0.147	0.140	0.145	0.160	0.155	0.179	0.215
	Test 3	0.130	0.127	0.142	0.141	0.147	0.168	0.156	0.188	0.222
i_{corr}/(μA cm^{-2})	Test 1	17.91	13.90	2.78	10.85	2.08	2.72	11.88	2.66	2.38
	Test 2	16.93	12.06	2.99	12.53	2.53	2.50	14.72	2.24	2.85
	Test 3	20.64	12.83	2.41	11.35	2.67	2.13	10.05	2.29	2.69
R_p /(Ω·cm^2)	Test 1	1415	1222	3483	1578	4023	3094	1746	2643	3649
	Test 2	1825	1542	5446	1454	3801	4261	1275	3050	3421
	Test 3	1518	1339	4389	1614	3605	4102	1792	3123	4052

7.3.4 Potentiostatic tests with the optimal levels of the polypyrrole coating

Polypyrrole-coated SS316L (condition 5) was chosen for the potentiostatic tests because it had one of the higher corrosion resistances and the coating time required was relatively short (30mins). The total test time for the potentiostatic tests was 10 hours for the simulated anode and cathode conditions. However, the software used could only store 16,800 points (about 4.67h) at 1 point/s speed. Therefore, Fig 7.17 shows only part of the total potentiostatic test curve. Fig 7.17 shows that the corrosion current density is negative in the simulated anode side. However, it is positive in the simulated cathode side. This is because OCP of polypyrrole-coated SS316L is around 0.2Vvs SCE. The

simulated anode and cathode are -0.1Vvs SCE and 0.6Vvs SCE, respectively. Therefore, the potential of the simulated anode is anodic to the potential of polypyrrole-coated SS316L and the potential of the simulated cathode is cathodic to the potential of polypyrrole-coated SS316L. This negative current density can provide cathodic protection for the metallic bipolar plate materials.
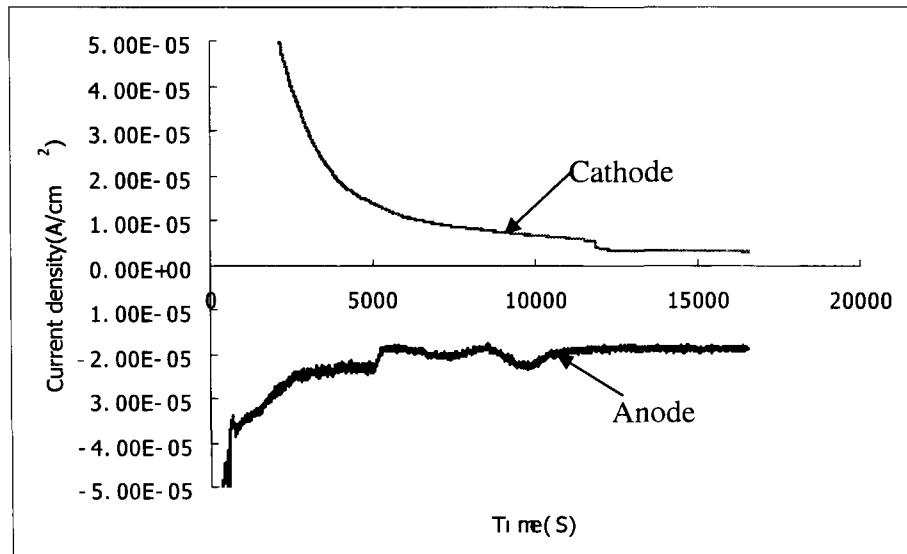
Fig 7.17 Potentiostatic curve for polypyrrole-coated SS316L in the simulated anode and cathode environments

7.3.5 SEM and EDX tests of polypyrrole-coated SS316L after potentiostatic tests

Fig 7.18 presents SEM micrographs and associated EDX spectra of the coatings after potentiostatic testing. The polypyrrole coatings were still intact and covered the whole surface after 10-hour potentiostatic tests in both the simulated anode and cathode environments. In the EDX spectra, the elemental peaks for C, N, O and S are from the polypyrrole, whereas the Fe, Cr, Ni and Si peaks arise from the SS316L base material since the polypyrrole-coating is quite thin.

169
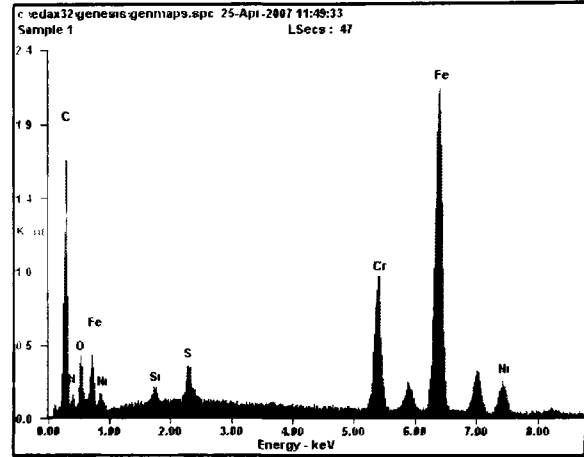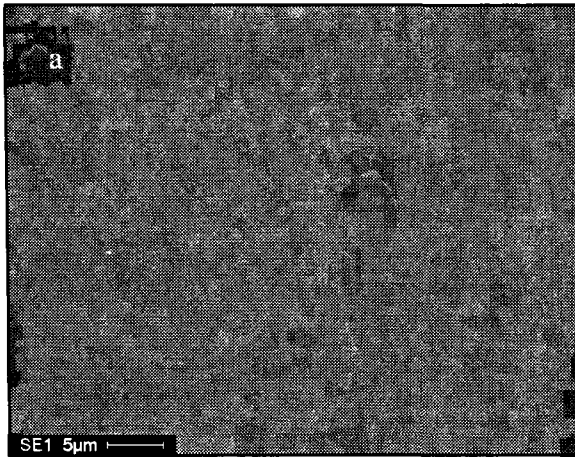
Element	Wt%	At%
CK	47.23	73.15
NK	04.44	05.89
OK	05.36	06.24
SiK	00.30	00.20
SK	00.77	00.44
CrK	07.61	02.72
FeK	29.93	09.97
NiK	04.38	01.39
Matrix	Correction	ZAF
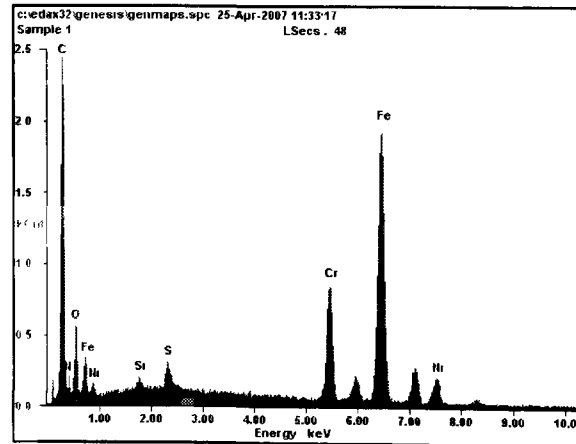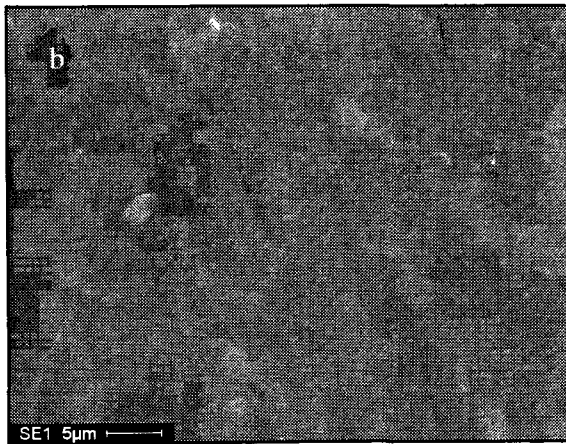
Element	Wt%	At%
CK	41.35	69.91
NK	04.22	06.12
OK	03.98	05.05
SiK	00.42	00.30
SK	01.02	00.65
CrK	08.87	03.46
FeK	35.03	12.74
NiK	05.12	01.77
Matrix	Correction	ZAF

Fig 7.18. SEM and EDX after 10-hour potentiostatic tests in the simulated anode and cathode environments of PEM fuel cells, (a) anode (b) cathode

7.3.6 ICP-OES tests with the optimal levels of the polypyrrole coating

Table 7.7 summarizes the metal ion concentrations in the 10hr potentiostatic tests in the simulated anode and cathode conditions for a PEM fuel cell. Comparing the data in the Table 7.7, we find that metal ion concentration at the cathode is much higher than that at the anode for all the elements analysed for both uncoated and polypyrrole-coated samples. Also, comparing the results of uncoated and polypyrrole-coated SS316L, we find that the metal ion concentration in solution for polypyrrole-coated SS316L is only about half that for the uncoated samples. For example, the Fe ion concentrations for uncoated SS316L are 770.9 or 1245.8 µg/L in the simulated anode and cathode environments, respectively. The Fe ion concentrations for polypyrrole-coated SS316L are 434.7 or 826.6 µg/L in the simulated anode and cathode environments, respectively. Therefore, based on our research results, metal corrosion is more severe in the cathode environment, which is consistent with the potentiostatic test results. The metal ion concentrations measured in the simulated anode conditions seems at odds with the potentiostatic tests because the negative current should provide cathodic protection for SS316L. The reason why we still get a relatively high metal ion concentration at the anode is that the negative protection is only partial and it can not provide full protection for the SS316L.Therefore, SS316L can be corroded in both the anode and cathode environments, and corrosion in the cathode environment is the hot spot.

If the corrosion rate remains the same for the 5000h lifetime of the fuel cell, Fe, Cr, Ni, Mn ion concentrations will reach 375, 64.5, 40.4, 9.1ppm at the anode, and 613, 115, 90.1, 18.2ppm at the cathode after 5000h for uncoated SS316L. Fe, Cr, Ni, Mn metal ion concentrations will reach 147, 29.4, 25.1, 5.1ppm at the anode, and 318, 30.0, 45.6, 8.8ppm at the cathode after 5000h for polypyrrole-coated SS316L. Let us suppose that 5% percent of metal ions remain in solution, and then the total metal concentrations are 24.5 and 41.8ppm at the anode and cathode for uncoated SS316L, respectively, and 10.3ppm at the anode and 20.1ppm at the cathode, respectively, after 5000h for polypyrrole-coated SS316L. Although such levels of metal ion concentration are still too high for satisfactory PEM fuel cell performance for the uncoated SS316L, they are approaching satisfactory levels for the polypyrrole-coated SS316L.

Table 7.7 Metal ion concentrations in solution after potentiostatic tests

Environment	Dissolved metal concentration(μg/L)				Total concentration
	Fe	Cr	Ni	Mn	of metal ions (ug/L)
Base solution	20.71	<IDL	<IDL	1.36	22.07
Uncoated SS316L at anode side	770.90	129.00	80.88	19.58	1000.34
Uncoated SS316L at cathode side	1245.79	230.34	180.27	36.38	1692.78
Coated SS316L at anode side	314.22	58.83	50.17	11.46	434.68
Coated SS316L at cathode side	656.34	60.06	91.26	18.89	826.55

Note: IDL is the identification limit.

7.3.7 Contact resistance tests

Fig 7.19 shows the variation of contact resistance of SS316L and polypyrrole-coated SS316L with compaction pressure. The polypyrrole coating (condition 5) was chosen for the contact resistance tests in order to be consistent with the corrosion tests. Also, we have found that the contact resistance does not change significantly when we change the coating thickness. With increasing compaction pressure from $20N/cm^2$ to $220N/cm^2$, the contact resistance decreased rapidly at low compaction pressures and then decreased gradually, probably due to a decrease in interfacial resistance [15]. Comparing the two curves, we can see that the contact resistance of polypyrrole coated SS316L is lower than that of SS316L from $20N/cm^2$ to $130N/cm^2$, and then contact resistance of polypyrrole-coated SS316L become slightly higher than that of SS316L from $130N/cm^2$ to $220N/cm^2$ The basic finding is that the contact resistance of SS316L is only changed slightly after coating with polypyrrole.
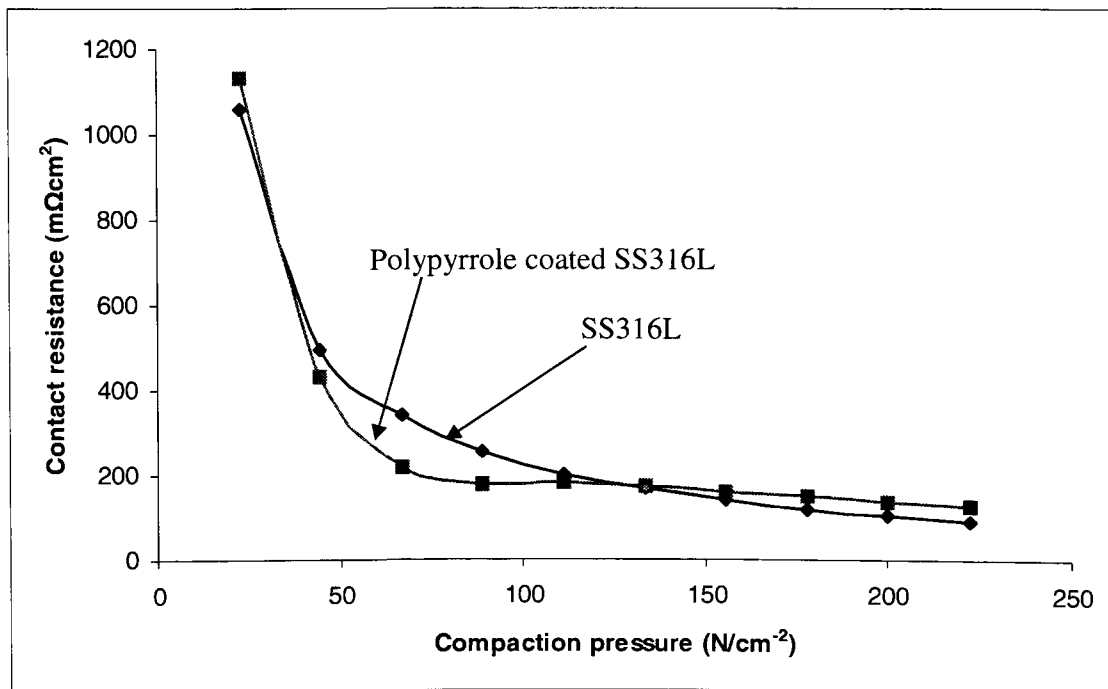
Fig 7.19 Interfacial contact resistances for SS316L and polypyrrole coated SS316L

173

7.4 The effects of a nano gold interlayer on polypyrrole coatings on 316L stainless steel for the bipolar plates of PEM fuel cells

In order to further lower the metal ion concentration in the solution, a nano-thick layer Au was coated on SS316L surface using a Polaron SC502 Sputter Coater and a 15 second coating time. The Au coating was about 10nm thick, and the surface had a somewhat golden color after Au-coating.

7.4.1 Nucleation and growth mechanism of polypyrrole on Au-coated SS316L

Fig 7.20 presents the nucleation and growth curves of polypyrrole on an Au-coated SS316L surface at different applied potentials. At 0.6V, the coating current density is very low for the whole process. Therefore, the coating rate is very low at 0.6V and we could not see any coating on the metal surface. At 0.8V, the coating current density is about $2 \times 10^{-3} A/cm^2$ and only decreases very slightly for the complete coating process. Therefore, the polypyrrole growth rate remains approximately constant. At 1.0V and 1.2V, the coating current gradually decreased to a very small value. The area under the current density-time curve and x-axis was the largest at 0.8V Therefore, there was more polypyrrole coated on the Au-coated SS316L surface at 0.8V This is reasonable considering the nucleation potential is around 0.8V We can not compare the nucleation and growth curves with the theoretical 2-D and 3-D nucleation and growth curves derived by Harrison and Thirsk [13] because there is no peak current density in the nucleation and growth curves of polypyrrole/Au/SS316L. However, for the polypyrrole/SS316L, there was a peak current density at 0.6V, 0.8V, 1.0V and 1.2V (Section 7.2.1). In the nucleation and growth curves for polypyrrole on Au-coated SS316L, we cannot see the overlapping time because there is no peak current density in Fig 7.20. Therefore, the base material affects the nucleation and growth of the polypyrrole coating. After coating with Au, the nucleation and growth characteristics of polypyrrole on Au-coated SS316L are different from those for uncoated SS316L.

174
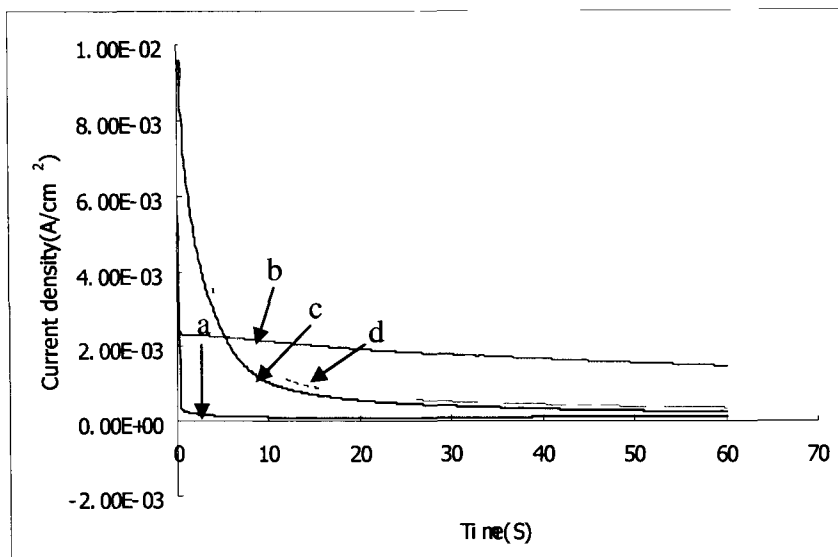
Fig 7.20 Chronoamperometric curves of polypyrrole deposited on Au-coated SS316L at different potentials at ambient temperature, (a) 0.6V, (b) 0.8V, (c) 1.0V, (d) 1.2V

7.4.2 Optical microscopy

Fig 7.21 presents optical micrographs of the polypyrrole coatings produced on an Au-coated SS316L surface at different applied potentials. These micrographs were taken at the same brightness level so that the micrographs reflect any color differences. [At 0.6V because of the very small amount of polypyrrole, the brightness had to be reduced compared to 0.8V, 1.0V and 1.2V.] In Fig 7.21(a), we can only see the grinding marks on the surface. In Fig 7.21(b), there are some "worm-like" polypyrrole particles beside the grinding marks. In Figs 7.21(c) and (d), we can see that the polypyrrole particles have a globular shape. Comparing Figs 7.21(b),(c) and (d), we can see that the color of Fig 7.21(b) is totally different from that for Figs 7.21(c) and (d). Therefore, at the different coating potentials, the coating morphology is different. The color and morphology of the polypyrrole coatings produced at 1.0V and 1.2V are similar, which is consistent with the chronoamperometric curves.

175
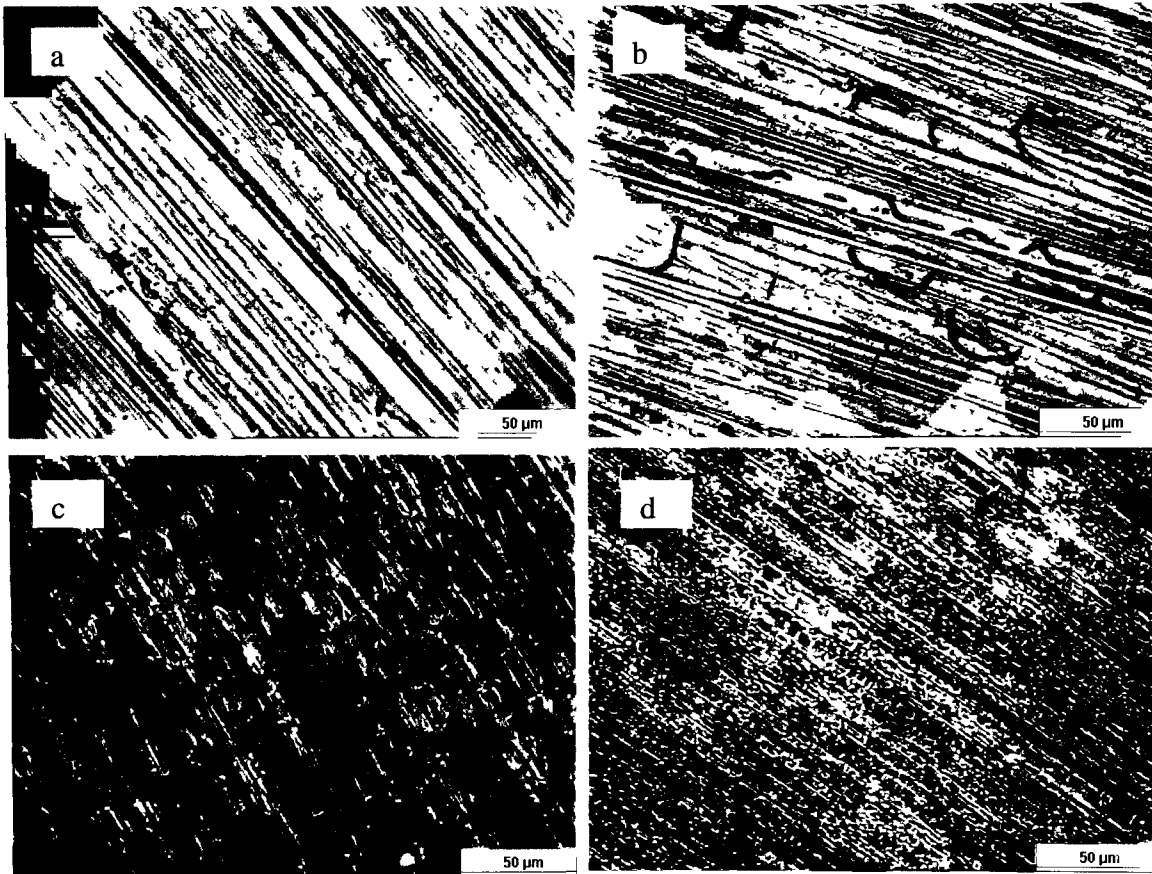
Fig 7.21. Optical microscopy of polypyrrole coatings at different coating potentials for a
60s coating time, (a) 0.6V, (b) 0.8V, (c) 1.0V, (d) 1.2V

7.4.3 Potentiodynamic tests

Potentiodynamic tests were done to investigate the corrosion resistance of the polypyrrole/Au/SS316L. Fig 7.22 presents the potentiodynamic curve of polypyrrole/Au/SS316L. From the linear polarization results, we determined that the polarization resistance and corrosion current density were $1850\Omega\bullet cm^2$, $5.46\mu A/cm^2$, respectively.

We had determined that the polarization resistance and corrosion current density of uncoated SS316L were 328 $\Omega\bullet cm^2$ and 40 $\mu A/cm^2$ before, respectively. Therefore, after coating SS316L with Au and polypyrrole, the polarization resistance is increased about 6 times and the corrosion current density is decreased about 7 times. Also. the corrosion potential of uncoated SS316L was about –0.25V vs SCE, whereas the corrosion potential of SS316L after Au and polypyrrole coating was about 0.1V vs SCE. The corrosion

potential is thus anodically shiftly, which therefore retards the corrosion of the base material. However, there was no passivation area after coating with Au and polypyrrole.
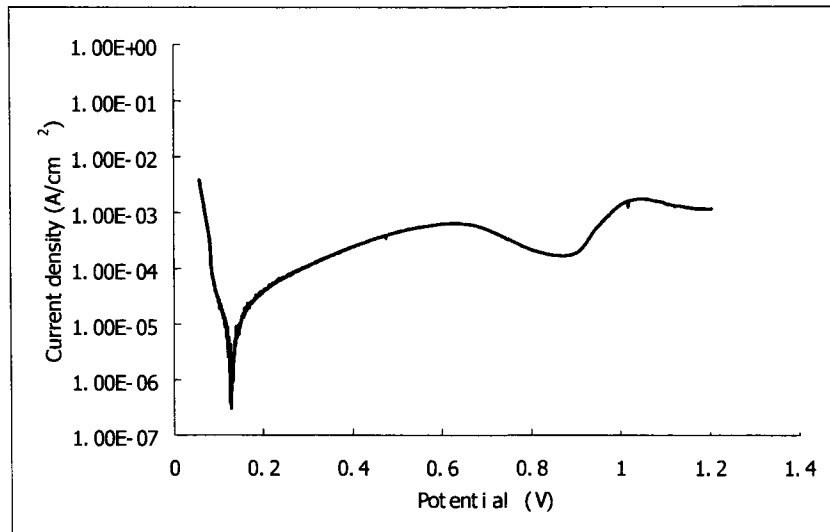
Fig 7.22 Potentiodynamic curve for polypyrrole coating on Au-coated SS316L at 70°C

7.4.4 Potentiostatic tests

Fig 7.23 presents the potentiostatic tests for the Au and polypyrrole coated SS316L in the simulated anode and cathode conditions. In the simulated anode conditions, the current density is quickly reduced to a negative value, then gradually increased to where the current density stabilized at about $-2 \times 10^{-5} A/cm^2$ The stable current density is negative because H^+ changes to H_2. This negative current density can provide either partial or complete protection for the metal at the anode. In the simulated cathode conditions, the current density was gradually reduced to a value of about $6 \sim 7 \times 10^{-6} A/cm^2$ Therefore, the corrosion is much more severe in the cathode environment than that in the anode environment.
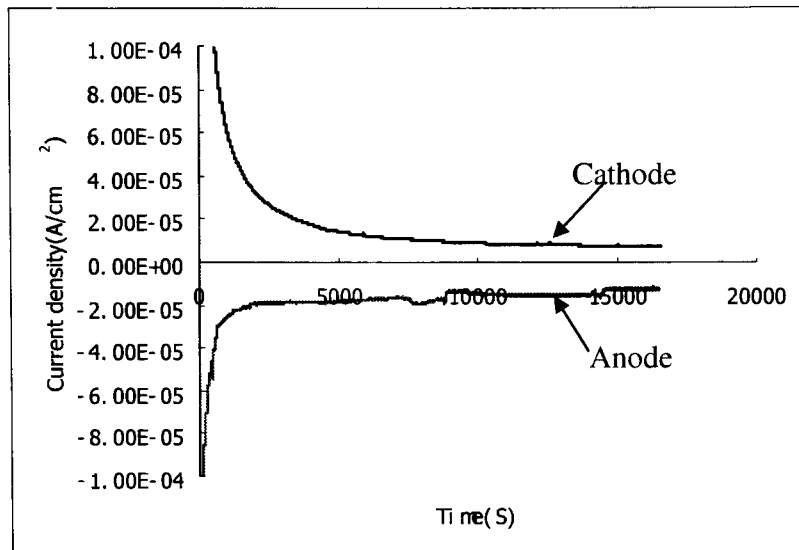
Fig 7.23 Potentiostatic curve for polypyrrole coating on Au-coated SS316L in the simulated anode and cathode environments for PEM fuel cells

7.4.5 SEM with EDX after 10 hours potentiostatic tests

Fig 7.24 presents secondary electron images of the polypyrrole coatings on Au-coated SS316L after the 10 hours potentiostatic tests. We can readily see the particle shape of the polypyrrole.. After 10 hours potentiostatic testing in the simulated anode and cathode environments, the polypyrrole coating still completely covered the metal surface. Comparing Fig 7.24(a) and 7.24(b), we cannot see any significant differences after 10 hours potentiostatic testing in either the simulated anode or cathode environments. However, we have established that corrosion is more severe in the simulated cathode environment: these differences are not readily apparent in the SEM micrographs.

Fig 7.25 presents the back-scattered electron images and EDX results for polypyrrole coatings in the simulated anode side. Figs 7.25(a) and 7.25(b) are the elemental analyses for one point and Fig7.25(c) is the elemental analyses for the total area. From the elemental analyses, we can see the polypyrrole coating (C, N), the Au coating (Au) and the SS316L (Fe, Ni, Cr, Mn, Mo, Si). There are two possible sources of the oxygen (O) peak, one is because of the oxidation of SS316L, and the other is oxidation of the polypyrrole. Therefore, the electrons for the EDX analyses penetrate through the polypyrrole and Au coatings into SS316L. Comparing elemental analyses in Fig 7.25, we can see that some very small differences from point to point. Fig7.26 present the back-

178

scattered electron images and EDX results for the polypyrrole coatings in the simulated cathode side. Comparison of Figs7.25 and 7.26, shows little, or no, differences in elemental analyses.
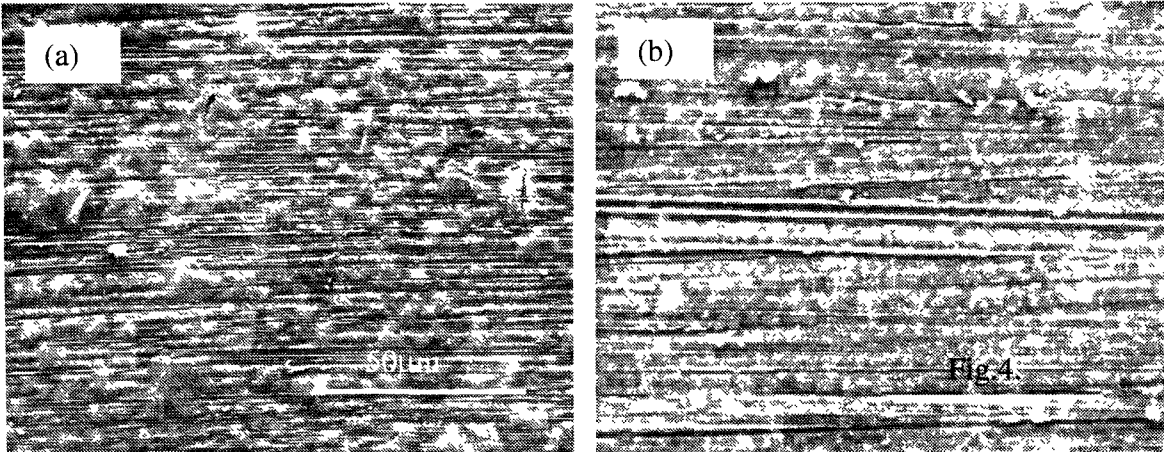
Fig 7.24 SEM results after 10 hours potentiostatic tests, (a) at –0.1V vs SCE purged with H₂, (b) at 0.6V vs SCE purged with O₂ (Secondary electron microscopy)
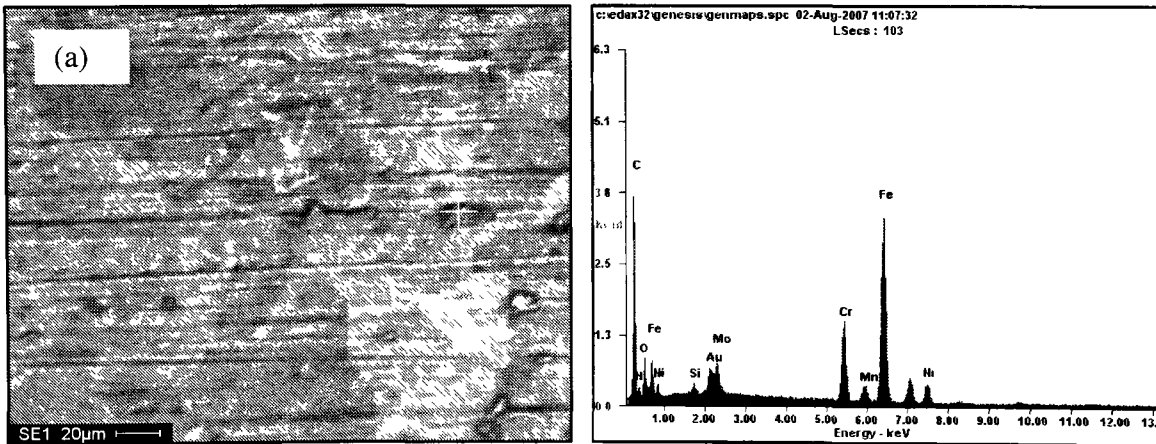
Element	Wt%	At%
CK	42.18	71.58
NK	03.68	05.36
OK	04.81	06.13
SiK	00.32	00.23
AuM	03.38	00.35
MoL	02.83	00.60
CrK	07.73	03.03
MnK	01.02	00.38
FeK	29.44	10.74
NiK	04.62	01.60
Matrix	Correction	ZAF
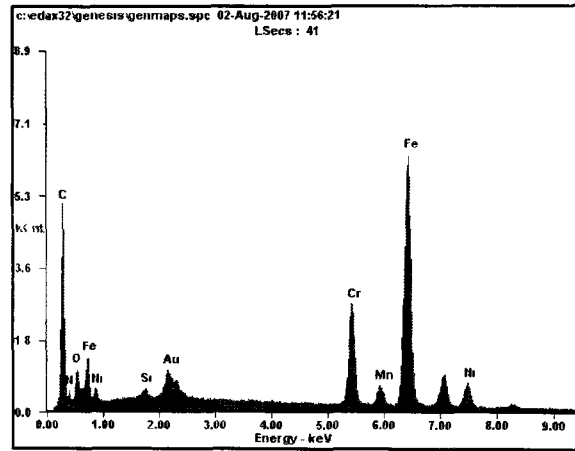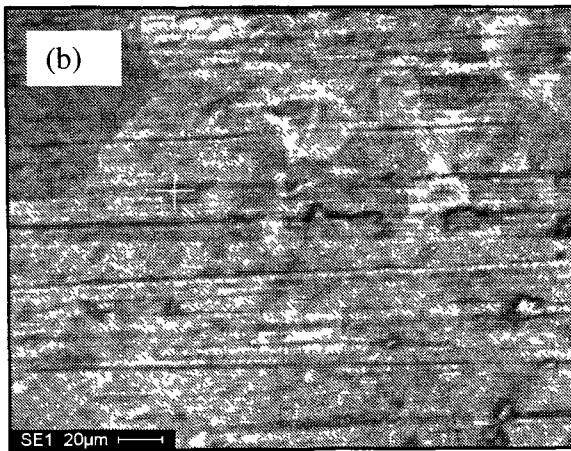
Element	Wt%	At%
CK	39.35	68.98
NK	04.35	06.53
OK	03.96	05.22
SiK	00.32	00.24
AuM	02.70	00.29
CrK	08.72	03.53
MnK	00.97	00.37
FeK	34.46	12.99
NiK	05.17	01.86
Matrix	Correction	ZAF
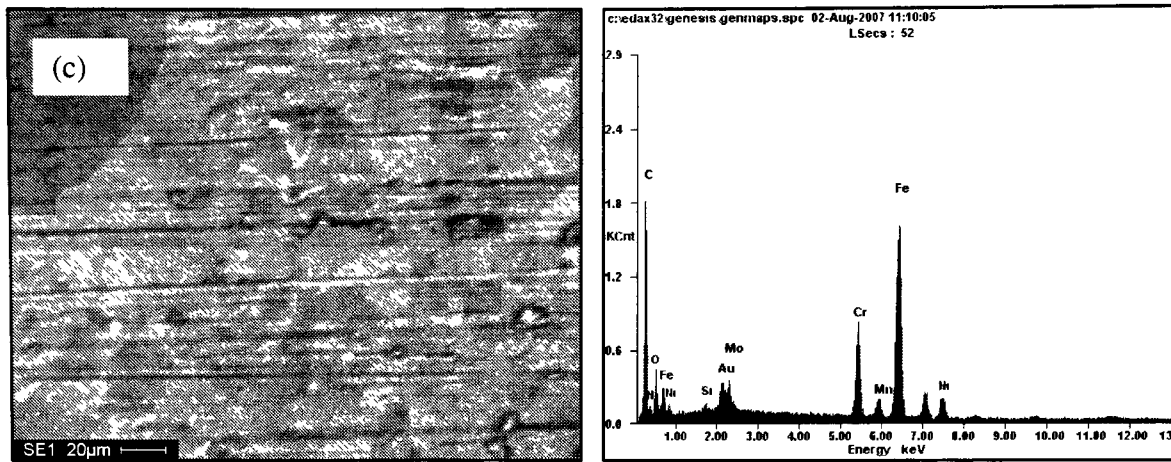
Element	Wt%	At%
CK	41.46	70.97
NK	03.46	05.08
OK	05.18	06.65
SiK	00.30	00.22
AuM	03.65	00.38
MoL	02.30	00.49
CrK	07.97	03.15
MnK	00.98	00.37
FeK	29.92	11.01
NiK	04.78	01.67
Matrix	Correction	ZAF

Fig 7.25 SEM with EDX results after 10 hours potentiostatic tests at –0.1V vs SCE purged with H_2 i.e anode, (a) and (b) element analyses for one point, (c) element analyses for the whole area (Back-scattered microscopy)

(a)
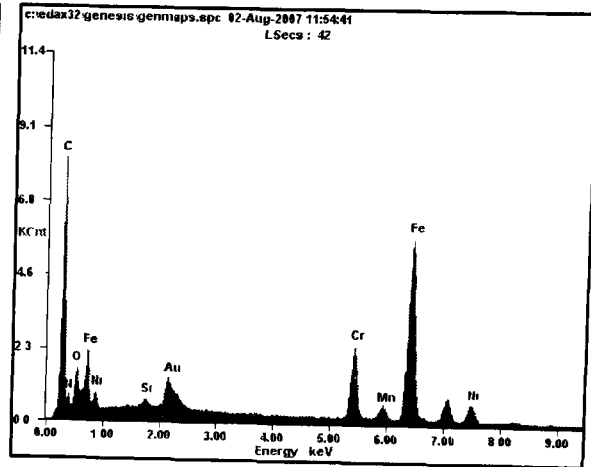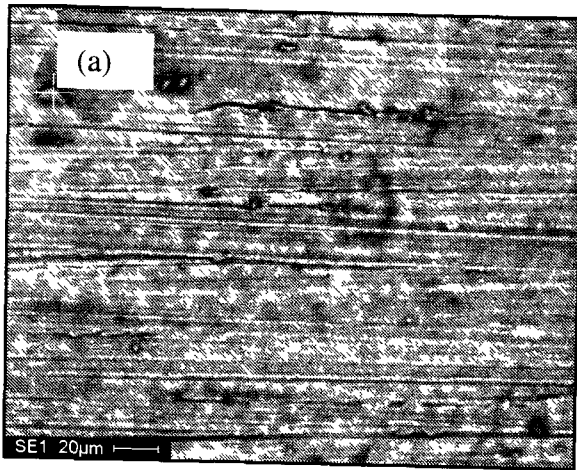
Element	Wt%	At%
CK	45.64	71.15
NK	06.48	08.67
OK	05.78	06.76
SiK	00.27	00.18
AuM	03.71	00.35
CrK	06.79	02.45
MnK	00.76	00.26
FeK	26.44	08.87
NiK	04.12	01.32
Matrix	Correction	ZAF
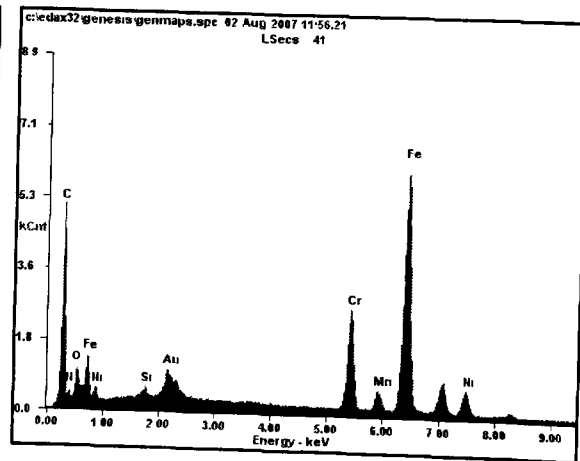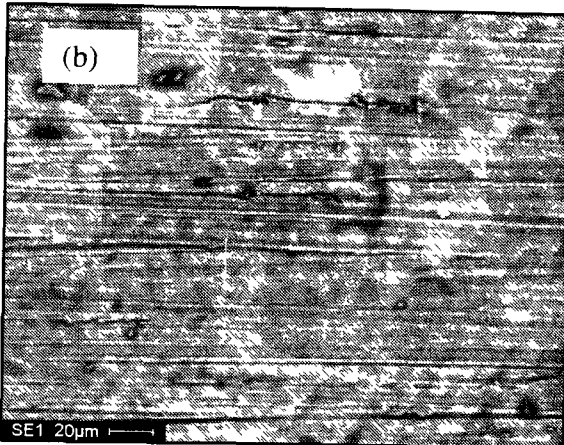
(b)

Element	Wt%	At%
CK	39.35	68.98
NK	04.35	06.53
OK	03.96	05.22
SiK	00.32	00.24
AuM	02.70	00.29
CrK	08.72	03.53
MnK	00.97	00.37
FeK	34.46	12.99
NiK	05.17	01.86
Matrix	Correction	ZAF
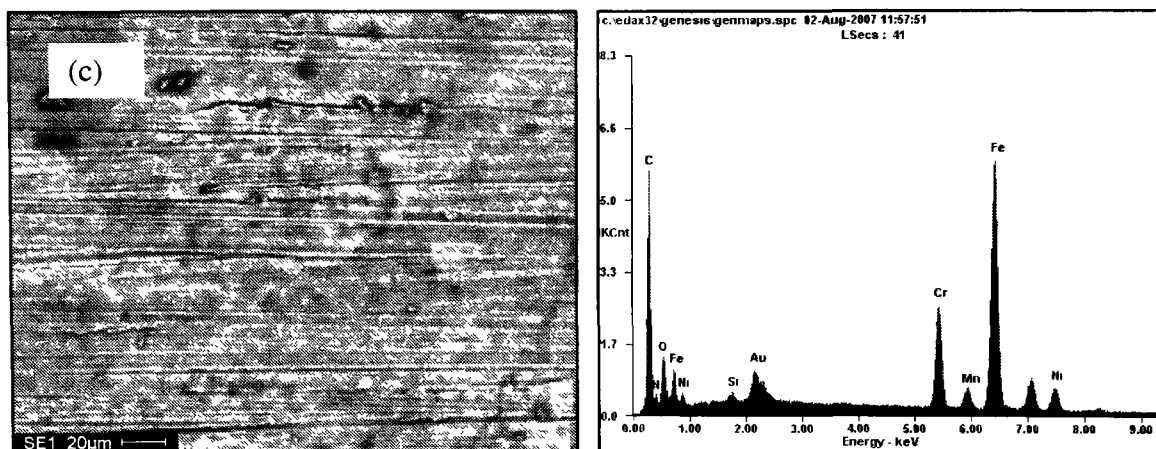
Element	Wt%	At%
CK	40.93	69.89
NK	03.89	05.70
OK	05.29	06.78
SiK	00.26	00.19
AuM	03.52	00.37
CrK	08.29	03.27
MnK	01.04	00.39
FeK	31.98	11.74
NiK	04.80	01.68
Matrix	Correction	ZAF

Fig 7.26 SEM with EDX results after 10 hours potentiostatic tests at 0.6V vs SCE purged with O_2 i.e cathode, (a) and (b) element analyses for one point, (c) element analyses for the whole area (Back scattered microscopy)

7.4.6 ICP-MS

Table 7.8 shows us the metal ion concentration in solution values for the simulated anode and cathode conditions. Comparing the data in the Table 7.8, we find that the metal ion concentrations are similar at the cathode and anode. If, indeed, metal ion concentrations over 10ppm can adversely affect membrane performance, then metal ion concentration build-up must not exceed 1ppm/500h. Suppose that 5% percent of metal ions stay in solution, and then after 5000 hours the total metal concentration in solution would be 10ppm at the anode and 11.5ppm at the cathode after 5000h for polypyrrole/Au/SS316L. Therefore, the Au/polypyrrole coated material has met the target of 10ppm after 5000 hours of fuel cell operation.

Table 7.8 Metal ion concentration in solution after potentiostatic tests for 10 hours

Environment	Dissolved metal ion concentration (ppm)				Total concentration of metal ions (ppm)
	Fe	Cr	Ni	Mn	
Polypyrrole and Au coated SS316L at cathode side	0.36	0.05	0.04	0.01	0.46
Polypyrrole and Au coated SS316L at anode side	0.32	0.05	0.02	0.01	0.4

7.5 Summary

Polypyrrole films have been electro-polymerized on SS316L and Au-coated SS316L surface. Nucleation and growth mechanism have been studied based on the theoretical nucleation and growth curves. A Taguchi DOE method has been used to optimize the polypyrrole-coating parameters for SS316L for metallic bipolar plate application. The detailed corrosion parameters for the base SS316L, polypyrrole coated SS316L, and polypyrrole/Au coated SS316L are summarized in Table 7.9.

Table 7.9 Corrosion parameters for the base SS316L, polypyrrole coated SS316L and polypyrrle/Au coated SS316L at 70°C

	SS316L	Polypyrrole coated SS316L	Polypyrrole and Au coated SS316L
Polarization resistance $R_p/(\Omega \cdot cm^2)$	328	3459	1850
Polarization current density $i_{corr}/(\mu A/cm^2)$	40.01	2.38	5.46
Corrosion current density at the anode (A/cm^2)	-1×10^{-5}	$1 \sim -2 \times 10^{-5}$	-2×10^{-5}
Corrosion current density at the cathode ($\mu A/cm^2$)	8×10^{-6}	1×10^{-5}	$6 \sim 7 \times 10^{-6}$
Metal ions at anode (ppm) after 5000hours	24.5	10.3	10
Metal ions at cathode (ppm) after 5000 hours	41.8	20.1	11.5

References

1. D.Kumar and R.C.Sharma, Advances in conductive polymers. Eur.Polym.J, 34(1998)1053-1060.

2. N.Cunningham, D.Guay, J.P.Dodelet, Y.Meng, A.R.Hill, and A.S.Hay, New materials and procedures to protect metallic PEM fuel cell bipolar plates. J.Electrochem. Soc., 149(7)(2002)A905-A911.

3. K.Shah, Y.Zhu, J.O.Iroh, and O.Popoola, Corrosion protection properties of polyaniline- polypyrrole composite coatings on Al 2024. Surf Eng., 17(5)(2001)405-412.

4. G.S.Akundy, J.O.Iroh, Polypyrrole coatings on aluminum- synthesis and characterization. Polymer, 42(2001)9665-9669.

5. S.Joseph, J.C.McClure, R.Chianelli, P.Pich, P.J.Sebastian, Conducting polymer-coated stainless steel bipolar plates for proton exchange membrane fuel cells (PEMFC). Int.J.Hydrogen Energy, 30(2005)1339-1344.

6. M.A.Lucio García, M.A. Smit, Study of electrodeposited polypyrrole coatings for the corrosion protection of stainless steel bipolar plates for the PEM fuel cell. J.Power Sources, 158(2006)397-402.

7 D.P.Schweinsberg, H.J.Flitt, Some practical considerations relevant to the recording of corrosion data, Corrosion & Prevention 2005, Paper 047, PP1-13, Australian Corrosion Association, ISSN 1442-0139 (2005).

8. B.J.Hwang, R.Santhanam, Y.L.Lin, Nucleation and growth mechanism of electroformation of polypyrrole on a heat-treated gold/highly oriented pyrolytic graphite. Electrochimica Acta, 46(2001)2843-2853.

9. S.Y.Abé, L.Ugalde, M.A del Valle, Y.Trégouët, and J.C.Bernède, Nucleation and growth mechanism of polycarbazole deposited by electrochemistry. J.Braz.Chem.Soc., 118(2007)601-606.

10. R.Schrebler, P.Grez, P.Cury, C.Veas, M.Merino, H.Gómez, R.Córdova, M.A.del Valle, Nucleation and growth mechanisms of poly(thiophene) Part 1. Effect of electrolyte and monomer concentration in dichloromethane. J.Electroanal.Chem. 430(1997)77-90.

11. M.A.del Valle, L.Ugalde, F.del Pino, F.R.Díaz and J.C.Bernède, Solvent effect on the nucleation and growth mechanisms of poly(thiophene). Electrochim. Acta 48(2002)397-405.

12. M.A.del Valle, F.R.Díaz, M.E.Bodini, G.Alfonso, G.M.Soto, E.Borrego, Electrosynthesis and characterization of o-phenylenediamine oligomers. Polym. Int. 54(2005)526-532.

13. J.A.Harrison, H.R.Thirsk, in: A.J.Bard (Ed.), Electroanalytical Chemistry, vol.5, Marcel Dekker, New York, 1971, PP67.

14. P.J.Ross, "Taguchi Techniques for Quality Engineering", McGraw-Hill International Editions, USA, 1988.

15. E.A.Cho, U.S.Jeon, S.A.Hong, I.H.Oh, S.G.Kang, Performance of a 1 kW-class PEMFC stack using TiN-coated 316 stainless steel bipolar plates. J.Power Sources, 142(2005)177-183.

CHAPTER 8

CONCLUSIONS FROM THIS DISSERTATION

Six alloys, including SS316L, SS347, SS410, A36 steel, Al6061 and Grade 2 Ti were studied as the potential bipolar plate materials. The corrosion mechanism of metallic bipolar plates was investigated by electrochemical methods and promising metallic bipolar plate materials are proposed. A TiN coating was then applied using a PVD method on SS316L and SS410, and polypyrrole coating was applied using an electrochemical method on SS316L in order to increase the corrosion resistance. The main conclusions from this study were as follows.

1. The six different alloys investigated show different levels of corrosion resistance in the PEM fuel cell environments. SS316L, SS347 and Grade 2 Ti had better corrosion resistance than SS410, Al6061 and A36 steel. In general, the corrosion current increased when the temperature was increased. The corrosion current density was higher in the simulated cathode environment than that in the simulated anode environment for all materials except SS410. The corrosion current densities for SS316L, SS347 and Grade 2 Ti at the anode and cathode are almost the same, but they are positive for the cathode side and negative for the anode side. The positive current is because of the metal corrosion, and the negative current arises because the reaction $2H^+ + 2e^- \rightarrow H_2$ can take place on the metal electrode and the reaction $2H_2O \rightarrow 4H^+ + O_2 + 4e^-$ takes place on the platinum electrode. The negative current provides partial cathodic protection for the metal. The differences between the anodic current density and the cathodic current density for SS410, Al6061 and A36 steel are quite large. The cathodic corrosion current density is several orders of magnitude higher than the anodic corrosion current density for both Al6061 and the A36 steel because the polarization potential is increased at the cathode. However, the anodic corrosion current density is much higher than the cathodic corrosion current density for SS410 because SS410 can passivate at the cathode.

2. From the corrosion criteria, SS316L, SS347 and Ti are much better bipolar plate candidate materials than SS410, Al6061 and A36 steel. From an interfacial contact resistance standpoint, Al6061 is the best material. The interfacial contact resistances of SS316L, SS347. SS410 and Ti are slightly higher than for Al 6061. A36 steel has the highest contact resistance. Therefore, based on the corrosion and interfacial contact resistance results, SS316L, SS347 and Ti are the most promising bipolar plate materials of the 6 materials investigated. Ti is more expensive compared to stainless steel. SS347 has similar structure and composition to SS316L, but is more expensive. Therefore, SS316L was chosen as the candidate bipolar plate material for further investigation.

3. With a corrosion current of about 10^{-5}A/cm^2, metal ion concentrations in solution will be 60ppm for Fe^{2+}, 18.5ppm for Al^{3+} and 50ppm for Ti^{2+} after 5000h. These metal ion concentrations are much larger than the 10ppm maximum specified. If these metals are used as un-coated metallic bipolar plates, the concentration of metal ions in solution will reach 10ppm after less than 5000h and the membrane and the fuel cell performance will begin to degrade. Therefore, these metals must be coated with other materials such as nitrides, carbides or conductive polymers in order to be used as bipolar plates.

4. Potential-PH diagrams can be used to predict the corrosion behaviour of the metallic bipolar plates under PEMFC working conditions. The results of both the potentiostatic testing and SEM metallography are consistent with the predictions from the potential-PH diagrams. Al alloy 6061 corrodes at both the anode and cathode in a PEMFC working environment and the corrosion product is Al^{3+} A36 steel (Fe) corrodes at the anode and cathode in a PEMFC working environment and the corrosion product is Fe^{2+} at the anode and Fe^{3+} at the cathode. Grade 2 Ti is oxidized at both the anode and cathode and the oxidation product is TiO$_2$, which is harmful to the PEM fuel cell performance because it will increase the contact resistance. Although potential-PH diagrams predict the stable phases for given values of potential and PH in simulated PEMFC conditions, they give no information on the rates of any corrosion reactions.

5. The OCP of SS316L is higher in an O$_2$-containing environment than in a H$_2$-containing environment because e_{O_2/H_2O} is higher than e_{H^+/H_2} Potentiodynamic tests produced intergranular and pitting corrosion in SS316L in both the O$_2$-containing and H$_2$-containing environments. The corrosion resistance of SS316L in the O$_2$-containing

189

environment is about 4 times higher than that in the H_2-containing environment. In 'real' PEM fuel cell conditions, the anode and cathode are at corrosion potentials which are different from the open circuit corrosion. In the simulated anode environment, the cathodic protection (from a negative current) can provide partial protection for SS316L and less corrosion is observed by optical microscopy and SEM than in the cathode environment. Based on the ICP-OES results, we find that metal ion concentrations would be about 25 and 42ppm at the anode and cathode, respectively, after 5000-hour potentiostatic tests. Such levels of metal ion concentration would adversely affect membrane performance.

6. TiN was successfully coated on SS316L and the coatings were about 15μm thick. The TiN-coating increased the polarization resistance by a factor of 30 and reduced the corrosion current density by a factor of 40. EIS showed that the electrochemical impedance of TiN-coated SS316L was considerably higher than for uncoated SS316L, which is consistent with the polarization resistance measurements from the potentiodynamic tests. In the simulated anode environment, the corrosion current density of TiN-coated SS316L immediately becomes negative, which would provide cathodic protection to the metallic bipolar plates. In the simulated cathode environment, the TiN-coating increased the measured corrosion current density because of the presence of pitting corrosion. Therefore, the cathode side will have corrosion problems if TiN-coated SS316L is used for the bipolar plates of PEM fuel cells. Improved TiN coatings, which do not contain defects such as pinholes, are required if TiN-coated SS316L is to be used to fabricate bipolar plates, particularly for use in the cathode environment.

7. Polypyrrole films have been electro-polymerized on SS316L using both galvanostatic and cyclic voltammometric methods. Comparing the polypyrrole coatings formed using the two different electrochemical methods, the morphologies are quite different. For galvanostatic coatings, the particle size increases with increasing applied current. For cyclic voltammometric coatings, the particle size increases with increasing cycle number. For a low current and low cycle number coating, the polishing marks can still be seen on the SS316L substrate. The potentiodynamic tests show that the corrosion potential is increased from -0.27 to 0.171V and the corrosion current density is decreased from 40.01 to 2.38 μA/cm^2 and polarization resistance is increased from 328 to 3459

$\Omega\cdot cm^2$ by coating with polypyrrole. Optical microscopy showed that there is less intergranular corrosion after coating with polypyrrole. However, in the simulated cathode environments of a PEMFC, we did not see a reduction in corrosion current because polypyrrole can be oxidized at 0.6V In the simulated anode environments of a PEMFC, the current density immediately becomes negative at -0.1V This is because the corrosion potential is increased after polypyrrole coating. A negative current can provide cathodic protection for the SS316L substrate.

8. Polypyrrole was coated on a SS316L surface using a potentiostatic method in a 0.02M sulphuric acid and 0.02M pyrrole solution. Different surface appearances were formed at different coating potentials. The peak current time and the width of the peak current density decreased at higher potentials because of severe oxidation of the polypyrrole. The nucleation and growth of polypyrrole can be divided into three stages. The first stage is the incubation period. The second stage is a combination of instantaneous nucleation with 2-D (IN2D) or 3-D growth (IN3D). The third stage is a combination of instantaneous nucleation or progressive nucleation and 3-D growth (IN3D and PN3D). Optical microscopy and AFM examination supported some hypothesis of nucleation and growth.

9. A Taguchi DOE method was used to optimize the polypyrrole-coating parameters for SS316L for metallic bipolar plate application. The potentiodynamic and SEM test results have shown that the relatively thick polypyrrole coatings can provide good corrosion resistance, with corrosion rates being decreased about 10 times relative to the uncoated samples. In the simulated anode conditions of a PEM fuel cell, the corrosion current for polypyrrole-coated SS316L is negative, which can provide partial protection for the metal. In the simulated cathode conditions of a PEM fuel cell, the corrosion current is positive. Therefore, the corrosion was more severe at the cathode. From the ICP-OES test results, we found that the total metal ion concentrations were 24.5 and 41.8ppm at the anode and cathode, respectively, for uncoated SS316L, and 10.3ppm and 20.1ppm at the anode and cathode, respectively, for polypyrrole-coated SS316L. This is approaching the target of 10ppm (total metal ion concentration) for the 5000h lifetime of a PEM fuel cell.

10. The nucleation and growth behavior of the polypyrrole coating on Au-coated SS316L was different from that observed for a polypyrrole coating on bare SS316L. The nature of the base material can therefore affect the nucleation and growth behavior of the polypyrrole coating. After coating with Au and polypyrrole, the polarization resistance of SS316L is increased about 6 times, and the corrosion current density is decreased about 7 times, compared to the base SS316L. Also, the corrosion is much more severe in the PEMFC cathode environment than in the anode environment. From the ICP-MS results, we determined that the polypyrrole/Au/SS316L led to the lowest metal ion concentration in solution compared to uncoated SS316L and polypyrrole-coated SS316L. Our calculations show that the metal ion concentration in solution for the polypyrrole/Au/SS316L had met the target of 10ppm after 5000 hours fuel cell operation.

An overall summary of all materials and their corrosion properties is given in Table 8.1.

Table 8.1. An overall summary of all materials and their corrosion properties

Material	SS316L	SS347	SS410	Al6061	A36	Ti	TiN-coated SS316L	Polypyrrole-coated SS316L	Au/polypyrrole-coated SS316L
Polarization resistance R_p/(Ω·cm²)	328	1927	60	672	56	4110	9930	3459	1850
Polarization current density i_{corr}/(μA/cm²)	40.01	11.24	380.94	64.78	805.11	7.65	1.02	2.38	5.46
Corrosion current density at the anode (A/cm²)	-1×10^{-5}	-6×10^{-6}	2.5×10^{-2} then changes to 4×10^{-3}	4×10^{-3}	5×10^{-3}	-8×10^{-6}	-4×10^{-5}	$-1 \sim -2 \times 10^{-5}$	-2×10^{-5}
Corrosion current density at the cathode (μA/cm²)	8×10^{-6}	7×10^{-6}	4×10^{-3}	1.5×10^{-2}, then changes to 4×10^{-3}	2.5×10^{-2}, then changes to 4×10^{-3}	2×10^{-5}	2.5×10^{-5}	1×10^{-5}	$6 \sim 7 \times 10^{-6}$
Metal ions at anode (ppm) after 5000hours	24.5	N/A	N/A	N/A	N/A	N/A	12.3	10.3	10
Metal ions at cathode (ppm) after 5000 hours	41.8	N/A	N/A	N/A	N/A	N/A	59.3	20.1	11.5

CHAPTER 9

RECOMMENDATIONS FOR FUTURE WORK

Based on the results of the present study, the following research areas are suggested for future work.

1.Other commercially available metallic materials, eg. Ni, Cu with high corrosion resistance should be investigated in the PEM fuel cell environments.

2.Optimization of TiN coating parameters.

1) Change the coating thickness. The thickness of the coating can affect the corrosion resistance of the coated metals. Therefore, it is important to find the optimum coating thickness for TiN coating.

2) N/Ti ratio. The ratio of N and Ti can affect the structure and properties of the coatings. Change the N/Ti ratio to maintain a uniform coating. From the phase diagram of TiN, we know that TiN has a wide range of composition and Ti_2N has a specific composition. Therefore, different compositions of TiN have different properties. From the standard XRD diffraction data, we know that there are the following Ti-N compounds. ($TiN_{0.26}$, $TiN_{0.30}$, Ti_2N, $TiN_{0.98}$, TiN, Ti_4N_{2-x}, Ti_3N_{2-x})

3) Produce a functionally-graded coating. Functionally-graded coatings can increase the corrosion resistance of the coating and the adhesion between the coating and base material. Two types of functionally graded coatings are proposed.

    A. From high N to low N

    B. From low N to high N

4) Effects of Ti interlayer on the properties of the coatings. TiN has a columnar structure and there are micro-pores and pinholes on the coating surface. The electrolyte can diffuse to the base material and cause pitting corrosion and galvanic corrosion. Through our tests on the TiN coating on SS316L, we found that the corrosion rate of TiN coated SS316L is higher than the uncoated SS316L at 0.6VvsSCE. We, therefore, propose to add a Ti interlayer between the base material and the TiN coating.

5) Multilayer Ti interlayer. In order to improve the properties of the coatings, a mutilayered structure is proposed.

Ti+TiN+Ti+TiN............coating(the last layer should be TiN because Ti can be corroded in PEM fuel cell environments)

3. Investigate the effects of different metal ions on the conductivity of the membrane. Different metal ions have different effects on the membrane performance. By determining the effects of different metal ions on the performance of the membrane, we should be able to select and design more suitable metals and coatings.

4. Recently some researchers from National Renewable Energy Laboratory have measured the proton conductivity in a real fuel cell operation condition, and found > 100 ppm metal ion tolerance for the proton exchange membrane. The levels of metal ions is much higher than that found by Ma el al, which is the basis in this dissertation. Therefore, more work about effects of metal ions on the conductivity of membrane needs to be done to decide the tolerant metal ion levels.

5. Design the flow channels in the best metallic material and test fuel cells with metallic bipolar plates and compare the results with non-porous graphite bipolar plates.

VITA AUCTORIS

NAME: Yan Wang

PLACE OF BIRTH   Tianjin, China

YEAR OF BIRTH   1978

EDUCATION   University of Windsor, Windsor, Ontario, Canada
                        2004-2008 PHD in Engineering Materials
                        Tianjin University, Tianjin, China
                        2001-2004 M.Sc in Electrochemical Engineering
                        Tianjin University, Tianjin, China
                        1997-2001 B.Sc in Electrochemical Engineering

AFFILIATIONS   American Electrochemical Society (ECS)

PUBLICATIONS AND PRESENTATIONS RESULTING FROM THIS DISSERTATION RESEARCH

Publications

(1) **Yan Wang**, Derek O. Northwood, An investigation on metallic bipolar plate corrosion in simulated anode and cathode environments of PEM fuel cells using potential-PH diagrams, International Journal of Electrochemical Science, 1(2006)447-455.

(2) **Yan Wang** and Derek O. Northwood, An investigation into polypyrrole coated 316L stainless steel as a bipolar plate material for PEM fuel cells, Journal of Power Sources, 163(2006)500-508.

(3) **Yan Wang** and Derek O. Northwood, An investigation into TiN-coated 316L stainless steel as a bipolar plate material for PEM Fuel Cells, Journal of Power Sources, 165(2007)293-298.

(4) **Yan Wang** and Derek O. Northwood, An investigation of the electrochemical properties of PVD TiN-coated SS410 in simulated PEM fuel cell environments, International Journal of Hydrogen Energy, 32(2007)895-902.

(5) **Yan Wang** and Derek O. Northwood, Effects of O_2 and H_2 on the corrosion of SS316L metallic bipolar plate materials in simulated anode and cathode environments of PEM fuel cells, Electrochimica Acta, 52(2007)6793-6798.

(6) **Yan Wang**, Derek O. Northwood, An investigation of commercial Grade 2 titanium as a bipolar plate material for PEM fuel cells, ECS Transactions, 11(2008)53-60.

(7) **Yan Wang**, Derek O. Northwood, An investigation into the effects of a nano gold interlayer on polypyrrole coatings on 316L stainless steel for the bipolar plates of PEM fuel cells, Journal of Power Sources, 175(2008)40-48.

(8) **Yan Wang**, Derek O. Northwood, Life-limiting Aspects of the Corrosion of Metallic Bipolar Plates for PEM Fuel Cells, Advanced Materials Research, 41-42(2008)469-475.

(9) **Yan Wang**, Derek O. Northwood, An investigation of electrochemically deposited polypyrrole coatings on stainless steel bipolar plates for a PEM fuel cell, 14th Asian-

Pacific Corrosion Control Conference, Shanghai, China, October 21-24,2006, Paper no 13-05, Published as CD-ROM, 6 pages.

(10) **Yan Wang** and Derek O.Northwood, An investigation into uncoated and coated metallic bipolar plate materials for PEM fuel cells, International Power Sources Symposium & Exhibition, Bath, UK, April 23 -25 2007, Published as CD-ROM, 12 pages.

(11) **Yan Wang**, Derek O. Northwood, An investigation into the nucleation and growth of an electropolymerized polypyrrole coating on a 316L stainless steel surface, Thin Solid Films, 516(2008)7427-7432.

(12) **Yan Wang**, Derek O. Northwood, Optimization of the Polypyrrole-coating Parameters for Proton Exchange Membrane Fuel Cell (PEMFC) Bipolar Plates using the Taguchi Method, Journal of Power Sources, 185(2008)226-232.

(13) **Yan Wang**, Derek O. Northwood, An Electrochemical Investigation of Potential Metallic Bipolar Plate Materials for PEM Fuel Cells, submitted to International Journal of Hydrogen Energy.

Presentations

(1) **Yan Wang**, Derek O. Northwood, An Electrochemical Investigation of Potential Metallic Bipolar Plate Materials for PEM Fuel Cells, Presented at International Symposium on Solar-Hydrogen-Fuel Cells, Cancun, Mexico, August 20-24,2006.

(2) **Yan Wang**, Derek O. Northwood, An investigation of electrochemically deposited polypyrrole coatings on stainless steel bipolar plates for a PEM fuel cell, 14th Asian-Pacific Corrosion Control Conference, Shanghai, China, October 21-24,2006.

(3) **Yan Wang** and Derek O.Northwood, An investigation into uncoated and coated metallic bipolar plate materials for PEM fuel cells, International Power Sources Symposium & Exhibition, Bath, UK, April 23 -25 2007

(4) **Yan Wang**, Derek O. Northwood, An investigation of commercial Grade 2 titanium as a bipolar plate material for PEM fuel cells, 212th ECS Meeting, Washington, DC, USA, October 7-12, 2007.

(5) **Yan Wang,** Derek O. Northwood, Optimization of the Polypyrrole-coating Parameters for PEM Fuel Cell Bipolar Plates using the Taguchi Method, Corrosion Control 007, Sydney, Australia, November 25-28, 2007

(6) **Yan Wang** and Derek O.Northwood, Life-limiting Aspects of the Corrosion of Metallic Bipolar Plates for PEM Fuel Cells, International Conference &Exhibition on Structural Integrity and Failure, Western Australia, Australia, July 9-11, 2008.

Book Chapter

(1) **Yan Wang**, Derek O. Northwood, The Development of Bipolar Plate Materials for Polymer Electrolyte Membrane Fuel Cells (PEMFCs), Accepted on July 29, 2008 by Nova Science Publishers, Inc, New York.

OTHER PUBLICATIONS DURING Ph.D STUDY

(1) **Y. Wang**, Z. Gong, M. Geng, J. Yan and D. O. Northwood, Improved high-temperature performance of advanced nickel-metal hydride batteries through materials development. Materials Forum, 27(2004)28-32.

(2) X. Zhang, Z. Gong, S. Zhao, M. Geng, **Y. Wang** and D. O. Northwood, High-temperature characteristics of advanced Ni-MH batteries using electrodes containing CaF_2. Journal of Power Sources, 175(2008)630-634.